

**EFFECT OF SEISMICITY AND DIKING ON HYDROTHERMAL
CIRCULATION AT MID-OCEAN RIDGES**

A Dissertation
Presented to
The Academic Faculty

by

Pierre Ramondenc

In Partial Fulfillment
of the Requirements for the Degree
Doctor of Philosophy in the
School of Civil and Environmental Engineering

Georgia Institute of Technology
April 2008

EFFECT OF SEISMICITY AND DIKING ON HYDROTHERMAL CIRCULATION AT MID-OCEAN RIDGES

Approved by:

Dr. Leonid N. Germanovich, Advisor
School of Civil and Environmental
Engineering
Georgia Institute of Technology

Dr. Haiying Huang
School of Civil and Environmental
Engineering
Georgia Institute of Technology

Dr. Glenn J. Rix
School of Civil and Environmental
Engineering
Georgia Institute of Technology

Dr. Robert P. Lowell
School of Earth and Atmospheric
Sciences
Georgia Institute of Technology

Dr. Wenyue Xu
School of Earth and Atmospheric
Sciences
Georgia Institute of Technology

Dr. Daniela Di Iorio
Department of Marine Sciences
University of Georgia

Date Approved: December 18, 2007

To Agnès, Hélène, Verónica and Philippe,
who always believed in me

ACKNOWLEDGEMENTS

I wish to thank Dr. Leonid N. Germanovich and Dr. Robert P. Lowell for their guidance and support throughout my research and studies at Georgia Tech. Their trust and encouragement were an invaluable strength and motivation for accomplishing the work presented here. Above all, their way of addressing challenges, whether scientific or not, gave me a whole new perspective of life that, I believe, will be a precious resource in my future.

I would like also to thank Dr. Daniela Di Iorio, Dr. Haiying Huang, Dr. Glenn J. Rix, and Dr. Wenye Xu for serving in my thesis committee. Their insightful comments and suggestions greatly improved this dissertation. I am particularly grateful to Dr. Daniela Di Iorio, as well as Dr. Karen L. Von Damm and Dr. Charles R. Fisher, for the opportunity to join their cruises and deploy our heat flow measurement devices.

The completion of this research was also possible through the contributions of the past and present members of the Rocks and Fracture Mechanics Group at Georgia Tech: Dr. Hong Chang, Dr. Jongwon Choi, Gence Genc, Charlie George, Devon Gwaba, Robert Hurt, Sihyun Kim, Dr. Cem Ozan, Chanin Ruangthaveekoon, Dr. Youngjong Sim, Dr. Peter Van Dyke, and Dr. Ruiting Wu. I am particularly in debt to Robert Hurt and Gence Genc for their help with the manufacturing of the devices described in this dissertation.

I cannot fail to thank my wife, Dr. Verónica Rebata Landa, for her love and endless encouragement. Her faith in me never weakened, no matter how altered mine was. I also want to express my deep gratitude to my beloved parents, Hélène and Philippe Ramondenc, and my dear sister, Agnès Vergne, for their continuous encouragement and unconditional support, no matter what it cost them.

Finally, I would like to thank the financial support provided by Ridge 2000, the National Science Foundation (grants OCE 0221974, OCE 0327126, and OCE 0527208), and Georgia Tech Foundation during the years of my Ph.D. studies.

TABLE OF CONTENTS

	Page
ACKNOWLEDGEMENTS	iv
LIST OF TABLES	ix
LIST OF FIGURES	x
SUMMARY	xiv
<u>CHAPTER</u>	
1 Introduction	1
1.1 References	15
2 The first measurements of hydrothermal heat output at 9°50' N, East Pacific Rise	21
2.1 Introduction	22
2.2 Geological setting	28
2.3 Measurement device	30
2.4 Measurement results	34
2.5 Discussion and conclusions	39
2.6 Acknowledgements	44
2.7 References	45
3 Modeling hydrothermal response to earthquakes at oceanic spreading centers	51
3.1 Introduction	52
3.1.1 Magmatic and tectonic events at mid-ocean ridges	53
3.1.2 The hydrothermal response	55
3.2 Mechanics of hydrothermal response	60
3.2.1 <i>Wilcock's</i> [2004] work	61

3.2.2	Approach in this paper	65
3.3	Formulation	68
3.3.1	Mixing in the shallow crust	68
3.3.2	Mass fluxes in the system and conservation laws	73
3.3.3	Boundary conditions	79
3.3.4	Initial conditions	80
3.4	Numerical results	81
3.5	Modeling the March 1995 East Pacific Rise event	88
3.5.1	A possibility of diking event	88
3.5.2	Heat from possible dike emplacement	92
3.5.3	Permeability enhancement	93
3.5.4	Discussion	97
3.6	Conclusion	101
3.7	Acknowledgements	101
3.8	References	103
4	Magmatic origin of the March 1995 earthquake swarm at 9°50' N, East Pacific Rise	113
4.1	Introduction	113
4.2	Mechanics of the March 1995 swarm	115
4.3	Hydrothermal modeling	120
4.4	Matching transient temperature records	133
4.5	Discussion	139
4.6	Conclusion	142
4.7	Acknowledgements	143
4.8	References	144
5	Conclusions and recommendations	150

5.1	Conclusions	150
5.2	Recommendations for future work	153
APPENDIX A:	Design of heat flow measurement devices	156
APPENDIX B:	Discussion of <i>Wilcock's</i> [2004] temperature perturbation model	175
B.1	References	178
APPENDIX C:	Dimensionless parameters	180
C.1	Summary of equations	180
C.2	Scaling of problem without mixing	183
C.3	Dimensionless equations	188
C.4	Concluding remarks	198
C.5	References	200
APPENDIX D:	FORTTRAN 90 source code	202
APPENDIX E:	Direction of dike propagation from the magma lens	213
E.1	References	214
APPENDIX F:	Flow regime in the upflow zone	215

LIST OF TABLES

	Page
Table 2.1: Thermal data from seafloor hydrothermal systems.	24
Table 2.2: Results from the flow measurements and heat output estimates.	31
Table 2.3: Heat output estimates for the 9°50.1' - 9°50.7' N EPR vent complex.	41
Table 3.1: Symbol definitions and parameter values.	64
Table 4.1: Symbol definitions and parameter values.	124

LIST OF FIGURES

	Page
Figure 1.1: Black smokers and surrounding biological communities.	2
Figure 1.2: Map of the global ridge crest system indicating the major mid-ocean ridge sections [<i>German and Von Damm, 2004</i>].	3
Figure 1.3: Crustal formation at mid-ocean ridges [<i>Nicolas, 1995</i>].	5
Figure 1.4: Hydrothermal circulation in the oceanic crust at mid-ocean ridges [<i>Alt, 1995</i>].	5
Figure 1.5: Cartoon of a single-pass hydrothermal circulation model at an ocean ridge crest at local ridge crest circulation scale [from <i>Germanovich et al., 2000</i>].	9
Figure 1.6: The 9°50' N area on the East Pacific Rise (EPR).	9
Figure 1.7: The Endeavour Segment on the Juan de Fuca Ridge.	10
Figure 1.8: The March 1995 seismic event on the East Pacific Rise at 9°50' N [<i>Sohn et al., 1999</i>].	11
Figure 2.1: Map showing the distribution of vents in the 9°49-51' N area on the East Pacific Rise.	29
Figure 2.2: Device in its two configurations: (a) view of the top of the device, and (b) view of the bottom of the device.	32
Figure 2.3: Deployment of the device for flux measurements of (a) high-temperature venting at Bio 9 (dive # 3992) and (b) diffuse flow venting at Tica (dive # 3991).	35
Figure 2.4: Example of flow velocity measurement at Tica vent area (dive # 3991).	36
Figure 2.5: Chimney samples collected from (a) P middle vent during <i>Alvin</i> 's dive # 3987 and (b) Marker 22 during <i>Alvin</i> 's dive # 3988, respectively.	38
Figure 3.1: Thermal response of the high-temperature Bio9 vent at East Pacific Rise 9°50' N [from <i>Sohn et al., 1998</i>].	59
Figure 3.2: Steady state temperature distribution in the discharge zone prior to the earthquake and definition of the boundary layer.	66

Figure 3.3: Cartoon of a single-pass hydrothermal circulation model at an ocean ridge crest at the local, ridge crest circulation scale.	67
Figure 3.4: Schematic representation of focusing with adjacent diffuse flow in the upper part of the upflow zone.	71
Figure 3.5: “Double-loop” single-pass model adapted from Figure 3.3.	72
Figure 3.6: Variation of the steady-state temperature profile with the thickness d of the impermeable thermal boundary layer situated between the magma chamber and the base of the hydrothermal system.	85
Figure 3.7: Variations similar to Figure 3.6 but for somewhat larger mass fluxes.	86
Figure 3.8: Temperature profile 1 year after changing the thickness d of the impermeable thermal boundary layer.	86
Figure 3.9: Temperature profile 5 years after changing the thickness d of the impermeable thermal boundary layer.	87
Figure 3.10: Temperature profile 1 year after changing the thickness d of the impermeable thermal boundary layer.	87
Figure 3.11: Temperature profile 5 years after changing the thickness d of the impermeable thermal boundary layer.	88
Figure 3.12: Ridge normal cross section of relocated north group events with 1σ error bars [modified from <i>Sohn et al.</i> , 1999] and finite element simulation of dike propagation from magma chamber.	89
Figure 3.13: Interpretation given by <i>Sohn et al.</i> [1999] of the March 1995 seismic swarm beneath Bio9 high-temperature vent field.	90
Figure 3.14: Evolutionary model from <i>Carbotte et al.</i> [2006] for axial rift topography.	91
Figure 3.15: Temperature profile 1 year after the emplacement of a dike.	93
Figure 3.16: Evolution of temperature profile in (a) the bottom of the upflow zone, (b) at the junction with the shallow recharge, and (c) in the first 50 cm below the seafloor ($d = 7.5$ m, $f = 5$ m, $w = 1$ m, and $k = 1.5 \times k_0$ around the dike margins).	95
Figure 3.17: Comparison of the calculated response ($d = 7.5$ m, $f = 5$ m, $w = 1$ m, and $k = 1.5 \times k_0$ around the dike margins) to a dike emplacement with the monitored response at Bio9 following the March 1995 East Pacific Rise event.	96

Figure 3.18: Comparison of the best fit to the March 1995 East Pacific Rise event ($d = 7.5$ m, $f = 5$ m, $w = 1$ m, and $k = 1.5 \times k_0$ around the dike margins) with other scenarios where only one parameter is modified at a time, all the others remaining the same.	99
Figure 4.1: Ridge normal cross-section of relocated events with error bars [Sohn <i>et al.</i> , 1998] and finite element simulation of dike propagation from magma chamber suggested on the cross-section.	116
Figure 4.2: Map of the 2006 East Pacific Rise eruption area with details of the erupted lava [Fornari <i>et al.</i> , 2006] and finite element simulation of dike propagation from the west margin of magma chamber.	119
Figure 4.3: Schematic of a “double-loop” single-pass model.	121
Figure 4.4: Variation of viscosity of water with temperature.	126
Figure 4.5: Typical steady-state temperature profiles along the discharge zone.	135
Figure 4.6: Comparison of the calculated temperature response of the black smoker to a dike emplacement with the monitored response at Bio9 following the March 1995 EPR event.	138
Figure 4.7: Finite element calculation of dike propagation from magma chamber.	142
Figure A.1: Blueprints of the first version of the heat flow measurement device.	158
Figure A.2: Blueprints of the parts used to build the first version of the heat flow measurement device.	160
Figure A.3: Second generation of the heat flow measurement device.	162
Figure A.4: Blueprints of the second version of the heat flow measurement device with a single central hole.	163
Figure A.5: Blueprints of the parts used to build the second version of the heat flow measurement device with a single central hole.	165
Figure A.6: Blueprints of the second version of the heat flow measurement device with multiple holes.	169
Figure A.7: Blueprints of the parts used to build the second version of the heat flow measurement device with multiple holes.	171
Figure A.8: Deployment of the device for flux measurements at Lau Basin during the September 2006 cruise.	173
Figure A.9: Deployment of the device for flux measurements in the 9°50' N area of the East Pacific Rise during the November 2006 cruise.	174

Figure B.1: Hydrothermal upflow of mean velocity v in a crack of width w_c situated between two half-spaces [modified from <i>Wilcock</i> , 2004].	176
Figure B.2: Solution of equation (B.4) plotted dimensionless at (a) the bottom and (b) the top of the upflow zone.	177
Figure B.3: Solution of equation (B.4) plotted dimensionless (a) along the upflow zone for $x = 0$, and (b) in the horizontal direction (x -axis) half way to the seafloor.	179
Figure C.1: Variation of viscosity of water with temperature.	186
Figure E.1: Dike trajectories.	214

SUMMARY

Seafloor hydrothermal systems play a key role in Earth's energy and geochemical budgets. They also support the existence and development of complex chemosynthetic biological ecosystems that use the mineral-laden fluids as a source of energy and nutrients. This dissertation focuses on two inter-related topics: (1) the heat output at mid-ocean ridge (MOR) hydrothermal sites, and (2) the hydrothermal response to earthquakes at mid-ocean ridges.

The response of mid-ocean ridge hydrothermal systems to seismic and magmatic activity could provide a means of using seafloor observations to assess processes occurring at crustal depths. Three decades of study of the ocean floor have made clear that tectonic/volcanic perturbations and changes in the hydrothermal activity are correlated. Yet, this relationship is still highly misunderstood. In this dissertation, we developed a mathematical model of hydrothermal circulation affected by magmatic and/or tectonic events occurring at depth. We showed that the perturbations they generate need not propagate through the entire upflow zone, as previously suggested, but need only affect the movement of the boundary layers. In this case, the fluid residence time in the discharge zone is on the order of years.

The determination of heat output at MOR hydrothermal sites provides important constraints on the physics of these processes. Yet, such measurements are still very limited, available only for ~30 sites out of the $\sim 10^3$ estimated worldwide. This dissertation reports the first measurements of hydrothermal heat output at 9°50' N on the

East Pacific Rise (EPR), which has been the most intensively studied site for the past 20 years ($\sim 10^2$ expeditions). The values we obtained helped constraining the aforementioned mathematical model, which was tested based on the March 1995 microearthquake swarm near $9^{\circ}50'$ N, EPR. Our results showed that the current interpretation based on a thermal cracking episode at the bottom of the upflow zone, may be incorrect. We argue that a diking scenario better explains the seismic and temperature data, while being consistent with the mechanics of inflation of the axial magma chamber in the $9^{\circ}50'$ N, EPR area between two major eruptions, in 1991 and 2006.

CHAPTER 1

INTRODUCTION

The discovery of hydrothermal activity [e.g., *Corliss et al.*, 1979; *Rona et al.*, 1975], followed by the one of “black smoker” vents (chimneys venting high-temperature fluids; Figure 1.1) on the East Pacific Rise [*Macdonald et al.*, 1980; *Spiess et al.*, 1980], revolutionized the understanding of seafloor processes in many aspects. It confirmed the idea that the discrepancy existing between conductive heat flow measurements through seafloor sediments and lithospheric heat loss determined from seafloor spreading models could be explained by hydrothermal circulation deep in the oceanic crust [*Anderson and Hobart*, 1976; *Lister*, 1972; *Williams et al.*, 1974; *Wolery and Sleep*, 1976]. Further studies later showed that seafloor hydrothermal systems (Figure 1.2) were responsible for approximately 25% of the Earth’s total heat flux, 10% of which may be due to high-temperature venting alone [*Elderfield and Schultz*, 1996; *Stein and Stein*, 1994; *Stein et al.*, 1995]. The circulation of hydrothermal seawater through the oceanic crust was shown to be highly influenced by tectonic and volcanic events occurring at crustal depths [e.g., *Baker et al.*, 1999; *Johnson et al.*, 2000; *Sohn et al.*, 1998]. It was also shown to have a great impact on the geochemical budget of oceans, some elements being washed out while others are enriched as a result of chemical reactions with crustal rocks [*Butterfield et al.*, 1997; *Butterfield and Massoth*, 1994; *Edmond et al.*, 1979; *Von Damm et al.*, 1995]. The resulting discharge then supports the existence and development of complex chemosynthetic biological ecosystems that use the mineral-laden fluids as a source of energy and nutrient [*Jannasch*, 1995; *Kelley et al.*, 2002; *Shank et al.*, 1998].

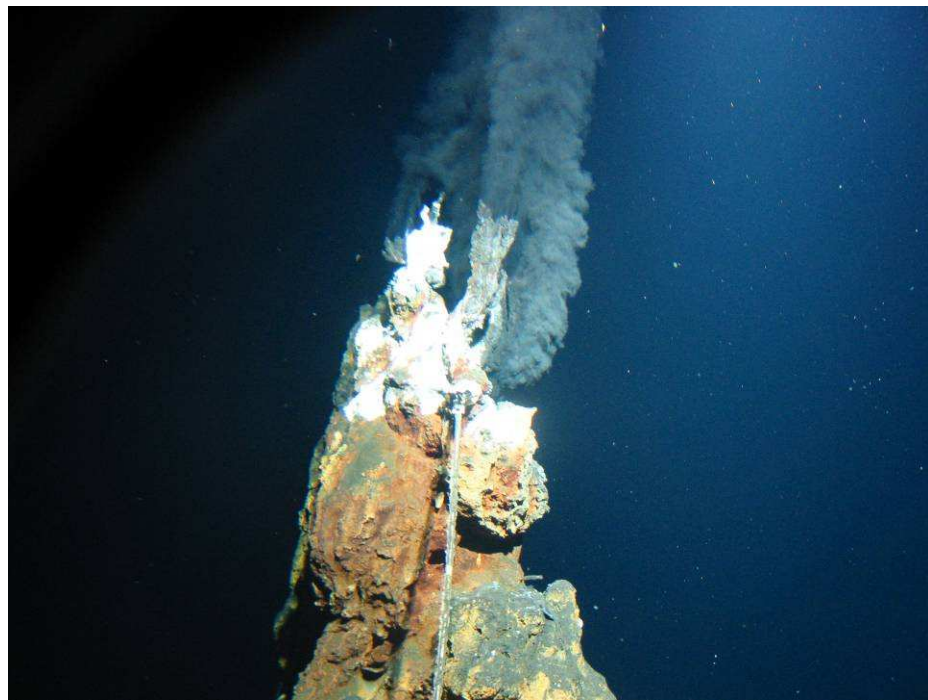
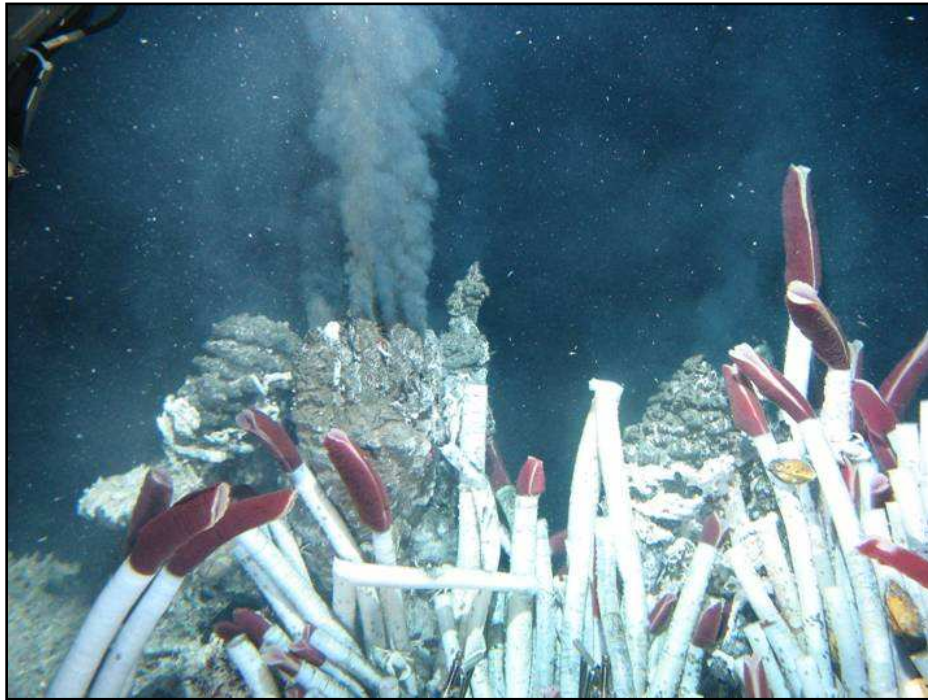
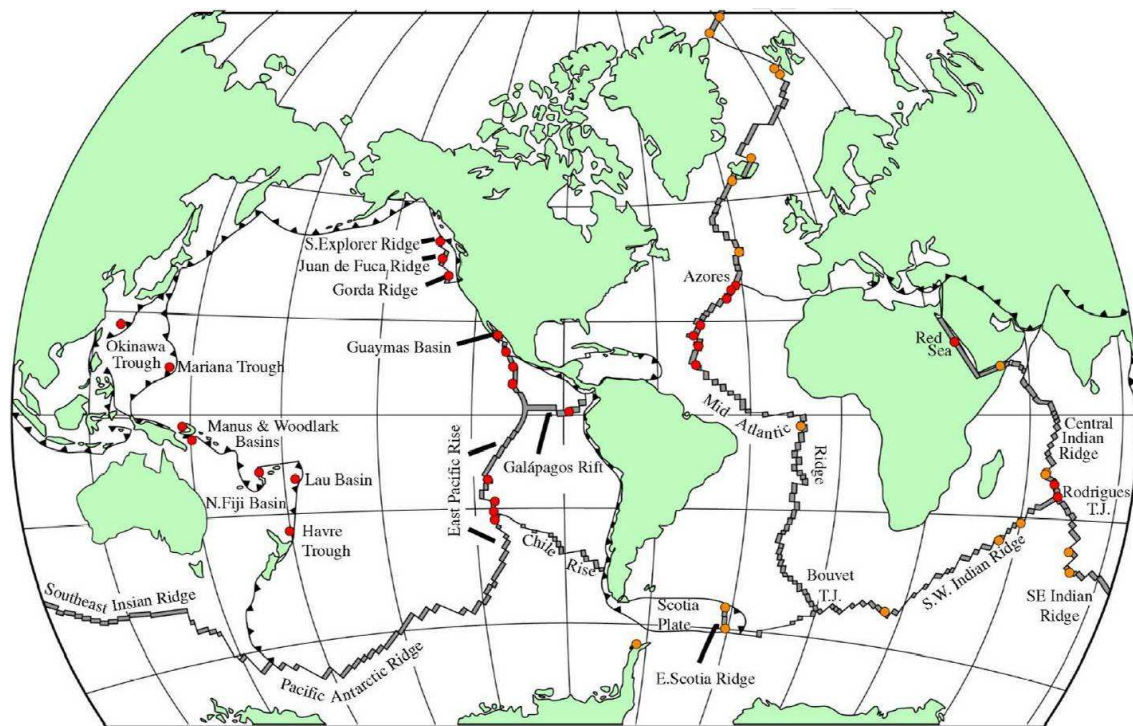


Figure 1.1. Black smokers and surrounding biological communities (tube worms, mussels and crabs). Pictures taken during dive #3987 of the March 2004 expedition (AT11-09) to 9°50' N, East Pacific Rise.



Locations of known hydrothermal activity along the global mid-ocean ridge system

● = known active sites ● = active sites indicated by midwater chemical anomalies

Figure 1.2. Map of the global ridge crest system indicating the major mid-ocean ridge sections [German and Von Damm, 2004]. Red circles represent sites where active hydrothermal vents have already been found. Orange circles show sites where hydrothermal activity is known to exist from the detection of characteristic chemical signals in the overlying water column.

This dissertation focuses on two inter-related topics: (1) heat output at mid-ocean ridge hydrothermal sites, and (2) hydrothermal response to earthquakes at mid-ocean ridges.

Seafloor hydrothermal activity at the ridge axis is closely related to the formation of the ocean floor (Figure 1.3). Through the extensive fractures resulting from ocean spreading mechanisms, seawater sinks into the crust and is heated at depth either by magmatic heat sources or due to serpentinization of mantle peridotites. The fluids then resurface, greatly modified due to chemical interactions with crustal rocks (Figure 1.4). The determination of heat output at the scale of an individual vent field is important for several reasons. First of all, when coupled with vent temperature, it provides important constraints on the physics of seafloor hydrothermal processes. Models using these two constraints have been used to infer crustal permeability at the ridge axis [*Lowell and Germanovich*, 1994, 2004; *Pascoe and Cann*, 1995; *Wilcock and McNabb*, 1996], an important fluid flow parameter that cannot be reliably determined by other means. Also, the observational data provide important constraints on the thickness of the conductive boundary layer separating hydrothermal circulation from the underlying magmatic heat source [e.g., *Lister*, 1983; *Lowell and Germanovich*, 1994]. Finally, heat output, and hence fluid flow rate, may provide important information on nutrient transport to biological ecosystems. Determination of heat output at hydrothermal sites is thus critical to an integrated understanding of ridge crest processes.

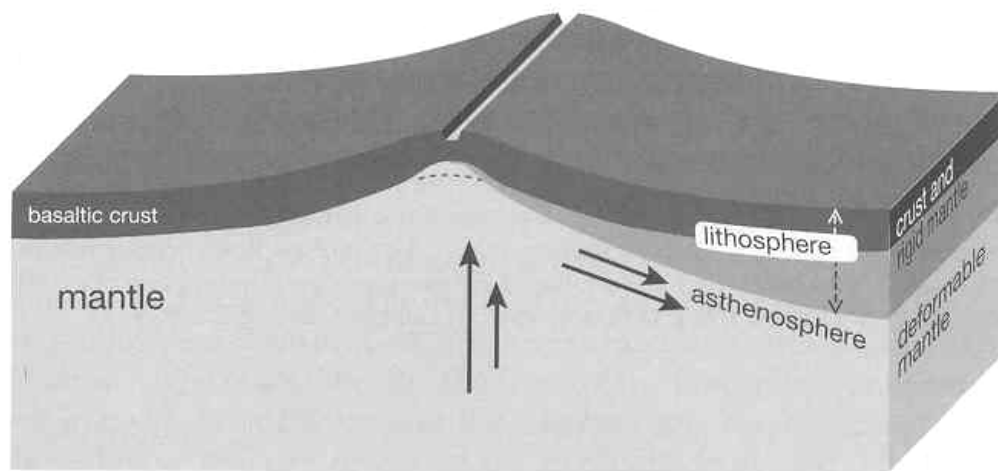


Figure 1.3. Crustal formation at mid-ocean ridges [Nicolas, 1995].

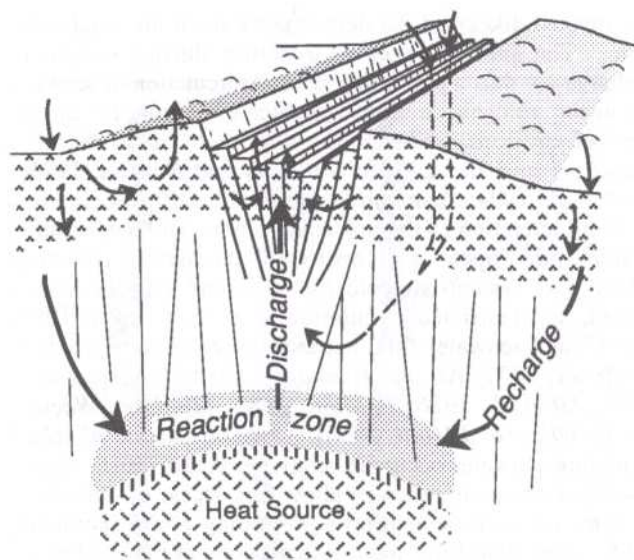


Figure 1.4. Hydrothermal circulation in the oceanic crust at mid-ocean ridges [Alt, 1995]. Note the two types of recharge: deep and shallow.

Despite this importance, direct measurements of hydrothermal heat output at active hydrothermal vent sites are very limited. Of the $\sim 10^3$ active high-temperature vent sites predicted to occur along the 67,000 km of ocean ridge [Baker and German, 2004; German and Von Damm, 2004; Lowell and DuBose, 2005] fewer than 30% (~ 280) have been identified (Figure 1.2). Heat output has been determined at fewer than 10% (~ 30) of known hydrothermal sites. In this work, we were particularly interested in exploring the partitioning between diffuse and focused flow components. This is of prime importance in order to better constrain the modeling of hydrothermal circulation in the oceanic crust. Our main objective was to design a simple and robust device in order to make direct seafloor measurements of advective fluid flow, which provide hydrothermal heat output when coupled with temperature data. We tested our device during the March 2004 expedition (AT11-09) to the $9^{\circ}50'$ N area of the East Pacific Rise. Despite the intensive study for the past 15 years, no heat output data had been obtained for this RIDGE 2000 Integrated Study Site. The measurements we made were the first ones on this portion of the ridge system. However, since these are just snapshots at a particular time, our long-term goal is to promote the development of regular such measurements. We thus improved the design of this device to make it widely available to any investigator exploring the seafloor at mid-ocean ridges.

The second topic of this dissertation is the modeling of the hydrothermal response to earthquakes at mid-ocean ridges. Their study is of considerable significance because they may provide better constraints on subsurface properties than steady state models. It is still difficult today to clearly identify and differentiate magmatic and tectonic events at mid-ocean ridges. The main reason resides in the difficulty to observe and monitor such

environments, despite advances in seafloor imagery and exploration systems [e.g., *Fornari et al.*, 2004; *White et al.*, 2006]. Additionally, many physical parameters of the crust, such as permeability and fluid flow rate, are still unknown or poorly constrained, even though some fluid parameters (temperature and chemical variations of the venting fluids, evolution of biological communities, and in some cases, estimates of the flow rate and heat output, as discussed previously) can be recorded at the seafloor. Although seismic [e.g., *Crawford and Webb*, 2002; *Vera et al.*, 1990] and borehole drillings [e.g., *Becker and Davis*, 2003; *Becker et al.*, 1989; *Wheat et al.*, 2004] data has gradually become available, what happens in the crust in most cases still remains a black box.

Tectonic and volcanic perturbations in the crust generally lead to changes of the hydrothermal system flow regime, its chemical signature, as well as the biological ecosystems that it is hosting [*Cowen et al.*, 2004; *Haymon et al.*, 1993; *Shank et al.*, 1998; *Von Damm*, 2000]. While most of the studies to date suggest a clear correlation between hydrothermal system alterations and tectonic and/or magmatic events situated directly below [*Baker et al.*, 1999; *Sohn et al.*, 1998] or at a regional distance [*Johnson et al.*, 2001; *Johnson et al.*, 2000] from the vent fields, *Dziak et al.* [2003] also presented evidence that large transform earthquakes can have a significant impact, even when situated across tectonic regions. The generation of “event plumes” (or “megaplumes”), result of the rapid release of large quantities of buoyant, heated fluid, is the most spectacular manifestation of the physical alteration of the hydrothermal flow. These plumes may discharge up to 10^{14} - 10^{17} J of heat in a few days [*Baker*, 1998; *Baker et al.*, 1987; *Baker et al.*, 1995], while featuring rapid variations of the chemical and biological compositions of the hydrothermal fluid [*Cowen et al.*, 2004]. In comparison, a typical

black smoker field discharges only $10^{10} - 10^{12}$ J during the same time [e.g., *Baker et al.*, 1998; *Rona et al.*, 1993].

Three decades of study of the ocean floor have made clear that tectonic/volcanic perturbations and changes in the hydrothermal activity are correlated. Yet, this relationship is still highly misunderstood. This work is an attempt to make a step in this direction. We employed a single-pass model (Figure 1.5) [*Germanovich et al.*, 2000; *Lowell and Germanovich*, 2004; *Pascoe and Cann*, 1995], to which we added a second loop modeling the shallow recharge of cold seawater in the shallow crust (also called “extrusives”). An advantage of this approach is that the same model formulation can be used to address perturbations to high-temperature systems such as Bio9 vent on the 9°50' N area, East Pacific Rise (Figure 1.6), as well as low-temperature diffuse flow systems such as those observed on the Endeavour Segment, Juan de Fuca Ridge (Figure 1.7). We recognized that during porous discharge lateral heat losses and mixing in the shallow subsurface resulted in thin thermal boundary layers near the seafloor and at the junction where mixing with the shallow recharge occurs. Therefore, as a magmatic and/or tectonic event occurs at depth, the perturbation it generates need not propagate through the entire discharge zone as previously suggested [*Fornari et al.*, 1998; *Sohn et al.*, 1998; *Sohn et al.*, 1999; *Wilcock*, 2004], but need only affect the movement of the boundary layers. In this case, the fluid residence time in the discharge zone is on the order of years.

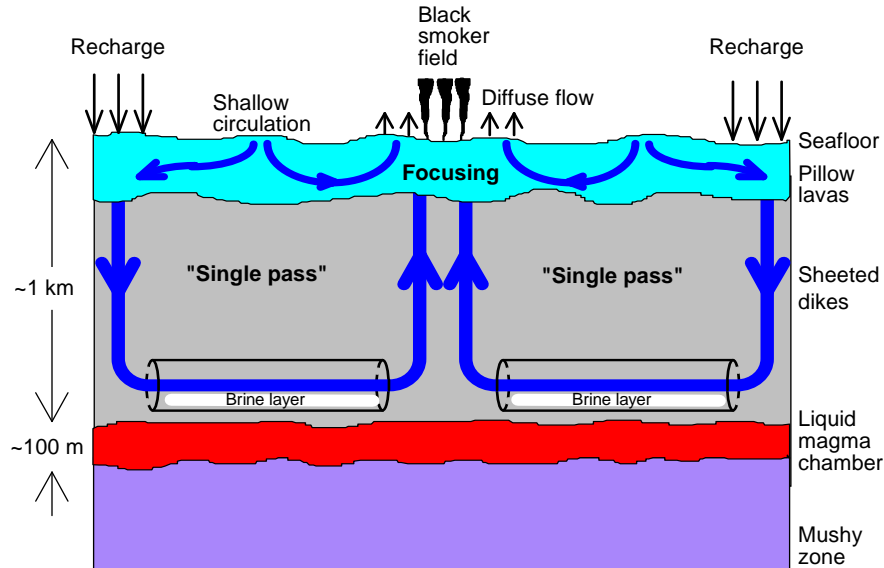


Figure 1.5. Cartoon of a single-pass hydrothermal circulation model at an ocean ridge crest at local ridge crest circulation scale [from *Germanovich et al.*, 2000].

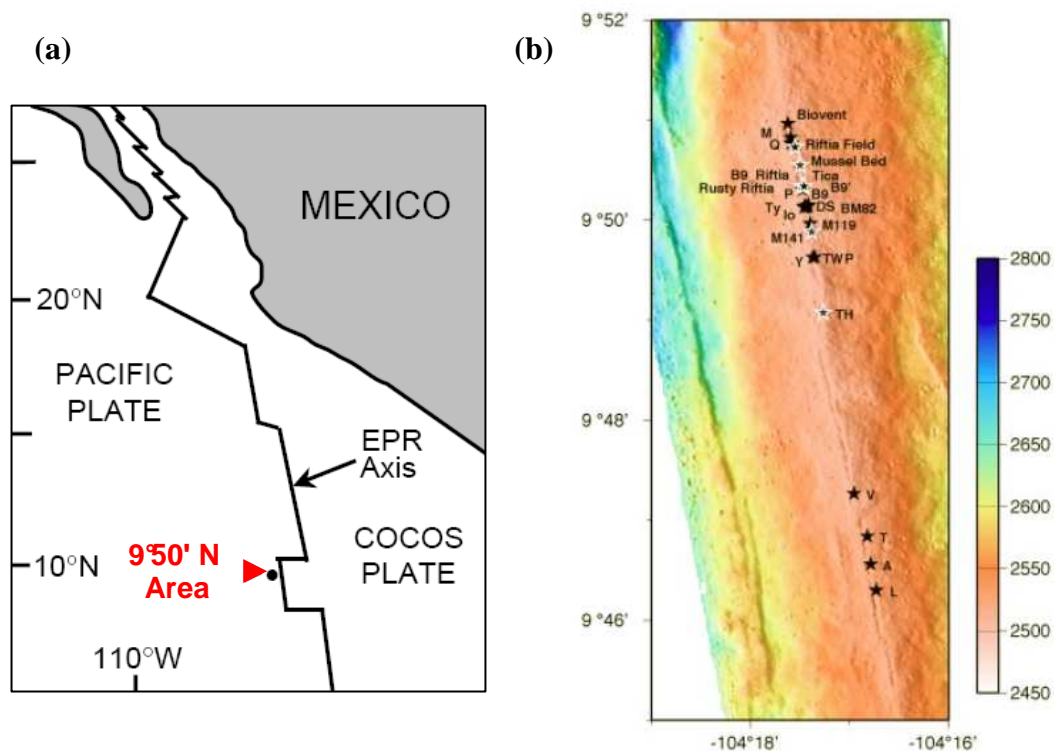


Figure 1.6. The 9°50' N area on the East Pacific Rise (EPR). (a) Location of the 9°50' N area, and ridge and transform plate boundary geometry [from *Sohn et al.*, 1998]. (b) Location of hydrothermal vents within the 9°50' N area vent field [www.ridge2000.org/science/iss/eprProjects.html].

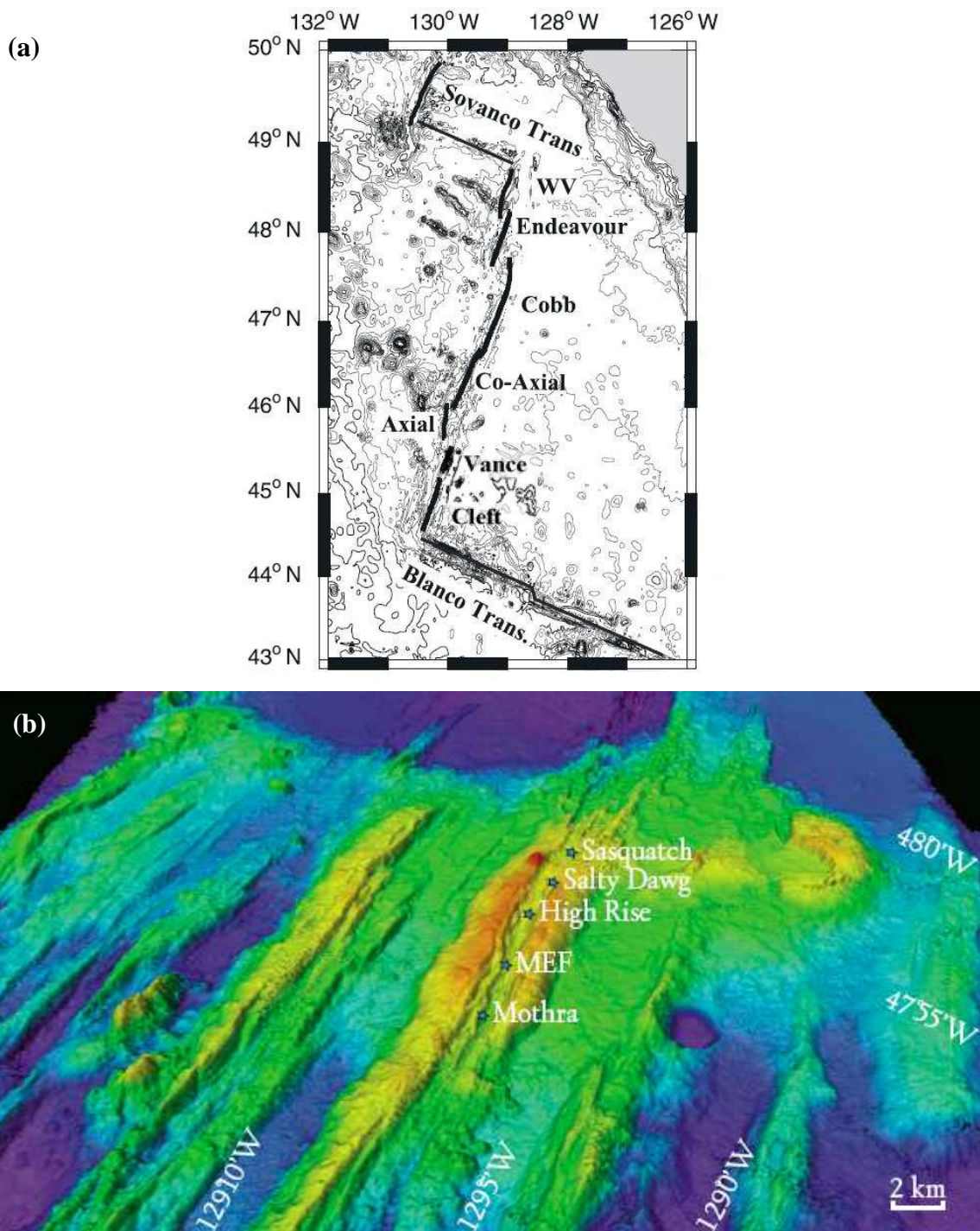


Figure 1.7. The Endeavour Segment on the Juan de Fuca Ridge. (a) Regional map of the Juan de Fuca Ridge system in the northeast Pacific Ocean, with location of the Endeavour Segment [from *Bohnenstiehl et al.*, 2004]. (b) Location of hydrothermal vent fields on the Endeavour Segment [*Glickson et al.*, 2007]. Each vent field gathers both high-temperature focused (black smokers) and low-temperature diffuse venting sites.

To test our mathematical and numerical models, we focused on the March 1995 microearthquake swarm on the East Pacific Rise near 9°50' N (Figure 1.8). This event is of particular importance because of its thorough documentation. It is also one of the very few events that feature both seismic and hydrological data. Our results showed that the current interpretation based on a thermal cracking episode at the bottom of the discharge zone [Fornari *et al.*, 1998; Sohn *et al.*, 1998; Sohn *et al.*, 1999] may be incorrect. We argue in this work that a diking scenario better explains the seismic and temperature data, while being in line with the mechanics of inflation of the axial magma chamber in the 9°50' N area of the East Pacific Rise.

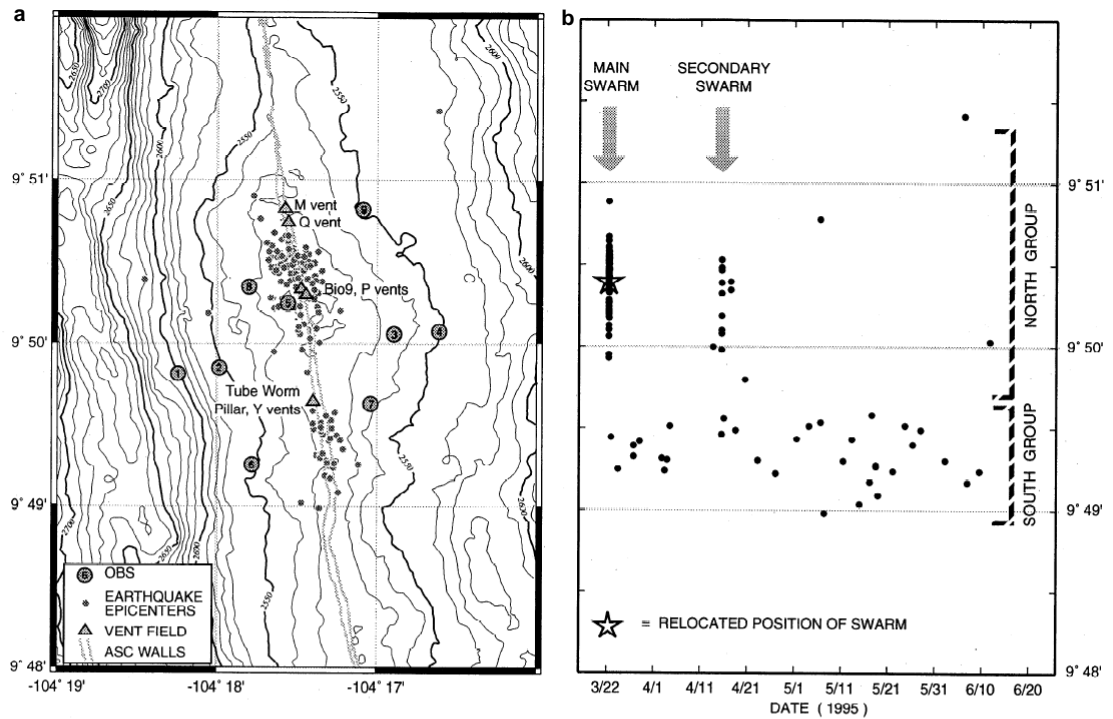


Figure 1.8. The March 1995 seismic event on the East Pacific Rise at 9°50' N [Sohn *et al.*, 1999]. (a) Map of the area with location of epicenters. (b) Chronology of microearthquakes with respect to latitude.

To present the work introduced above, this dissertation is organized into three relatively independent chapters. Each chapter is prepared in the format of a paper either already published, or submitted for publication, or intended for future publishing. Each one has its own introduction and list of references. Chapter 2 is devoted to the first discussed topic, while chapter 3 and 4 deal with the second one. An overview of each chapter follows.

Chapter 2 “*The first measurements of hydrothermal heat output at 9°50' N, East Pacific Rise*” [Ramondenc *et al.*, 2006]. This chapter reports the first measurements of hydrothermal heat output at the RIDGE 2000 Integrated Study Site on the East Pacific Rise. We focused our work on the Bio 9 complex, situated at 9°50' N, where there has been an extensive measurement and sampling program since 1991. This site is located along the eruptive fissure of the 1991/1992 event and the site of the 1995 earthquake swarm. We made direct measurements of advective heat output at several individual vents and at one site of diffuse flow (Tica). Although these data do not describe the complete heat flux picture at this vent field, the data yield a total hydrothermal heat output of $\sim 325 \text{ MW} \pm 160 \text{ MW}$ with $\sim 42 \text{ MW} \pm 21 \text{ MW}$ coming from high-temperature vents along this 2 km segment of ridge. This result assumes a diffuse flux similar to that measured at Tica occurs at each high-temperature vent site. Our initial measurements thus suggest that the heat output of the low-temperature diffuse venting is approximately 10 times that of the high-temperature vents, but may also be one or two orders of magnitude greater.

Chapter 3 “*Modeling hydrothermal response to earthquakes at oceanic spreading centers*” [Ramondenc *et al.*, 2008]. We develop a two-branch single-pass modeling approach to investigate the response of hydrothermal systems to earthquakes at oceanic spreading centers. In this approach, deep circulation gives rise to high temperature fluids that are assumed to arrive at the seafloor as focused, black smoker-like vents, whereas shallow circulation within the extrusives results in low-temperature diffuse flow. The diffuse flow is a mixture of black smoker fluid and seawater; consequently, seismic events that alter the permeability of the crust may affect both high-temperature vents and the low-temperature diffuse flow. In this model, ascending fluid in both the high- and low-temperature branches is nearly isothermal except within thin boundary layers at the seafloor and at the junction where fluid mixing occurs. As a result, thermal perturbations at depth do not need to traverse the entire upflow zone, but rather just need to affect the boundary layers. We show that cracking events, which generate new permeability and thereby increase the rate of heat transfer in a narrow zone at the base of the system, do not give rise to rapid temperature changes at the seafloor; however, only modest increases in permeability occurring over a region of a few hundred meters within the deep discharge zone are sufficient to generate observable thermal perturbations. Moreover, the response of the dynamically coupled circulation systems simultaneously results in an initial positive temperature pulse as well as the observed longer-lived temperature decrease in both the high- and low- temperature fluid.

Chapter 4 “*Magmatic origin of the March 1995 earthquake swarm at 9°50' N, East Pacific Rise*” [Germanovich *et al.*, 2008]. The response of mid-ocean ridge hydrothermal systems to seismic and magmatic activity could provide a means of using

seafloor observations to assess processes occurring at crustal depths. The correct interpretation of the March 1995 seismic activity and the subsequent hydrothermal response on the East Pacific Rise (EPR) near 9°50' N is of critical importance for understanding the links among magmatic, tectonic, and hydrothermal processes at mid-ocean ridges. We suggest that this seismic activity was caused by a small diking event that occurred during an interval of magma lens inflation that was bracketed by two major eruptions in 1991 and 2006. The diking scenario yields quantitative results that are in excellent agreement with temperature observations. This scenario explains seemingly different observations from the unified stand point of fracture mechanics. In particular, the diking explanation is consistent with both the thin, lens-like shape of the EPR magma chamber and with the seismic pattern displaced to its west margin.

1.1 References

- Alt, J. C. (1995), Subseafloor Processes in Mid-Ocean Ridge Hydrothermal Systems, in *Seafloor Hydrothermal Systems: Physical, Chemical, Biological, and Geological Interactions*, *Geophys. Monogr. Ser.*, vol. 91, edited by S. E. Humphris, et al., pp. 85-114, AGU, Washington, DC.
- Anderson, R. N., and M. A. Hobart (1976), The relation between heat flow, sediment thickness, and age in eastern Pacific, *J. Geophys. Res.*, 81(17), 2968-2989.
- Baker, E. T. (1998), Patterns of event and chronic hydrothermal venting following a magmatic intrusion: new perspectives from the 1996 Gorda Ridge eruption, *Deep Sea Res. II*, 45, 2599-2618.
- Baker, E. T., C. G. Fox, and J. P. Cowen (1999), In situ observations of the onset of hydrothermal discharge during the 1998 submarine eruption of Axial Volcano, Juan de Fuca Ridge, *Geophys. Res. Lett.*, 26(23), 3445-3448.
- Baker, E. T., and C. R. German (2004), On the Global Distribution of Hydrothermal Vent Fields, in *Mid-Ocean Ridges: Hydrothermal Interactions Between the Lithosphere and Oceans*, *Geophys. Monogr. Ser.*, vol. 148, edited by C. R. German, et al., pp. 245-266, AGU, Washington, DC.
- Baker, E. T., G. J. Massoth, and R. A. Feely (1987), Cataclysmic hydrothermal venting on the Juan de Fuca Ridge, *Nature*, 329, 149-151.
- Baker, E. T., G. J. Massoth, R. A. Feely, G. A. Cannon, and R. E. Thomson (1998), The rise and fall of the CoAxial hydrothermal site, 1993-1996, *J. Geophys. Res.*, 103(B5), 9791-9806.
- Baker, E. T., G. J. Massoth, R. A. Feely, R. W. Embley, R. E. Thomson, and B. J. Burd (1995), Hydrothermal event plumes from the CoAxial seafloor eruption site, Juan de Fuca Ridge, *Geophys. Res. Lett.*, 22(2), 147-150.
- Becker, K., and E. E. Davis (2003), New evidence for age variation and scale effects of permeabilities of young oceanic crust from borehole thermal and pressure measurements, *Earth Planet. Sci. Lett.*, 210, 499-508.

Becker, K., et al. (1989), Drilling deep into young oceanic crust, Hole 504B, Costa Rica Rift, *Rev. Geophys.*, 27, 79-102.

Bohnenstiehl, D. R., R. P. Dziak, M. Tolstoy, C. G. Fox, and M. Fowler (2004), Temporal and spatial history of the 1999-2000 Endeavour Segment seismic series, Juan de Fuca Ridge, *Geochem. Geophys. Geosyst.*, 5, Q09003, doi:10.1029/2004GC000735.

Butterfield, D. A., I. R. Jonasson, G. J. Massoth, R. A. Feely, K. K. Roe, R. E. Embley, J. F. Holden, R. E. McDuff, M. D. Lilley, and J. R. Delaney (1997), Seafloor eruptions and evolution of hydrothermal fluid chemistry, *Philos. Trans. R. Soc. Lond., Ser. A*, 355, 369-386.

Butterfield, D. A., and G. J. Massoth (1994), Geochemistry of North Cleft segment vent fluids: temporal changes in chlorinity and their possible relation to recent volcanism, *J. Geophys. Res.*, 99(B3), 4951-4968.

Corliss, J. B., et al. (1979), Submarine Thermal Springs on the Galápagos Rift, *Science*, 203, 1073-1083.

Cowen, J. P., E. T. Baker, and R. W. Embley (2004), Detection of and Response to Mid-Ocean Ridge Magmatic Events: Implications for the Subsurface Biosphere, in *The Subseafloor Biosphere at Mid-Ocean Ridges, Geophys. Monogr. Ser.*, vol. 144, edited by W. S. D. Wilcock, et al., pp. 227-243, AGU, Washington, DC.

Crawford, W. C., and S. C. Webb (2002), Variations in the distribution of magma in the lower crust and at the Moho beneath the East Pacific Rise at 9 degrees-10 degrees N, *Earth Planet. Sci. Lett.*, 203, 117-130.

Dziak, R. P., W. W. Chadwick, Jr., C. G. Fox, and R. W. Embley (2003), Hydrothermal temperature changes at the southern Juan de Fuca Ridge associated with M_w 6.2 Blanco Transform earthquake, *Geology*, 31, 119-122.

Edmond, J. M., C. Measures, R. E. McDuff, L. H. Chan, R. Collier, B. Grant, L. I. Gordon, and J. B. Corliss (1979), Ridge crest hydrothermal activity and the balances of the major and minor elements in the ocean: The Galapagos data, *Earth Planet. Sci. Lett.*, 46, 1-18.

Elderfield, H., and A. Schultz (1996), Mid-ocean ridge hydrothermal fluxes and the chemical composition of the ocean, *Annu. Rev. Earth Planet. Sci.*, 24, 191-224.

Fornari, D., et al. (2004), Submarine Lava Flow Emplacement at the East Pacific Rise 9°50'N: Implications for Uppermost Ocean Crust Stratigraphy and Hydrothermal Fluid Circulation, in *Mid-Ocean Ridges: Hydrothermal Interactions Between the Lithosphere and Oceans*, *Geophys. Monogr. Ser.*, vol. 148, edited by C. R. German, et al., pp. 187-217, AGU, Washington, DC.

Fornari, D. J., T. Shank, K. L. Von Damm, T. K. P. Gregg, M. Lilley, G. Levai, A. Bray, R. M. Haymon, M. R. Perfit, and R. Lutz (1998), Time-series temperature measurements at high-temperature hydrothermal vents, East Pacific Rise 9°49'-51'N: evidence for monitoring a crustal cracking event, *Earth Planet. Sci. Lett.*, *160*, 419-431.

German, C. R., and K. L. Von Damm (2004), Hydrothermal processes, in *The oceans and marine geochemistry, Treatise on geochemistry*, vol. 6, edited by H. D. Holland, et al., pp. 181-222, Elsevier-Pergamon, Oxford, UK.

Germanovich, L. N., R. P. Lowell, and D. K. Astakhov (2000), Stress-dependent permeability and the formation of seafloor event plumes, *J. Geophys. Res.*, *105*(B4), 8341-8354.

Germanovich, L. N., R. P. Lowell, P. Ramondenc, and Y. Sim (2008), Magmatic origin of the March 1995 earthquake swarm at 9°50' N, East Pacific Rise, *J. Geophys. Res.*, *in review*.

Glickson, D. A., D. S. Kelley, and J. R. Delaney (2007), Geology and hydrothermal evolution of the Mothra Hydrothermal Field, Endeavour Segment, Juan de Fuca Ridge, *Geochem. Geophys. Geosyst.*, *8*, Q06010, doi:10.1029/2007GC001588.

Haymon, R. M., et al. (1993), Volcanic eruption of the mid-ocean ridge along the East Pacific Rise crest at 9°45-52' N: Direct submersible observations of seafloor phenomena associated with an eruption event in April, 1991, *Earth Planet. Sci. Lett.*, *119*, 85-101.

Jannasch, H. W. (1995), Microbial Interactions With Hydrothermal Fluids, in *Seafloor Hydrothermal Systems: Physical, Chemical, Biological, and Geological Interactions*, *Geophys. Monogr. Ser.*, vol. 91, edited by S. E. Humphris, et al., pp. 273-296, AGU, Washington, DC.

Johnson, H. P., R. P. Dziak, C. R. Fisher, C. G. Fox, and M. J. Pruis (2001), Earthquakes' Impact on Hydrothermal Systems May Be Far-Reaching, *Eos Trans. AGU*, *82*(21), 233.

- Johnson, H. P., M. Hutnak, R. P. Dziak, C. G. Fox, I. Urcuyo, J. P. Cowen, J. Nabelek, and C. Fisher (2000), Earthquake-induced changes in a hydrothermal system on the Juan de Fuca mid-ocean ridge, *Nature*, 407, 174-177.
- Kelley, D. S., J. A. Baross, and J. R. Delaney (2002), Volcanoes, Fluids, and Life at Mid-Ocean Ridge Spreading Centers, *Annu. Rev. Earth Planet. Sci.*, 30, 385-491.
- Lister, C. R. B. (1972), On the Thermal Balance of a Mid-Ocean Ridge, *Geophys. J. R. Astron. Soc.*, 26, 515-535.
- Lister, C. R. B. (1983), The Basic Physics of Water Penetration Into Hot Rock, in *Hydrothermal Processes at Seafloor Spreading Centers*, edited by P. A. Rona, et al., pp. 141-168, Plenum Press, New York and London.
- Lowell, R. P., and M. DuBose (2005), Hydrothermal systems on Europa, *Geophys. Res. Lett.*, 32, L05202, doi:10.1029/2005GL022375.
- Lowell, R. P., and L. N. Germanovich (1994), On the temporal evolution of high-temperature hydrothermal systems at ocean ridge crests, *J. Geophys. Res.*, 99(B1), 565-575.
- Lowell, R. P., and L. N. Germanovich (2004), Hydrothermal Processes at Mid-Ocean Ridges: Results From Scale Analysis and Single-Pass Models, in *Mid-Ocean Ridges: Hydrothermal Interactions Between the Lithosphere and Oceans*, *Geophys. Monogr. Ser.*, vol. 148, edited by C. R. German, et al., pp. 219-244, AGU, Washington, DC.
- Macdonald, K. C., K. Becker, F. N. Spiess, and R. D. Ballard (1980), Hydrothermal heat flux of the "black smoker" vents on the East Pacific Rise, *Earth Planet. Sci. Lett.*, 48, 1-7.
- Nicolas, A. (1995), *The Mid-Oceanic Ridges, Mountains Below Sea Level*, 200 pp., Springer-Verlag, Berlin.
- Pascoe, A. R., and J. R. Cann (1995), Modeling diffuse hydrothermal flow in black smoker vent fields, in *Hydrothermal Vents and Processes*, *Geological Society Special Publication*, vol. 87, edited by L. M. Parson, et al., pp. 159-173, The Geological Society, London, UK.
- Ramondenc, P., L. N. Germanovich, and R. P. Lowell (2008), Modeling hydrothermal response to earthquakes at oceanic spreading centers, in *Modeling Hydrothermal*

Processes at Oceanic Spreading Centers: Magma to Microbe, *Geophys. Monogr. Ser.*, edited by R. P. Lowell, et al., in review.

Ramondenc, P., L. N. Germanovich, K. L. Von Damm, and R. P. Lowell (2006), The first measurements of hydrothermal heat output at 9°50'N, East Pacific Rise, *Earth Planet. Sci. Lett.*, 245, 487-497, doi:10.1016/j.epsl.2006.03.023.

Rona, P. A., M. D. Hannington, C. V. Raman, G. Thompson, M. K. Tivey, S. E. Humphris, C. Lalou, and S. Petersen (1993), Active and relict Sea-Floor Hydrothermal Mineralization at the TAG Hydrothermal Field, Mid-Atlantic Ridge, *Econ. Geol.*, 88, 1989-2017.

Rona, P. A., B. A. McGregor, P. R. Betzer, G. W. Bolger, and D. C. Krause (1975), Anomalous water temperatures over Mid-Atlantic Ridge Crest at 26°N latitude, *Deep Sea Res.*, 22, 611-618.

Shank, T. M., D. J. Fornari, K. L. Von Damm, M. D. Lilley, R. M. Haymon, and R. A. Lutz (1998), Temporal and spatial patterns of biological community development at nascent deep-sea hydrothermal vents (9°50'N, East Pacific Rise), *Deep Sea Res. II*, 45, 465-515.

Sohn, R. A., D. J. Fornari, K. L. Von Damm, J. A. Hildebrand, and S. C. Webb (1998), Seismic and hydrothermal evidence for a cracking event on the East Pacific Rise crest at 9°50' N, *Nature*, 396, 159-161.

Sohn, R. A., J. A. Hildebrand, and S. C. Webb (1999), A microearthquake survey of the high-temperature vent fields on the volcanically active East Pacific Rise (9°50'N), *J. Geophys. Res.*, 104(B11), 25,367-25,377.

Spiess, F. N., et al. (1980), East Pacific Rise: Hot Springs and Geophysical Experiments, *Science*, 207, 1421-1433.

Stein, C. A., and S. Stein (1994), Constraints on hydrothermal heat flux through the oceanic lithosphere from global heat flow, *J. Geophys. Res.*, 99(B2), 3081-3095.

Stein, C. A., S. Stein, and A. Pelayo (1995), Heat Flow and Hydrothermal Circulation, in *Seafloor Hydrothermal Systems: Physical, Chemical, Biological, and Geological Interactions*, *Geophys. Monogr. Ser.*, vol. 91, edited by S. E. Humphris, et al., pp. 425-445, AGU, Washington, DC.

- Vera, E. E., J. C. Mutter, P. Buhl, J. A. Orcutt, A. J. Harding, M. E. Kappus, R. S. Detrick, and T. M. Brocher (1990), The Structure of 0- to 0.2-m.y.-Old Oceanic Crust at 9°N on the East Pacific Rise From Expanded Spread Profiles, *J. Geophys. Res.*, *95*(B10), 15,529-15,556.
- Von Damm, K. L. (2000), Chemistry of hydrothermal vent fluids from 9°-10°N, East Pacific Rise: "Time zero," the immediate post-eruptive period, *J. Geophys. Res.*, *105*(B5), 11,203-11,222.
- Von Damm, K. L., S. E. Oosting, R. Kozlowski, L. G. Buttermore, D. C. Colodner, H. N. Edmonds, J. M. Edmond, and J. M. Grebmeier (1995), Evolution of East Pacific Rise hydrothermal vent fluids following a volcanic eruption, *Nature*, *375*, 47-50.
- Wheat, C. G., H. W. Jannasch, M. Kastner, J. N. Plant, E. H. DeCarlo, and G. Lebon (2004), Venting formation fluids from deep-sea boreholes in a ridge flank setting: ODP Sites 1025 and 1026, *Geochem. Geophys. Geosyst.*, *5*, Q08007, doi:10.1029/2004GC000710.
- White, S. M., R. M. Haymon, and S. Carbotte (2006), A new view of ridge segmentation and near-axis volcanism at the East Pacific Rise, 8°-12°N, from EM300 multibeam bathymetry, *Geochem. Geophys. Geosyst.*, *7*, Q12O05, doi:10.1029/2006GC001407.
- Wilcock, W. S. D. (2004), Physical response of mid-ocean ridge hydrothermal systems to local earthquakes, *Geochem. Geophys. Geosyst.*, *5*, Q11009, doi:10.1029/2004GC000701.
- Wilcock, W. S. D., and A. McNabb (1996), Estimates of crustal permeability on the Endeavour segment of the Juan de Fuca mid-ocean ridge, *Earth Planet. Sci. Lett.*, *138*, 83-91.
- Williams, D. L., R. P. Von Herzen, J. G. Sclater, and R. N. Anderson (1974), The Galapagos spreading center: Lithospheric cooling and hydrothermal circulation, *Geophys. J. R. Astron. Soc.*, *38*, 587-608.
- Wolery, T. J., and N. H. Sleep (1976), Hydrothermal circulation and geochemical flux at mid-ocean ridges, *Journal of Geology*, *84*, 249-275.

CHAPTER 2

THE FIRST MEASUREMENTS OF HYDROTHERMAL HEAT OUTPUT AT 9°50' N, EAST PACIFIC RISE

Abstract. Despite the importance of the heat output of seafloor hydrothermal systems for the Earth's energy budget, hydrothermal heat output measurements have been very limited. In this paper, we report the first measurements of hydrothermal heat output at the RIDGE 2000 Integrated Study Site on the East Pacific Rise. We focused our work on the Bio 9 complex, situated at 9°50' N, where there has been an extensive measurement and sampling program since 1991. This site is located along the eruptive fissure of the 1991/1992 event and the site of the 1995 earthquake swarm. We made direct measurements of advective heat output at several individual vents and at one site of diffuse flow (Tica). Although these data do not describe the complete heat flux picture at this vent field, the data yield a total hydrothermal heat output of $\sim 325 \text{ MW} \pm 160 \text{ MW}$ with $\sim 42 \text{ MW} \pm 21 \text{ MW}$ coming from high-temperature vents along this 2 km segment of ridge. This result assumes a diffuse flux similar to that measured at Tica occurs at each high-temperature vent site. Our initial measurements thus suggest that the heat output of the low-temperature diffuse venting is approximately 10 times that of the high-temperature vents, but may also be one or two orders of magnitude greater.

2.1 Introduction

Seafloor hydrothermal systems play a key role in Earth's energy budget. Approximately 25% of Earth's global heat flux is lost through hydrothermal venting [Elderfield and Schultz, 1996; Stein and Stein, 1994; Stein *et al.*, 1995]. High-temperature venting along mid-ocean ridge axes alone may account for up to 10% of the global heat loss [Bemis *et al.*, 1993; Elderfield and Schultz, 1996; Ginster *et al.*, 1994]. These estimates are derived indirectly from the discrepancy between conductive heat flow measurements through seafloor sediments and lithospheric heat loss determined from seafloor spreading models.

Although plate-scale estimates of hydrothermal heat flux point to the global importance of hydrothermal heat loss through the seafloor, these data provide no information at the scale of an individual vent or vent field. Determination of the heat output at the scale of an individual vent field is important for several reasons. First, heat output, when coupled with vent temperature, provides important constraints on the physics of seafloor hydrothermal processes. Models using these two constraints have been used to infer crustal permeability at the ridge axis [Lowell and Germanovich, 1994, 2004], an important fluid flow parameter that cannot be reliably determined by other means. The observational data also provide important constraints on the thickness of the conductive boundary layer separating hydrothermal circulation from the underlying magmatic heat source [e.g., Lister, 1983; Lowell and Germanovich, 1994]. Finally, heat output, and hence fluid flow rate, may provide important information on nutrient transport to biological ecosystems. Determinations of heat output at hydrothermal sites are thus critical to an integrated understanding of ridge crest processes.

Despite its importance, direct measurements of hydrothermal heat output at active hydrothermal vent sites are very limited. Of the $\sim 10^3$ active high-temperature vent sites predicted to occur along the 67,000 km of ocean ridge [Baker and German, 2004; Lowell and DuBose, 2005] fewer than 30% have been identified. Heat output has been determined at fewer than 10% of known hydrothermal sites (Table 2.1). Despite the intensive study for the past 15 years, no heat output data have been obtained for the RIDGE 2000 Integrated Study Site between 8 and 11° N on the East Pacific Rise.

The paucity of direct measurements of hydrothermal heat output stems in part from the complex nature of hydrothermal venting. High-temperature venting occurs through discrete point sources such as sulfide chimneys and fissures as well as from flanges protruding from the walls of large sulfide edifices [Delaney *et al.*, 1992]. The contribution of flanges and fissures is usually hard to estimate [Ginster *et al.*, 1994]. In addition, low-temperature diffuse flow resulting from a combination of thermal conduction and mixing between hydrothermal fluid and seawater often occurs over much larger areas (up to tens of meters in diameter) of the sea floor [Baker *et al.*, 1993; Bemis *et al.*, 1993; Rona and Trivett, 1992]. Diffuse venting also occurs on sulfide structures themselves [Ginster *et al.*, 1994].

Table 2.1. Thermal data from seafloor hydrothermal systems. “Vent field area” corresponds to the area investigated in the specific study. The actual area of the vent field may be different. “Vent fluid flow rate” corresponds to the flow rate estimated at the exit of discrete venting. In this table, JdFR stands for Juan de Fuca Ridge, GB for Guaymas Basin, EPR for East Pacific Rise, MAR for Mid-Atlantic Ridge and CIR for Central Indian Ridge. If the flow type (discrete or diffuse) is not indicated in the last column, this means the total (combined) flow.

Reference	Location	Vent Field Area (m ²)	Vent Fluid Flow Rate (m/s)	T (°C)	Vent Heat Flux (MW)	Integrated Heat Flux (GW)	Basis For Estimation / Remarks
<i>Rona and Trivet</i> [1992]	Axial Volcano (JdFR)	1.E+04	0.2 - 0.9	108 - 326	2.4 - 6.4		<i>Discrete</i> : direct measurements <i>Diffuse</i> : standard plume model
<i>Baker et al.</i> [1990]	Axial Volcano (JdFR)	2.E+05			15 - 75	0.8	Water column survey
<i>Rosenberg et al.</i> [1988]	Endeavour (JdFR)	4.E+04		up to 400		1 - 5	Radon (²²² Rn) measurements
<i>Thomson et al.</i> [1992]	Endeavour (JdFR)	8.E+07				6 - 18	Water column survey
<i>Schultz et al.</i> [1992]	Endeavour (JdFR)	2.E+01	0.07 - 0.15	7 - 13	53.5 - 62.9		<i>Diffuse</i> : Electro-magnetic flow meter
<i>Veirs et al.</i> [2005]	Endeavour (JdFR)	2.E+05			8 - 42		Horizontal heat flux from plume survey
<i>Bemis et al.</i> [1993]	Endeavour (JdFR)					0.07 - 0.24	Simple plume theory with buoyant plumes
	South Cleft (JdFR)					0.02 - 0.07	Simple plume theory with buoyant plumes
<i>Ginster et al.</i> [1994]	Endeavour (JdFR)		0.6 - 6.2	296 - 374	3.6 - 87.3	0.29 - 0.44	Direct measurements and sum over # of smokers
	South Cleft (JdFR)		1.3 - 3.5	235 - 350	7.9 - 10.4	0.04 - 0.06	Direct measurements and sum over # of smokers
<i>Baker and Massoth</i> [1986]	South Cleft (JdFR)					0.29 - 0.87	Deep-tow survey and plume model
<i>Baker and Massoth</i> [1987]	Endeavour (JdFR)					0.6 - 2.8	Deep-tow survey and plume model
	South Cleft (JdFR)					0.23 - 0.92	Deep-tow survey and plume model
<i>Baker et al.</i> [1993]	North Cleft (JdFR)			104 - 324	161 - 319	0.48 - 0.96	<i>Discrete</i> : Linear plume theory and mixing model
					324 - 642		<i>Diffuse</i> : Linear plume theory and mixing model
<i>Baker</i> [1994]	North Cleft (JdFR)					0.38 - 0.94	Deep-tow survey and non-buoyant plume theory
<i>Gendron et al.</i> [1994]	North Cleft (JdFR)					1.4 - 4	Radon (²²² Rn) measurements
<i>Baker et al.</i> [1998]	CoAxial (JdFR)					0.25 - 25	Deep-tow survey and plume model

Table 2.1. (continued)

Reference	Location	Vent Field Area (m ²)	Vent Fluid Flow Rate (m/s)	T (°C)	Vent Heat Flux (MW)	Integrated Heat Flux (GW)	Basis For Estimation / Remarks
<i>Stein and Fisher</i> [2001]	Middle Valley (JdFR)	3.E+08		180 - 276	0.13		<i>Advective:</i> individual buoyant plume measurements <i>Conductive + advective</i> (conductive may also contain a diffuse flow component)
<i>Lonsdale and Becker</i> [1985]	Southern Trough (GB)		1 - 2	270 - 314	86 - 201		<i>Discrete:</i> assuming 10 chimneys of 80 cm ² orifice <i>Conductive + advective</i> (conductive may also contain a diffuse flow component)
<i>Fisher and Becker</i> [1991]	Southern Trough (GB)	3.E+07				0.01 – 0.25	Direct measurements and orifices 3 cm in diameter Non-linear plume theory
<i>McConachy et al.</i> [1986]	11°N (EPR)	3.E+03	0.4 - 1.2	347	3.0 - 25		Direct measurements and orifices 30 cm in diameter Flow meter measurements
<i>Little et al.</i> [1987]	11°N (EPR)	3.E+03			2.9 - 4.5		
<i>Macdonald et al.</i> [1980]	21°N (EPR)			344 - 356	0.2 - 0.3		
<i>Converse et al.</i> [1984]	21°N (EPR)		0.7 - 2.4	275 - 350	140 - 300		
<i>Rudnicki and Elderfield</i> [1992]	TAG (MAR)			360 - 364		0.5 - 0.9	Solution to entrainment in buoyant plume
<i>Rona et al.</i> [1993]	TAG (MAR)	3.E+04		365	200 - 250		Simple plume theory with buoyant plumes
<i>Murton et al.</i> [1999]	Broken Spur (MAR)					0.25 - 0.3	Plume theory
<i>Hashimoto et al.</i> [2001]	Kairei (CIR)	3.E+03		360			
<i>Rudnicki and German</i> [2002]	Kairei (CIR)	3.E+03		360		0.07 - 0.12	Standard plume theory
This study	9°50' N (EPR)	1.E+05	0.1 - 0.3	345 - 388	40		<i>Discrete:</i> Extrapolation of direct measurements
			0.04	10	300 - 1.6 x 10 ⁴		<i>Diffuse:</i> Extrapolation of direct measurements

Advective heat flux from discrete high-temperature vents can be determined directly. Temperature can be recorded accurately from submersible or during deep-tow surveys, and flow velocity can be determined either using a flow meter [*Converse et al.*, 1984] or by tracking particles and eddies in the ascending fluid on the video tapes of the dives [*Converse et al.*, 1984; *Macdonald et al.*, 1980; *Rona and Trivett*, 1992]. The size of the vent orifice is usually estimated visually [*Little et al.*, 1987]. Because each vent is different, and a vent field may contain a large number of discrete vents, it is difficult to determine the heat output at the vent field scale from direct measurements alone [*Baker and Massoth*, 1986]. Direct methods for determining the heat output from discrete vents cannot be easily implemented for diffuse venting because of its relatively low temperature, velocity, and its uneven distribution, but some measurements have been made [*Rona and Trivett*, 1992; *Schultz et al.*, 1992].

Heat output from individual vents has also been determined from measurements in the buoyant plume [*Little et al.*, 1987; *Rona et al.*, 1993]. When the hydrothermal fluid exits the oceanic crust and rises in the water column, it mixes with ambient seawater, eventually forming a neutrally buoyant plume ~ 100 - 200 m thick at a height ~ 150 - 200 m above the seafloor [*Baker and Massoth*, 1987; *Gendron et al.*, 1994]. Because the neutrally buoyant plume represents the coalescence of fluids from multiple point sources, and may contain a diffuse flow component as well, measurements in the neutrally buoyant plume provide an integrated estimate of heat flux on the vent field scale [*Baker*, 1994; *Baker and Cannon*, 1993; *Baker et al.*, 1994; *Baker and Massoth*, 1987; *Baker et al.*, 1998]. It is difficult to separate the relative contributions of focused and diffuse flow

in the neutrally buoyant plume. Table 2.1 shows, however, that integrated water column measurements yield much higher heat outputs than direct measurements at vents.

The relative contributions of discrete and diffuse flow to the total vent field heat output have been a matter of considerable interest. Early estimates at the Main Endeavour Vent Field on the Juan de Fuca Ridge (JdFR) [Schultz *et al.*, 1992] suggested that up to 90% of the heat output resulted from the diffuse flow component. Data from the TAG field on the Mid-Atlantic Ridge (MAR) also suggest that diffuse flow may be as much as 5 to 10 times larger than the combined convective flux from black smokers [Rona *et al.*, 1993]. Furthermore, Rona and Trivett [1992] found the diffuse heat output to be an order of magnitude greater than the focused one at Axial Volcano site (Juan de Fuca Ridge). On the other hand, recent water column measurements over the Main Endeavor Vent Field suggest the ratio between focused and diffuse flow is ≈ 50 -50 [Veirs *et al.*, 2005].

In this chapter, we report the first measurements of hydrothermal heat output at the RIDGE 2000 Integrated Study Site on the East Pacific Rise (EPR). We focused our work on the Bio 9 complex, situated at 9°50' N, where there has been an extensive measurement and sampling program since 1991. This site is located along the eruptive fissure of the 1991/2 event [Fornari *et al.*, 2004; Haymon *et al.*, 1993; Von Damm, 2004] and the site of the 1995 earthquake swarm [Sohn *et al.*, 1998; Sohn *et al.*, 1999].

As described below, we made direct measurements of advective heat output at several individual vents and at one site of diffuse flow (Tica). Although these data do not describe the complete heat flux picture at this vent field, the data provide insight into the partitioning between focused and diffuse flow components at a fast spreading ridge crest.

Moreover, heat flow data coupled with temperature data may help constrain models of the hydrothermal response to earthquakes. There have been several earthquakes in this region since the 1991/1992 volcanic events for which the data have not been analyzed. The hydrothermal response to the 1995 swarm [Fornari *et al.*, 1998; Sohn *et al.*, 1998; Sohn *et al.*, 1999], recently modeled by Wilcock [2004] and Ramondenc *et al.* [2005] is constrained only by temperature data obtained at Bio 9, so heat flow data could provide an additional constraint on such models.

2.2 Geological setting

The East Pacific Rise at 9°50' N represents a key region within the broader RIDGE 2000 Integrated Study Site extending from 8-11° N [<http://ridge2000.bio.psu.edu/science/iss/epr.html>]. This region of the EPR is a fast spreading center with a full rate of 11 cm/yr [Carbotte and Macdonald, 1992]. The ridge crest, which is situated 2500 (\pm 10) m below sea level [Von Damm, 2004], is relatively smooth and deepens as one moves away from the 9°50' N area. Multi-channel seismic data show the presence of a thin crustal magma chamber approximately 1.5 km below the seafloor [Detrick *et al.*, 1987]. This section of the EPR has been extensively studied since an ARGO-1 survey in 1989 found abundant evidence of hydrothermal activity [Haymon *et al.*, 1991] and a 1991 *Alvin* submersible study showed evidence of fresh volcanic activity and dramatic changes in the hydrothermal systems and associated biological communities [Haymon *et al.*, 1993; Shank *et al.*, 1998; Von Damm, 2000]. Repeated visits to this area since the 1991 eruption have shown that substantial changes are still occurring [Von Damm, 2004; Von Damm and Lilley, 2004].

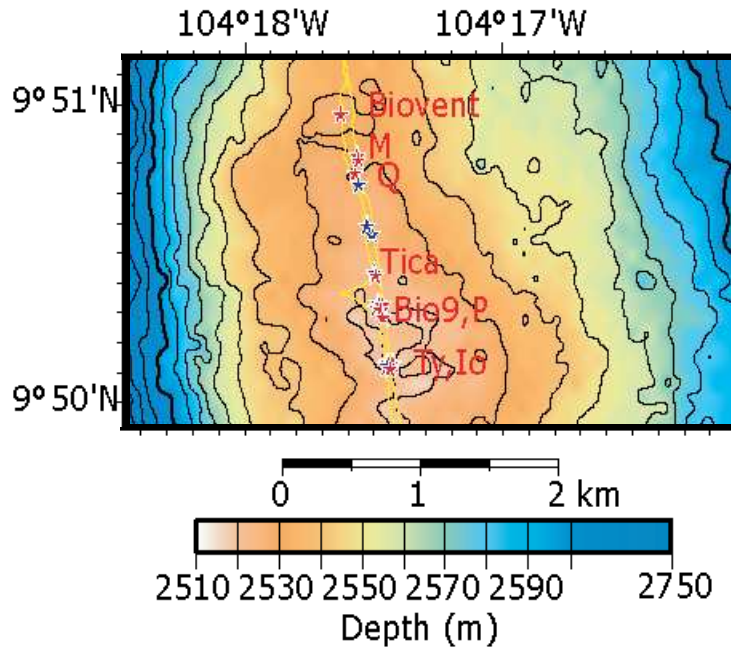


Figure 2.1. Map showing the distribution of vents in the 9°49-51' N area on the East Pacific Rise. High-temperature vents are shown in red (with their names adjacent to the stars) and sites of diffuse flow venting are shown in blue. Figure modified from *Von Damm* [2004].

The vents in the 9°50' N area are clustered within the axial summit collapse trough (ASCT) in a ~ 2 km long region of the axis (Figure 2.1). The Bio 9 complex and P vent, which are located about 60 m apart in a local widening of the ASCT referred as the “Hole to Hell”, represent two loci of hydrothermal activity, each with multiple vents, right at 9°50' N. The Bio 9 complex with at least three black smokers - Bio 9, Bio 9' (that became active around 1994) and Bio 9" (sampled for the first time in 2002) - is the more active of the two, with abundant diffuse flow and the highest discharge temperature. P vent is situated 60 m south and a second vent, P middle, was first sampled in 2002 [*Von Damm*, 2004]. Four high-temperature vent areas (Biovent, M, Q, and Tica) lie to the north of the Bio 9 complex and two (Ty and Io) lie to the south [*Von Damm*, 2004]. The

entire area has been quite dynamic in the past decade as new vents have evolved and others (e.g., TWP vent) have become extinct [Von Damm, 2004]. We collected heat flow data at M, Q, Bio 9, Bio 9'' and P vents and in a region of diffuse flow near Tica vent (Table 2.2) during a sampling cruise in March 2004 [Von Damm *et al.*, 2004]. These vents lie approximately 7 km north of another cluster of high-temperature vents at 9°47' N, where the ridge crest lies some 30 m deeper [Fornari *et al.*, 2004]. The diffuse venting zone was chosen for its particularly robust flow (this is actually the most robust of the study area). Nearly two decades of study of the 9°50' N area have shown that in the past, and especially close to the time of the 1991 eruption, most of the diffuse flow areas were similar to Tica.

2.3 Measurement device

In principle, our approach was similar to that of Macdonald *et al.* [1980] and Rona and Trivett [1992] at 21° N (EPR) and Axial Volcano (JdFR), respectively. Their heat flux estimates were obtained by combining a measurement of vent temperature using Alvin's temperature probe with a visual estimate of flow rate and vent orifice diameter. Flow rate was determined by placing a graduated rod vertically in the vicinity of a black smoker and tracking the rate of upward eddy movement using a video camera. Because the flow estimates were obtained from the margin of the black smoker plume, these estimates of heat flux are likely too low.

Table 2.2. Results from the flow measurements and heat output estimates.

Vent name	Type of venting	Particle displacement (cm)	Time (s)	Velocity (m/s)	T (°C)	Orifice heat flux (MW)	Diffuse heat flux (MW)
M vent	Black Smoker	10.9	0.28	0.39	368	1.5	n/a
		7.7	0.18	0.43			
		12.3	0.67	0.18			
		8.9	0.46	0.19			
		<i>Average</i>		0.30			
Q vent	Black Smoker	5.4	0.53	0.10	345	0.5	n/a
		4.2	0.4	0.11			
		6.4	0.53	0.12			
		6.2	0.73	0.08			
		<i>Average</i>		0.10			
Tica	Diffuse 5 × 5 m ² area	3.2	0.8	0.04	10	n/a	40.7
		3.4	0.73	0.05			
		3.7	0.8	0.05			
		2.8	0.93	0.03			
		<i>Average</i>		0.04			
Bio 9	Black Smoker	7.9	0.25	0.32	388	1.3	n/a
		7.3	0.46	0.16			
		9.2	0.46	0.20			
		7.3	0.33	0.22			
		8.5	0.33	0.26			
		10.8	0.33	0.33			
		10.8	0.4	0.27			
		8.5	0.4	0.21			
		11.1	0.53	0.21			
		<i>Average</i>		0.24			
Bio 9"	Black Smoker	10.0	0.31	0.32	378	1.4	n/a
		8.5	0.33	0.26			
		8.9	0.4	0.22			
		12.1	0.4	0.30			
		11.1	0.47	0.24			
		9.5	0.33	0.29			
		10.6	0.4	0.27			
		14.1	0.53	0.27			
		12.1	0.4	0.30			
		<i>Average</i>		0.27			
P-vent	Black Smoker	5.1	0.4	0.13	369	0.8	n/a
		6.2	0.34	0.18			
		<i>Average</i>		0.16			

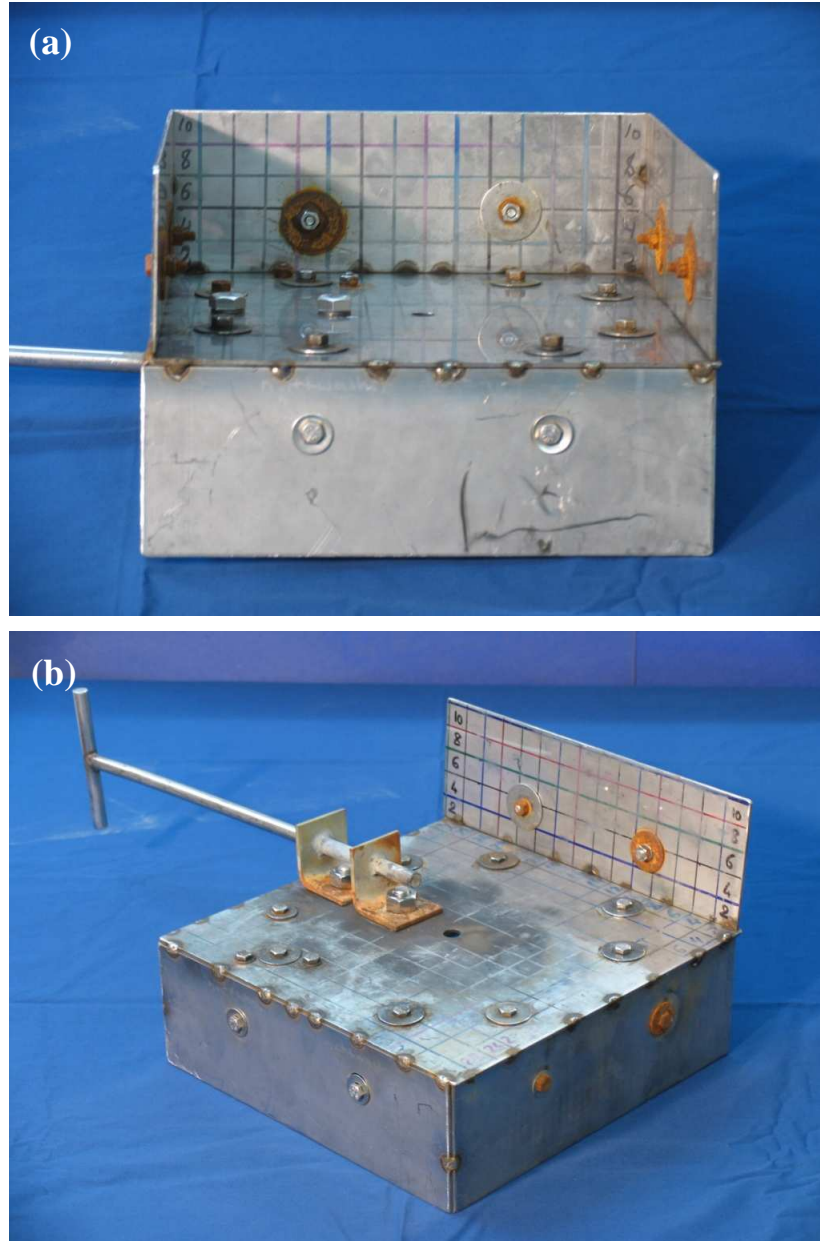


Figure 2.2. Device in its two configurations. (a) View of the top of the device. Note the graduation placed on the walls in order to track easily fluid eddies or particles. Note also the effect of the venting fluids on the material used for the device (unaffected stainless steel versus highly corroded aluminum parts). (b) View of the bottom of the device. The handle used by *Alvin*'s arm is visible as well as the central hole used to focus the fluid jet. The hole diameter is 1.3 cm. As discussed in text, the device was actually employed as depicted in (b).

For our study, the flow measuring device consisted of a 30 × 30 cm stainless steel plate, with a hole 1.3 cm in diameter in the center, and vertical plates (walls) 10 cm in height around the perimeter (Figure 2.2a). The vertical plates had a graduated scale at 2 cm intervals and their height was limited to 10 cm because beyond this height, the hot fluid had mixed with seawater and decelerated significantly. When the plate was placed horizontally over the vent using *Alvin*'s robotic arm, vent fluid flowed through the hole. A digital video camera was installed on *Alvin*'s other arm to record the flow for approximately two minutes, as perpendicular to its direction as possible. Then, the video records were used to track fluid eddies or particles in reference to the scale fixed on the vertical plates as a function of time and hence to determine the velocity.

Unlike a funnel, whose inclined walls would focus the flow and force it through a smaller opening, our device just cut part of the flow, discarding its major part toward the sides. Moreover, since the thickness of the plate (3 mm) is much smaller than the diameter of the hole (1.3 cm), change of the velocity of the fluid passing through the hole is insignificant. Consequently, the velocity of the fluid flowing through the measurement device can be considered to be the actual velocity of the fluid exiting the vent. Originally, we planned to use the device with the front wall oriented downward and the other three upward (Figure 2.2a). We believed this configuration would prevent the black hydrothermal fluid from being diverted between the camera and the flow, and thus permit a clear recording of the experiment. While this design worked well, the first dives showed that three upward walls were not necessary because in practice the hot fluid was moving upward due to the buoyancy effect and was not obscuring the videotaped zone. By turning the device upside down (i.e., with the back wall oriented upward and the other

three downward as shown in Figure 2.2b), we actually improved the visibility for both discrete and diffuse measurements and enabled easier analysis of the videos.

Figure 2.3 shows two examples of deployment of the measurement device, one at a high-temperature venting site, and one at a low-temperature diffuse venting site. More details about the devices and their upgrades are provided in Appendix A.

2.4 Measurement results

Figure 2.4 shows an example of how the velocity of the flow was inferred from the digital video records. The method consists of tracking specific fluid eddies or particles, calculating the distance d they moved during a certain time interval t . The latter is estimated frame by frame, with a precision of 0.07 s. We tried to select only particles that had the most direct path possible (and avoid the ones caught in turbulent eddies).

From these values, one can estimate the velocity $v = d/t$. The heat flux is then calculated as follows:

$$H = C_f v (T_f - T_0) A \quad (2.1)$$

where T_f and T_0 are the temperatures of the vent fluid and ambient seawater, respectively, and $C_f = \rho_f c_f \approx 4 \times 10^6 \text{ J/(m}^3\text{°C)}$ is the volumetric heat capacity of the fluid, with ρ_f and c_f being the fluid density and specific heat of the vent fluid, respectively. In expression (2.1), A is the area over which the calculation is performed. For high-temperature venting,

$$A = n\pi r^2 \quad (2.2)$$

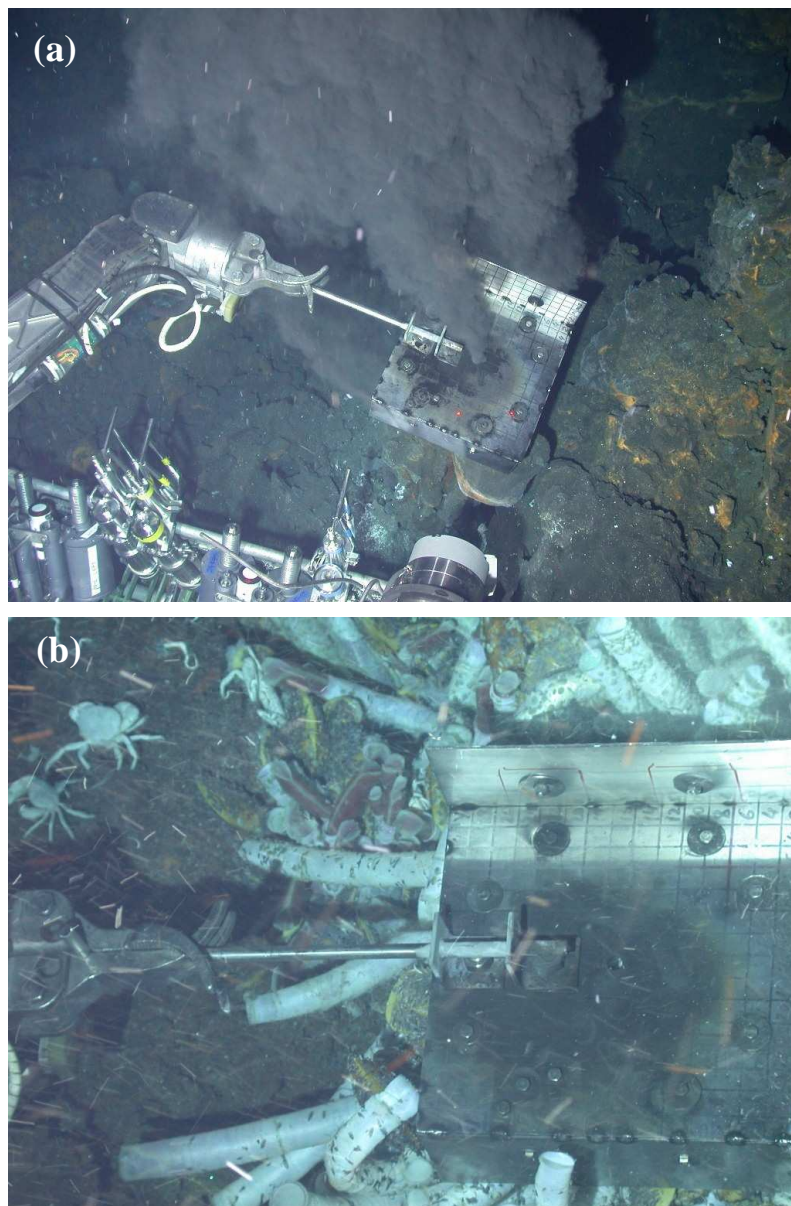


Figure 2.3. Deployment of the device for flux measurements of (a) high-temperature venting at Bio 9 (dive # 3992) and (b) diffuse flow venting at Tica (dive # 3991).

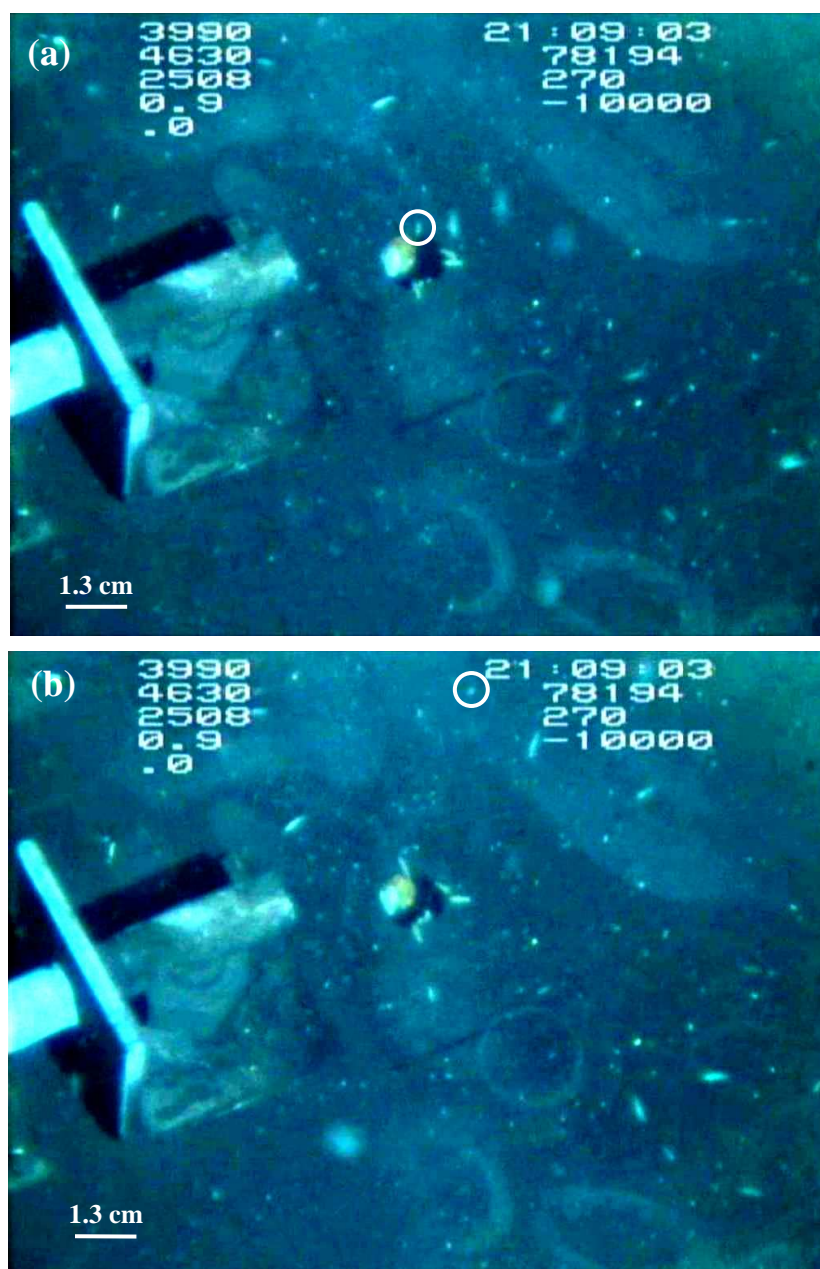


Figure 2.4. Example of flow velocity measurement at Tica vent area (dive # 3991). A particle is tracked using the video tape recorded during the dive. Using the known time between the frames, fluid velocity is calculated for the observed particle motion.

where r is the radius of a vent orifice, which is assumed to be circular, and n is the number of orifices present on the sulfide structure. The assumption that each vent orifice has the same radius is, of course, a simplification. It was impractical to measure the area of each orifice independently, however. In fact it is not a trivial matter to even identify each orifice.

Since it was difficult to obtain a clear count, we chose $n = 3$ as the typical average number of orifices on a black smoker, our visual estimates varying between 1 and 6. Our estimate of the mean area of an orifice was based on chimney samples collected from P middle vent and Marker 22 during *Alvin's* dives # 3987 and # 3988, respectively (Figure 2.5). The first sample (Figure 2.5a) features 5 orifices, 3 of which are rather small. These small orifices have an area ranging from 3 to 7 cm² and are situated on the sides of the structure. The other two orifices, situated at the top of the sulfide chimney, are much larger, of the order of 25-45 cm². For this reason, and because the flow coming from the side of the sulfide chimney cannot be used for velocity estimation (it has already mixed with the ambient seawater before reaching the device by buoyancy), only the top openings have been used for the estimation of an average opening size. They yielded an equivalent radius $r = 3.3$ cm ($\pi r^2 = 35$ cm²). The second sample had only one orifice with the same equivalent radius. From our computations, its value may vary by ± 0.5 cm which implies an uncertainty of ± 40 -50% for the estimation of the heat flux.



Figure 2.5. Chimney samples collected from (a) P middle vent during *Alvin*'s dive # 3987 and (b) Marker 22 during *Alvin*'s dive # 3988, respectively. The first sample (a) features two orifices at its top (i.e., foreground of the picture), while the second sample (b) has a single orifice.

In the case of the diffuse venting flow, A corresponds to the entire area of the diffuse zone. Again, an exact estimate was not practical. For the diffuse flow at Tica we used $A = 5 \times 5 \text{ m}^2$, which approximately corresponds to the area of the seafloor around the chimney where the diffuse flow was visually noticeable.

In summary, our device was used on three different dives: dives # 3987, at M vent, dive # 3991, at Tica and Q vents, and dive # 3992, at Bio9, Bio9'', and P vents. Results are summarized in Table 2.2.

2.5 Discussion and conclusions

From Table 2.2, the average flow velocity at a low-temperature diffuse venting zone is an order of magnitude smaller than that obtained at the high-temperature vents (10^{-2} m/s versus 10^{-1} m/s). Although the absolute velocities are different, the velocity ratio obtained here is similar to that obtained by *Ginster et al.* [1994] and *Schultz et al.* [1992] for the Main Endeavour vent field on the intermediate rate spreading JdFR. Similarly, our measurements indicate that the heat output of the low-temperature diffuse venting at $9^{\circ}50' \text{ N}$ EPR is approximately 10 times that of the high-temperature vents, but may also be one or two orders of magnitude greater. We arrived at this conclusion by extrapolating our limited measurements to the entire vent complex situated between $9^{\circ}50.1' \text{ N}$ and $9^{\circ}50.7' \text{ N}$ (Figure 2.1). Our main assumptions are specified in Table 2.3, which also includes the results of our estimates of the total (discrete plus diffuse) heat flux and flux ratios (discrete / diffuse) under a range of assumed values of diffuse flow that may be present in the EPR area. As a lower limit, we assumed that only actually observed diffuse sites are present (blue stars in Figure 2.1) and the area of each diffuse

site is $5 \times 5 \text{ m}^2$ (as for Tica site in Table 2.2). In this case, the total hydrothermal heat output from the $9^\circ 50' \text{ N}$ area amounts to approximately 325 MW, 13% of which is due to the high-temperature venting. Table 2.3 also gives heat output estimates assuming diffuse venting occurs over 1% and 10% of the entire area ($\sim 2 \text{ km} \times 50 \text{ m}$) of the $9^\circ 50' \text{ N}$ complex. Then Table 2.3 indicates that high-temperature heat output would amount to 3% and 0.3% of the diffuse flow heat output, accordingly. It has to be noted that the value given for our first case highly depends on the estimate of the area of the diffuse flow sites. At present, it is very difficult to accurately estimate the size of a diffuse venting zone, because this evaluation is mainly visual and therefore subjective. Moreover, what is termed a zone of “diffuse venting” is actually an area where patches of venting have been summed up. Also, the estimate of the heat output coming from areas of diffuse venting suffers from the paucity of measurements in such settings. With these initial, limited measurements, the authors could only extrapolate their results for Tica to the other suspected sites of diffuse venting. This error may be reduced considerably by increasing the number of measurements. This was not possible at the time of the cruise.

Table 2.3. Heat output estimates for the 9°50.1' - 9°50.7' N EPR vent complex.

High-temperature venting				
Black smoker site	Observed number of vents (chimneys)	Assumed number of orifices per vent (chimney)	Typical orifice flux based on Table 2.2 (MW)	Estimated site heat flux (MW)
Biovent	1	3	1	3
M vent	2	3	1	6
Q vent	2	3	1	6
Tica	1	3	1	3
Bio 9	3	3	1	9
P vent	2	3	1	6
Ty	1	3	1	3
lo	1	3	1	3
Damocles Sword	1	3	1	3
<i>Total high temperature heat flux (MW)</i>				42
Low-temperature venting				
Number of diffuse flow sites (Figure 2.1) and assumed diffuse flow conditions	Diffuse heat flux from Table 2.2 (MW/m²)	Diffuse flow area (m²)	Total diffuse heat flux (MW)	Flux ratio (high-temperature / low-temperature)
7 sites, 5 × 5 m ² each	40.7 MW / 25 m ² = = 1.63	25	285	0.15
1% of total area	1.63	10 ³	1.63 × 10 ³	0.03
10% of total area	1.63	10 ⁴	1.63 × 10 ⁴	3 × 10 ⁻³

As *Little et al.* [1987] pointed out, multiplying the heat flux of one measurement by the number of observed orifices on the same sulfide structure is a significant assumption. Indeed, it cannot entirely account for the geometry variation of the orifices, and neither can it represent the heat flow that would be expected if considering both discrete and diffuse venting in detail. Moreover, as *Converse et al.* [1984] indicate, the fact that particles are entrained by turbulent and rapidly decelerating fluids adds some difficulty and uncertainty to the method of determining the flow rate. The sensitivity of the results to these assumptions and difficulties may be reduced somewhat when studying heat output at the scale of the vent field.

In our measurements, to determine the heat flux, we made a number of estimates of the flow rate at each orifice and calculated the mean velocity to insert into equation (2.1). Overall, we estimate the precision of our measurements as $\pm 50\%$ at best and, more likely, as $\pm 100\%$. Unfortunately, with the few measurements available, it is not currently possible to estimate an uncertainty in the velocity more accurately from the standard deviation of the mean. Also, while Bio 9 and Bio 9' yielded many estimates, the other high-temperature vents (M, Q, and P) provided a limited number of exploitable results. It undoubtedly generates some inaccuracy that could only be mitigated by longer sampling times. This option may be available in the future.

Even with these uncertainties, the accuracy of these heat flow measurements is similar to that of other heat flow studies at ridge crest hydrothermal systems (Table 2.1). Moreover, as was pointed out previously, our study provides the first heat output estimates at 9°50' N, East Pacific Rise, as well as one of only a few *direct* measurements

of diffuse venting at mid-ocean ridges. The use of a mechanical flow meter [e.g., *Converse et al.*, 1984] is an alternative means of measuring the flow rate. Such devices tend to become jammed by particles at high-temperature venting sites and are insensitive to slow flow rates, which makes them impractical for measuring diffuse flow below a certain threshold (e.g., 0.3 m/s in *Converse et al.* [1984]). An interesting indirect method of flow measurements was suggested by *Schultz et al.* [1992] based on the effect of electromagnetic induction due to the fluid flow through the conducting coil. Their estimate of the rate of diffuse venting at Endeavour (Table 2.1) is of the same order as our result for 9°50' N EPR (Table 2.2). Finally, to the best of our knowledge, only one plume survey has been conducted in this area, but it did not yield any assessment of the heat output [*Baker et al.*, 1994]. Estimating the heat output solely from the rise height of a plume is not particularly reliable when several vent sites of varying flux contribute to the same coalesced plume [*Baker*, personal communication].

Our device, though simple, proved particularly robust and easy to operate by such a deep submergence vehicle as *Alvin* for both discrete and diffuse venting regimes. The data obtained can be used to better constrain modeling efforts aimed at understanding both the basic physics of hydrothermal flow at the EPR Integrated Studies Site and its response to seismic and volcanic events. Since the ratio of focused and diffuse flows appears to be a fundamental property of hydrothermal systems, further measurements, particularly of the diffuse flow component, are required at 9°50' N EPR (see Table 2.2). Fortunately, due to the non-vigorous character of diffuse flow, it is relatively straightforward to use our device for this purpose.

2.6 Acknowledgments

The authors thank the Associate Editor, Henry Elderfield, and two anonymous reviewers for their helpful comments on this manuscript. The authors also appreciate financial support provided by NSF through grant OCE 0221974 (LNG and RPL) and grant OCE 0327126 (KVD).

2.7 References

- Baker, E. T. (1994), A 6-year time series of hydrothermal plumes over the Cleft segment of the Juan de Fuca Ridge, *J. Geophys. Res.*, 99(B3), 4889-4904.
- Baker, E. T., and G. A. Cannon (1993), Long-term monitoring of hydrothermal heat flux using moored temperature sensors, Cleft Segment, Juan de Fuca Ridge, *Geophys. Res. Lett.*, 20(17), 1855-1858.
- Baker, E. T., R. A. Feely, M. J. Mottl, F. T. Sansone, C. G. Wheat, J. A. Resing, and J. E. Lupton (1994), Hydrothermal plumes along the East Pacific Rise, 8°40' to 11°50'N: Plume distribution and relationship to the apparent magmatic budget, *Earth Planet. Sci. Lett.*, 128, 1-17.
- Baker, E. T., and C. R. German (2004), On the Global Distribution of Hydrothermal Vent Fields, in *Mid-Ocean Ridges: Hydrothermal Interactions Between the Lithosphere and Oceans*, *Geophys. Monogr. Ser.*, vol. 148, edited by C. R. German, et al., pp. 245-266, AGU, Washington, DC.
- Baker, E. T., and G. J. Massoth (1986), Hydrothermal Plume Measurements: A Regional Perspective, *Science*, 234, 980-982.
- Baker, E. T., and G. J. Massoth (1987), Characteristics of hydrothermal plumes from two vent fields on the Juan de Fuca Ridge, northeast Pacific Ocean, *Earth Planet. Sci. Lett.*, 85, 59-73.
- Baker, E. T., G. J. Massoth, R. A. Feely, G. A. Cannon, and R. E. Thomson (1998), The rise and fall of the CoAxial hydrothermal site, 1993-1996, *J. Geophys. Res.*, 103(B5), 9791-9806.
- Baker, E. T., G. J. Massoth, S. L. Walker, and R. W. Embley (1993), A method for quantitatively estimating diffuse and discrete hydrothermal discharge, *Earth Planet. Sci. Lett.*, 118, 235-249.
- Baker, E. T., R. E. McDuff, and G. J. Massoth (1990), Hydrothermal venting from the summit of a ridge axis seamount: Axial Volcano, Juan de Fuca Ridge, *J. Geophys. Res.*, 95(B8), 12,843-12,854.

- Bemis, K. G., R. P. Von Herzen, and M. J. Mottl (1993), Geothermal heat flux from hydrothermal plumes on the Juan de Fuca Ridge, *J. Geophys. Res.*, 98(B4), 6351-6365.
- Carbotte, S., and K. Macdonald (1992), East Pacific Rise 8°-10°30'N: Evolution of ridge segments and discontinuities from Seamarc II and three-dimensional magnetic studies, *J. Geophys. Res.*, 97(B5), 6959-6982.
- Converse, D. R., H. D. Holland, and J. M. Edmond (1984), Flow rates in the axial hot springs of the East Pacific Rise (21°N): implications for the heat budget and the formation of massive sulfide deposits, *Earth Planet. Sci. Lett.*, 69, 159-175.
- Delaney, J. R., V. Robigou, and R. E. McDuff (1992), Geology of a vigorous hydrothermal system on the Endeavour Segment, Juan de Fuca Ridge, *J. Geophys. Res.*, 97(B13), 19,663-19,682.
- Detrick, R. S., P. Buhl, E. Vera, J. Mutter, J. Orcutt, J. Madsen, and T. Brocher (1987), Multi-channel seismic imaging of a crustal magma chamber along the East Pacific Rise, *Nature*, 326, 35-41.
- Elderfield, H., and A. Schultz (1996), Mid-ocean ridge hydrothermal fluxes and the chemical composition of the ocean, *Annu. Rev. Earth Planet. Sci.*, 24, 191-224.
- Fisher, A. T., and K. Becker (1991), Heat flow, hydrothermal circulation and basalt intrusions in the Guaymas Basin, Gulf of California, *Earth Planet. Sci. Lett.*, 103, 84-99.
- Fornari, D., et al. (2004), Submarine Lava Flow Emplacement at the East Pacific Rise 9°50'N: Implications for Uppermost Ocean Crust Stratigraphy and Hydrothermal Fluid Circulation, in *Mid-Ocean Ridges: Hydrothermal Interactions Between the Lithosphere and Oceans*, *Geophys. Monogr. Ser.*, vol. 148, edited by C. R. German, et al., pp. 187-217, AGU, Washington, DC.
- Fornari, D. J., T. Shank, K. L. Von Damm, T. K. P. Gregg, M. Lilley, G. Levai, A. Bray, R. M. Haymon, M. R. Perfit, and R. Lutz (1998), Time-series temperature measurements at high-temperature hydrothermal vents, East Pacific Rise 9°49'-51'N: evidence for monitoring a crustal cracking event, *Earth Planet. Sci. Lett.*, 160, 419-431.
- Gendron, J. F., J. F. Todd, R. A. Feely, E. T. Baker, and D. C. Kadko (1994), Excess ²²²Rn above the Cleft segment of the Juan de Fuca Ridge, *J. Geophys. Res.*, 99(B3), 5007-5015.

Ginster, U., M. J. Mottl, and R. P. Von Herzen (1994), Heat flux from black smokers on the Endeavour and Cleft segments, Juan de Fuca Ridge, *J. Geophys. Res.*, 99(B3), 4937-4950.

Hashimoto, J., S. Ohta, T. Gamo, H. Chiba, T. Yamaguchi, S. Tsuchida, T. Okudaira, H. Watabe, T. Yamanaka, and M. Kitazawa (2001), Hydrothermal vents and associated biological communities in the Indian Ocean, *InterRidge News*, 10(1), 21-22.

Haymon, R. M., D. J. Fornari, M. H. Edwards, S. Carbotte, D. Wright, and K. C. Macdonald (1991), Hydrothermal vent distribution along the East Pacific Rise crest (9°09'-54' N) and its relationship to magmatic and tectonic processes on fast-spreading mid-ocean ridges, *Earth Planet. Sci. Lett.*, 104, 513-534.

Haymon, R. M., et al. (1993), Volcanic eruption of the mid-ocean ridge along the East Pacific Rise crest at 9°45'-52' N: Direct submersible observations of seafloor phenomena associated with an eruption event in April, 1991, *Earth Planet. Sci. Lett.*, 119, 85-101.

Lister, C. R. B. (1983), The Basic Physics of Water Penetration Into Hot Rock, in *Hydrothermal Processes at Seafloor Spreading Centers*, edited by P. A. Rona, et al., pp. 141-168, Plenum Press, New York and London.

Little, S. A., K. D. Stolzenbach, and R. P. Von Herzen (1987), Measurements of plume flow from a hydrothermal vent field, *J. Geophys. Res.*, 92(B3), 2587-2596.

Lonsdale, P., and K. Becker (1985), Hydrothermal plumes, hot springs, and conductive heat flow in the Southern Trough of Guaymas Basin, *Earth Planet. Sci. Lett.*, 73, 211-225.

Lowell, R. P., and M. DuBose (2005), Hydrothermal systems on Europa, *Geophys. Res. Lett.*, 32, L05202, doi:10.1029/2005GL022375.

Lowell, R. P., and L. N. Germanovich (1994), On the temporal evolution of high-temperature hydrothermal systems at ocean ridge crests, *J. Geophys. Res.*, 99(B1), 565-575.

Lowell, R. P., and L. N. Germanovich (2004), Hydrothermal Processes at Mid-Ocean Ridges: Results From Scale Analysis and Single-Pass Models, in *Mid-Ocean Ridges: Hydrothermal Interactions Between the Lithosphere and Oceans*, *Geophys. Monogr. Ser.*, vol. 148, edited by C. R. German, et al., pp. 219-244, AGU, Washington, DC.

Macdonald, K. C., K. Becker, F. N. Spiess, and R. D. Ballard (1980), Hydrothermal heat flux of the "black smoker" vents on the East Pacific Rise, *Earth Planet. Sci. Lett.*, *48*, 1-7.

McConachy, T. F., R. D. Ballard, M. J. Mottl, and R. P. Von Herzen (1986), Geologic form and setting of a hydrothermal vent field at lat 10°56'N, East Pacific Rise: A detailed study using Angus and Alvin, *Geology*, *14*, 295-298.

Murton, B. J., L. J. Redbourn, C. R. German, and E. T. Baker (1999), Sources and fluxes of hydrothermal heat, chemicals and biology within a segment of the Mid-Atlantic Ridge, *Earth Planet. Sci. Lett.*, *171*, 301-317.

Ramondenc, P., L. N. Germanovich, and R. P. Lowell (2005), Modeling hydrothermal response to earthquakes at mid-ocean ridges: EPR, *Eos Trans. AGU*, *86*(52), Abstract T31B-0500.

Rona, P. A., M. D. Hannington, C. V. Raman, G. Thompson, M. K. Tivey, S. E. Humphris, C. Lalou, and S. Petersen (1993), Active and relict Sea-Floor Hydrothermal Mineralization at the TAG Hydrothermal Field, Mid-Atlantic Ridge, *Econ. Geol.*, *88*, 1989-2017.

Rona, P. A., and D. A. Trivett (1992), Discrete and diffuse heat transfer at ASHES vent field, Axial Volcano, Juan de Fuca Ridge, *Earth Planet. Sci. Lett.*, *109*, 57-71.

Rosenberg, N. D., J. E. Lupton, D. Kadko, R. Collier, M. D. Lilley, and H. Pak (1988), Estimation of heat and chemical fluxes from a seafloor hydrothermal vent field using radon measurements, *Nature*, *334*, 604-607.

Rudnicki, M. D., and H. Elderfield (1992), Theory applied to the Mid-Atlantic Ridge hydrothermal plumes: the finite-difference approach, *J. Volcanol. Geotherm. Res.*, *50*, 161-172.

Rudnicki, M. D., and C. R. German (2002), Temporal variability of the hydrothermal plume above the Kairei vent field, 25°S, Central Indian Ridge, *Geochem. Geophys. Geosyst.*, *3*(2), doi:10.1029/2001GC000240.

Schultz, A., J. R. Delaney, and R. E. McDuff (1992), On the partitioning of heat flux between diffuse and point source seafloor venting, *J. Geophys. Res.*, *97*(B9), 12,299-12,314.

- Shank, T. M., D. J. Fornari, K. L. Von Damm, M. D. Lilley, R. M. Haymon, and R. A. Lutz (1998), Temporal and spatial patterns of biological community development at nascent deep-sea hydrothermal vents (9°50'N, East Pacific Rise), *Deep Sea Res. II*, 45, 465-515.
- Sohn, R. A., D. J. Fornari, K. L. Von Damm, J. A. Hildebrand, and S. C. Webb (1998), Seismic and hydrothermal evidence for a cracking event on the East Pacific Rise crest at 9°50' N, *Nature*, 396, 159-161.
- Sohn, R. A., J. A. Hildebrand, and S. C. Webb (1999), A microearthquake survey of the high-temperature vent fields on the volcanically active East Pacific Rise (9°50'N), *J. Geophys. Res.*, 104(B11), 25,367-25,377.
- Stein, C. A., and S. Stein (1994), Constraints on hydrothermal heat flux through the oceanic lithosphere from global heat flow, *J. Geophys. Res.*, 99(B2), 3081-3095.
- Stein, C. A., S. Stein, and A. Pelayo (1995), Heat Flow and Hydrothermal Circulation, in *Seafloor Hydrothermal Systems: Physical, Chemical, Biological, and Geological Interactions*, *Geophys. Monogr. Ser.*, vol. 91, edited by S. E. Humphris, et al., pp. 425-445, AGU, Washington, DC.
- Stein, J. S., and A. T. Fisher (2001), Multiple scales of hydrothermal circulation in Middle Valley, northern Juan de Fuca Ridge: Physical constraints and geologic models, *J. Geophys. Res.*, 106(B5), 8563-8580.
- Thomson, R. E., J. R. Delaney, R. E. McDuff, D. R. Janecky, and J. S. McClain (1992), Physical characteristics of the Endeavour Ridge hydrothermal plume during July 1988, *Earth Planet. Sci. Lett.*, 111, 141-154.
- Veirs, S. R., R. E. McDuff, and F. R. Stahr (2005), Magnitude and variance of near-bottom horizontal heat flux at the Main Endeavour hydrothermal vent field, *Geochem. Geophys. Geosyst.*, in press.
- Von Damm, K. L. (2000), Chemistry of hydrothermal vent fluids from 9°-10°N, East Pacific Rise: "Time zero," the immediate post-eruptive period, *J. Geophys. Res.*, 105(B5), 11,203-11,222.
- Von Damm, K. L. (2004), Evolution of the Hydrothermal System at East Pacific Rise 9°50'N: Geochemical Evidence for Changes in the Upper Oceanic Crust, in *Mid-Ocean Ridges: Hydrothermal Interactions Between the Lithosphere and Oceans*, *Geophys.*

Monogr. Ser., vol. 148, edited by C. R. German, et al., pp. 285-304, AGU, Washington, DC.

Von Damm, K. L., and M. D. Lilley (2004), Diffuse Flow Hydrothermal Fluids from 9°50' N East Pacific Rise: Origin, Evolution and Biogeochemical Controls, in *The Subseafloor Biosphere at Mid-Ocean Ridges, Geophys. Monogr. Ser.*, vol. 144, edited by W. S. D. Wilcock, et al., pp. 245-268, AGU, Washington, DC.

Von Damm, K. L., C. M. Parker, K. A. Beers, A. A. Hyde, and PIRATES-1 Science Party (2004), Continuing evolution of the hydrothermal system at the RIDGE2000 ISS, 9-10°N EPR: 1991-2004, *Eos Trans. AGU*, 85(47), Abstract T21C-0538.

Wilcock, W. S. D. (2004), Physical response of mid-ocean ridge hydrothermal systems to local earthquakes, *Geochem. Geophys. Geosyst.*, 5, Q11009, doi:10.1029/2004GC000701.

CHAPTER 3

MODELING HYDROTHERMAL RESPONSE TO EARTHQUAKES AT OCEANIC SPREADING CENTERS

Abstract. We develop a two-branch single-pass modeling approach to investigate the response of hydrothermal systems to earthquakes at oceanic spreading centers. In this approach, deep circulation gives rise to high temperature fluids that are assumed to arrive at the seafloor as focused, black smoker-like vents, whereas shallow circulation within the extrusives results in low-temperature diffuse flow. The diffuse flow is a mixture of black smoker fluid and seawater; consequently, seismic events that alter the permeability of the crust may affect both high-temperature vents and the low-temperature diffuse flow. In this model, ascending fluid in both the high- and low-temperature branches is nearly isothermal except within thin boundary layers at the seafloor and at the junction where fluid mixing occurs. As a result, thermal perturbations at depth do not need to traverse the entire upflow zone, but rather just need to affect the boundary layers. We show that cracking events, which generate new permeability and thereby increase the rate of heat transfer in a narrow zone at the base of the system, do not give rise to rapid temperature changes at the seafloor; however, only modest increases in permeability occurring over a region of a few hundred meters within the deep discharge zone are sufficient to generate observable thermal perturbations. Moreover, the response of the dynamically coupled circulation systems simultaneously results in an initial positive temperature pulse as well

as the observed longer-lived temperature decrease in both the high- and low- temperature fluid.

3.1 Introduction

High temperature hydrothermal systems at oceanic spreading centers are characterized by a complex interplay among magmatic, tectonic and biogeochemical reactive transport processes. Magmatic processes provide the principal heat source, whereas all three processes affect the permeability structures through which the fluid circulates. A complete understanding of hydrothermal systems at oceanic spreading centers thus requires the development of integrated mathematical models that describe the combined effects of these processes. Although steady state models provide important insight into the behavior of hydrothermal systems, much information can be obtained by investigating the response to the system as a result of temporal changes in various forcing functions. *Lowell et al.* [2007a] discuss some temporal aspects of magmatic and biogeochemical processes in the context of multiphase, multi-component fluid flow. Here we focus on the volcanic-tectonic aspects by investigating the response of hydrothermal systems to earthquakes. Because tectonic processes, including earthquakes, may be associated with magmatic processes such as diking, the separation between magmatic and tectonic processes is not pure. We introduce this material by briefly reviewing issues related to the detection and monitoring of the earthquakes themselves and then by reviewing the limited data on the hydrothermal response. A more thorough analysis of earthquakes at oceanic spreading centers is given by *Tolstoy* [2007].

3.1.1 *Magmatic and tectonic events at mid-ocean ridges*

Despite considerable improvements over the last two decades, the characterization of magmatic and tectonic events at mid-ocean ridges remains difficult. The first discoveries of diking and eruptive events at the seafloor were serendipitous [*Baker et al.*, 1987; *Haymon et al.*, 1993], because earthquakes associated with volcanic events at fast and intermediate spreading ridges generally have magnitudes below $M = 4$, which is the threshold for global detection by land-based seismometers [*Fox et al.*, 2001]. *Fox et al.* [1993/94] showed that hydrophone arrays recording tertiary waves (or T-waves) could detect seismicity (as low as $M = 1.8$). Their work and the use of the U.S. Navy's Sound Surveillance System (SOSUS) [e.g., *Cowen et al.*, 2004], allowed a better monitoring of the activity of the intermediate spreading Juan de Fuca Ridge in the northeast Pacific Ocean, thought to be "aseismic" up to that point [*Dziak et al.*, 2006]. Today, Iceland and the northeast Pacific are the only parts of the mid-ocean ridge system covered by a continuous real-time hydroacoustic monitoring system [*Embley and Lupton*, 2004]. This remains, at present, the best available method to remotely detect seafloor volcanic and tectonic activity. Other places, such as the northern East Pacific Rise [*Fox et al.*, 2001] and the northern Mid-Atlantic Ridge [*Smith et al.*, 2002], have benefited from autonomous hydrophones arrays, whose performances are comparable to SOSUS. Deployed in the late 90's, these systems are permanent but lack real-time capabilities. They need to be maintained periodically, and earthquakes are only available after a certain time lag, which can reach ~ 2.5 years [*Dziak et al.*, 2004]. Both hydrophone arrays allowed the detection of several earthquake swarms that have been associated with volcanic activity [*Fox et al.*, 2001; *Smith et al.*, 2002]. In particular, the March 2001

Lucky Strike event [Dziak *et al.*, 2004] on the Mid-Atlantic Ridge was interpreted as a dike intrusion in the shallow crust, the first dike emplacement episode that was detected along the slow-spreading Mid-Atlantic Ridge.

The detection of seismic activity by hydroacoustic arrays needs to be followed by response cruises for a detailed assessment of the events and actual in-situ measurements [Cowen *et al.*, 2004]. In this respect, SOSUS real-time monitoring is particularly interesting because it considerably reduces the response time. Since its implementation in June 1993, six response cruises have been organized to look for magmatic and/or hydrothermal activity based on the seismic characteristics of the detected swarms [see Figure 1 from Dziak *et al.*, 2006]. Three of these events were interpreted as dike injection with eruption at the seafloor, as response cruises found fresh lava flows, microbial-mineral flocs and enhanced chronic venting: in June 1993 on the CoAxial segment (Juan de Fuca Ridge) [Baker *et al.*, 1998; Baker *et al.*, 1995; Dziak *et al.*, 1995; Embley *et al.*, 1995; Fox, 1995; Fox *et al.*, 1995; Juniper *et al.*, 1995], in February 1996 on the North Gorda Ridge [Baker, 1998; Fox and Dziak, 1998], and in January 1998 at Axial Volcano (Juan de Fuca Ridge) [Baker *et al.*, 1999; Dziak and Fox, 1999; Embley and Baker, 1999]. The other three events provided valuable information through their unexpected responses. The 2001 Gorda Ridge swarm showed that the lack of lateral migration of earthquake epicenters may be an indication that the magma failed to reach the seafloor. The 2001 Middle Valley (Juan de Fuca Ridge) event was the first to occur at a sedimented ridge and the absence of water column signal may have been due to the sediment cap (~ 100 m thick) that prevented the dike from reaching the seafloor [Cowen *et al.*, 2004]. Also, in contrast to the usual increase in hydrothermal discharge, the fluid

pressure transients were found to be negative [Davis *et al.*, 2004], perhaps as the result of dilatation of the upper permeable crust. The most recent earthquake swarm on the Juan de Fuca Ridge occurred on 27 January 2005. Despite a lower rate and distance of migration, a response cruise was sent out, but did not find any sign of a seafloor eruption or the release of an event plume [Dziak *et al.*, 2006]. Yet this sixth response effort, along with the analysis of all the others, allowed Dziak *et al.* [2006] to identify two factors that may indicate eruption and hydrothermal discharge during an event: the earthquake migration rate and timing.

3.1.2 The hydrothermal response

Although the detection and analysis of seafloor seismic events has progressed over the last two decades, it provides only one piece of the information needed to understand the response of seafloor hydrothermal systems to tectonic and/or magmatic perturbations in the crust. Vent fluid temperature and flux data are also needed. Yet, instrumentation is seldom deployed and recording during the course of a perturbation. Most examples concern short-term experiments that happened to be deployed at the right time. Axial Volcano, on the Juan de Fuca Ridge represents perhaps the best example of a long-term, multi-disciplinary seafloor observatory that has recorded data during a seafloor spreading event [Baker *et al.*, 1999; Embley and Baker, 1999]. The temperature data was of particular interest, featuring a nearly instantaneous increase in the hydrothermal output just after the eruption, followed by a gradual decrease for two weeks, and again a slight increase to stabilize at a value approximately 0.1°C higher than the pre-event level [Baker *et al.*, 1999]. The 9°50' N area of the East Pacific Rise has also benefited from continuous temperature monitoring for nearly two decades [Scheirer *et*

al., 2006]. The most recent spreading event was recorded in this area in 2006 [*Tolstoy et al.*, 2006].

The best-documented cases of hydrothermal response to crustal perturbation are associated with two non-eruptive events. On the Endeavour segment of the Juan de Fuca Ridge, the pattern of the June 1999 swarm contrasted with the usual submarine volcanic activity pattern. Instead of steady low-level seismicity, it featured a main shock followed by five days of aftershocks that decayed quasi-exponentially and seemed devoid of volcanic tremor [*Johnson et al.*, 2000]. The ridge community decided not to send a response cruise after the detection by SOSUS [*Cowen et al.*, 2004]. Submersible dives in the area, which occurred three months later, did not find evidence of volcanic activity, but observed an increase of the same particulate matter ejected by “snowblower” vents associated with eruptive events [*Johnson et al.*, 2000]. Vent fluid chemistry changes [*Lilley et al.*, 2003; *Seyfried et al.*, 2003] showed strong evidence of subseafloor magmatic activity. Moreover, a multichannel seismic reflection experiment conducted across and along the full length of the Juan de Fuca Ridge in 2002 clearly detected an axial magma chamber 2.3 - 2.6 km below the zone where the swarm occurred [*Detrick et al.*, 2002]. Based on these data and reanalysis of the hydroacoustic data, *Bohnenstiehl et al.* [2004] suggested that the swarm resulted from lateral propagation of a dike initiated from the shallow magma chamber.

The continuous recording of temperature evolution on the Endeavour segment at three diffuse vents situated tens of kilometers from the swarm epicenters showed that the previous 10 months were stable. Fluid temperatures first started increasing 4 (± 1) days

after the onset of seismicity at the Easter Island site, situated within 10 m of a high-temperature smoker. The other two sites, situated several hundreds of meters away from the adjacent high-temperature fields and 2 km apart from each other, showed a temperature increase approximately 11 days after the initiation of seismicity. Once the maximum rise was reached, large-amplitude oscillations (up to $\pm 5^{\circ}\text{C}$) took place at the three sites, with periods between 8 and 12 days, and lasted for approximately a month. Although the oscillations were correlated within each site, they showed poor correlation between them [Johnson *et al.*, 2000]. Johnson *et al.* [2000] suggested that the oscillations resulted from the non-uniform advance of a cracking front at depth to mine heat, plugging and unblocking due to biological activity in the sub-surface, or the unsteady evolution of convection toward a new equilibrium after the disturbance. Based on the temperature records and assuming the reservoir of crustal fluid was a porous medium, they estimated that the vent flow rate had increased by one order of magnitude over the course of at least 80 days along the whole ridge segment. Vent fluid monitoring at Axial Seamount, approximately 220 km from the epicenter, also showed a temperature increase following the onset of seismicity. This occurred no more than 8 hours after the main shock, sooner than at vent fields located much closer to the epicenters [Johnson *et al.*, 2001]. Davis *et al.* [2001] also reported crustal fluid pressure variations in a series of Ocean Drilling Program boreholes, which they interpreted as the result of partially aseismic fault-related slip.

Another significant event occurred in March 1995 in the $9^{\circ}50' \text{N}$ area of the East Pacific Rise, where an array of nine ocean-bottom seismometers had been deployed for a microearthquake survey [Sohn *et al.*, 1998; Sohn *et al.*, 1999]. This site has been the

focus of continuous investigation since the fortuitous discovery of a fresh volcanic eruption in 1991 [Haymon *et al.*, 1993]. The three month deployment of an ocean bottom seismometer array allowed the detection of 283 microearthquakes (with local magnitudes of $-1 \leq M_L \leq 0$) whose epicenters formed two separate clusters along the ridge axis. The larger was situated north of the 9°50' N area and close to Bio9 and P vents, and the smaller was located further south near the Tube Worm Pillar and Y vent. The north earthquake cluster occurred in two distinct swarms. The first occurred on March 22, with 162 events in less than 3 hours, and the second occurred 22 days later, with 25 events. The south cluster showed a nearly continuous low-level seismicity over the span of the survey. Sohn *et al.* [1999] estimated 147 hypocenters from the recovered seismic data (115 for the north group, 32 for the south one), all in the upper 1.2 km of the crust. Relocation of 65 of these hypocenters suggested a particularly high density between 0.7 and 1.1 km depth, just above the axial magma chamber whose depth has been estimated at 1.4 km [Kent *et al.*, 1993]. Based on this hypocentral pattern, Sohn *et al.* [1999] considered a diking event unlikely. They also discounted a tectonic origin. Rather, the microearthquake activity was attributed to the release of thermal stresses at the base of the hydrothermal system. The analysis of vent fluid chemistry also supported the hypothesis of crack-deepening of the hydrothermal reaction zone [Fornari *et al.*, 1998; Sohn *et al.*, 1998].

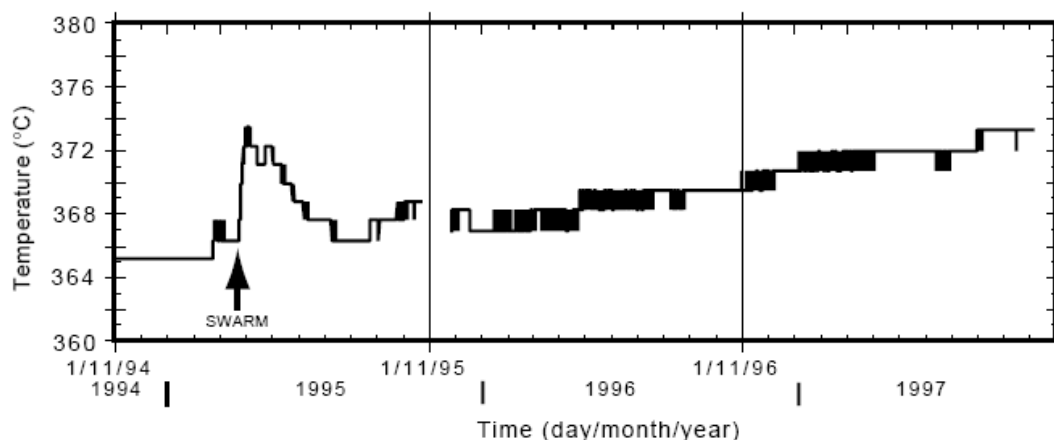


Figure 3.1. Thermal response of the high-temperature Bio9 vent at East Pacific Rise 9°50' N [from *Sohn et al.*, 1998].

Monitoring of vent fluid temperature and chemistry of the 9°50' N area following the 1991 magmatic eruption has allowed correlation between the March 1995 seismic activity and changes in the hydrothermal systems situated above the epicenters [*Fornari et al.*, 1998; *Sohn et al.*, 1998; *Sohn et al.*, 1999]. The temperature data (Figure 3.1) collected by *Fornari et al.* [1998] for the Bio9 vent showed that vent temperature was stable for approximately 15 months prior to the March 1995 event, at $365 \pm 1^\circ\text{C}$. On March 26, a 7°C increase was observed over 8 days. Temperature stabilized at $372 \pm 1^\circ\text{C}$ until April 16, then gradually decreased to $366 \pm 1^\circ\text{C}$ over approximately 3.5 months before steadily increasing again for several months. In November 1995, the temperature probe was found embedded into the chimney and replaced. The replacement probe showed the same steady temperature increase, with temperature reaching $373 \pm 1^\circ\text{C}$ in November 1997 (Figure 3.1). Two surveys of animal communities around the Bio9 area (October 1994 and November 1995) also reflected an overall increase in venting temperature. Bio9 is the only vent in the 9°50' N area that had continuous monitoring

between October 1994 and November 1995. Point measurements and other probe records showed that temperatures steadily increased by more than 40°C at M vent between March 1992 and November 1995, while they remained nearly constant at Biovent, however.

In this chapter, we focus on the March 1995 East Pacific Rise events due to the availability of well-documented data during, prior, and subsequent to the earthquake swarms [Fornari *et al.*, 1998; Sohn *et al.*, 1998; Sohn *et al.*, 1999]. Records of diffuse venting do not exist [Scheirer *et al.*, 2006], consequently we will focus on the high-temperature variations near the epicenters. Our model can be used to study the combined evolution of low-temperature diffuse and high-temperature focused venting systems, however.

3.2 Mechanics of hydrothermal response

For both the March 1995 East Pacific Rise and June 1999 Juan de Fuca events, the interval between the onset of seismicity and temperature variations at the seafloor was interpreted as the fluid residence time [Fornari *et al.*, 1998; Sohn *et al.*, 1998; Johnson *et al.*, 2000]. This residence time was significantly smaller than the previous constraint of ~ 3 years that Kadko and Moore [1988] suggested based on a study of $^{210}\text{Pb}/\text{Pb}$ and $^{228}\text{Ra}/^{226}\text{Ra}$ ratios on the Endeavour segment of the Juan de Fuca Ridge. Johnson *et al.* [2000] suggested that the time delay may be a characteristic time constant associated with the response of the hydrothermal system to the disturbance. Comparison of temperature time-series obtained on both the Main Endeavour field and Axial Seamount (Juan de Fuca Ridge) during the June 1999 swarm showed that this time constant may vary over a wide range, from 8 hours to 36 days [Johnson *et al.*, 2001]. In

comparison, land-based hydrothermal systems tend to respond nearly instantaneously to seismic activity [e.g., *Hill et al.*, 1993; *Roeloffs*, 1996]. *Dziak and Johnson* [2002] explain this dissimilarity by a difference of crustal architecture, noting that on-land systems present diverse fluid reservoir geometries, and that the observed hydrological response is usually linked to seismic waves compressing and dilating the pore space of these reservoirs. At mid-ocean ridges, the aquifer is thought to be more uniform and continuous; and the hydrothermal circulation is thermally driven.

3.2.1 *Wilcock's [2004] work*

Wilcock [2004] showed that Darcian flow through a porous medium could propagate a temperature perturbation a distance of ~ 1 km in a few days, provided the permeability of the discharge zone is $\sim 10^{-9} \text{ m}^2$. This is much higher than the usual range of 10^{-12} – 10^{-13} m^2 inferred for high-temperature hydrothermal systems [*Lowell and Germanovich*, 1994; *Pascoe and Cann*, 1995; *Wilcock and McNabb*, 1996; *Cherkaoui et al.*, 1997; *Fisher*, 1998; *Wilcock and Fisher*, 2004]. *Wilcock* [2004] also showed that pressure anomalies and permeability variations at depth could generate the temperature variations observed at the seafloor. The delay observed at the seafloor depends on the depth of the pressure perturbation as well as the permeability. For a pressure anomaly at ~ 1 km depth, a permeability of $\sim 10^{-14} \text{ m}^2$ or smaller is required to delay the response at the seafloor by a few days [*Wilcock*, 2004]. This is smaller than the afore-mentioned range of 10^{-12} – 10^{-13} m^2 that is characteristic of high temperature venting.

One of *Wilcock's* [2004] interpretations of the March 1995 seismic activity at 9°50' N, East Pacific Rise is a cracking event that opened up a new pathway to hot rock

at the base of the hydrothermal system [Fornari *et al.*, 1998; Sohn *et al.*, 1999]. Following Bodvarsson [1969], Wilcock [2004] first considered the temperature distribution in a single planar crack embedded in an infinite medium with an oscillatory fluid temperature imposed at the base of the crack. To fit the observed temperature anomaly (Figure 3.1), he then assumed that the initial swarm was accompanied by a basal temperature increase of $\sim 50^\circ\text{C}$ that linearly decreased over 16 days, followed by a smaller temperature increase of 17°C at the time of a secondary swarm, which in turn decayed over 25 days (see Appendix B for discussion about Wilcock's [2004] method). He obtained a good fit to the first 90 days of the data shown in Figure 3.1 with a crack 0.6 mm wide.

A similar approach to temperature perturbation at the base of hydrothermal system was considered by Lowell [1975, 1976]. His model considers flow in an isolated narrow fracture (or set of fractures) embedded in impermeable rock. In this case, the temperature change, ΔT_v , at the vent related to an instantaneous temperature step, ΔT_b , at depth, z , is given by

$$\frac{\Delta T_v}{\Delta T_b} = \text{erfc}\left(\frac{\lambda_r z}{q c_f \sqrt{a t}}\right) \quad (3.1)$$

where q is the mass flux per unit length of the crack, λ_r is the thermal conductivity of the rock, $a = \lambda_r / (c_f \rho_f)$ is the effective thermal diffusivity, c_f is the specific heat of water, and t is time, respectively. Table 3.1 summarizes all the symbols used in the formulation and their range of values. Given an assumed $\Delta T_b \sim 50^\circ\text{C}$, $z = 1$ km, reasonable values of thermal parameters (see Table 3.1), and observed values of ΔT_v and time t (respectively $\sim 10^\circ\text{C}$ and ~ 10 days at Bio 9), the mass flux calculated from (3.1) is $q \sim 1$ kg/(m \times sec).

Assuming buoyancy-driven flow through a single effective crack, the effective crack width d_c can be calculated from [e.g., *Bear*, 1972]

$$d_c = \left(\frac{12\nu q}{g \Delta\rho} \right)^{1/3} \quad (3.2)$$

where ν is the kinematic viscosity of the fluid, $\Delta\rho \sim 0.4 \text{ kg/m}^3$ is the density difference between descending and ascending fluids, and g is the acceleration due to gravity, respectively. For typical parameters, equation (3.2) gives $d_c \sim 1 \text{ mm}$. The subsequent temperature decay in Figure 3.1 could be modeled by invoking a temperature decrease at the base of the crack.

Both of these temperature perturbation models fit the rapid temperature increase and secular decay following an eruption reasonably well; the initial temperature delay being related to conductive cooling along the flow path. Neither model, however, explains the secular rise in temperature observed over the ensuing years (Figure 3.1). Moreover, the imposed temperature perturbations do not have a firm physical basis; and the high effective permeability in these single crack models yields a fluid residence time in the upflow zone of less than one hour. Hence we consider these single crack models to be somewhat unrealistic.

Table 3.1. Symbol definitions and parameter values.

Symbol	Definition	Value
a	effective thermal diffusivity, $\lambda_r/(\rho_r c_r)$	$\sim 10^{-6} \text{ m}^2/\text{s}$
a_*	effective thermal diffusivity in equation (3.24)	
a_r	thermal diffusivity of rock, $\lambda_r/(\rho_r c_r)$	$\sim 10^{-6} \text{ m}^2/\text{s}$
A_1	cross-sectional area of the upper part of the upflow zone	10^4 m^2
A_2	cross-sectional area of the lower part of the upflow zone	10^4 m^2
A_3	cross-sectional area of the horizontal limb of the deep recharge	10^4 m^2
A_4	cross-sectional area of the horizontal limb of the shallow recharge	$10^2\text{-}10^3 \text{ m}^2$
b	length of vent field along strike	100 m
b_*	parameter in equation (3.24)	
c_f	specific heat of water	$4 \times 10^3 \text{ J}/(\text{kg}^\circ\text{C})$
c_r	specific heat of rock	$1 \times 10^3 \text{ J}/(\text{kg}^\circ\text{C})$
d	basal thermal boundary layer thickness	2-20 m
d_c	effective crack width	
f	height of the junction between upflow and shallow recharge limb	1-10 m
g	acceleration due to gravity	9.8 m/s^2
H	length of the upflow zone	1.5 km
$H(x)$	Heaviside function	
h	depth of the shallow recharge	100 m
h_d	height of the dike emplacement	600 m
I	source of material produced by the shallow recharge	
k	(temperature dependent) permeability	
k_0	initial permeability	$10^{-13}\text{-}10^{-12} \text{ m}^2$
k_{res}	residual permeability	$10^{-2}k_0$
L	length of the horizontal limb of the deep recharge	1 km
L_m	latent heat of crystallization	$4 \times 10^5 \text{ J/kg}$
P	pressure	
P_0	pressure at the seafloor	200-300 bars
P_H	pressure at the depth H below the seafloor	
Q_i	mass flux in the i^{th} limb	
q	mass flux per unit length of the crack	
q_d	heat source density per unit time and unit volume of the dike	
q_m	basal heat flux (heat uptake rate)	
q_w	lateral heat transfer density per unit time and unit volume	
r_i	hydrodynamic resistance per unit area in the I^{th} limb	
s	“curvilinear” spatial variable along the flow path (deep limb and upflow)	
t	time	
t_c	time of dike crystallization	
t_d	time of dike emplacement	
T	temperature in the upflow zone	
T_0	temperature at undisturbed ocean floor conditions	0°C
T_*	effective temperature in equation (3.24)	
$T_{diffuse}$	temperature monitored at sites of diffuse venting	$5\text{-}30^\circ\text{C}$
T_{in}	initial steady-state temperature	
T_j	temperature of the fluid from the shallow recharge at junction point	
T_m	melting temperature of basalt	1200°C
T_{rech}	far-field temperature in the recharge zone (for deep recharge)	$0\text{-}100^\circ\text{C}$
T_{sh}	far-field temperature in the recharge zone (for shallow recharge)	$0\text{-}10^\circ\text{C}$
ΔT_b	temperature change at the base of the upflow zone	
ΔT_v	temperature change at the vent	
v	Darcian flow velocity (specific discharge)	
v_0	initial Darcian flow velocity	
w	dike width (opening)	1 m

Table 3.1. (continued)

Symbol	Definition	Value
w_u	width of vent field (upflow zone)	100 m
z	depth	
α_r	linear thermal expansion coefficient of rock	$2 \times 10^{-5} / ^\circ\text{C}$
α_f	coefficient of thermal expansion of water	$10^{-3} / ^\circ\text{C}$
δ	thermal boundary layer thickness	a/v
$\delta(s)$	Dirac delta function	
ϕ_0	initial porosity of the upflow zone	0.1-10 %
γ	ratio α_r/ϕ_0	10^{-4} - 10^{-1}
η	(temperature dependent) dynamic viscosity of water	
ν	kinematic viscosity of water	η/ρ
λ	parameter related to the rate of dike freezing [Germanovich et al., 2000]	1
λ_r	coefficient of thermal conductivity of rock	$2.5 \text{ W}/(\text{m}^\circ\text{C})$
ρ_f	(temperature dependent) density of water	
ρ_r	rock density	$3 \times 10^3 \text{ kg}/\text{m}^3$
ρ_0	initial density of water at the ocean floor	$10^3 \text{ kg}/\text{m}^3$
$\Delta\rho$	density difference between descending and ascending fluids	$\sim 0.4 \text{ kg}/\text{m}^3$

3.2.2 Approach in this paper

During porous discharge, lateral heat losses and mixing in the shallow subsurface result in a thin thermal boundary layer near the seafloor. This boundary layer can be derived from the equation of steady state heat transfer

$$v_0 \frac{dT}{dz} = a \frac{d^2T}{dz^2} \quad (3.3)$$

where v_0 is the initial Darcian velocity (specific discharge) in the discharge zone and a is the effective thermal diffusivity. The thickness of the boundary layer is $\delta \sim a/v_0$, and since advection prevails in the rest of the upflow zone, the temperature profile is almost constant everywhere except in the boundary layer (Figure 3.2). In this case, neither the fluid flow nor the temperature response to the earthquake has to propagate through the entire discharge zone, but need only affect the movement of the boundary layer. For a typical value of thermal diffusivity $a \sim 10^{-6} \text{ m}^2/\text{s}$ and a Darcian velocity of $v \sim 10^{-6} \text{ m/s}$,

should the boundary layer be altered, the expected response time would be $\sim \delta/v \sim 10$ days.

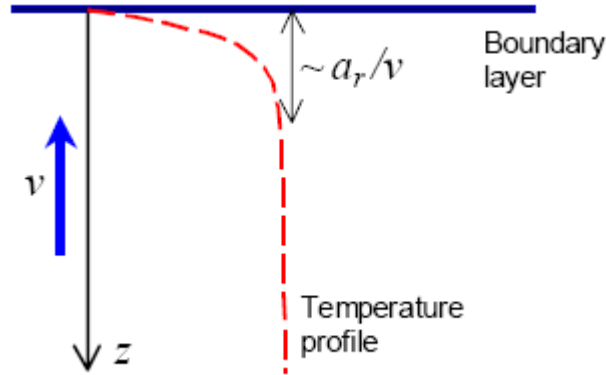


Figure 3.2. Steady state temperature distribution in the discharge zone prior to the earthquake and definition of the boundary layer.

One can apply this simple model to the case of high temperature venting by using a heat transfer boundary condition at the upper boundary [Germanovich *et al.*, 2001]. This condition can be interpreted as representing the mixing between high-temperature discharge and overlying low temperature fluids in the upper crust. Such a boundary condition can be used in the context of a single-pass model (Figure 3.3) as well as in a one-dimensional upflow model. An advantage of using this boundary condition is that the same model formulation can be used to address perturbations to both high-temperature systems, such as Bio9 vent, and low-temperature diffuse flow systems, such as those observed on the Juan de Fuca Ridge. Using this model, we have shown that an increase in permeability can sufficiently perturb the boundary layer to give the observed temperature

increases at Bio9 at the time scale of a week [Ramondenc *et al.*, 2005]. Changes in the stress field resulting from earthquakes tend to create or reopen fractures thereby increasing permeability [Brodsky *et al.*, 2003; Elkhoury *et al.*, 2006; Rojstaczer and Wolf, 1992; Rojstaczer *et al.*, 1995]. It is also possible that permeability increases would appear in the case of dike intrusion, especially near the margins of the dike [Delaney *et al.*, 1986; Germanovich *et al.*, 2000; Pollard, 1987]. Our simulations [Ramondenc *et al.*, 2005] indicate that the fluid residence time in the discharge zone is on the order of years, which is consistent with the general scaling of the upflow zone [e.g., Lowell and Germanovich, 2004].

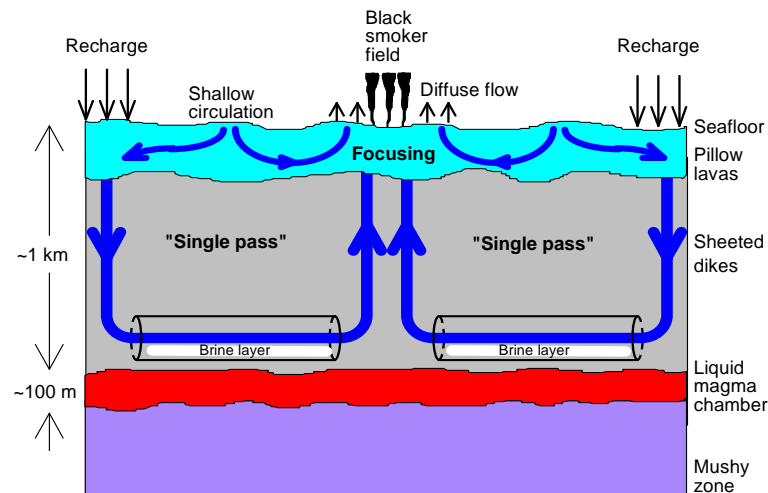


Figure 3.3. Cartoon of a single-pass hydrothermal circulation model at an ocean ridge crest at the local, ridge crest circulation scale. The fracture-like segment at the base of the sheeted dikes represents the region where chemical reactions and heat uptake from the magma chamber occur, and where brine may reside. The focused, high temperature flow is thought to occur in the main single-pass limb. Diffuse flow may occur as a result of mixing of the deep circulation with shallow circulation in the shallow extrusive basalts. Chemical reactions occur throughout the circulation path. Biogeochemical processes also occur in the extrusives [from Germanovich *et al.*, 2001].

Our initial approach [Ramondenc *et al.*, 2005] did not address the decay of the temperature spike, which occurs on a time scale of months, nor the longer term temperature rise at Bio9, which occurs over a time scale of years (Figure 3.1). In this chapter, however, we extend the idea of thermal boundary layer using a “double-loop” model (described in Section 3.3) to explain the observed temperature history within the first year after the seismic event at 9°50' N, East Pacific Rise. We also suggest a mechanism to explain the later rise of the observed temperature.

Lowell et al. [2007b] have recently developed numerical models of single-pass convection in the presence of a high-permeability extrusive layer. Their results show that mixing between ascending hydrothermal fluid and seawater circulating in the extrusives can lead to either black smoker flow together with nearby diffuse flow or to a system exhibiting only low temperature diffuse flow. The nature of the hydrothermal output depends mainly upon the permeability ratio between the extrusives and the deep discharge channel, and secondarily on the thickness of the extrusives [see also, *Lowell et al.* 2007a], although relatively small changes in permeability may affect system evolution towards low- or high-temperature venting [Germanovich *et al.*, 2001]. *Lowell et al.* [2007b] did not consider the effects of magmatic or tectonic events, however.

3.3 Formulation

3.3.1 *Mixing in the shallow crust*

At the seafloor, high-temperature venting occurs through discrete point sources such as sulfide chimneys, fissures, or flanges protruding from the walls of large sulfide edifices [Delaney *et al.*, 1992]. Low-temperature diffuse flow usually occurs over much

larger areas of the seafloor [*Baker et al.*, 1993; *Bemis et al.*, 1993; *Rona and Trivett*, 1992]. The relationship between diffuse and focused flows remains puzzling. In general, focused venting constitutes only a fraction of the diffuse flow [Table 1 from *Ramondenc et al.*, 2006]. At some vent sites only diffuse, low-temperature venting occurs (e.g., at the Galapagos Spreading Center [*Corliss et al.*, 1979; *Edmond et al.*, 1979]), whereas at others black smokers and low-temperature diffuse flow co-exist (e.g., the TAG vent field on the Mid-Atlantic Ridge [*Edmond et al.*, 1995; *Humphris and Tivey*, 2000; *James and Elderfield*, 1996], the Endeavour segment on the Juan de Fuca Ridge [*Schultz et al.*, 1992], or the 9°-10° N zone on the East Pacific Rise [*Scheirer et al.*, 2006; *Von Damm and Lilley*, 2004]). The V vent, at 9°47' N, East Pacific Rise, is as an example of diffuse flow that evolved towards high-temperature focused discharge in less than 10 years [*Von Damm*, 2000]. Similar geochemical changes occurred simultaneously in both diffuse and focused flows on the northern part of the 9°49-51' N area (also called “Bio-GeoTransect”) on the East Pacific Rise [*Von Damm*, 2004], suggesting a coupling between focused and diffuse flows.

The chemistry of diffuse flow fluids sampled from the Transect on the East Pacific Rise between 1991 and 2000 implies some reaction at high temperature. *Von Damm and Lilley* [2004] argue that phase separation, requiring temperatures > 389°C in this area, is the only consistent way to explain the chlorinity content in the sampled fluids, which is significantly lower than ambient seawater for most samples. The analysis of non-bioactive elements and the use of geochemical modeling show that the diffuse flow fluids in this area can be considered to be a nearly conservative mixture of seawater and high temperature fluids, with additional conductive heating [*Von Damm and Lilley*,

2004]. Furthermore, Li-isotope data [Bray, 2001] suggest that, once mixed, these fluids would have a short residence time (months or less) at a temperature less than 150°C. High-temperature vent fluid samples are generally thought to represent a mixture between end-member, 0-Mg fluid and seawater, but small amounts of mixing with partially-reacted seawater heated to less than 150°C appears to occur in some vents [Ravizza *et al.*, 2001].

As a result of these observations, we conceptualize the upper part of the upflow zone as shown schematically in Figure 3.4. Following Lowell *et al.* [2003], we assume that sulfate-rich seawater circulating in the extrusive layer mixes with the hot sulfate-depleted ascending hydrothermal fluid. As a result anhydrite is precipitated, thus forming low permeability barriers that channel high-temperature fluids to their discharge points as black smokers. There appears to be little mixing of black smoker fluids with ambient seawater during their ascent [Von Damm and Lilley, 2004]. Because little conductive cooling occurs along the channels during rapid ascent, we consider black smokers to be “temperature probes” corresponding to the temperature at the base of the focusing zone, where the hot ascending fluid enters the focusing channels. In other words, black smoker fluid is a proxy of the high-temperature part of the upflow zone. In this model, black smoker fluid represents an end-member 0-Mg fluid mixed with a small amount of partially reacted seawater at the junction (Figure 3.4) as observed for Bio vent [Ravizza *et al.*, 2001]. In the extrusive layer outside the channels, low-temperature diffuse flow occurs. This fluid is a mixture of high-temperature fluid with the seawater circulating in the extrusives.

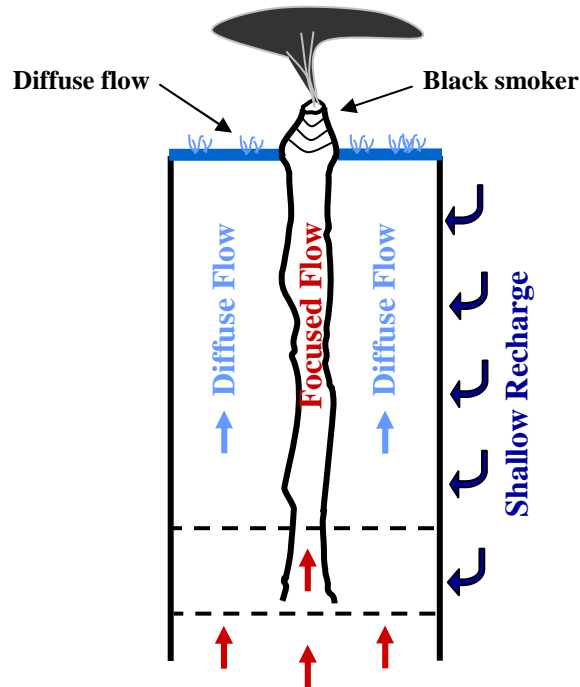


Figure 3.4. Schematic representation of focusing with adjacent diffuse flow in the upper part of the upflow zone. The dashed lines represent the junction at which mixing between hydrothermal fluid and seawater occurs.

We will therefore add the effect of shallow circulation occurring in the shallow crust to the standard single-pass model [e.g., *Pascoe and Cann, 1995; Lowell et al., 2003*] (Figure 3.5). This shallow circulation provides a mechanism of temperature regulation that can explain the variations observed following the temperature peak at Bio9 following the March 1995 event. In addition to facilitating the focusing mechanism, input of cold water from the shallow circulation system creates a thermal boundary layer in the junction zone, where the entrance to the focusing channels is located (Figure 3.5). In our model, the evolution of this boundary layer controls the black smoker temperature. When the temperature rises due to a perturbation at depth, the density decrease triggers an influx of cold fluid from the shallow circulation system. Temperature in the junction then

drops, decreasing the input of cold fluid. The system gradually evolves towards a new steady state. Diffuse venting is affected by variations of another boundary layer that occurs at the seafloor. These variations arise from the interaction with cold seawater near the surface as well as from mixing between hot ascending fluid and cold recharge in the junction.

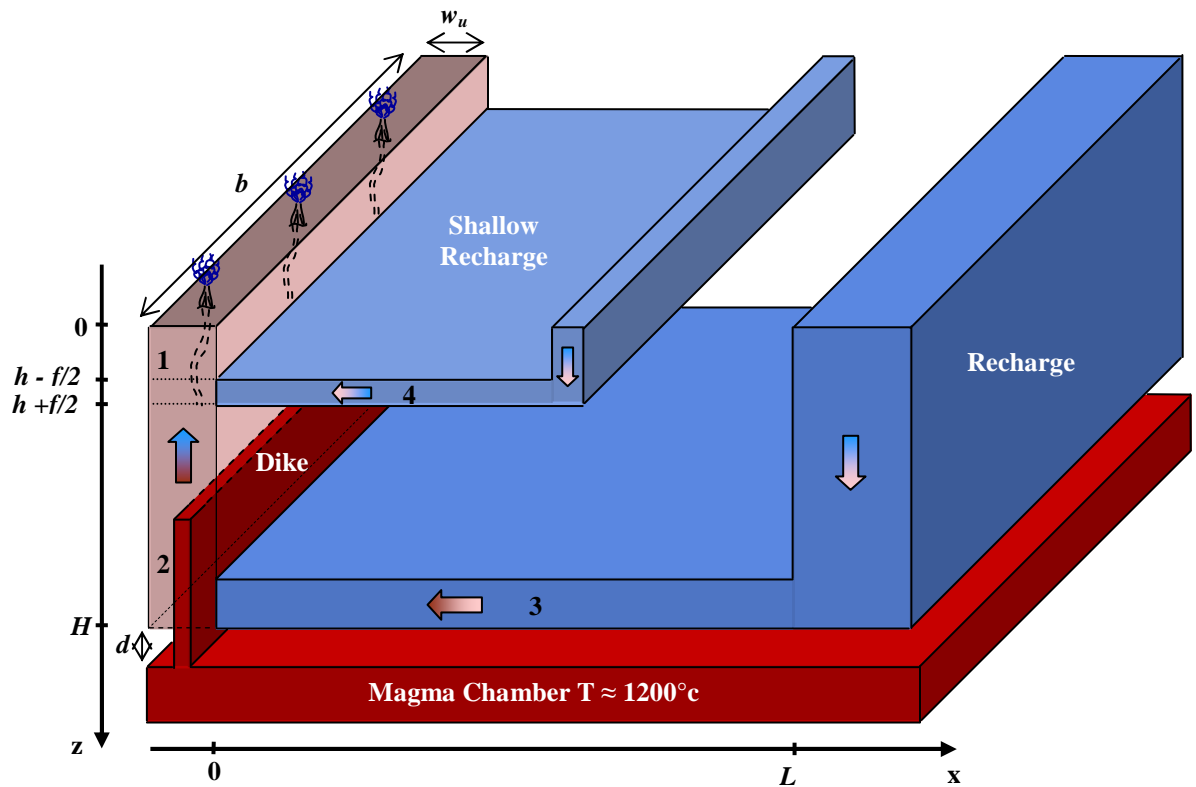


Figure 3.5. “Double-loop” single-pass model adapted from Figure 3.3. The region between $h - f/2$ and $h + f/2$ is the junction zone where high temperature black smoker fluid from below mixes with seawater from the extrusives. Thermal boundary layers are located at the junction zone, the seafloor, and at the bottom of the system between liquid magma and the hydrothermal system, denoted by d .

3.3.2 Mass fluxes in the system and conservation laws

The single-pass model shown in Figure 3.5 is considered one-dimensional since the only dimension we are interested in is the distance from the discharge point at the seafloor. The z - and x -axis are here directed *against* the fluid flow in all the limbs of the model, that is, downward in the upflow zone and from left to right in the bottom horizontal limb. In order to write all the subsequent equations with respect to a unique coordinate along the fluid path in the deep horizontal limb and the upflow zone, we introduced a “curvilinear” coordinate s defined as

$$\begin{cases} s = z & \text{if } s \leq H \\ s = z + x & \text{if } H < s \leq H + L \end{cases} \quad (3.4)$$

For an easier formulation, we divided the fluid path into four main limbs, represented hereafter by the index i , where i takes values from 1 to 4 representing the limb (see Figure 3.5).

With this notation, Darcy’s law in the vertical limbs can be written as

$$v = -\frac{k(T)}{\eta(T)} \left[\frac{\partial P}{\partial s} - \rho(T) g \right] \quad (3.5)$$

For the horizontal limbs ($i = 3, 4$), the same expression is used without the gravity term $\rho(T)g$. The temperature T is a function of time t and coordinate s . Hereafter, we use the subscript i (where $i = 1, 2, 3, 4$) when a physical value refers to a specific limb.

Let us first consider the case where the heat input from the shallow recharge is modeled as a concentrated (or point) source. At the junction point $s = h$, conservation of mass can be written as $Q_1 = Q_2 + Q_4$. By convention, we choose $Q_i > 0$, while $v_i < 0$ is

imposed by the orientation of the z - and x -axis in (3.5). Moreover, we consider that at any time step, the velocity v_i is constant in the i^{th} limb. This implies that the mass fluxes $Q_i = -\rho A_i v_i$ are also constant in each limb at any time step, since we invoke Boussinesq's approximation.

Rewriting Darcy's law in terms of Q and combining with the kinematic viscosity, $\nu(T) = \eta(T)/\rho(T)$, we obtain

$$\frac{\partial P}{\partial s} = \frac{Q_i}{A_i} \frac{\nu(T)}{k(T)} + \rho(T) g \quad (i = 1, 2, 3, 4) \quad (3.6)$$

where the last term on the right-hand side should be omitted for horizontal limbs ($i = 3, 4$). The hydrostatic pressures at the bottom of the shallow and deep recharges, respectively, can be written as

$$P(h+l) = P_0 + g \int_0^h \rho(T_{sh}) ds \quad P(H+L) = P_0 + g \int_0^H \rho(T_{rech}) ds \quad (3.7)$$

where T_{sh} and T_{rech} are the far-field temperature in the shallow and deep recharge zones, respectively.

Also, since pressure is continuous at $s = h$ and $s = H$, we have:

$$P(h+l) - P_0 = \int_0^{h+l} \frac{\partial P}{\partial s} ds \quad P(H+L) - P_0 = \int_0^{H+L} \frac{\partial P}{\partial s} ds \quad (3.8)$$

We further introduce the hydrodynamic resistance

$$r = \int_{s_1}^{s_2} \frac{\nu(T)}{k(T)} \frac{ds}{A(s)} \quad (3.9)$$

where $A(s)$ is the cross-sectional area between $s = s_1$ and s_2 . Combining (3.6), (3.7) and (3.8), and using the conservation of mass, we finally obtain

$$\begin{cases} Q_1 = Q_2 + Q_4 \\ Q_1 = -Q_4 \frac{r_4}{r_1} + \frac{g}{r_1} \int_0^h [\rho(T_{sh}) - \rho(T)] ds \\ Q_2 = Q_3 \\ Q_4 = \frac{g}{(r_2 + r_3)(r_1 + r_4) + r_1 r_4} \left\{ (r_1 + r_2 + r_3) \int_0^h [\rho(T_{sh}) - \rho(T)] ds - r_1 \int_0^H [\rho(T_{rech}) - \rho(T)] ds \right\} \end{cases} \quad (3.10)$$

where r_i is the resistance of the i^{th} limb. Expressions (3.10) can also be obtained by considering the electric current analogy.

Lowell [1990] and Germanovich and Lowell [1992] showed that thermoelastic stresses induced by hot hydrothermal fluid flowing through cooler rocks may close some pathways and thus focus flow. Therefore, the permeability of the upflow zone is assumed to be temperature dependent and represented by [Germanovich *et al.*, 2000, 2001]

$$k(T) = k_0 [1 - \gamma(T - T_{in})]^3 H[1 - \gamma(T - T_{in})] + k_{res} \quad (3.11)$$

where k_0 is the permeability of the upflow zone at the initial steady-state temperature T_{in} , $\gamma = \alpha_r / \phi_0$ is the ratio of the thermal expansion coefficient of the rock to the initial porosity, $H(x)$ is the Heaviside step function [$H(x) = 0$ if $x \leq 0$ and $H(x) = 1$ if $x > 0$], and k_{res} is the residual permeability. The factor multiplying k_0 represents the effect of thermo-elastic stresses while k_{res} reflects the permeability remaining after the closure of the major fractures and asperities as temperature increases. Specifically, if $T < T_{in} + 1/\gamma$,

$H[1 - \gamma(T - T_{in})] = 1$ in (3.11) and $k(T) = k_0 [1 - \gamma(T - T_{in})]^3 + k_{res}$. Although typically $k_{res} \ll k_0$, k_{res} cannot be ignored here since the first term is reducing to zero with

increasing temperature. Once $T \geq T_{in} + 1/\gamma$, $H[1 - \gamma(T - T_{in})] = 0$ and $k(T) = k_{res}$. The dependence of the permeability on pressure is negligible compared to that on temperature for the conditions considered in this study. The temperature dependence of fluid viscosity η is approximated as [Germanovich *et al.*, 2000]

$$\eta(T) = \frac{C_1}{T + C_2} \quad (3.12)$$

where $C_1 = 0.032 \text{ Pa}\cdot\text{s}^\circ\text{C}$, and $C_2 = 15.4^\circ\text{C}$. Finally, the dependence of fluid density on temperature is given by

$$\rho_f = \rho_0 [1 - \alpha_f (T - T_0)] \quad (3.13)$$

We now modify the formulation of Germanovich *et al.* [2000, 2001] to take into account recharge at the base of the extrusives and heat transfer from the magma body at the base of the hydrothermal system. Then, conservation of energy along the flow path 1-2-3 (Figure 3.5) can be written as

$$c_r \rho_r A \frac{\partial T}{\partial t} - c_f Q \frac{\partial T}{\partial s} = \lambda_r A \frac{\partial^2 T}{\partial s^2} - 2b(q_w + q_d) + 2c_f (T_j - T) A I + b q_m \quad (3.14)$$

where the source term I represents the mass flux per unit volume delivered by the shallow recharge to the junction region $h - f/2 \leq s \leq h + f/2$ (Figure 3.5) and q_m represents basal heat transfer from the magma body to the base of the hydrothermal system. The quantity $2I(T_j - T)$ represents cooling of the system, where T_j denotes the temperature of the fluid from the shallow recharge at the junction point (Figure 3.5), and $T > T_j$. Here, $I = [Q_4 / (A_4 w_u)] \delta(s - h)$, where $\delta(s - h)$ is the Dirac delta function that models the concentrated influx of the shallow recharge into the upflow zone (corresponding to $f \rightarrow 0$

in Figure 3.5). In (3.14), q_w represents lateral heat transfer through the walls of the upflow zone, and q_d the heat from the freezing and cooling of a dike (when dike emplacement is modeled, as in Section 3.5). Their asymptotic approximations are discussed in *Germanovich et al.* [2000] and can be written as follows:

$$q_w = -\frac{2}{\sqrt{\pi}} \frac{\lambda_r (T - T_{in})}{\sqrt{a_r t}} \quad (3.15)$$

$$q_d(z, t) = \begin{cases} -\frac{\lambda_r}{\sqrt{\pi} \operatorname{erf}(\lambda)} \frac{T_m - T}{\sqrt{a_r t}} & \text{if } 0 < t < t_c \\ -\frac{\lambda_r (T_m - T)}{\sqrt{\pi} \operatorname{erf}(\lambda) \sqrt{a_r t_c}} \exp\left(-\frac{\pi^2 a_r (t - t_c)}{w^2}\right) & \text{if } t \geq t_c \end{cases} \quad (3.16)$$

The upper and lower expressions in (3.16) correspond to the freezing and cooling stages after dike emplacement, $t_c \approx w^2(16a_r\lambda)^{-1}$ is the time for dike solidification, w is the dike width, and T_m is the temperature of the basalt melt emplaced by the dike. In (3.16), λ is the root of equation $\lambda \exp(\lambda^2) \operatorname{erf}(\lambda) = c_r(T_m - T)(L_m \pi^{1/2})^{-1}$. For typical parameter values (Table 3.1) and $T_m - T \sim 10^3$ °C, $\lambda \approx 1$ [*Germanovich et al.*, 2000]. Then, for $a_r = 10^{-6}$ m²/s and $w = 1$ m, $t_c \sim 1$ day [*Carslaw and Jaeger*, 1986].

When a dike is suddenly emplaced in fluid-saturated country rock, rapid heating will tend to pressurize the adjacent fluid and drive flow away from the dike wall [*Delaney*, 1982]. In turn, pressurization of the fluid may lead to fracturing of the adjacent rock [e.g., *Germanovich and Lowell*, 1995]. Local boiling and phase separation may also occur. For seafloor systems with high permeability and ambient pressure of ~ 30 MPa, the pressure increment is negligible [*Delaney*, 1982], and so is the corresponding increase of the sizes of pre-existing fractures [*Germanovich and Lowell*, 1995]. If an increase of

permeability results from fluid pressurization, it is incorporated into the permeability increase that we assume results from dike emplacement (see Section 3.5.3). The width of the two-phase zone is only ~ 10 cm [Lewis and Lowell, 2004], and hence we neglect it. As noted by Wilcock [2004] and Germanovich and Lowell [1995], heating adjacent to the dike may lead to large pressure increases but only within a narrow region.

In (3.14), $q_m = 0$ everywhere except along the horizontal limb 3, where heat is conducted without heat loss through an impermeable thermal boundary layer of thickness d . If T_m is the temperature of the magma body, then asymptotically [Germanovich *et al.*, 2001; Lowell and Germanovich, 2004]

$$q_m = \frac{\lambda_r (T_m - T)}{d} \quad (3.17)$$

Heat input from the shallow recharge modeled as a concentrated (or point) source has an important limitation. If T_j is the temperature of the fluid coming from the shallow recharge, the heat balance yields $Q_2[T(h^+) - T_j] = Q_1[T(h^-) - T_j]$. This expression can be satisfied only if $Q_1 = Q_2$, which is not our case. Therefore, in the point source model, the temperature has a discontinuity at the junction. To avoid computational inconvenience, we model the input from the shallow recharge over a finite area between the depths $z = s = h - f/2$ and $z = s = h + f/2$, f being the vertical dimension of junction zone (Figure 3.5). Then, in (3.14), $I = Q_4 / (A_4 w_u)$ within the junction zone and

$$I(z) = \begin{cases} \frac{Q_4}{A_4 w_u} & \text{if } h - f/2 \leq s \leq h + f/2 \\ 0 & \text{otherwise} \end{cases} \quad (3.18)$$

Within the junction interval $h - f/2 \leq s \leq h + f/2$, $\partial Q / \partial s = -AI$, where $A = A_1 = A_2$, and the mass flux

$$Q(z, t) = Q_2(t) - AI \cdot \left(z - h - \frac{f}{2} \right) \quad (3.19)$$

is linearly distributed along this interval. In the numerical calculations described below, we adjusted Q in the energy balance expression (3.14) based on (3.19); however, the correction to the mass balance expression (3.10) proved to be negligible because $f \ll h$. Because the geochemical analyses of *Bray* [2001] suggest that the residence time of the diffuse flow fluid is on the order of a few months, we assumed that focusing occurred in the upper 100 m of the crust and placed the junction zone at that depth.

3.3.3 *Boundary conditions*

In previous works on the single-pass model [*Germanovich et al.*, 2000, 2001], we did not include explicitly the deep horizontal limb (limb 3 in Figure 3.5), which required specifying a separate boundary condition at the bottom of the upflow zone [*Germanovich et al.*, 2001; Equation (14)]. Here, this horizontal limb and its effect are explicitly included, and we now have the following boundary conditions:

$$T = T_{diffuse} \quad \text{if} \quad s = 0, t \geq 0 \quad (3.20)$$

and

$$T = T_{rech}(H) \quad \text{if} \quad s = H + L, t \geq 0 \quad (3.21)$$

where $T_{diffuse}$ is the temperature monitored at sites of diffuse venting. To limit the number of unknowns, we model the recharge zone by a linear temperature distribution (as also discussed in Section 3.4).

To solve equations (3.10), we estimate the hydrodynamic resistance of the shallow limb 4 directly from (3.9). Assuming that the temperature in horizontal limb 4 is constant and equal to the temperature of the far-field recharge at this depth, then

$$r_4 \approx \frac{\nu_4 (s_2 - s_1)}{k_4 A_4} \quad (3.22)$$

where the subscript 4 refers to limb 4, while s_1 and s_2 refer to the two ends of the path along which the resistance is calculated. The permeability and the recharge fluid viscosity are calculated using (3.11) and (3.12), respectively.

3.3.4 Initial conditions

We define the initial conditions as the steady-state of the system prior to any perturbation. In steady-state, equation (3.14) becomes

$$-c_f Q \frac{dT}{ds} = \lambda_r A \frac{d^2 T}{ds^2} + 2c_f (T_j - T) AI + b q_m \quad (3.23)$$

so that the initial condition is given by the solution of (3.23) with the boundary conditions (3.20) and (3.21). Given (3.17), equation (3.23) can be written as

$$a_* \frac{d^2 (T - T_*)}{ds^2} - Q \frac{d(T - T_*)}{ds} - b_* (T - T_*) = 0 \quad (3.24)$$

where $a_* = \lambda_r A / (-c_f)$; $T_* = T_m$ in the deep horizontal limb 3, $T_* = T_j$ in the junction of the upflow zone with the shallow recharge, and $T_* = 0$ everywhere else; and b_* is defined as either $b_* = -(\lambda_r b) / (c_f d)$ in limb 3, $b_* = -2AI$ in the junction, or $b_* = 0$ elsewhere. The general solution of the linear, homogeneous ODE (3.24) is

$$T = T_* + C_1 \exp\left(\frac{Q + \sqrt{Q^2 + 4a_*b_*}}{2a_*} s\right) + C_2 \exp\left(\frac{Q - \sqrt{Q^2 + 4a_*b_*}}{2a_*} s\right) \quad (3.25)$$

where constants C_1 and C_2 are different for limbs 1, 2, 3, and the junction zone. They are determined from the boundary conditions (3.20), (3.21), and the continuity of temperatures and heat flows between the intervals.

One obtains these constants as functions of the corresponding mass fluxes. Then, (3.25) is substituted into (3.10) and the resulting algebraic equations are solved to obtain the mass fluxes Q_i in the steady-state configuration. Alternatively, equation (3.23) can be solved numerically to obtain the steady-state solution using the numerical technique described below for solving transient problems.

Dimensionless expressions corresponding to the problem presented in this chapter are given in Appendix C.

3.4 Numerical results

We chose an implicit numerical scheme that uses a finite difference discretization with a zeroth-order approximation with respect to time. At each time step, the mass fluxes (and velocities) are considered to be constant. This allows solving the system of equations using the standard elimination method [Samaraskii, 2001]. The mass fluxes and velocities are then recalculated, along with values of density, permeability and viscosity, prior to the next step. We consider the flow path from the bottom of the recharge zone to the top of the upflow zone. The bottom boundary condition corresponds to the temperature at the bottom of the deep recharge. This temperature is not well constrained,

but test computations showed that the results were not sensitive to temperatures ranging between 50 to 100°C. For results presented here, we assumed a linear gradient in the recharge zone with 0°C at the seafloor and 100°C at the bottom (i.e., at the depth of 1.5 km).

In all the calculations, we chose a uniform grid density with a grid spacing of 1 cm. We checked the accuracy of the computations by comparing the results with different grid spacing and time steps. The difference between the grids with a 10-cm spacing and 1-cm spacing did not exceed 1%. Similarly, increasing the time step from 0.1% of the time modeled to 1% did not affect the results by more than 1%. The program was implemented as a FORTRAN 90 [Press *et al.*, 1992] code (see Appendix D). Our typical simulation for the 2.5 km long spatial domain (upflow zone plus deep horizontal limb) discretized at 250,000 grid points required 5 minutes for 10^3 time steps on a personal computer running with 3 GB of RAM and a 2 GHz processor.

Figure 3.6a shows how the steady-state temperature profile varies with the thickness d of the impermeable thermal boundary layer situated between the top of the magma chamber and the base of the hydrothermal system. Note that for the results presented from this point on, the term “depth” represents the (curvilinear) distance s from the seafloor along the flow path 1-2-3. Therefore, in Figure 3.6 and following, the upper part of the upflow zone, representing the diffuse flux, corresponds to depth 0-100 m; the lower part of the upflow zone to depth 100-1500 m, with conditions at 100 m representing the focused flux; and the deep horizontal limb to depth 1500-2500 m. For a fixed mass flux in the horizontal limb, as d gets thinner, the amount of heat that is

conducted into the fluids increases and the fluid temperature rises. In the example presented here, a difference of 1 m generates a shift of $\sim 20\text{-}30^\circ\text{C}$ in the lower part of the upflow zone. At the junction, however, (Figure 3.6b), all the profiles become identical. This is a result of the long-term regulating role of the cold shallow recharge. As can be seen in Figure 3.6c, the boundary layer at the seafloor remains the same in all the cases.

The hydrodynamic resistances of the simulations presented in Figure 3.6 are such that the mass fluxes are moderate ($Q_1 = 37$ kg/s, $Q_2 = 14$ kg/s, and $Q_4 = 23$ kg/s). Figure 3.7 presents the similar results but for smaller resistances, and thus higher fluxes of $Q_1 = 53$ kg/s, $Q_2 = 26$ kg/s, and $Q_4 = 27$ kg/s. The latter case requires smaller values of d , of the order of 7 – 8 m, to obtain temperatures representative of East Pacific Rise conditions. Also, smaller variations of d are required to generate shifts of the temperature profile in the lower part of the upflow zone.

We then tested the transient response of the system to an instantaneous change in the thickness d of the boundary layer (Figure 3.8 and 3.9). Instantaneous thinning of this boundary layer corresponds to a downward cracking event and the formation of new permeability near the top of the magma chamber. For this example, the mass fluxes are the same as for Figure 3.6. After 1 year, a slight change in the profile of the horizontal limb can be observed whereas the thermal boundary layers at the junction zone (Figure 3.8b) and beneath the seafloor are unchanged. After 5 years, the perturbation has started to propagate upwards in the upflow region, but the junction zone is unchanged (Figure 3.9b). Figure 3.10 and Figure 3.11 illustrate the same scenario but with larger mass fluxes ($Q_1 = 53$ kg/s, $Q_2 = 26$ kg/s, and $Q_4 = 27$ kg/s). After 1 year (Figure 3.10a), the

temperature profile has begun to be modified in the horizontal limb and at the base of the upflow zone. Compared to the case with smaller fluxes (Figure 3.8a), the profile modification is more important although the change in d is more limited. After 5 years (Figure 3.11a), the profile in the horizontal limb and the lower part of the upflow zone is even more altered. Yet, Figure 3.10b and Figure 3.11b shows that the effect on the boundary layer at the junction zone is nearly non-existent.

These simulations illustrate that any modification of the thickness of the bottom boundary layer d would have only long-term effects. It would take many years before the flow regime is altered enough to modify the boundary layers at the junction zone and at the seafloor. Because the conductive boundary layer d is already quite thin, the new permeability generated by a deep cracking event that further thins the boundary layer is not likely to cause a rapid perturbation in the vent temperature.

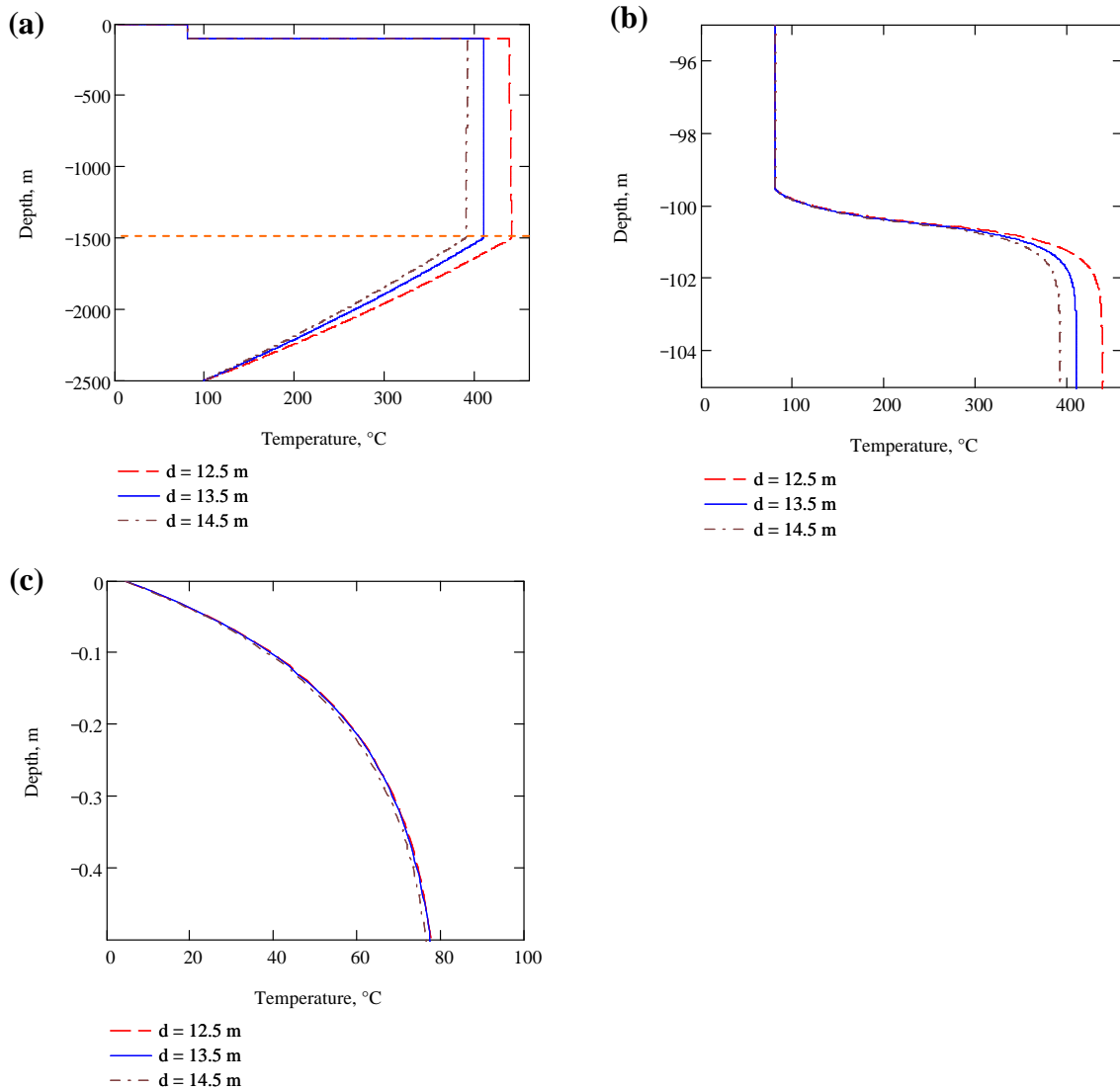


Figure 3.6. (a) Variation of the steady-state temperature profile with the thickness d of the impermeable thermal boundary layer situated between the magma chamber and the base of the hydrothermal system. The dashed line corresponds to $d = 12.5$ m, the solid line to $d = 13.5$ m, and the dash-dot line to $d = 14.5$ m. The dashed horizontal line marks the base of the upflow zone. (b) Detail of the profile between $s = -95$ m and $s = -105$ m. (c) Detail of the profile in the boundary layer near the seafloor.

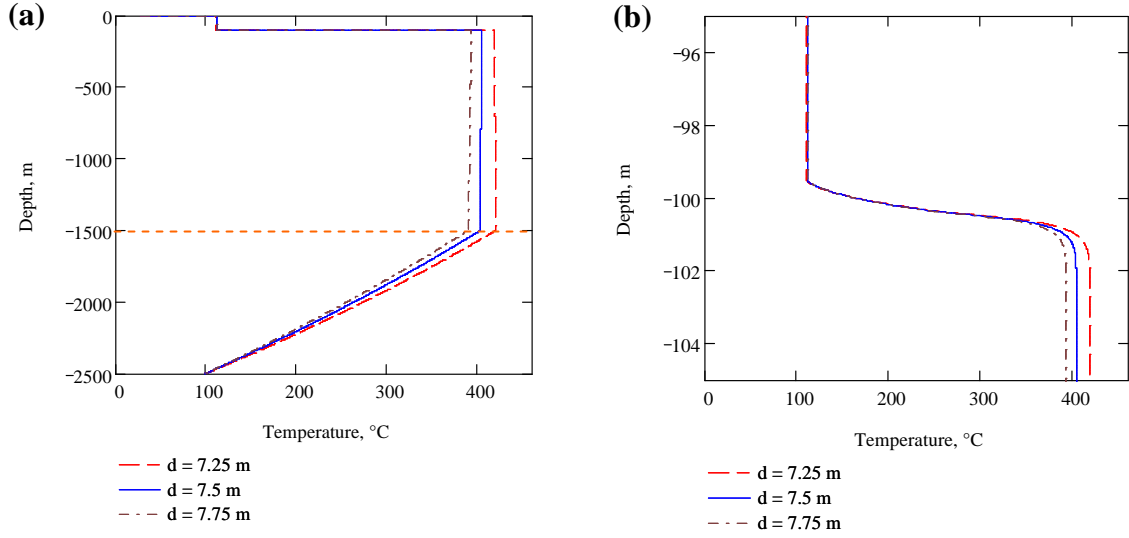


Figure 3.7. (a) Similar to Figure 3.6 but for somewhat larger mass fluxes (see text for details). The dashed horizontal line marks the base of the upflow zone. (b) Detail of the profile between $s = -95$ m and $s = -105$ m.

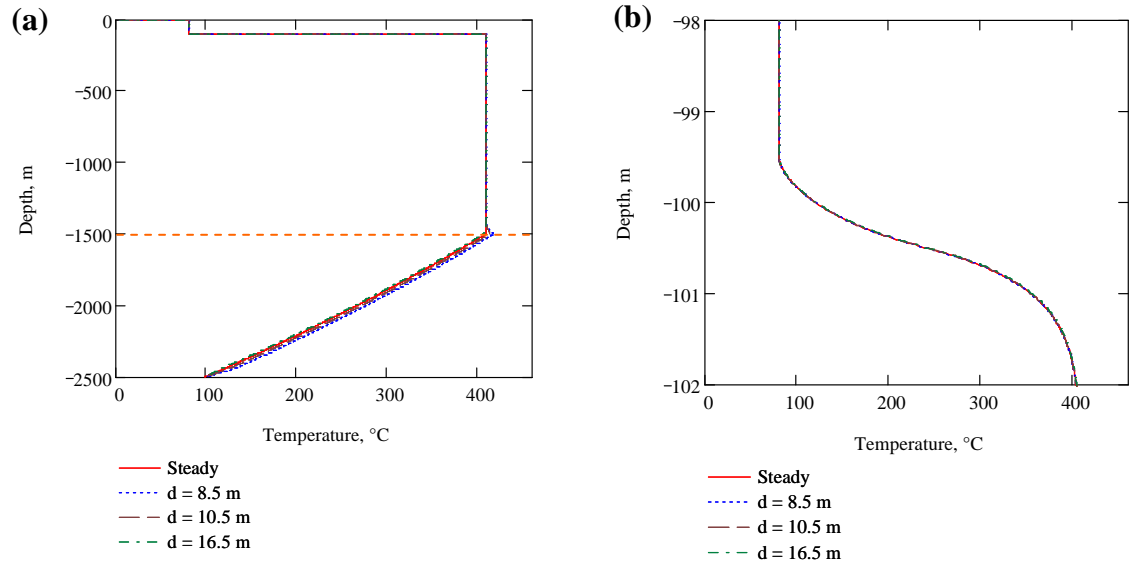


Figure 3.8. (a) Temperature profile 1 year after changing the thickness d of the impermeable thermal boundary layer. Steady-state corresponds to $d = 13.5$ m, and the other curves correspond to values of d after perturbation. The dashed horizontal line marks the base of the upflow zone. (b) Detail of the profile at the junction zone, between $s = -98$ m and $s = -102$ m.

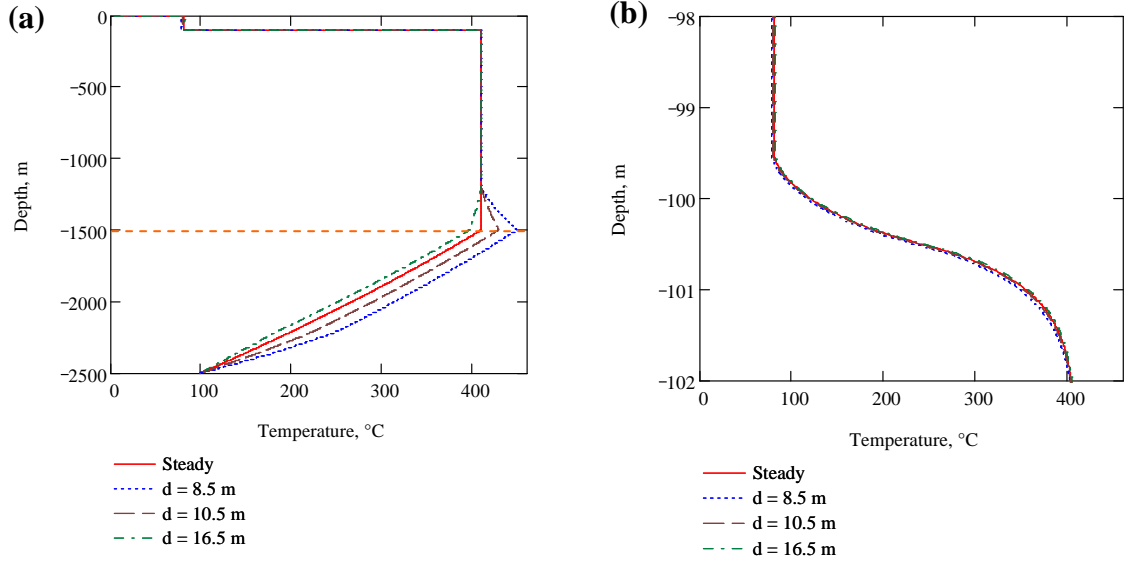


Figure 3.9. (a) Temperature profile 5 years after changing the thickness d of the impermeable thermal boundary layer. Steady-state corresponds to $d = 13.5$ m, and the other curves correspond to the values of d after perturbation. The dashed horizontal line marks the base of the upflow zone. (b) Detail of the profile at the junction zone, between $s = -98$ m and $s = -102$ m.

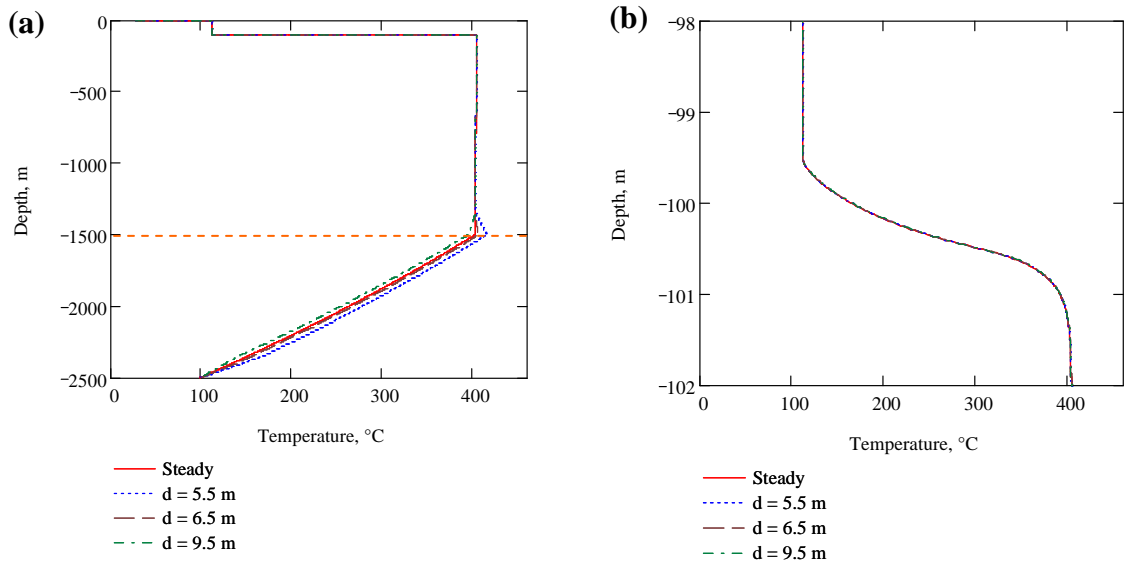


Figure 3.10. (a) Temperature profile 1 year after changing the thickness d of the impermeable thermal boundary layer. Steady-state corresponds to $d = 7.5$ m, and the other curves correspond to values of d after perturbation. The dashed horizontal line marks the base of the upflow zone. (b) Detail of the profile at the junction zone, between $s = -98$ m and $s = -102$ m.

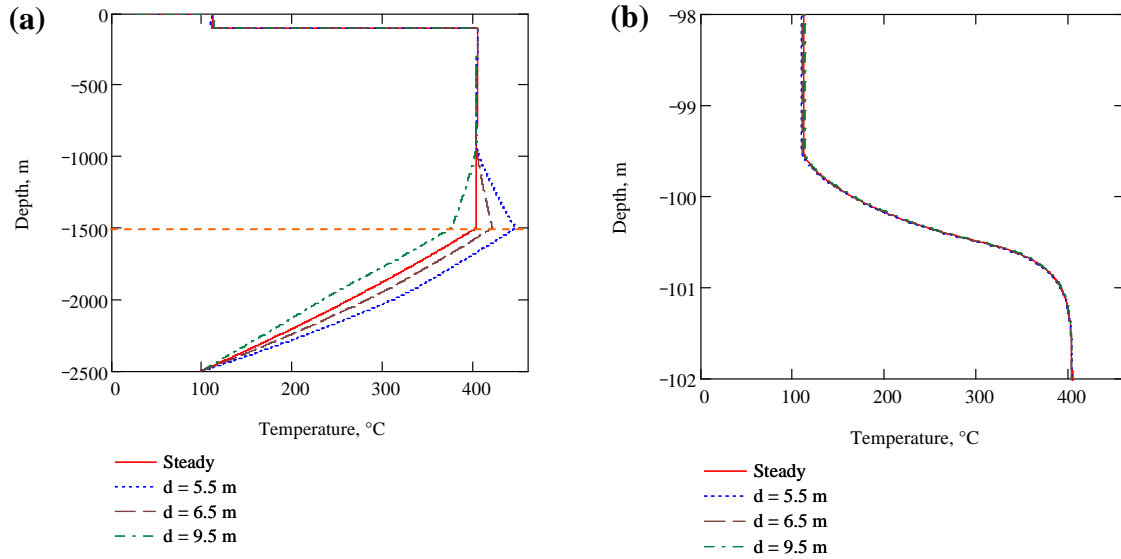


Figure 3.11. (a) Temperature profile 5 years after changing the thickness d of the impermeable thermal boundary layer. Steady-state corresponds to $d = 7.5$ m, and the other curves correspond to the values of d after perturbation. The dashed horizontal line marks the base of the upflow zone. (b) Detail of the profile at the junction zone, between $s = -98$ m and $s = -102$ m.

3.5 Modeling the March 1995 East Pacific Rise event

3.5.1 A possibility of diking event

The March 1995 East Pacific Rise swarm is typically explained as a thermal cracking episode, enabling hydrothermal fluid to mine heat deeper in the reaction zone [Fornari *et al.*, 1998; Sohn *et al.*, 1998; Sohn *et al.*, 1999]. The observed seismic pattern (Figure 3.12a) was interpreted as a slip along a vertical fault (Figure 3.13a) generated by the release of thermal stresses at the base of the hydrothermal system [Sinha and Evans, 2004; Sohn *et al.*, 1999]. The slip would have rapidly propagated downwards, as the axial magma chamber lid subsided (Figure 3.13b), opening pathways (Figure 3.13c) for the fluid that presumably reached the seafloor and caused the temperature anomaly four days

later [Fornari *et al.*, 1998; Sohn *et al.*, 1998; Sohn *et al.*, 1999]. Here, we suggest an alternative interpretation based on the fact that the micro-earthquakes are located well above the margins of the magma lens (Figure 3.12a).

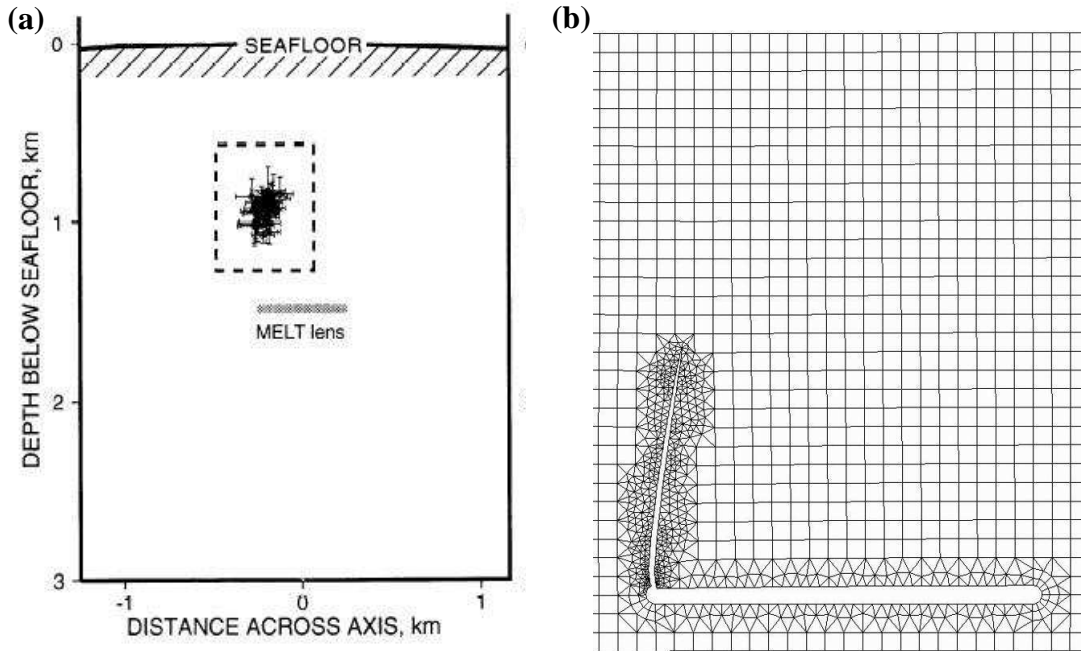


Figure 3.12. (a) Ridge normal cross section of relocated north group events with 1σ error bars. Dashed box delineates 1σ confidence limits for relocated groups [modified from Sohn *et al.*, 1999]. (b) Finite element simulation of dike propagation from magma chamber suggested in (a). We used a pressurized 1.5-km deep, 1-km wide, and 50-m thick magma lens, and propagated the dike 600 m in order to match the hypocentral pattern shown in (a).

As shown by Sim [2004] and Sim *et al.* [2004], the pressurization of a lens-shaped magma chamber results in the tensile stress concentration near the tips of the lens while the rest of the host rock is in compression. This implies that an episode of pressurization is likely to result in dikes initiating near the lens tips, and not its center, as often assumed (Figure 3.14). Finite element calculations [Sim, 2004; Sim *et al.*, 2004] show that the dike

then propagates almost vertically towards the seafloor from the lens tips (Figure 3.12b). The hypocentral pattern in Figure 3.12a could thus be the expression of dike emplacement initiated at the tip of the axial magma chamber lying beneath the ridge. As noted by *Sohn et al.* [1999], the events shown in Figure 3.12a are compatible with dike-induced seismicity.

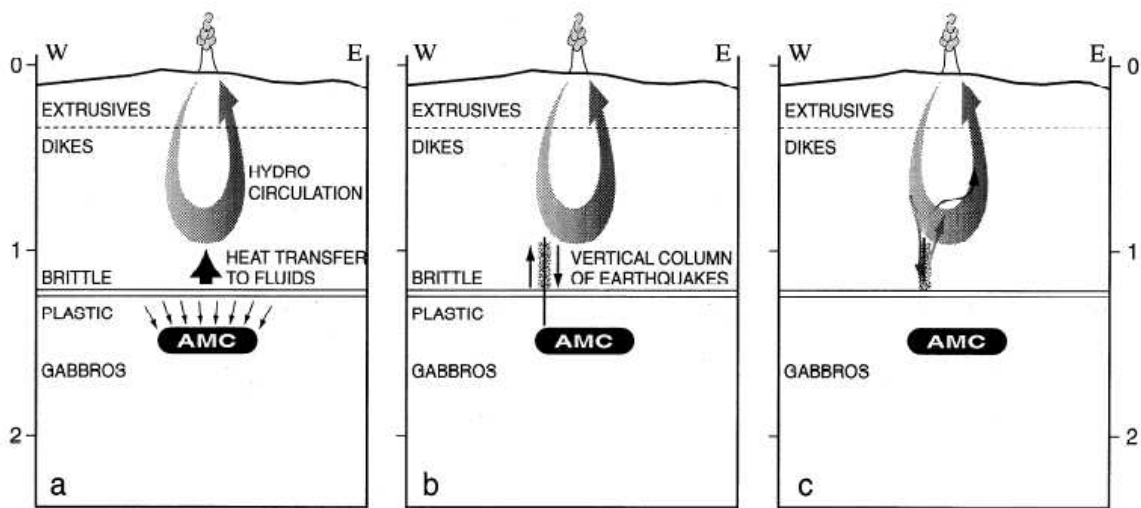


Figure 3.13. Interpretation given by *Sohn et al.* [1999] of the March 1995 seismic swarm beneath Bio9 high-temperature vent field. Sections in all plots are oriented in all plots across the rise axis from west to east. (a) Magma chamber cools and contracts (e.g., melt to mush) as hydrothermal convection removes heat. (b) Differential contraction generates slip along vertical fault over west margin of axial magma chamber (AMC). (c) Hydrothermal fluids rapidly penetrate new fractures and extract heat from fresh rock. Exit fluid temperature in Bio9 vent temporarily increase.

Although we prefer the diking explanation of the March 1995 seismic swarm (see discussion in Chapter 4), both fault slip and dike propagation are likely to enhance the permeability in the upflow zone [*Brodsky et al.*, 2003; *Delaney et al.*, 1986; *Germanovich et al.*, 2000; *Pollard*, 1987; *Rojstaczer and Wolf*, 1992; *Rojstaczer et al.*, 1995]. Though

Sohn et al. [1999] do not describe this explicitly, their model can be interpreted as the slip of a vertical fault enhancing permeability in the area around the hypocenters and below (Figure 3.12a). In this section, we consider the hydrothermal implications of the change of permeability above the west margin of the axial magma chamber when the seismic swarm was observed. Mechanical implications are discussed in more details in the next chapter.

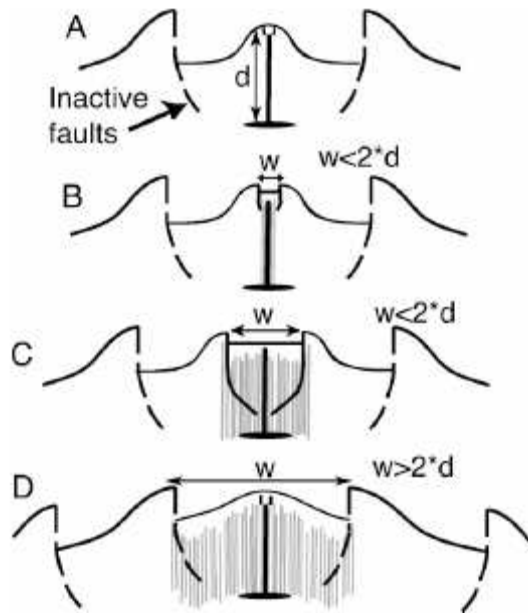


Figure 3.14. Evolutionary model from *Carbotte et al.* [2006] for axial rift topography. A: Narrow grabens form above dikes during dike intrusion and are readily buried by lavas contributing to axial volcanic ridge (AVR) relief. B, C: With ongoing dike intrusion, fault slip becomes localized on preferred graben faults, which grow with successive dike events. Graben widens and eruptions become confined by graben walls. D: Graben faults cease to be active as they are transported beyond zone of influence of stress perturbations due to dikes intruded from magma sill. New AVR construction begins.

3.5.2 Heat from possible dike emplacement

Before studying the impact of permeability enhancement in the upflow zone, we first consider the influence of heat input in the case of a dike intrusion. To test this hypothesis, the heat flux q_d from dike emplacement is accounted for when solving (3.14), and an emplacement height of $h_d = 600$ m is invoked to match the hypocentral pattern in Figure 3.12a (as sketched in Figure 3.5). Figure 3.15 shows the modified temperature profile for various dike thicknesses, one year after the emplacement. For this simulation, we chose the large mass fluxes used in the previous section. Only the temperature of the fluid situated around the dike was significantly altered (Figure 3.15a). The additional heat results in a slight increase of the mass flux and, consequently, a moderate upward displacement in the boundary layers at the junction zone and at the seafloor. This increase is then followed by a gradual decrease of the mass fluxes, which results in a downward displacement of the boundary layers, and a decrease in temperature at any fixed point in the boundary layers. The system eventually evolves towards a new steady-state. The temperature behavior is shown in Figure 3.15b. This simulation demonstrates that shallow recharge regulates the outlet temperatures of the system. The rapid decrease of fluid density in the upflow zone increases for wider dikes because the heat input from wider dikes is larger than for smaller ones. The increased buoyancy in turn drives an enhanced response of the shallow recharge, which explains why the subsequent temperature decrease is amplified for thicker dikes. The same simulation conducted with smaller steady-state mass fluxes showed a similar response, though more attenuated [Ramondenc *et al.*, 2005]. These simulations suggest that unless the dike is exceptionally

wide (~ 10 m or wider), additional heat from the dike alone does not result in the observed changes in black smoker temperatures.

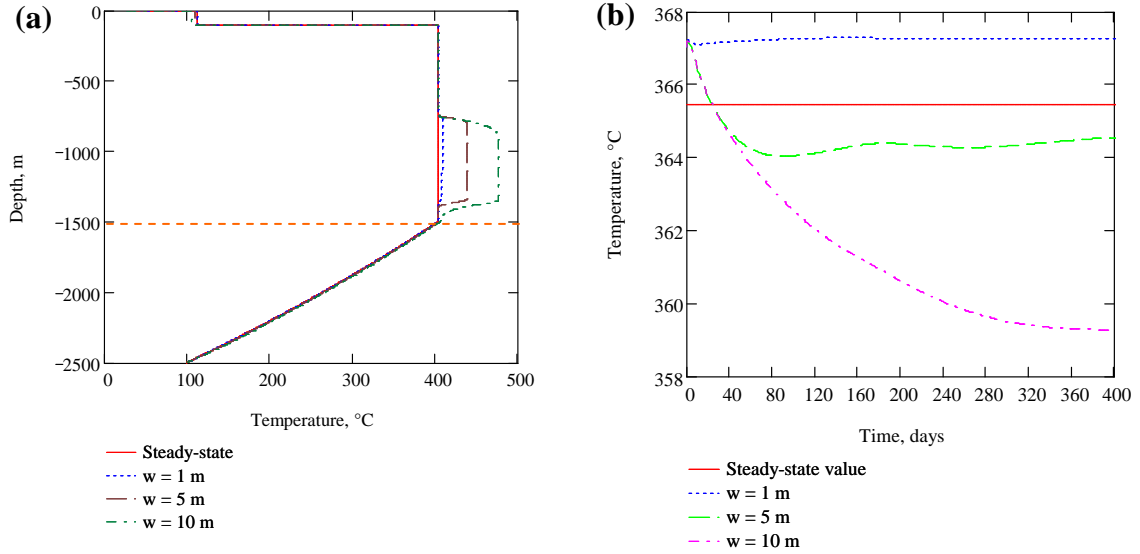


Figure 3.15. (a) Temperature profile 1 year after the emplacement of a dike. The steady-state corresponds to $d = 7.5$ m. The other curves correspond to different dike widths w . The dashed horizontal line marks the base of the upflow zone. (b) Temperature evolution in the junction zone at a fixed point of depth $s = -100.73$ m for different dike widths w .

3.5.3 Permeability enhancement

Although the simulation described above shows that heat alone cannot induce temperature variations such as those observed at East Pacific Rise during the March 1995 swarm, it is likely that dike emplacement is accompanied by permeability enhancement around the margins of the dike [Delaney *et al.*, 1986; Germanovich *et al.*, 2000; Pollard, 1987]. Figure 3.16 shows the evolution of the temperature profile over time when both added heating and enhanced permeability are taken into account. The dike thickness was chosen to be $w = 1$ m, based on our mechanical computations (Figure 3.12b). Test

simulations showed that for mass fluxes of the order of 15 kg/s in the upflow zone, the system response does not result in temperature decreases following the initial increase. Therefore, a thin thermal boundary layer at the top of the magma chamber ($d = 7.5$ m) was used in order to achieve the higher steady-state mass fluxes described in Section 3.4 (i.e., $Q_1 = 53$ kg/s, $Q_2 = 26$ kg/s, and $Q_4 = 27$ kg/s). Finally, the permeability was multiplied by a factor of 1.5 in the 600 meter section of the upflow zone where the dike was emplaced (no permeability changes occurred above the dike), and the height of the junction with the shallow recharge of cold fluid was taken to be 5 m, rather than 1 m as in the previous examples. These values provide the best fit for the temperature variations at Bio9 following the earthquake swarm.

Figure 3.16a shows the resulting evolution of the temperature profile at the bottom of the upflow zone. Temperature increases for approximately 7 days after the emplacement of the dike, and then gradually decreases as the fluid flows upwards. Figure 3.16b shows the evolution of temperature at the junction with shallow recharge, representing the behavior of black smokers. Temperature immediately increases in the junction zone after the dike is emplaced, before decreasing approximately one week later. This decrease results from the input of cold fluid from shallow recharge.

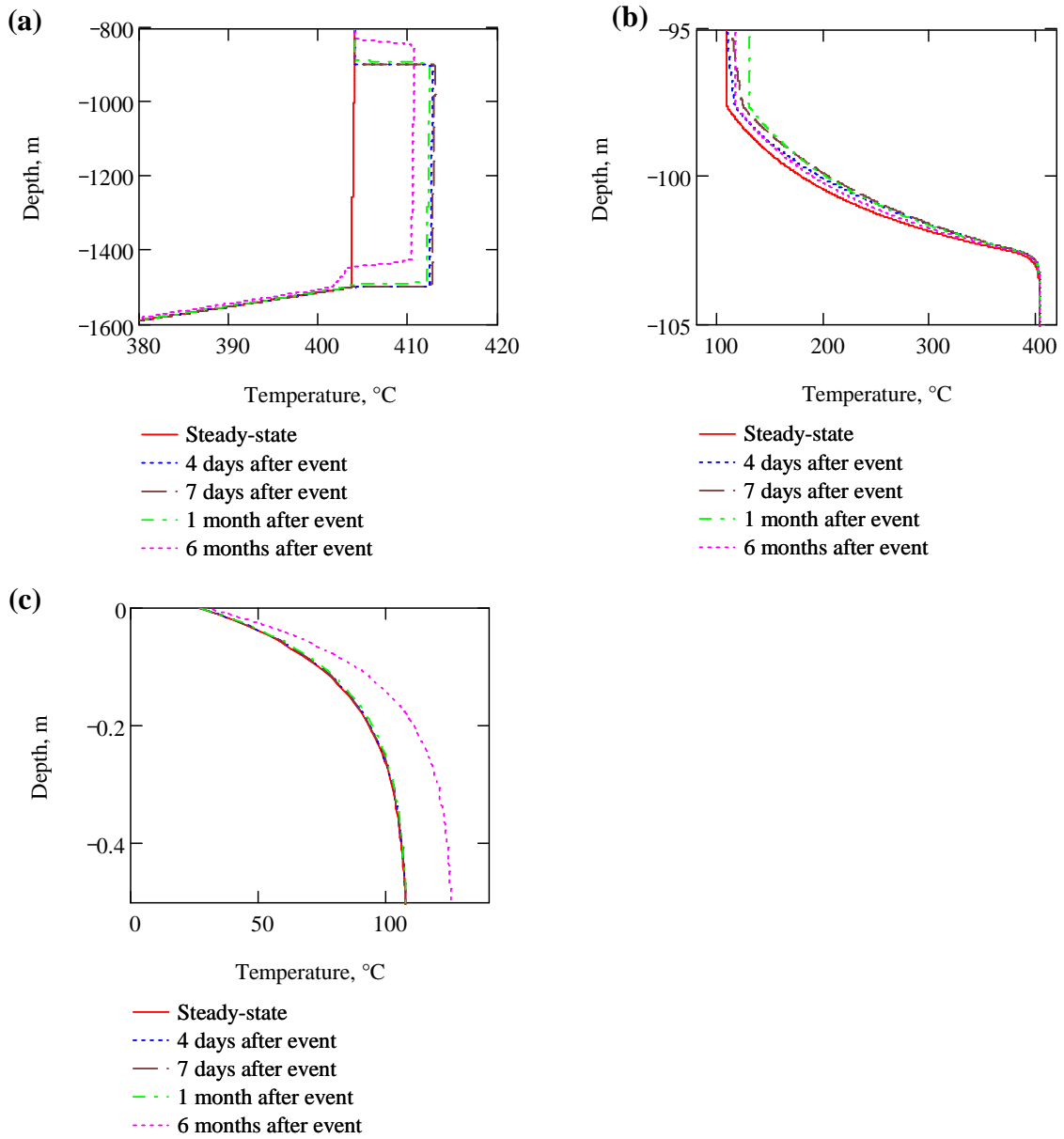


Figure 3.16. Evolution of temperature profile (a) in the bottom of the upflow zone, (b) at the junction with the shallow recharge, and (c) in the first 50 cm below the seafloor ($d = 7.5$ m, $f = 5$ m, $w = 1$ m, and $k = 1.5 \times k_0$ around the dike margins). Note that the black smoker temperature is represented by the temperature at some fixed point within the junction zone shown in (b), while (c) corresponds to low-temperature diffuse flow.

Figure 3.17a shows temperature as a function of time at the point near the junction zone that best matches the temperatures observed at Bio9 prior and during the event (at depth $z = 102.40$ m). Our model matches the different variations over the first year that have been observed in the temperature time series (Figure 17a). The large-scale oscillations in the model are related to the interplay between cold recharge from the shallow part of the system and hot discharge from below as the system evolves to a new steady state. The fit is further improved after translating the record post November 1995 by 3°C (Figure 17b), time at which the temperature probe (or hobo) was replaced [Fornari *et al.*, 1998; Fornari, personal communication, 2006].

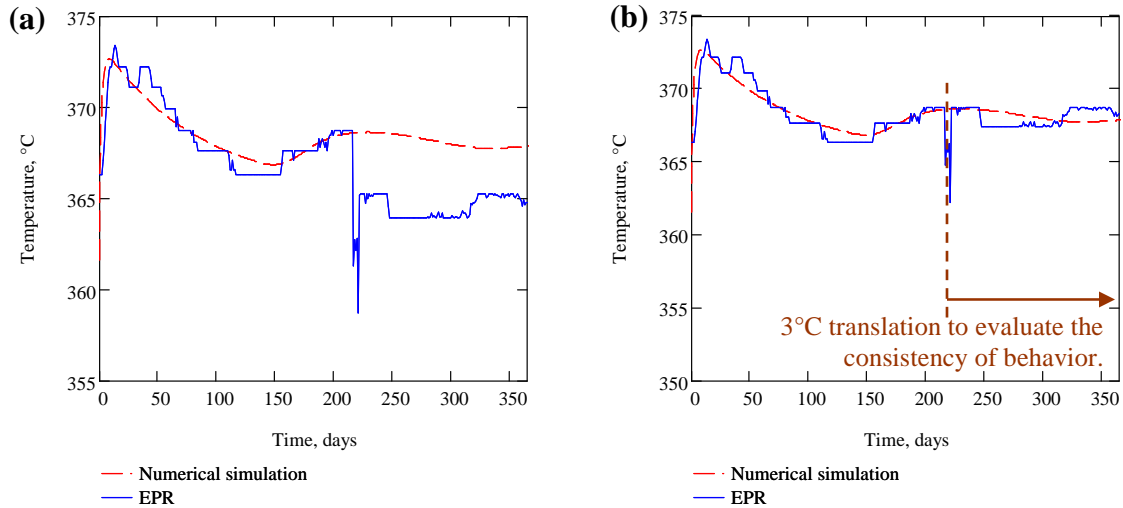


Figure 3.17. Comparison of the calculated response ($d = 7.5$ m, $f = 5$ m, $w = 1$ m, and $k = 1.5 \times k_0$ around the dike margins) to dike emplacement with the observed response at Bio9 following the March 1995 East Pacific Rise event. In (b) we applied a 3°C translation to the records at the time of temperature probe replacement.

3.5.4 Discussion

In the model presented in this work, we assumed that black smokers represent “temperature probes” (proxies) of the base of the focusing zone. In turn, we assumed that focusing occurs in the narrow junction where the upflow meets the shallow recharge of cold seawater (Figure 3.5). One can argue, however, that this recharge may occur over a much larger portion of the extrusives (Figure 3.4). In essence, our approach consists in using an “equivalent” shallow recharge, delivering the same amount of cooling that may occur in reality. From this point of view, our model captures relatively well the physics of shallow recharge. In this context, the depth of the junction scales with the depth of the shallow recharge zone and its exact value is relatively unimportant. One way to obtain a better estimate of the position of shallow recharge would be to compare both the diffuse low-temperature and focused high-temperature responses to seismic activity. Unfortunately, there was no temperature sensor deployed in the diffuse venting zone of Bio9 area during the 1995 activity [Scheirer *et al.* 2006].

Furthermore, using diffuse flow temperature records for modeling similar to that presented here may be less reliable than using black smoker temperatures. Diffuse flow is typically much broader and is not easily defined [e.g., Ramondenc *et al.*, 2006]. In any patch of diffuse venting, the temperature may range from nearly ambient seawater temperature to tens of degrees. Moreover, the temperature of diffuse venting is often measured at only a few selected points. Consequently, the average temperature of diffuse venting, which is determined in our model, as well as in most of other models, is not well constrained. This is why we did not attempt to model the June 1999 Endeavour event at the Juan de Fuca Ridge [Johnson *et al.*, 2000; Seyfried *et al.*, 2003]. In that case, only

diffuse venting records at several points are available and no black smoker temperature was recorded.

Nevertheless, in principle our model can be used to simulate the temperature-averaged behavior of diffuse venting. Figure 3.16c represents the evolution in the first 50 cm below the ocean floor. Displacements of the boundary layer are nearly non-existent in the first couple of months following the event, whereas the response after 6 months is larger. This can be explained by the arrival of the temperature spike from the junction zone that resulted from dike emplacement at depth. As is the case in the lower part of the upflow zone, this spike is gradually advected towards the seafloor at the same time as the fluid loses heat through the walls of the upflow zone. Although there are no data on diffuse venting from Bio9 vent, temperature time series are available for the Bio9 Riftia community starting November 1995 [Scheirer *et al.*, 2006]. These records indicate a sudden temperature increase at the beginning of 1996, followed by a gradual decrease over several years. This behavior is consistent with the delayed response that our model suggests for sites of diffuse venting.

The main advantage of our model is that, despite the apparently large number of parameters, essentially only two control the behavior of the system: the thickness d of the thermal boundary layer between the top of the magma chamber and the hydrothermal system, and the permeability k of the upflow zone. Figure 3.18 shows that at the time scale of a year, permeability is the main controlling parameter, whereas for longer time scales, mainly the thickness d of the basal boundary layer affects the evolution of the system. Even doubling this thickness has little effect over time scales shorter than a year

(Figure 3.18a). In contrast, our best fit requires multiplying the steady-state permeability by 1.5, and increasing this to a factor of 2 has a large effect, that is, it would make the temperature response 60% larger at the seafloor. In comparison, the permeability of on-land hydrological systems in Southern California has been shown to undergo increases by a factor as high as 3 at the time of earthquakes [Elkhoury *et al.*, 2006]. The sensitivity to permeability changes would become greater if changes occur over a larger portion of the upflow zone.

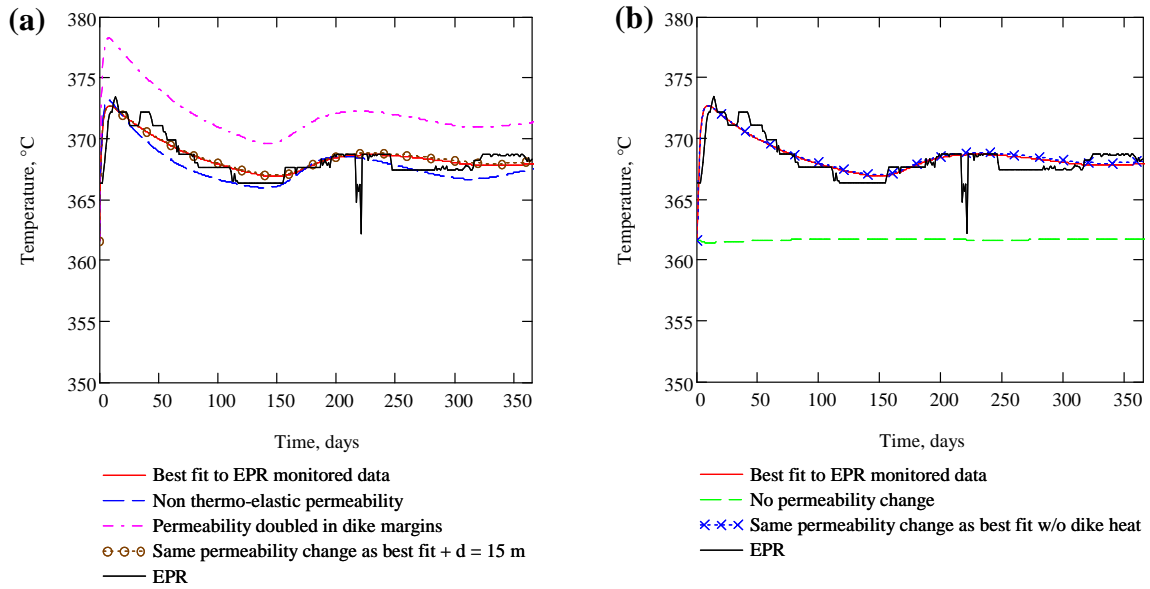


Figure 3.18. Comparison of the best fit to the March 1995 East Pacific Rise event ($d = 7.5$ m, $f = 5$ m, $w = 1$ m, and $k = 1.5 \times k_0$ around the dike margins) with other scenarios; only one parameter is modified at a time, all the others remaining the same. (a) Comparison of two types of permeability changes; doubling the thickness of the thermal boundary layer d does not affect the results. (b) Comparison of cases where heat alone is taken into account (without any permeability change), and only permeability change is considered (without any heat).

Figure 3.18b further illustrates the fact that heat alone cannot generate the observed temperature variations; however, permeability enhancement without heating could produce satisfactory results. This shows that permeability is the main controlling parameter, at least when the dike thickness w is less than 10 m (Figure 3.15b). If the dike were considerably thicker than $w = 1 - 10$ m assumed here (Figure 3.15b), the temperature changes in the junction zone may be large enough to counterbalance the response to the permeability change. Thus, dike thickness has some influence on the response of the system.

To address the longer term (> 1 year) temperature increase (Figure 3.1), our model would need to be complemented by some other factor. A gradual decrease in permeability either deep in the system or at the mixing junction would lead to a gradual increase in vent temperature. Our model does not consider mineral precipitation. In the junction zone, the temperature fluctuations that result from mixing may lead to clogging by precipitation of anhydrite [Lowell *et al.*, 2003] or some other mineral. This would reduce the input of cold shallow recharge, thus leading to a slow increase of temperature at black smokers. In addition to inorganic mineral precipitation, subsurface microbial activity may clog the pore space, though recent modeling of snowblower vents at $9^{\circ}50' N$ on the East Pacific Rise suggests that this effect may be small [Crowell *et al.*, 2007; Lowell *et al.*, 2007a]. Mineral precipitation may also occur deep in the crust and eventually clog the permeability that was enhanced as a result of the hypothesized dike emplacement [Lowell *et al.*, 1993; Martin and Lowell, 2000].

3.6 Conclusion

The mechanisms of hydrothermal response of mid-ocean ridge venting systems to seismic and/or magmatic activity remain a matter of debate. Our model of hydrothermal circulation within the crust offers a way to study different types of perturbations while invoking relatively simple circulation pathways. It allows simultaneous consideration of both low-temperature diffuse and high-temperature focused venting through the introduction of shallow recharge of cold fluid within the shallow crust. The most important result of this work is that a thermal perturbation at depth need not be advected along the entire discharge zone; it only needs to affect thermal boundary layers near the seafloor and at the junction with the shallow recharge in order to generate the observed temperature variations. Moreover, our results show that a deep cracking event alone that generates new permeability near the base of the system is not likely to cause a rapid perturbation in the vent temperature. If modest permeability increases resulting from seismic activity or dike emplacement above the west margin of the axial magma chamber where the seismic swarm was observed in March 1995 at the East Pacific Rise occur, our model yields results that are in good agreement with the observed temperature behavior there.

3.7 Acknowledgments

We thank Robert Reves-Sohn, Maya Tolstoy, and the editor Jeff Seewald for their thorough and thoughtful reviews of this manuscript. We are particularly grateful to the anonymous reviewer not only for their technical comments but for the thorough job of copy-editing the original manuscript. We are in debt to Karen Von Damm for insightful

discussions and the opportunity to join her 2004 and 2006 cruises to the 9°50' N area. We thank Dan Fornari for generously sharing his information about his data set and the March 1995 event. We are also grateful to Marv Lilley for his helpful comments and suggestions. This work was supported in part by NSF Grants OCE-0221974 and OCE-0527208 to R.P.L and L.N.G.

3.8 References

- Baker, E. T. (1998), Patterns of event and chronic hydrothermal venting following a magmatic intrusion: new perspectives from the 1996 Gorda Ridge eruption, *Deep Sea Res. II*, 45, 2599-2618.
- Baker, E. T., C. G. Fox, and J. P. Cowen (1999), In situ observations of the onset of hydrothermal discharge during the 1998 submarine eruption of Axial Volcano, Juan de Fuca Ridge, *Geophys. Res. Lett.*, 26(23), 3445-3448.
- Baker, E. T., G. J. Massoth, and R. A. Feely (1987), Cataclysmic hydrothermal venting on the Juan de Fuca Ridge, *Nature*, 329, 149-151.
- Baker, E. T., G. J. Massoth, R. A. Feely, G. A. Cannon, and R. E. Thomson (1998), The rise and fall of the CoAxial hydrothermal site, 1993-1996, *J. Geophys. Res.*, 103(B5), 9791-9806.
- Baker, E. T., G. J. Massoth, R. A. Feely, R. W. Embley, R. E. Thomson, and B. J. Burd (1995), Hydrothermal event plumes from the CoAxial seafloor eruption site, Juan de Fuca Ridge, *Geophys. Res. Lett.*, 22(2), 147-150.
- Baker, E. T., G. J. Massoth, S. L. Walker, and R. W. Embley (1993), A method for quantitatively estimating diffuse and discrete hydrothermal discharge, *Earth Planet. Sci. Lett.*, 118, 235-249.
- Bear, J. (1972), *Dynamics of Fluids in Porous Materials*, Elsevier, NY, 1972.
- Bemis, K. G., R. P. Von Herzen, and M. J. Mottl (1993), Geothermal heat flux from hydrothermal plumes on the Juan de Fuca Ridge, *J. Geophys. Res.*, 98(B4), 6351-6365.
- Bodvarsson, G. (1969), On Temperature of Water Flowing through Fractures, *J. Geophys. Res.*, 74(8), 1987-1992.
- Bohnenstiehl, D. R., R. P. Dziak, M. Tolstoy, C. G. Fox, and M. Fowler (2004), Temporal and spatial history of the 1999-2000 Endeavour Segment seismic series, Juan de Fuca Ridge, *Geochem. Geophys. Geosyst.*, 5, Q09003, doi:10.1029/2004GC000735.

Bray, A. M. (2001), The geochemistry of boron and lithium in mid-ocean ridge hydrothermal vent fluids, Ph.D. thesis, 125 pp, University of New Hampshire, Durham.

Brodsky, E. E., E. Roeloffs, D. Woodcock, I. Gall, and M. Manga (2003), A mechanism for sustained groundwater pressure changes induced by distant earthquakes, *J. Geophys. Res.*, *108*(B8), 2390.

Carlsaw, H.S. and J.C. Jaeger (1986), *Conduction of Heat in Solids*, 2nd ed., Clarendon Press, Oxford, New York, 510 pp.

Carbotte, S. M., R. S. Detrick, A. Harding, J. P. Canales, J. Babcock, G. Kent, E. Van Ark, M. Nedimovic, and J. Diebold (2006), Rift topography linked to magmatism at the intermediate spreading Juan de Fuca Ridge, *Geology*, *34*, 209-212, doi:10.113/G21969.1.

Cherkaoui, A. S. M., W. S. D. Wilcock, and E. T. Baker (1997), Thermal fluxes associated with the 1993 diking event on the CoAxial segment, Juan de Fuca Ridge: A model for the convective cooling of a dike, *J. Geophys. Res.*, *102*(B11), 24,887-24,902.

Corliss, J. B., et al. (1979), Submarine Thermal Springs on the Galápagos Rift, *Science*, *203*, 1073-1083.

Cowen, J. P., E. T. Baker, and R. W. Embley (2004), Detection of and Response to Mid-Ocean Ridge Magmatic Events: Implications for the Subsurface Biosphere, in *The Subseafloor Biosphere at Mid-Ocean Ridges, Geophys. Monogr. Ser.*, vol. 144, edited by W. S. D. Wilcock, et al., pp. 227-243, AGU, Washington, DC.

Crowell, B. W., R. P. Lowell, and K. L. Von Damm (2007), On the production of biological sulfur floc and "snowblower vents" at mid-ocean ridges, *submitted to Science*.

Davis, E., K. Becker, R. Dziak, J. Cassidy, K. Wang, and M. Lilley (2004), Hydrological response to a seafloor spreading episode on the Juan de Fuca ridge, *Nature*, *430*, 335-338, doi:10.1038/nature02755.

Davis, E. E., K. Wang, R. E. Thomson, K. Becker, and J. F. Cassidy (2001), An episode of seafloor spreading and associated plate deformation inferred from crustal fluid pressure transients, *J. Geophys. Res.*, *106*(B10), 21,953-21,963.

Delaney, J. R., V. Robigou, and R. E. McDuff (1992), Geology of a vigorous hydrothermal system on the Endeavour Segment, Juan de Fuca Ridge, *J. Geophys. Res.*, 97(B13), 19,663-19,682.

Delaney, P.T. (1982), Rapid intrusion of magma into wet rock: Groundwater flow due to pore pressure increases, *J. Geophys. Res.*, 87, 7739-7756.

Delaney, P. T., D. D. Pollard, J. I. Ziony, and E. H. Mckee (1986), Field relations between dikes and joints: Emplacement processes and paleostress analysis, *J. Geophys. Res.*, 91(B5), 4920-4938.

Detrick, R. S., S. M. Carbotte, E. van Ark, J. P. Canales, G. M. Kent, A. Harding, J. B. Diebold, and M. R. Nedimović (2002), New multi-channel seismic constraints on the crustal structure of the Endeavour Segment, Juan de Fuca Ridge: Evidence for a crustal magma chamber, *Eos Trans. AGU*, 83(47), Abstract T21B-1316.

Dziak, R., B. Chadwick, J. Cowen, E. Baker, R. Embley, D. Bohnenstiehl, and J. Resing (2006), Detecting Volcanic Events in the Northeast Pacific, *Eos Trans. AGU*, 87(4), 37.

Dziak, R. P., and C. G. Fox (1999), The January 1998 Earthquake Swarm at Axial Volcano, Juan de Fuca Ridge: Hydroacoustic Evidence of Seafloor Volcanic Activity, *Geophys. Res. Lett.*, 26(23), 3429-3432.

Dziak, R. P., C. G. Fox, and A. E. Schreiner (1995), The June-July 1993 seismo-acoustic event at CoAxial segment, Juan de Fuca Ridge: Evidence for a lateral dike injection, *Geophys. Res. Lett.*, 22(2), 135-138.

Dziak, R. P., and H. P. Johnson (2002), Stirring the Oceanic Incubator, *Science*, 296, 1406-1407.

Dziak, R. P., D. K. Smith, D. R. Bohnenstiehl, C. G. Fox, D. Desbruyeres, H. Matsumoto, M. Tolstoy, and D. J. Fornari (2004), Evidence of a recent magma dike intrusion at the slow spreading Lucky Strike segment, Mid-Atlantic Ridge, *J. Geophys. Res.*, 109, B12102, doi:10.1029/2004JB003141.

Edmond, J. M., A. C. Campbell, M. R. Palmer, G. P. Klinkhammer, C. R. German, H. N. Edmonds, H. Elderfield, G. Thompson, and P. A. Rona (1995), Time series studies of vent fluids from the TAG and MARK sites (1986, 1990) Mid-Atlantic Ridge: A new solution chemistry model and a mechanism for Cu/Zn zonation in massive sulphide ore

bodies, in *Hydrothermal Vents and Processes*, Geological Society Special Publication, vol. 87, edited by L. M. Parson, et al., pp. 77-86, The Geological Society, London, UK.

Edmond, J. M., C. Measures, R. E. McDuff, L. H. Chan, R. Collier, B. Grant, L. I. Gordon, and J. B. Corliss (1979), Ridge crest hydrothermal activity and the balances of the major and minor elements in the ocean: The Galapagos data, *Earth Planet. Sci. Lett.*, 46, 1-18.

Elkhoury, J. E., E. E. Brodsky, and D. C. Agnew (2006), Seismic waves increase permeability, *Nature*, 441, 1135-1138, doi:10.1038/nature04798.

Embley, R., and E. Baker (1999), Interdisciplinary Group Explores Seafloor Eruption with Remotely Operated Vehicle, *Eos Trans. AGU*, 80(19), 213.

Embley, R. W., W. W. Chadwick, Jr., I. R. Jonasson, D. A. Butterfield, and E. T. Baker (1995), Initial results of the rapid response to the 1993 CoAxial event: Relationships between hydrothermal and volcanic processes, *Geophys. Res. Lett.*, 22(2), 143-146.

Embley, R. W., and J. E. Lupton (2004), Diking, Event Plumes, and the Subsurface Biosphere at Mid-Ocean Ridges, in *The Subseafloor Biosphere at Mid-Ocean Ridges*, *Geophys. Monogr. Ser.*, vol. 144, edited by W. S. D. Wilcock, et al., pp. 75-97, AGU, Washington, DC.

Fisher, A. T. (1998), Permeability within basaltic oceanic crust, *Rev. Geophys.*, 36(2), 143-182.

Fornari, D. J., T. Shank, K. L. Von Damm, T. K. P. Gregg, M. Lilley, G. Levai, A. Bray, R. M. Haymon, M. R. Perfit, and R. Lutz (1998), Time-series temperature measurements at high-temperature hydrothermal vents, East Pacific Rise 9°49'-51'N: evidence for monitoring a crustal cracking event, *Earth Planet. Sci. Lett.*, 160, 419-431.

Fox, C. G. (1995), Special collection on the June 1993 volcanic eruption on the Coaxial Segment, Juan de Fuca Ridge, *Geophys. Res. Lett.*, 22(2), 129-130.

Fox, C. G., and R. P. Dziak (1998), Hydroacoustic detection of volcanic activity on the Gorda Ridge, February-March 1996, *Deep Sea Res. II*, 45, 2513-2530.

Fox, C. G., R. P. Dziak, H. Matsumoto, and A. E. Schreiner (1993/94), Potential for monitoring low-level seismicity on the Juan de Fuca Ridge using military hydrophone arrays, *Mar. Tech. Soc. Jour.*, 27, 22-30.

Fox, C. G., H. Matsumoto, and T. K. A. Lau (2001), Monitoring Pacific Ocean seismicity from an autonomous hydrophone array, *J. Geophys. Res.*, 106(B3), 4183-4206.

Fox, C. G., W. E. Radford, R. P. Dziak, T. K. Lau, H. Matsumoto, and A. E. Schreiner (1995), Acoustic detection of a seafloor spreading episode on the Juan de Fuca Ridge using military hydrophone arrays, *Geophys. Res. Lett.*, 22(2), 131-134.

Germanovich, L. N., and R. P. Lowell (1992), Percolation Theory, Thermoelasticity, and Discrete Hydrothermal Venting in the Earth's Crust, *Science*, 255, 1564-1567.

Germanovich, L. N., and R. P. Lowell (1995), The mechanism of phreatic eruptions, *J. Geophys. Res.*, 100(B5), 8417-8434.

Germanovich, L. N., R. P. Lowell, and D. K. Astakhov (2000), Stress-dependent permeability and the formation of seafloor event plumes, *J. Geophys. Res.*, 105(B4), 8341-8354.

Germanovich, L. N., R. P. Lowell, and D. K. Astakhov (2001), Temperature-dependent permeability and bifurcations in hydrothermal flow, *J. Geophys. Res.*, 106(B1), 473-495.

Haymon, R. M., et al. (1993), Volcanic eruption of the mid-ocean ridge along the East Pacific Rise crest at 9°45'-52' N: Direct submersible observations of seafloor phenomena associated with an eruption event in April, 1991, *Earth Planet. Sci. Lett.*, 119, 85-101.

Hill, D. P., et al. (1993), Seismicity Remotely Triggered by the Magnitude 7.3 Landers, California, Earthquake, *Science*, 260, 1617-1623.

Humphris, S. E., and M. K. Tivey (2000), A synthesis of geological and geochemical investigations of the TAG hydrothermal fluid: Insights into fluid flow and mixing processes in a hydrothermal system, in *Ophiolites and oceanic crust: New insights from field studies and the Ocean Drilling Program, Special Paper*, vol. 349, edited by Y. Dilek, et al., pp. 213-235, Geological Society of America, Boulder, CO.

James, R. H., and H. Elderfield (1996), Chemistry of ore-forming fluids and mineral formation rates in an active hydrothermal sulfide deposit on the Mid-Atlantic Ridge, *Geology*, 24, 1147-1150.

Johnson, H. P., R. P. Dziak, C. R. Fisher, C. G. Fox, and M. J. Pruis (2001), Earthquakes' Impact on Hydrothermal Systems May Be Far-Reaching, *Eos Trans. AGU*, 82(21), 233.

Johnson, H. P., M. Hutnak, R. P. Dziak, C. G. Fox, I. Urcuyo, J. P. Cowen, J. Nabelek, and C. Fisher (2000), Earthquake-induced changes in a hydrothermal system on the Juan de Fuca mid-ocean ridge, *Nature*, 407, 174-177.

Juniper, S. K., P. Martineu, J. Sarrazin, and Y. Gelinis (1995), Microbial-mineral floc associated with nascent hydrothermal activity on CoAxial segment, Juan de Fuca Ridge, *Geophys. Res. Lett.*, 22(2), 179-182.

Kadko, D., and W. Moore (1988), Radiochemical constraints on the crustal residence time of submarine hydrothermal fluids: Endeavour Ridge, *Geochim. Cosmochim. Acta*, 52, 659-668.

Kent, G. M., A. J. Harding, and J. A. Orcutt (1993), Distribution of magma beneath the East Pacific Rise between the Clipperton transform and the 9°17'N deval from forward modeling of common depth point data, *J. Geophys. Res.*, 98(B8), 13,945-13,969.

Lewis, K.C. and R.P. Lowell (2004), Mathematical modeling of phase separation of seawater near an igneous dike, *Geofluids*, 4, 197-209.

Lilley, M. D., D. A. Butterfield, J. E. Lupton, and E. J. Olson (2003), Magmatic events can produce rapid changes in hydrothermal vent chemistry, *Nature*, 422, 878-881, doi:10.1038/nature01569.

Lowell, R. P. (1975), Circulation in Fractures, Hot Springs, and Convective Heat Transport on Mid-Ocean Ridge Crests, *Geophys. J. R. Astron. Soc.*, 40, 351-365.

Lowell, R. P. (1976), Comments on 'Theory of Heat Extraction From Fractured Hot Dry Rock' by A. C. Gringarten, P.A. Witherspoon, and Yuzo Ohnishi, *J. Geophys. Res.*, 81(2), 359.

Lowell, R. P. (1990), Thermoelasticity and the Formation of Black Smokers, *Geophys. Res. Lett.*, 17(6), 709-712.

Lowell, R. P., B. W. Crowell, K. Lewis, and L. Liu (2007a), Modeling multi-phase processes at oceanic spreading centers: magma to microbes, in *Modeling Hydrothermal Processes at Oceanic Spreading Centers: Magma to Microbe*, *Geophys. Monogr. Ser.*, edited by R. P. Lowell, et al., in review.

Lowell, R. P., S. R. Gosnell, and Y. Yang (2007b), Numerical simulations of single-pass hydrothermal convection at mid-ocean ridges: Effects of the extrusive layer and temperature dependent permeability, *Geochem. Geophys. Geosystems*, in press.

Lowell, R. P., and L. N. Germanovich (1994), On the temporal evolution of high-temperature hydrothermal systems at ocean ridge crests, *J. Geophys. Res.*, 99(B1), 565-575.

Lowell, R. P., and L. N. Germanovich (2004), Hydrothermal Processes at Mid-Ocean Ridges: Results From Scale Analysis and Single-Pass Models, in *Mid-Ocean Ridges: Hydrothermal Interactions Between the Lithosphere and Oceans*, *Geophys. Monogr. Ser.*, vol. 148, edited by C. R. German, et al., pp. 219-244, AGU, Washington, DC.

Lowell, R. P., P. Van Cappellen, and L. N. Germanovich (1993), Silica Precipitation in Fractures and the Evolution of Permeability in Hydrothermal Upflow Zones, *Science*, 260, 192-194.

Lowell, R. P., Y. Yao, and L. N. Germanovich (2003), Anhydrite precipitation and the relationship between focused and diffuse flow in seafloor hydrothermal systems, *J. Geophys. Res.*, 108(B9), 2424, doi:10.1029/2002JB002371.

Martin, J. T., and R. P. Lowell (2000), Precipitation of quartz during high-temperature, fracture controlled hydrothermal upflow at ocean ridges: Equilibrium versus linear kinetics, *J. Geophys. Res.*, 105(B1), 869-882.

Pascoe, A. R., and J. R. Cann (1995), Modeling diffuse hydrothermal flow in black smoker vent fields, in *Hydrothermal Vents and Processes*, *Geological Society Special Publication*, vol. 87, edited by L. M. Parson, et al., pp. 159-173, The Geological Society, London, UK.

Pollard, D. D. (1987), Elementary fracture mechanics applied to the structural interpretation of dikes, in *Mafic Dyke Swarms*, *Spec. Pap. Geol. Assoc. Can.*, edited by H. C. Halls and W. F. Fahrig, pp. 5-24.

Press, W. H., B. P. Flannery, S. A. Teukolsky, and W. T. Vetterling (1992), *Numerical Recipes in FORTRAN: The Art of Scientific Computing*, 2nd ed., 992 pp., Cambridge University Press, New York.

Ramondenc, P., L. N. Germanovich, and R. P. Lowell (2005), Modeling hydrothermal response to earthquakes at mid-ocean ridges: EPR, *Eos Trans. AGU*, 86(52), Abstract T31B-0500.

Ramondenc, P., L. N. Germanovich, K. L. Von Damm, and R. P. Lowell (2006), The first measurements of hydrothermal heat output at 9°50'N, East Pacific Rise, *Earth Planet. Sci. Lett.*, 245, 487-497, doi:10.1016/j.epsl.2006.03.023.

Ravizza, G., J. Blusztain, K. L. Von Damm, A. M. Bray, W. Bach, and S. R. Hart (2001), Sr isotope variations in vent fluids from 9°46'-9°54' N East Pacific Rise: Evidence of a non-zero-Mg fluid component, *Geochim. Cosmchim. Acta*, 65, 729-739.

Roeloffs, E. (1996), Poroelastic techniques in the study of earthquake-related hydrologic phenomena, *Adv. Geophys.*, 37, 135-195.

Rojstaczer, S., and S. Wolf (1992), Permeability changes associated with large earthquakes: An example from Loma Prieta, California, *Geology*, 20, 211-214.

Rojstaczer, S., S. Wolf, and R. Michel (1995), Permeability enhancement in the shallow crust as a cause of earthquake-induced hydrological changes, *Nature*, 373, 237-239.

Rona, P. A., and D. A. Trivett (1992), Discrete and diffuse heat transfer at ASHES vent field, Axial Volcano, Juan de Fuca Ridge, *Earth Planet. Sci. Lett.*, 109, 57-71.

Samarskii, A. A. (2001), *The theory of difference schemes*, 786 pp., Marcel Dekker Inc., New York.

Scheirer, D. S., T. M. Shank, and D. J. Fornari (2006), Temperature variations at diffuse and focused flow hydrothermal vent sites along the northern East Pacific Rise, *Geochem. Geophys. Geosyst.*, 7, Q03002, doi:10.1029/2005GC001094.

Schultz, A., J. R. Delaney, and R. E. McDuff (1992), On the partitioning of heat flux between diffuse and point source seafloor venting, *J. Geophys. Res.*, 97(B9), 12,299-12,314.

Seyfried, W. E., Jr., J. S. Seewald, M. E. Berndt, K. Ding, and D. I. Foustoukos (2003), Chemistry of hydrothermal vent fluids from the Main Endeavour Field, northern Juan de Fuca Ridge: Geochemical controls in the aftermath of June 1999 seismic events, *J. Geophys. Res.*, 108(B9), 2429, doi:10.1029/2002JB001957.

Sim, Y. (2004), Mechanics of Complex Hydraulic Fractures in the Earth's Crust, Ph.D. thesis, 324 pp, Georgia Institute of Technology, Atlanta.

Sim, Y., L. N. Germanovich, R. P. Lowell, and P. Ramondenc (2004), Diking, magma lenses, and location of hydrothermal sites at mid-ocean ridges, *Eos Trans. AGU*, 85(47), Abstract B13A-0206.

Sinha, M. C., and R. L. Evans (2004), Geophysical Constraints Upon the Thermal Regime of the Ocean Crust, in *Mid-Ocean Ridges: Hydrothermal Interactions Between the Lithosphere and Oceans*, *Geophys. Monogr. Ser.*, vol. 148, edited by C. R. German, et al., pp. 19-62, AGU, Washington, DC.

Smith, D. K., M. Tolstoy, C. G. Fox, D. R. Bohnenstiehl, H. Matsumoto, and M. J. Fowler (2002), Hydroacoustic monitoring of seismicity at the slow-spreading Mid-Atlantic Ridge, *Geophys. Res. Lett.*, 29(11), 1518, doi:10.1029/2001GL013912.

Sohn, R. A., D. J. Fornari, K. L. Von Damm, J. A. Hildebrand, and S. C. Webb (1998), Seismic and hydrothermal evidence for a cracking event on the East Pacific Rise crest at 9°50' N, *Nature*, 396, 159-161.

Sohn, R. A., J. A. Hildebrand, and S. C. Webb (1999), A microearthquake survey of the high-temperature vent fields on the volcanically active East Pacific Rise (9°50'N), *J. Geophys. Res.*, 104(B11), 25,367-25,377.

Tolstoy, M. (2007), Seismological constraints on magmatic and hydrothermal processes at ridges, in *Modeling Hydrothermal Processes at Oceanic Spreading Centers: Magma to Microbe*, edited by R. P. Lowell, et al., in review.

Tolstoy, M., et al. (2006), A Sea-Floor Spreading Event Captured by Seismometers, *Science*, 314, 1920-1922, doi:10.1126/science.1133950.

Von Damm, K. L. (2000), Chemistry of hydrothermal vent fluids from 9°-10°N, East Pacific Rise: "Time zero," the immediate post-eruptive period, *J. Geophys. Res.*, 105(B5), 11,203-11,222.

Von Damm, K. L. (2004), Evolution of the Hydrothermal System at East Pacific Rise 9°50'N: Geochemical Evidence for Changes in the Upper Oceanic Crust, in *Mid-Ocean Ridges: Hydrothermal Interactions Between the Lithosphere and Oceans*, *Geophys. Monogr. Ser.*, vol. 148, edited by C. R. German, et al., pp. 285-304, AGU, Washington, DC.

Von Damm, K. L., and M. D. Lilley (2004), Diffuse Flow Hydrothermal Fluids from 9°50' N East Pacific Rise: Origin, Evolution and Biogeochemical Controls, in *The Subseafloor Biosphere at Mid-Ocean Ridges*, *Geophys. Monogr. Ser.*, vol. 144, edited by W. S. D. Wilcock, et al., pp. 245-268, AGU, Washington, DC.

Wilcock, W. S. D. (2004), Physical response of mid-ocean ridge hydrothermal systems to local earthquakes, *Geochem. Geophys. Geosyst.*, 5, Q11009, doi:10.1029/2004GC000701.

Wilcock, W. S. D., and A. T. Fisher (2004), Geophysical Constraints on the Subseafloor Environment Near Mid-Ocean Ridges, in *The Subseafloor Biosphere at Mid-Ocean Ridges*, *Geophys. Monogr. Ser.*, vol. 144, edited by W. S. D. Wilcock, et al., pp. 51-74, AGU, Washington, DC.

Wilcock, W. S. D., and A. McNabb (1996), Estimates of crustal permeability on the Endeavour segment of the Juan de Fuca mid-ocean ridge, *Earth Planet. Sci. Lett.*, 138, 83-91.

CHAPTER 4

MAGMATIC ORIGIN OF THE MARCH 1995 EARTHQUAKE SWARM AT 9°50' N, EAST PACIFIC RISE

Abstract. The response of mid-ocean ridge hydrothermal systems to seismic and magmatic activity could provide a means of using seafloor observations to assess processes occurring at crustal depths. The correct interpretation of the March 1995 seismic activity and the subsequent hydrothermal response on the East Pacific Rise (EPR) near 9°50' N is of critical importance for understanding the links among magmatic, tectonic, and hydrothermal processes at mid-ocean ridges. We suggest that this seismic activity was caused by a small diking event that occurred during an interval of magma lens inflation that was bracketed by two major eruptions in 1991 and 2006. The diking scenario yields quantitative results that are in excellent agreement with temperature observations. This scenario explains seemingly different observations from the unified stand point of fracture mechanics. In particular, the diking explanation is consistent with both the thin, lens-like shape of the EPR magma chamber and with the seismic pattern displaced to its west margin.

4.1 Introduction

The 9°50' N area of the East Pacific Rise (EPR) has become an important study area after fresh volcanic activity and dramatic changes in the hydrothermal systems and associated biological communities were fortuitously found in 1991 [*Haymon et al.*, 1993;

Von Damm, 2004]. Since then, the region has been the focus of a continuous seismic, biological, and geochemical investigation. In 1995, the three-month deployment of an array of seismometers allowed the detection of a microearthquake swarm. Based on the recovered seismic, thermal, and chemical data, this seismic activity was interpreted as a thermal cracking episode that enabled hydrothermal fluid to mine heat deeper in the reaction zone overlying the magma lens located beneath the ridge [*Fornari et al.*, 1998; *Sohn et al.*, 1998; *Sohn et al.*, 1999]. In this work, we show that the hypocentral pattern and mechanics of dike propagation from the magma lens, together with the temperature variations observed at the seafloor, suggest that the seismic swarm is more likely the result of dike emplacement initiated at the west margin of the axial magma chamber (AMC). Current explanations, based on a thermal cracking episode at the bottom of the upflow zone, require fluid flow through a km-scale discharge zone in a matter of an hour [*Wilcock*, 2004] or a few days [*Fornari et al.*, 1998; *Sohn et al.*, 1998; *Sohn et al.*, 1999], which is unrealistically fast [*Kadko et al.*, 1985; *Lowell and Germanovich*, 2004]. We argue that such an episode, which affects the rate of heat transfer at the base of the hydrothermal system, cannot give rise to rapid temperature changes at the seafloor. We also argue that a dike resulting only in modest changes in permeability within the discharge zone is sufficient to cause the observed seafloor temperature perturbations. Contrary to the thermal cracking hypotheses [*Fornari et al.*, 1998; *Sohn et al.*, 1998; *Sohn et al.*, 1999; *Wilcock*, 2004], the diking interpretation is consistent with the fluid residence time within the hydrothermal system in the order of years [*Kadko et al.*, 1985; *Lowell and Germanovich*, 2004; *Pascoe and Cann*, 1995]. It also provides some indications on AMC dynamics between two major eruptions, in 1991 [*Haymon et al.*,

1993; *Von Damm*, 2004] and 2006 [*Fornari et al.*, 2006; *Soule et al.*, 2006; *Tolstoy et al.*, 2006].

4.2 Mechanics of the March 1995 swarm

Sohn et al. [1998; 1999] presented initial analyses of the seismic data from the March 1995 microearthquake swarm and *Fornari et al.* [1998] reported the temperature records monitored at the Bio9 venting chimney (“black smoker”). This site of high-temperature focused venting is of particular interest since it is situated just above the March 1995 seismic activity. This is also the only vent of the 9°50' N area that has been continuously monitored since October 1994. The relocation of 65 out of the 147 hypocenters estimated from the recovered seismic data suggested a particularly high density between 0.7 and 1.1 km depth, just above the west margin of the AMC, the depth of which has been estimated at 1.4 km [*Kent et al.*, 1993]. This seismic pattern (Figure 4.1a) was interpreted as a slip along a vertical fault generated by the release of thermal stresses at the base of the hydrothermal system [*Sinha and Evans*, 2004; *Sohn et al.*, 1998; *Sohn et al.*, 1999]. The slip would have rapidly propagated downwards, as the AMC lid subsided, opening pathways for the fluid that presumably reached the seafloor and caused the temperature anomaly four days later. This interpretation was partly based on a first assessment of fluid chemistries, which did not show magmatic evidences for the 8 months subsequent to seismicity, and on the assumption that the fluid residence time in the hydrothermal system was of the order of days [*Fornari et al.*, 1998; *Sohn et al.*, 1998; *Sohn et al.*, 1999]. However, when considering a fluid residence time of the order of months to years, as scaling of the discharge zone suggests [*Lowell and Germanovich*,

2004; *Pascoe and Cann*, 1995], a change of chemistry at the bottom of the discharge would also take months to years before being detected at the surface. Furthermore, recent work showed that the evolution of the Cl and Si contents of venting fluids, both at the time of and after the seismic event, could also be consistent with magma injection [*Von Damm*, 2004].

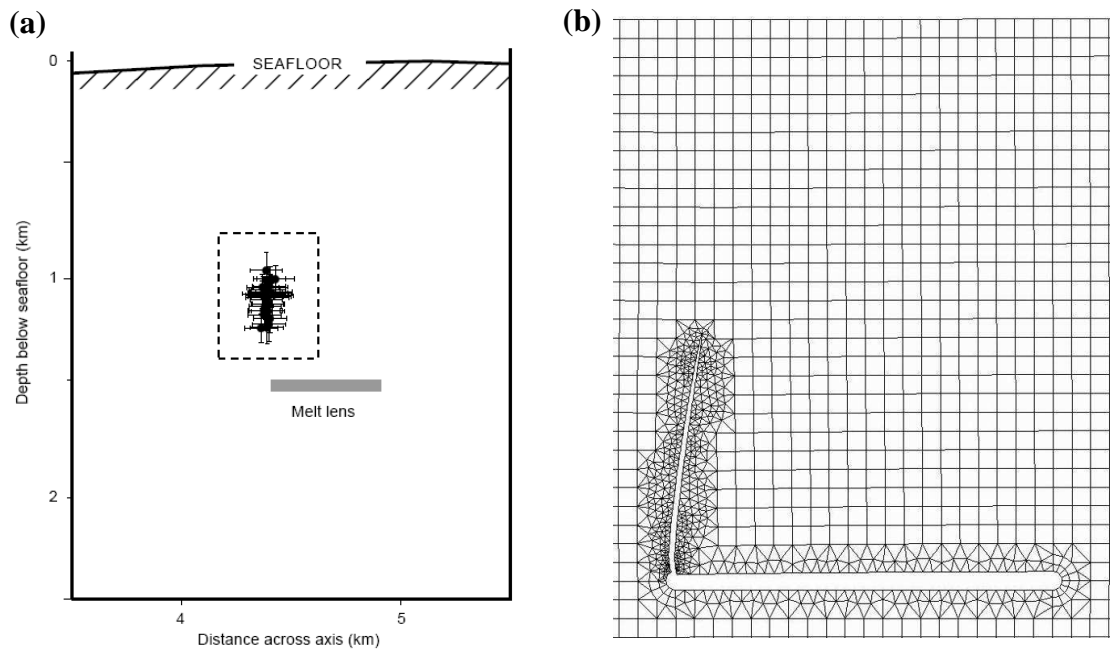


Figure 4.1. Cross-sections of study area. (a) Ridge normal cross-section of relocated events with error bars [*Sohn et al.*, 1998]. (b) Finite element simulation of dike propagation from the magma chamber shown in Figure 4.1a. The entire simulation domain has dimensions of 6 by 10 km (depth and width, respectively). We imposed zero-displacement on the lateral and bottom boundaries, in horizontal and vertical directions, respectively.

Sohn et al. [1999] further suggested that the hypocenter pattern shown in Figure 4.1a would be difficult to interpret as dike-induced seismicity. We argue that this is not necessarily correct. From the point of view of fracture mechanics, the observed seismic

pattern (Figure 4.1a) is actually in complete agreement with a dike propagating at the lens margin. For a thin, crack-like lens shape, the pressurization (inflation) of a magma chamber results in tensile stress concentration near the tips of the lens while the rest of the host rock is in compression. This implies that pressurization is likely to result in dikes initiating near the lens tips. Further propagation of the dike can be described by the principles of fracture mechanics [Rice, 1968]. In particular, finite element calculations show that for EPR conditions, the dike propagates almost vertically (as discussed in Appendix E) towards the seafloor, because in this setting, the least in-situ stress is horizontal and perpendicular to the ridge axis.

An example is shown in Figure 4.1b. We considered a pressurized 1.5-km deep, 1-km wide, and 50-m thick magma lens, which is characteristic for EPR conditions [e.g., Crawford *et al.*, 1999; Vera *et al.*, 1990], and propagated the dike 600 m in order to match the hypocentral pattern shown in Figure 4.1a. Initially, the magma pressure in the lens was equal to the overburden and we gradually increased it until the maximum principal stress reached near the lens tip the tensile strength value (1 MPa). This happened at a pressure increase of 1.5%. In the simulations, the amount of magma in the dike plus the magma lens was conserved, so that, the pressure in the magma chamber decreases during dike propagation. As a result, the dike may or may not reach the surface. The conventional criteria of crack propagation, $K_I = K_{Ic}$, and crack propagation direction, $K_{II} = 0$, were employed [Broberg, 1999; Rice, 1968] (see also Appendix E).

The dike trajectory was nearly insensitive to the value of fracture toughness in the tested range of $K_{Ic} = 0\text{--}10^2 \text{ MPa}\sqrt{\text{m}}$, which probably covers the entire interval of possible

K_{Ic} for dikes and hydraulic fractures of this size [Delaney and Pollard, 1981; Rubin, 1993, 1995; Dyskin and Germanovich, 1993; Papanastasiou, 1999]. It is also not sensitive to the details of pressure distribution inside the dike. In the case of $K_{Ic} = 10 \text{ MPa}\sqrt{\text{m}}$, which is conventionally used for hydraulic fractures of similar dimensions [Shlyapobersky, 1985; Advani *et al.*, 1999], the widest dike opening (i.e., its width at the base) was 1.43 m. This gives the dike aspect ratio (opening/length) of 2.4×10^{-3} , consistent with that for fractures in elastic material ($\sim 10^{-3}$). Therefore, the mechanics of inflation of a thin magma lens suggests that the detected location of the microearthquakes (Figure 4.1a) is fully consistent with a dike emplacement initiated at the west tip of the AMC.

Inflation of the magma lens at 9°50' N EPR agrees with the observation of increased magmatic degassing (CO_2) starting late 1993, which was interpreted as the replenishment of the magma chamber in this area [Lilley *et al.*, 2002; Von Damm, 2004]. The low scale of both the seismicity in March 1995 and the emplaced dike (i.e., only ~ 1-m thick in Figure 4.1b) indicates a small level of AMC pressurization. Hence, the March 1995 seismic swarm suggests that at that time, the AMC was gradually inflating and, perhaps, the whole 9°50' N EPR site was already “building” toward the recent massive and extremely seismically active 2006 eruption [Tolstoy *et al.*, 2006]. This eruption, part of which occurred from an eruptive fissure (Figure 4.2a) parallel to the spreading axis and located 600-700 m east of it [Fornari *et al.*, 2006; Soule *et al.*, 2006], also suggests a diking event propagating from the east tip of the sub-axial magma lens. This is consistent with AMC pressurization, because the mechanics of dike emplacement predicts its occurrence at the margin of the inflating chamber rather than anywhere else. Therefore,

the March 1995 seismic swarm may have been caused by the AMC inflation between the two major eruptions of 1991 and 2006.

Furthermore, as noted by *Tolstoy et al.* [2008], dikes feeding the 1991 and 2006 eruptions were centered in the axial summit trough (AST), which lies to the western side of the AMC (Figure 4.2a). This suggests dike initiation near the margins of pressurized lens-like cavities [*Ramondenc et al.*, 2006a; *Sim*, 2004; *Sim et al.*, 2004], with subsequent propagation towards the seafloor as shown in Figure 4.2b. Hence, the major 1991 and 2006 eruptions may have also originated from the magma lens margins.

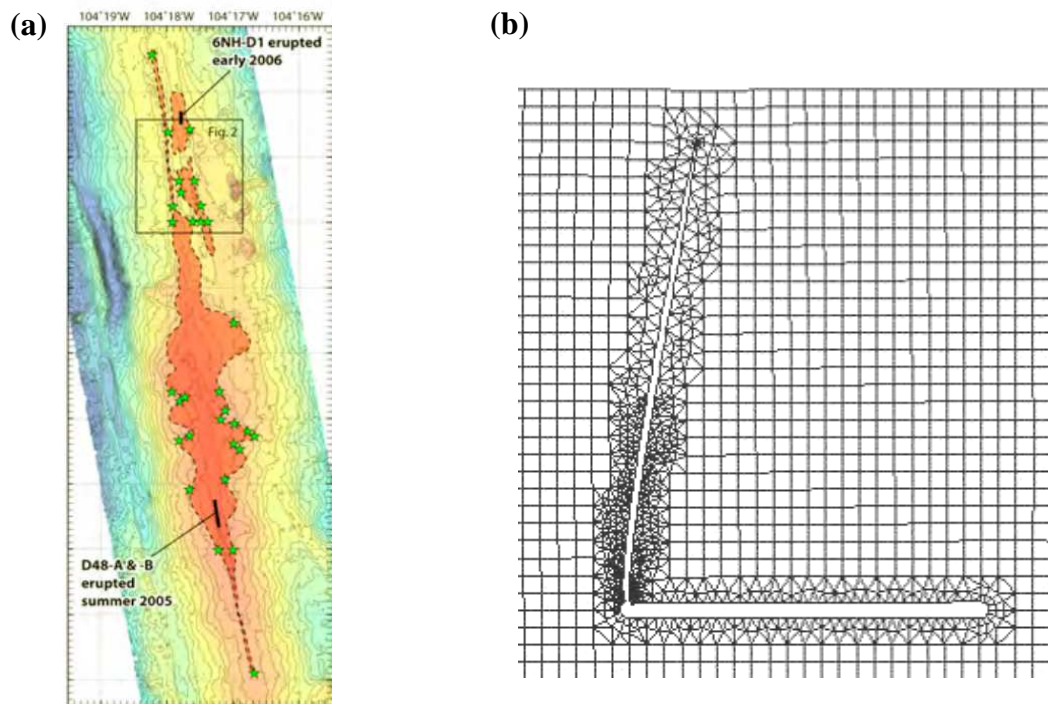


Figure 4.2. The 2006 East Pacific Rise eruption. (a) Map of the area with details of the erupted lava [*Fornari et al.*, 2006]. (b) Finite element simulation of dike propagation from the west margin of the magma chamber situated 1.5 km beneath the seafloor (EPR conditions). All simulation conditions and domain geometry are the same as those for propagation results presented in Figure 4.1b.

4.3 Hydrothermal modeling

To further test the hypothesis of response of the hydrothermal system to diking, we recognized permeability contrast [e.g., *Fisher*, 1998] and employed a two-branch single-pass model [*Pascoe and Cann*, 1995; *Lowell et al.*, 2003] in order to account for both deep high-temperature circulation and circulation of cold seawater in the upper crustal extrusives (Figure 4.3). Our approach rests on basic equations of fluid flow in porous medium. We suggest, however, that as the ascending, sulfate-depleted, hot hydrothermal fluid mixes with the sulfate-rich, shallow recharge of cold seawater in the extrusive layer, anhydrite and other minerals precipitate, resulting in permeable channels of focused flow separated from regions of low-temperature diffuse flow [*Lowell et al.*, 2003, 2007] (Figure 4.3). In this system, the ascending fluid in both the high- and low-temperature branches is nearly isothermal except within thin thermal boundary layers at the seafloor and within the extrusives (Figure 4.3) where fluid mixing occurs.

These boundary layers can be scaled by considering the steady state heat transfer in the discharge zone:

$$v \frac{dT}{dz} = a \frac{d^2T}{dz^2} \quad (4.1)$$

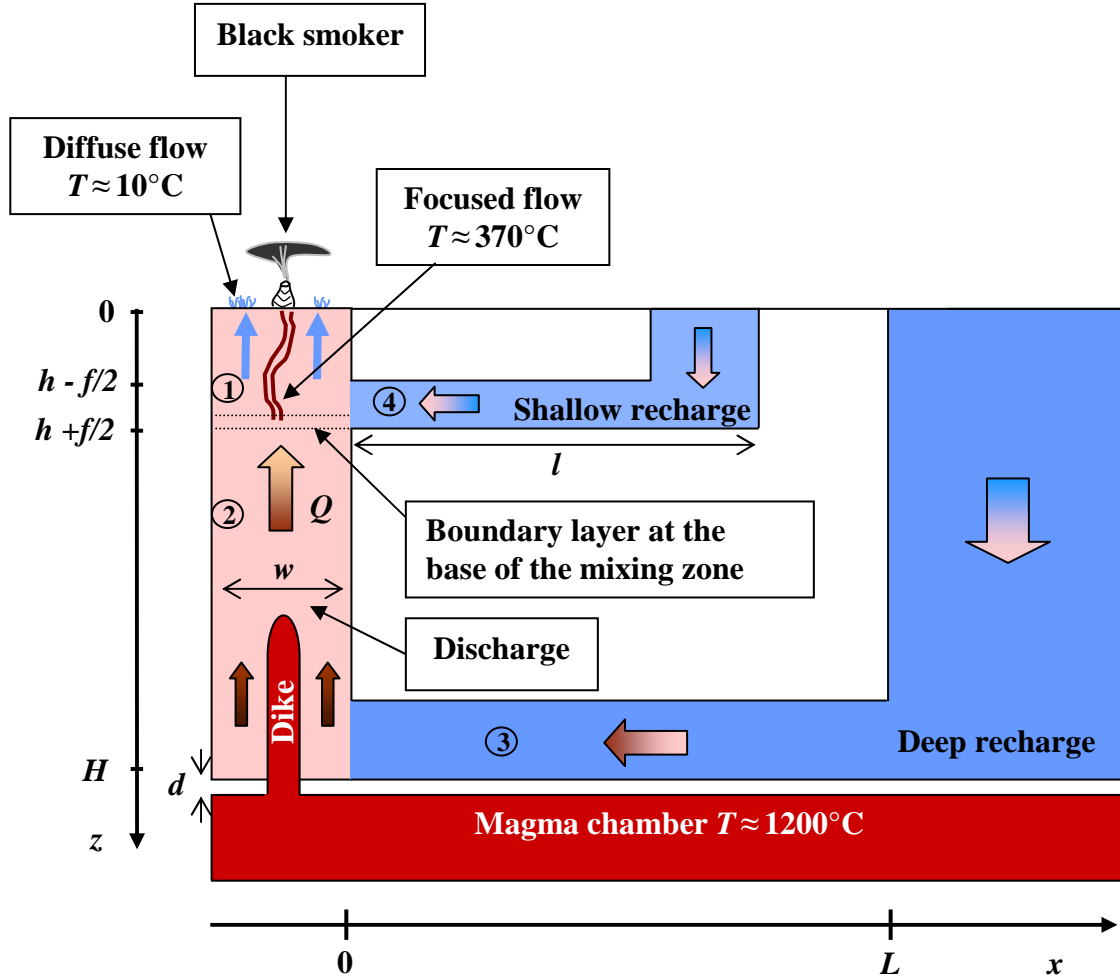


Figure 4.3. Schematic of a “double-loop” single-pass model. The characteristic ratio of high- to low-temperature fluid fluxes at EPR $9^\circ 50' \text{ N}$ is $\sim 1\text{--}10\%$ [Ramondenc *et al.*, 2006b]. Since the high-temperature focused fluids show little mixing with seawater [Von Damm and Lilley, 2004], and because little cooling occurs along the focusing channels, we view black smokers as “temperature probes” of the base of the focusing zone. The rest of the extrusives (i.e., outside the channels) is then associated with the low-temperature diffuse flow, which is a mixture of high-temperature fluids with cold seawater from the shallow recharge [Von Damm and Lilley, 2004]. In the simulations, we used $w \sim 10^2 \text{ m}$ for the width of the discharge zone. While this parameter is important from the standpoint of local geological setup (e.g., the width of the axial summit trough also scales with 10^2 m at the EPR $9^\circ 50' \text{ N}$ area), varying w does not affect our results (e.g., Figure 4.5 and Figure 4.6) as our calculations show for a range of $w = 10\text{--}10^3 \text{ m}$.

where T and v are the temperature and Darcian velocity (specific discharge) in the discharge zone, respectively, z is the the depth below the seafloor, $a = \lambda_r / (c_f \rho_f)$ is the effective thermal diffusivity, λ_r is the thermal conductivity of rock, c_f is the specific heat of the hydrothermal fluid, and ρ_f is the fluid density (all parameters and their values are given in Table 4.1). The thickness of the boundary layer is then scaled as $\delta \sim a/v$, and since the advection regime is prevailing in the rest of the discharge zone, the temperature is almost constant everywhere except in the boundary layers. Should the boundary layer be altered, the expected response time would be $\tau \sim \delta/v$. As a result, thermal perturbations at depth do not need to traverse the entire upflow zone, but rather just need to affect the thin boundary layers. The time during which the thermal perturbation propagates through the upflow zone is of the order of $H/v \gg \tau$, where H is the depth of the upflow zone, and for characteristic hydrothermal flow requires $H \gg \delta$.

The typical value of a is 10^{-6} m²/s while v needs to be obtained as a result of modeling. We first use the mass balance conditions [Lowell *et al.*, 2003; Ramondenc *et al.*, 2008]

$$\left\{ \begin{array}{l} Q_1 = Q_2 + Q_4 \\ Q_1 r_1 + Q_2 r_2 + Q_3 r_3 = g \int_0^H [\rho_f(T_{rech}) - \rho_f(T)] dz \\ Q_2 = Q_3 \\ Q_1 r_1 + Q_4 r_4 = g \int_0^h [\rho_f(T_{rech}) - \rho_f(T)] dz \end{array} \right. \quad (4.2)$$

where $Q_i = -\rho_f A_i v_i$ are the mass fluxes, A_i are the cross-sectionnall areas, v_i are the Darcian velocities (the subscript i referring to the i^{th} limb of the system; numbered 1 through 4 in Figure 4.3), and g is the acceleration due to gravity. Here velocities, v_i , are

negative as they are directed against z - and x -axis, while mass fluxes Q_i are assumed to be positive. All parameters and their values are given in Table 4.1. In expressions (4.2),

$$r_1 = \int_0^h \frac{\nu(T)}{k(T)} \frac{dz}{A_1}, \quad r_2 = \int_h^H \frac{\nu(T)}{k(T)} \frac{dz}{A_2}, \quad r_3 = \int_0^L \frac{\nu(T)}{k(T)} \frac{dx}{A_3}, \quad r_4 = \int_0^l \frac{\nu(T)}{k(T)} \frac{dx}{A_4} \quad (4.3)$$

are the hydrodynamic resistances in the limbs 1, 2, 3, and 4, respectively, $k(T)$ is the rock permeability, which in general can be temperature dependent [Germanovich *et al.*, 2000, 2001], and $\nu(T)$ is the kinematic viscosity of the hydrothermal fluid. In expressions (4.2), (4.3), and thereafter, z represents the depth below the seafloor, and x the horizontal coordinate in the deep horizontal limbs 3 and 4. For simplicity, the far-field temperature distributions in the deep and shallow recharge zones are assumed to be the same, that is, linearly distributed with depth, $T_{rech}(z) = \beta_{rech}z$, where β_{rech} is the thermal gradient in the recharge zone. Accordingly, we define $T_h = T_{rech}(h)$ and $T_H = T_{rech}(H)$. The bottom boundary condition of the entire flow path corresponds to the temperature at the bottom of the deep recharge (Figure 4.3), whose value is not very well constrained. We used $T_H = 100^\circ\text{C}$, which gives $T_h = 7^\circ\text{C}$ considering the linear gradient in the recharge zones, starting from $T_0 = 0^\circ\text{C}$ at the seafloor.

For scaling purposes, we assume a constant permeability along each limb, with $k_1 \sim k_4 > k_2 \sim k_3$ (the permeability is higher in the extrusive layer). As a first approximation, we ignore the conduction term and lateral heat loss through the walls of the system. The temperature is thus constant in the upflow limbs 1 and 2 (Figure 4.3), that are, $T = T_1$ and $T = T_2$, respectively. In the absence of shallow heat source, we also consider that the temperature is constant along the shallow horizontal limb 4, of length l , which is at $T = T_4 = T_h$.

Table 4.1. Symbol definitions and parameter values.

Symbol	Definition	Value
a	effective thermal diffusivity, $\lambda_r/(\rho_r c_r)$	$\sim 10^{-6} \text{ m}^2/\text{s}$
a_r	thermal diffusivity of rock, $\lambda_r/(\rho_r c_r)$	$\sim 10^{-6} \text{ m}^2/\text{s}$
A_i	cross-sectional area of the i^{th} limb	
b	length of vent field along strike	100 m
c_f	specific heat of water	$4 \times 10^3 \text{ J}/(\text{kg}^\circ\text{C})$
c_r	specific heat of rock	$1 \times 10^3 \text{ J}/(\text{kg}^\circ\text{C})$
d	basal thermal boundary layer thickness	2-20 m
f	height of the junction between upflow and shallow recharge limb	1-10 m
g	acceleration due to gravity	9.8 m/s^2
H	length of the upflow zone	1.5 km
$H(x)$	Heaviside function	
h	depth of the shallow recharge	100 m
I	source of material produced by the shallow recharge	
k	(temperature dependent) permeability	
k_i	(temperature dependent) permeability in the i^{th} limb	
k_0	initial permeability	$10^{-13} - 10^{-12} \text{ m}^2$
k_{res}	residual permeability	$10^{-2} k_0$
L	length of the horizontal limb of the deep recharge	$\sim 1 \text{ km}$
L_0	characteristic length of the deep horizontal limb	
l	length of the horizontal limb of the shallow recharge	1-10 m
Q_i	mass flux in the i^{th} limb	
q_d	heat source density per unit time and unit volume of the dike	
q_m	basal heat flux (heat uptake rate)	
q_w	lateral heat transfer density per unit time and unit volume	
r_i	hydrodynamic resistance per unit area in the i^{th} limb	
s	“curvilinear” spatial variable along the flow path (deep limb and upflow)	
t	time	
T	temperature in the upflow zone	
T_0	temperature at undisturbed ocean floor conditions	0°C
$T_{diffuse}$	temperature monitored at sites of diffuse venting	$5-30^\circ\text{C}$
T_h	temperature of recharge fluid at depth $z = h$	
T_H	temperature of recharge fluid at depth $z = H$ (bottom of recharge zone)	
T_j	temperature of the fluid from the shallow recharge at junction point	
T_m	melting temperature of basalt	1200°C
T_{rech}	far-field temperature in the recharge zone (for deep recharge)	$0-100^\circ\text{C}$
v	Darcian flow velocity (specific discharge)	
v_i	Darcian flow velocity (specific discharge) in the i^{th} limb	
v_0	characteristic Darcian flow velocity	
w	width of vent field (upflow zone)	100 m
x	coordinate along deep horizontal limb 3	
z	depth	
α_f	coefficient of thermal expansion of water	$10^{-3} / ^\circ\text{C}$
β_{rech}	thermal gradient in the recharge zone	
δ	thermal boundary layer thickness	a/v
η	(temperature dependent) dynamic viscosity of water	
ν	kinematic viscosity of water	η/ρ
ν_i	kinematic viscosity of water in the i^{th} limb	η/ρ
λ_r	coefficient of thermal conductivity of rock	$2.5 \text{ W}/(\text{m}^\circ\text{C})$
ρ_f	(temperature dependent) density of water	
ρ_r	rock density	$3 \times 10^3 \text{ kg/m}^3$
ρ_0	initial density of water at the ocean floor	10^3 kg/m^3

For order-of-magnitude analysis, we also assume that the viscosity of fluid is constant in each limb, with the viscosity characteristic of hot fluid in limbs 1, 2, and 3, and viscosity typical for cold fluid in limb 4. Temperature in limbs 1, 2, and 3 probably ranges from $\sim 100^\circ\text{C}$ to $\sim 400^\circ\text{C}$ while fluid in limb 4 is likely to be at temperature $T_h \sim 1 - 10^\circ\text{C}$. The diffuse flow can be at temperatures lower than tens of $^\circ\text{C}$, but only in a small (boundary) layer situated close to the seafloor.

Integrals in (4.2) can thus be estimated by

$$\left\{ \begin{array}{l} \int_0^h \rho_f (T_{rech}) dz = \rho_0 h \left(1 - \frac{1}{2} \alpha_f T_h \right), \quad \int_0^H \rho_f (T_{rech}) dz = \rho_0 H \left(1 - \frac{1}{2} \alpha_f T_H \right) \\ \int_0^h \rho_f (T_1) dz = \rho_0 h (1 - \alpha_f T_1), \quad \int_h^H \rho_f (T_2) dz = \rho_0 (H - h) (1 - \alpha_f T_2) \end{array} \right. \quad (4.4)$$

while hydrodynamic resistances scale as

$$r_1 = \frac{h \nu_1}{k_1 A_1}, \quad r_2 = \frac{(H - h) \nu_2}{k_2 A_2}, \quad r_3 = \frac{L \nu_3}{k_3 A_3}, \quad r_4 = \frac{l \nu_4}{k_4 A_4} \quad (4.5)$$

where $A_1 = A_2 = A_3 = bw$, $A_4 = bf$, b is the length of vent field along strike, and f is the height of the junction between upflow and shallow recharge limb (Figure 4.3).

In expressions (4.4), we used the dependence of fluid density on temperature given by

$$\rho_f = \rho_0 [1 - \alpha_f (T - T_0)] \quad (4.6)$$

where ρ_0 is the initial density of water at the ocean floor, α_f is the coefficient of thermal expansion of water, and $T_0 \approx 0^\circ\text{C}$ is the temperature at undisturbed ocean floor

conditions. The kinematic viscosity is defined as $\nu(T) = \eta(T)/\rho(T)$, where the dynamic viscosity η can be approximated by [Germanovich et al., 2000]

$$\eta(T) = \frac{C_1}{T + C_2} \quad (4.7)$$

with $C_1 = 0.032 \text{ Pa}\cdot\text{s}^\circ\text{C}$, and $C_2 = 15.4^\circ\text{C}$. Figure 4.4 shows the dependence of the kinematic viscosity on temperature plotted using expressions (4.6) and (4.7). Based on this figure, we chose $\nu_1 = \nu_2 = \nu_3 = 10^{-7} \text{ m}^2/\text{s}$, for the kinematic viscosity in “hot” limbs 1, 2 and 3, respectively, and an order of magnitude higher value, $\nu_4 = 10^{-6} \text{ m}^2/\text{s}$, in “cold” limb 4 (see also Appendix C).

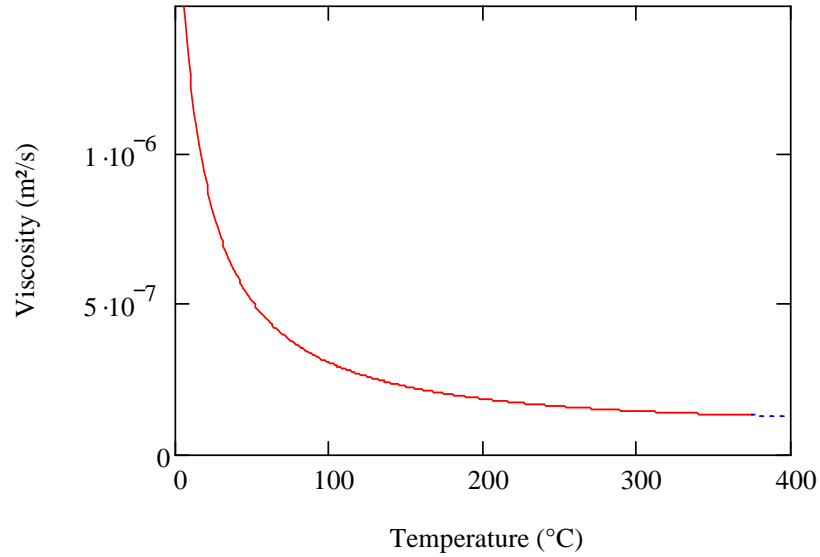


Figure 4.4. Variation of viscosity of water with temperature. The dashed line indicates the region where the seawater exhibit two-phase behavior.

In order to estimate T_2 , we need the temperature distribution $T(x)$ in the deep horizontal limb 3. This distribution can be obtained by considering the condition of

energy conservation [e.g., *Germanovich et al.*, 2000], in which the conduction term has been ignored

$$c_f Q_3 \frac{dT}{dx} = \lambda_r \frac{T - T_m}{d} b \quad (4.8)$$

where the boundary condition is $T(x) = T_H$ at $x = L$. Equation (4.8) simply states that heat transported by advection (left hand side) is equal to the heat that is conducted from the magma chamber at melting temperature T_m to the deep horizontal limb 3 through the thin rock layer of thickness d (Figure 4.3). The solution to this equation is

$$T(x) = T_m - (T_m - T_H) \exp\left(-\frac{L-x}{L_0}\right) \quad (4.9)$$

where $L_0 = (c_f Q_3 d) / (\lambda_r b)$ is a characteristic length and $Q_3 = Q_2$.

Substituting (4.4) into (4.2), and rearranging the terms yields

$$\begin{cases} Q_1 = \rho_0 g h \alpha_f \Delta T_2 \frac{\frac{r_4}{r_1} \left(\frac{\Delta T_1}{\Delta T_2} + \frac{H}{h} - 1 - \frac{\Delta T_{rech}}{\Delta T_2} \right) + \frac{r_2 + r_3}{r_1} \frac{\Delta T_1}{\Delta T_2}}{(r_1 + r_2 + r_3) \left(1 + \frac{r_4}{r_1} \right) - r_1} \\ Q_2 = \rho_0 g h \alpha_f \Delta T_2 \frac{\left(1 + \frac{r_4}{r_1} \right) \left(\frac{\Delta T_1}{\Delta T_2} + \frac{H}{h} - 1 - \frac{\Delta T_{rech}}{\Delta T_2} \right) - \frac{\Delta T_1}{\Delta T_2}}{(r_1 + r_2 + r_3) \left(1 + \frac{r_4}{r_1} \right) - r_1} \end{cases} \quad (4.10)$$

where $\Delta T_{rech} = (T_H - T_h)/2$, and $\Delta T_1 = T_1 - T_h/2$ and $\Delta T_2 = T_2 - T_H/2$ are the differences between average temperatures in the upflow limbs (respectively, 1 and 2) and the downflow zone.

The permeability of the extrusive layer is expected to be much higher than in the rest of the discharge zone, so that $k_1 \sim k_4 \gg k_2 \sim k_3$. Also, we consider a relatively shallow mixing zone (upper 100 m) based on *Bray's* [2001] geochemical analysis that suggests the residence time of the mixed, diffuse flow fluid to be in the order of a few months. This indicates that $h \sim 10^2$ m, which is significantly smaller than the typical depth $H \sim 10^3$ m of the upflow zone. Therefore,

$$\left\{ \begin{array}{l} \frac{H}{h} \gg 1 \\ \frac{k_3}{k_2} \sim 1, \quad \frac{k_1}{k_2} \gg 1 \\ \frac{v_3}{v_2} \sim 1, \quad \frac{v_1}{v_2} \sim 1, \quad \frac{v_2}{v_4} \ll 1 \end{array} \right. \quad (4.11)$$

We obtain from (4.5) and (4.11) that the hydrodynamic resistance of the extrusives in the upflow zone is small compared to the rest of the deep circulation limb ($r_1 \ll r_2 + r_3$). We further note that in (4.10), $\Delta T_{rech}/\Delta T_2 \leq 1$, which follows directly from $T_2 > T_H$. We also observe that for mid-ocean ridge conditions, $\Delta T_1/\Delta T_2 \sim 1$ (or $\Delta T_1/\Delta T_2 < 1$). This thus suggests that expressions (4.10) can be scaled as

$$\left\{ \begin{array}{l} Q_1 \sim Q_0 \frac{r_4 + (r_2 + r_3) \frac{h}{H}}{r_1 + r_4} \frac{\Delta T_1}{\Delta T_2}, \quad Q_2 \sim Q_0 \\ Q_0 = \frac{\rho_0 g H \alpha_f \Delta T_2}{r_1 + r_2 + r_3} \sim \frac{\rho_0 g H \alpha_f \Delta T_2}{r_2 + r_3} \end{array} \right. \quad (4.12)$$

where Q_0 is the heat flux in the one-loop system with no mixing zone [*Lowell and Germanovich*, 2004]. The same expression for Q_0 is directly obtained either from Q_1 or Q_2 in (4.10) for $r_4 \rightarrow \infty$ and $T_1 = T_2$.

It is interesting to note that resistance r_4 of the horizontal shallow limb 4 does not appear in the expression for Q_2 in (4.12). If conditions (4.11) are satisfied, shallow recharge does not have a strong impact on the flow within the deep horizontal limb 3 and the lower part of the upflow zone (limb 2). In other words, because the resistance of the extrusive layer is low, the presence of the extrusives does not affect the deep hydrothermal recharge, Q_2 . Resistance r_4 of the shallow recharge though appears in expression (4.12) for Q_1 , representing the influence of the cold recharge of fluid within the extrusives. In general, r_4 is not well constrained since beyond conceptual modeling [e.g., *Lowell and Germanoivch*, 1994], little is known about the actual structure of shallow circulation. Yet, in the next section we argue that analyzing the March 1995 earthquake swarm at 9°50' N, EPR allows us to conclude that r_4 is likely to be rather low (comparable to r_1). Otherwise, matching modeling results to post-seismic hydrothermal observations becomes quite difficult.

In the case when $L/L_0 \ll 1$, temperature T_2 in the upflow zone scales as

$$T_2 = T_H + (T_m - T_H) \frac{\lambda_r b L}{c_f Q_2 d} \quad (4.13)$$

where Q_2 can be replaced by the expression obtained in (4.12). We further assume that $T_H/2$ can be neglected compared to ΔT_2 (as discussed below). Then, considering that $\Delta T_2 = T_2 - T_H/2 \approx T_2$, and ignoring T_H in comparison with T_m , we obtain by inserting (4.12) for Q_2 in (4.13):

$$T_2 \sim T_0 = \left(\frac{\lambda_r b T_m L}{c_f d} \frac{r_1 + r_2 + r_3}{\rho_0 g H \alpha_f} \right)^{\frac{1}{2}} \sim \left(\frac{\lambda_r v_2 T_m L}{\rho_0 g \alpha_f c_f k_2 w d} \frac{H + L}{H} \right)^{1/2} \quad (4.14)$$

Here T_0 is the temperature in the one-loop system with no-mixing and, similarly to Q_0 in (4.12), can be obtained in the limit of $r_4 \rightarrow \infty$ (and $T_H = 0$). Finally, substituting (4.14) into expression (4.12) for Q_2 gives

$$Q_2 \sim b \left(\frac{T_m \rho_0 g k_2 w \alpha_f \lambda_r L}{\nu_2 c_f d} \frac{H}{H+L} \right)^{1/2} \quad (4.15)$$

We see, therefore, that both Q_2 and T_2 are unaffected by the presence of the extrusive layer. As mentioned above, this is expected since its hydrodynamic resistance is rather small (condition $r_1 \ll r_2 + r_3$). The absence of the temperature, T_H , of the downflow zone in expressions (4.15) is an unimportant simplification of these expressions and results from assumption $T_H/2 \ll \Delta T_2$. While the deep recharge is insignificantly affected by the shallow circulation, it does affect the latter as discussed below. Note that the limit $r_4 \rightarrow \infty$ above does not mean a large resistance of the shallow recharge, but only that it is not affecting deep circulation.

Temperature T_1 in limb 1 of the upflow zone can be obtained from the condition of energy conservation in the junction (mixing) zone, which gives $Q_1 T_1 = Q_2 T_2 + Q_4 T_4$. Assuming that the specific heat, c_f , is independent of temperature, and taking into account mass balance in the junction zone (i.e., the first expression in (4.2)), we have

$$T_1 - T_h = \frac{Q_2}{Q_1} (T_2 - T_h) \quad (4.16)$$

Given (4.12), this expression represents a quadratic equation with respect to T_1 . If the shallow recharge temperature, T_h , is small compared to T_1 (as usually expected in the

mixing zone), and, therefore, compared to T_2 (since $T_2 > T_1$), the solution of (4.16) can be written as

$$T_1 = 2T_0 \frac{1 + \frac{r_1}{r_4}}{1 + \sqrt{1 + 4 \frac{h}{H} \frac{r_2 + r_3}{r_4} \left(1 + \frac{r_1}{r_4}\right)}} \quad (4.17)$$

where T_0 is given by (4.14). The mass flux in the mixed zone (limb 1) is further determined by inserting (4.17) in the expression for Q_1 in (4.12).

With our parameters (Table 4.1) and for $b = 1$ km and $d = 10$ m, expressions (4.14) and (4.15) yield $T_2 \sim 350^\circ\text{C}$, and $Q_2 \sim 200$ kg/s, respectively. These values further lead to $L/L_0 \sim 10^{-1}$ in (4.9), which shows that considering linear distribution of the temperature (4.13) in the deep horizontal limb is appropriate for our parameters. In the case when parameters do not allow this approximation, one needs to substitute expression (4.12) for Q_2 into (4.8) and solve the obtained transcendental equation. This equation has a unique solution for $T_2 > 0$ for any combination of parameters. Also, in our case, $T_H \approx 100^\circ\text{C}$, and it seems possible to ignore $T_H/2 \approx 50^\circ\text{C}$ in comparison with $\Delta T_2 \approx 300^\circ\text{C}$ as we have done above. If, however, this approach is not sufficiently accurate, then a similar consideration would simply result in expressions for T_2 and Q_2 more cumbersome than (4.14) and (4.15), which would explicitly contain the recharge temperature T_H .

As mentioned above, it is difficult to constrain the resistance of the shallow recharge on the basis of scale analysis and, therefore, we simply consider an extreme case of small r_4 in (4.16). If $r_4 = 0$, so that the shallow recharge provides no resistance to the

fluid flow, (4.16) reduces to $T_1 = T_0[(H/h)r_1/(r_2 + r_3)]^{1/2}$, which for our parameters (Table 4.1) results in $T_1 \sim 90^\circ\text{C}$ and $Q_1 \sim 450 \text{ kg/s}$. If r_4 is small but not zero (i.e., as discussed above, comparable to r_1), then using directly (4.16) gives (for $r_4 = r_1$) quantities $T_1 \sim 110^\circ\text{C}$ and $Q_1 \sim 600 \text{ kg/s}$ of the same order of magnitude.

The velocities that corresponds to Q_1 and Q_2 , respectively, are given by $v_1 = Q_1/(\rho_0 A_1)$ and $v_2 = Q_2/(\rho_0 A_2)$. In particular, with our parameters, we obtain $v_2 \sim 10^{-6} \text{ m/s} \sim 10 \text{ m/year}$, which corresponds to a laminar regime (Appendix F). Recalling that heat conduction is important in the boundary layer near the seafloor (at $z = 0$) and the junction zone (near $z = h$), the thicknesses of the boundary layers near the seafloor (δ_1) and at the junction zone (δ_2) scale as $\delta_1 \sim a/v_1$ and $\delta_2 \sim a/v_2$, where $a = \lambda_r/(c_f \rho_f) \sim \lambda_r/(c_f \rho_0)$. The time scales associated with fluid flow through these boundary layers are $\tau_1 \sim \delta_1/v_1$ and $\tau_2 \sim \delta_2/v_2$. The second boundary layer is the one that regulates temperature variations at sites of focused venting, with black smoker being essentially a temperature probe of this boundary layer, as schematically shown in Figure 4.3. For our chosen parameters, $\delta_2 \sim 1 \text{ m}$. Using expression (4.12) for Q_2 , one obtains

$$\tau_2 \sim a \left[\frac{v_2(H+L)}{g\alpha_f k_2 \Delta T_2 H} \right]^2 \quad (4.18)$$

which yields $\tau_2 \sim 10^6 \text{ s} \sim 10 \text{ days}$. In our model, the time scale that controls the delay between the onset of seismicity and temperature variations at the seafloor is τ_2 .

There was a 4 day time lag between the onset of seismicity and temperature variations at the seafloor following the March 1995 event at the EPR. This time lag is of the same order of magnitude as the time scale, $\tau_2 \sim 10 \text{ days}$, for fluid flow through the

boundary layer situated at the junction (mixing) zone. Our consideration again shows that the perturbation due to the seismic event only needs to affect the boundary layer instead of propagating along the entire upflow zone, which would require orders of magnitude higher permeability and velocities. Because the orders of magnitude presented here are typical for fast and intermediate-spreading mid-ocean ridges, similar time delay is expected, should a similar perturbation occur in other places. In particular, it is interesting to note that the time delay between the onset of seismicity and the temperature variations at the seafloor was indeed 11 days at the sites of diffuse venting on the Endeavour Segment (Juan de Fuca Ridge) following the June 1999 seismic swarm.

4.4 Matching transient temperature records

The analysis presented above suggests the order of magnitude of the time delay between the onset of seismicity and temperature variations at the seafloor. There are two key elements in the proposed scenario: (1) the existence of the shallow circulation and (2) the diking event as a mechanism of the March 1995 earthquake swarm. In this scenario, dike emplacement provides the necessary heat and permeability variations to alter the hydrothermal flow in the upflow zone. The shallow circulation loop provides the boundary layer that allows the quick visualization of high temperature flow variations (associated with black smokers at the seafloor) in response to changes occurring at depth.

An example of steady-state temperature distribution in the boundary layers (prior to dike injection) is given in Figure 4.5. To plot this figure and for the subsequent transient modeling, we followed *Ramondenc et al.* [2008] and modified the formulation of *Germanovich et al.* [2000] to take into account the effect of the shallow recharge in the

extrusives and the heat transfer from the magma body at the base of the hydrothermal system (Figure 4.3). The mass balance is given by (4.2) while the conservation of energy along the flow path can be written as

$$c_r \rho_r w \frac{\partial T}{\partial t} - c_f \rho_f v w \frac{\partial T}{\partial z} = \lambda_r w \frac{\partial^2 T}{\partial z^2} - 2(q_w + q_d) + 2c_f(T_j - T)I + q_m \quad (4.19)$$

where q_m represents the basal heat transfer from the magma body to the base of the hydrothermal system (heat uptake rate) and I describes the source of fluid produced by the shallow recharge (i.e., the input from the shallow recharge along an interval in the extrusives within the upflow zone). The quantity $2I(T_j - T)$ represents the system cooling, while T_j denotes the temperature of the fluid where it leaves the shallow recharge and enters the discharge zone. In equation (4.19), q_w represents the lateral heat transfer through the walls of the upflow zone, and q_d the heat from the dike freezing and cooling (both per unit time and unit volume of the dike). Their asymptotic approximations are discussed by *Germanovich et al.* [2000]. We used the relatively well constrained material properties of rock and seawater given in Table 4.1. We chose an implicit numerical scheme that employs a finite difference discretization with a zeroth-order approximation with respect to time. At each time step, the mass fluxes (and velocities) were considered to be constant and then recalculated, as well as the new profiles of density, permeability and viscosity, in each limb (Figure 4.3), to be used for the next step.

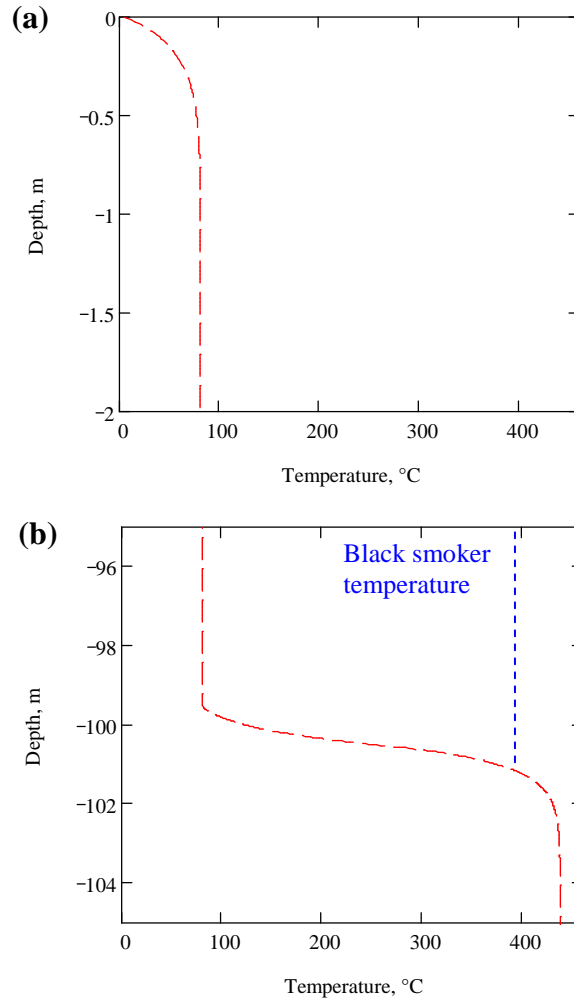


Figure 4.5. Typical steady-state temperature profiles along the discharge zone. The top and bottom profiles correspond to the boundary layers beneath the seafloor (a) and in the zone within the extrusives where mixing with the shallow recharge occurs (b), respectively. Note that between the depths 2 m and 95 m, the temperature remains practically constant. The profile is also nearly isothermal between the depths 105 m and 1500 m. In this example, the permeability of the system is $k = 10^{-12} \text{ m}^2$ in the mixing zone and $k = 10^{-13} \text{ m}^2$ in the rest of the discharge zone, the thickness of the thermal conductive layer between the magma chamber and the hydrothermal system is $d = 7.5 \text{ m}$, and $f = 5 \text{ m}$ (same values as for Figure 4.6). These values, as well as a reduced resistance, $r_3 \sim r_2/10$, in the deep horizontal limb, and $r_1 \sim r_4$ were needed to obtain the best fit of the temperature perturbation at Bio9 after the March 1995 seismic swarm (Figure 4.6). We chose a relatively shallow mixing zone (upper 100 m) based on the geochemical analysis of *Bray* [2001] that suggests the residence time of the mixed, diffuse flow fluid to be in the order of a few months. The bottom boundary condition of the entire flow path corresponds to the temperature at the bottom of the deep recharge, whose value is not very well constrained. We used 100°C and considered a linear gradient in the recharge zone, starting from 0°C at the seafloor.

For a detailed analysis of the available transient temperature data [Fornari *et al.*, 1998], numerical calculations based on equations (4.2) and (4.19) are required. It turns out, that the results of numerical analysis are quite sensitive to the choice of some parameters, particularly related to the shallow circulation zone. Therefore, matching these parameters with the measured data allowed us to somewhat constrain the model. Scale considerations presented in the previous section are less sensitive, although, fortunately, this did not affect the main results related to the deep circulation and the time delay (4.18) between the dike emplacement and hydrothermal response on the ocean floor.

To model the March 1995 EPR event (Figure 4.1a), an emplacement of a 600-m dike was considered to match the hypocentral pattern observed above the magma chamber in Figure 4.1b (as sketched in Figure 4.3). The dike thickness was chosen to be 1 m, as constrained by our mechanical computations (Figure 4.1b). Our numerical simulations showed that the best fit for the Bio9 temperature records required a thin thermal conductive layer at the top of the magma chamber ($d = 7.5$ m), high steady-state mass fluxes ($Q = 500$ kg/s discharge for a vent field that has a size of 1 km along the axis), and a modest permeability increase (by 50%) in the part of the upflow zone where the dike was emplaced (Figure 4.3). Also, to obtain the best fit, the resistance of the shallow horizontal limb (limb 4) needed to be of the order of that of shallow recharge ($r_1 \sim r_4$).

Figure 4.6 shows the temperature as a function of time at the point that models the black smoker monitored at Bio9 prior and during the event. The calculated response is in good agreement with the observed temperature after the earthquake swarm, matching the

variations that have been observed in the temperature time series over the entire first year of monitoring after the March 1995 event. It is interesting that the fit is further improved and becomes nearly ideal after translating the record post November 1995 by 3°C (Figure 4.6). At that time, the temperature probe was replaced. Accordingly, the observed temperature drop can be explained by a calibration difference and/or by the reported collapse of a part of the Bio9 chimney during the replacement [Fornari *et al.*, 1998].

To address the longer-term (> 1 year) temperature increase, the dike scenario needs to be complemented by some other factors. A gradual decrease in permeability either deep in the system or at the base of the mixing zone would lead to a gradual increase in vent temperature. Our calculations take into account the evolution of permeability with respect to thermo-elastic effects [Germanovich and Lowell, 1992], but do not consider mineral precipitation. In the junction zone, the temperature fluctuations that result from mixing may lead to clogging in connection with precipitation of anhydrite [Lowell *et al.*, 2003] or other minerals, such as quartz or silica. This would reduce the input of cold shallow recharge, thus leading to a slow increase of temperature at black smokers over several years. Mineral precipitation, e.g., quartz, may also occur deep in the crust and eventually clog the permeability that was enhanced as a result of the suggested dike emplacement [Lowell *et al.*, 1993].

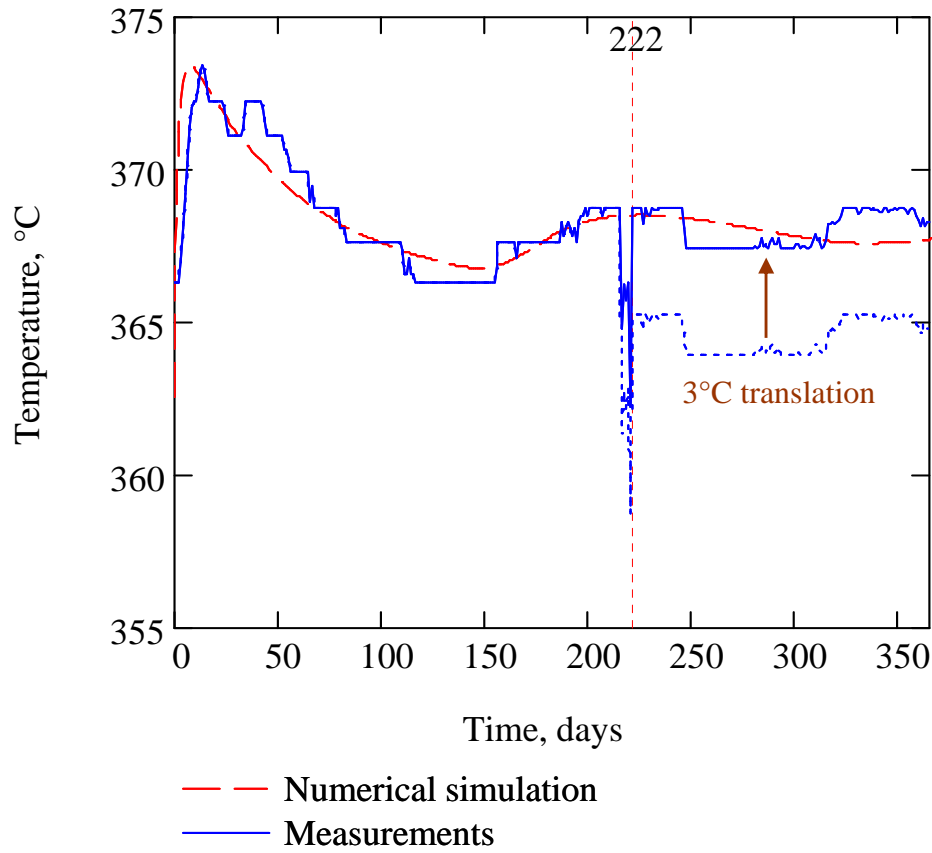


Figure 4.6. Comparison of the calculated temperature response of the black smoker to a dike emplacement with the monitored response at Bio9 following the March 1995 EPR event. The blue dots after day 222 (which corresponds to the replacement of the temperature probe) represent the unchanged monitored response, while the solid blue line corresponds to the record translated by 3°C. Only a modest permeability increase in the vicinity of the dike leads to temperature variations at the seafloor. The shown best fit corresponds to a 50% increase with respect to the original permeability $k = 10^{-13} \text{ m}^2$ (the detailed parametric study of the response of hydrothermal systems to seismic impact is reported in the work by *Ramondenc et al.* [2008]). One can note that the initial peak of 4 days has been underestimated. This issue could have been solved by introducing a larger number of parameters and considering the evolution of the dimensions of the shallow recharge (for instance, as precipitation occurs over time, f is likely to be modified). However, since we are interested in the evolution up to a year, our match was done at the expense of smaller time frames (at the order of days).

4.5 Discussion

In the model presented in this work, the length of the deep horizontal limb, L , and the permeability of limb 2 of the upflow zone, k_2 , are not well constrained. Essentially, these are fitting parameters required to obtain a match between the theoretical data and observations (Figure 4.6). The thickness of the layer situated between the top of the magma source and the base of the hydrothermal layer, d , is relatively well constrained through the scaling of the overall heat exchange at mid-ocean ridges [Lowell and Germanovich, 2004]. The width of the dike, w_d , is also relatively well constrained through numerical computations (e.g., FRANC2D simulations presented in this work). Finally, even though the along-strike length, b , can be chosen rather arbitrary, our results are independent of its value, except for the total mass fluxes Q , which are expressed with respect to a specific area. This was expected, however, because our model is one-dimensional, and along the strike of the mid-ocean ridge, all the results can be represented per unit of the ridge length.

When a dike is suddenly emplaced in fluid-saturated country rock, fracturing of the rock is likely to occur ahead of the dike tip, due to the tensile stresses induced by the latter [e.g., Pollard, 1987] or due to shear fracture mechanism [Warpinski, 2003; Rubin and Gillard, 1998]. Furthermore, rapid heating will tend to pressurize the adjacent fluid and drive flow away from the dike wall [Delaney, 1982]. In turn, pressurization of the fluid may lead to fracturing of the adjacent rock [e.g., Germanovich and Lowell, 1995]. Local boiling and phase separation may also occur. For seafloor systems with high permeability and ambient pressure of ~ 30 MPa, the pressure increment is negligible [Delaney, 1982], and so is the corresponding increase of the sizes of pre-existing

fractures [Germanovich and Lowell, 1995]. If an increase of permeability results from fluid pressurization [Takahashi et al., 2003], it is incorporated into the permeability increase that we assume results from dike emplacement. The width of the two-phase zone is only ~ 10 cm [Lewis and Lowell, 2004], and hence we neglect it. As noted by Wilcock [2004] and Lowell and Germanovich [1995], heating adjacent to the dike may lead to large pressure increases but only within a narrow region. Therefore, dike emplacement is likely to generate a region of high permeability in a substantial part of the upflow zone [Delaney et al., 1986; Germanovich et al., 2000], e.g., over 600 m out of 1.5 km in the case under consideration (Figure 4.1 and Figure 4.3). This is why diking affects the fluid flow in the entire upflow region, so that the boundary layers (Figure 4.5) can be altered on the order of days (Figure 4.6).

In principle, the slip of a vertical fault could also provide permeability enhancement. However, such a slip, its geometry in connection with the detected microearthquake swarm (Figure 4.1a), and its relation to the AMC long-term dynamics are not mechanically clear yet. Bohnenstiehl and Carbotte's [2001] boundary element model showed that faults nucleating above shallow magma chambers tend to be rotated due to the change in rheology and principal stresses at this place, thus precluding the possibility of a vertical fault. In addition, the focal mechanism of detected microearthquakes, that is, the presence of normal faulting with slip dipping at $60\text{-}70^\circ$ [Sohn et al., 1999], is more compatible with diking [Rubin and Gillard, 1998] than with vertical fault slip. The absence of hypocenters directly above the magma chamber (Figure 4.1a) can be explained [Sohn et al., 1999] by hotter material in this zone being less brittle than farther up.

The model presented here tests the hypothesis [Fornari *et al.*, 1998] that the temperature anomaly measured at Bio9 four days following the swarm was caused by a cracking front [Lister, 1983] penetrating into hot crustal rocks beneath the vent. Such a cracking event corresponds decreasing the distance, d , that separates the magma chamber and the base of the hydrothermal system [Lister, 1974, 1983]. The result is increased heat transfer, q_m , to the fluid in the deep horizontal limb (Figure 4.3). Our simulations show that the perturbation would take years to be observed at the surface, because the conductive change of q_m at the base of the system very slowly alters the boundary layers shown in Figure 4.5. Therefore, our results indicate that a deep cracking event alone is not likely to cause a perturbation in the vent temperature only several days later. Furthermore, it was suggested that the timing of the seismic swarm four days prior to the temperature anomaly provides a direct measurement of the residence time of fluid flow in the upflow limb of the hydrothermal system [Fornari *et al.*, 1998; Sohn *et al.*, 1998; Sohn *et al.*, 1999]. Understanding that this suggestion is not necessarily correct is important for the proper interpretation of geochemical data in general, and for the 9°50' N EPR site in particular.

At mid-ocean ridges, hydrothermal activity may be localized by diking events due to permeability enhancement near the dike margins [Delaney *et al.*, 1986; Germanovich *et al.*, 2000]. For example, the hydrothermal sites on the Endeavour segment, Juan de Fuca Ridge, are located near the west margin of the seismically imaged magma lens [Bohnenstiehl *et al.*, 2004; Van Ark *et al.*, 2007], which suggests that the venting activity at this site may also be localized by diking triggered by lens pressurization (Figure 4.7). Since a part of the 2006 9°50' N EPR eruption may have occurred in the form of a dike

propagating sub-vertically from the east tip of the magma lens (similar to Figure 4.1b, but reaching the seafloor 600-700 m east of the spreading axis [*Fornari et al.*, 2006; *Soule et al.*, 2006]), we expect that fresh hydrothermal activity has been initiated off-axis in response to this event. This region should perhaps be further explored.

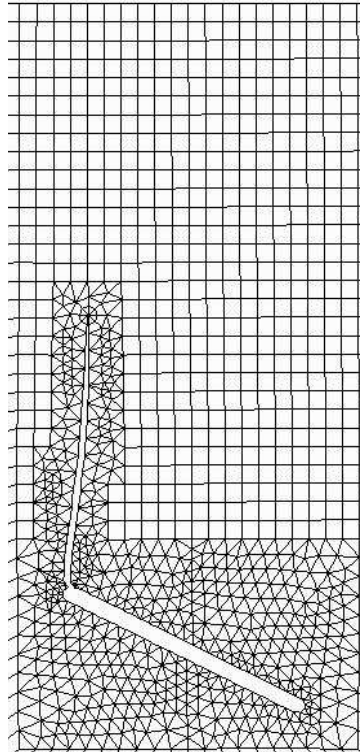


Figure 4.7. Finite element simulation of dike propagation from magma chamber. We used a pressurized inclined lens, between 2.1 and 2.5-km deep, 800-m wide, and 50-m thick magma lens, based on *Van Ark et al.* [2007]. Other conditions are the same as for the simulations prested in Figure 4.1b and 4.2b.

4.6 Conclusion

The response of mid-ocean ridge hydrothermal systems to seismic and magmatic activity may provide a means of using seafloor observations to assess processes occurring at depth. This subject is a matter of vigorous scientific debate. Conceivably, the correct interpretation of the March 1995 seismic activity and the subsequent hydrothermal

response is of critical importance for our understanding of the entire 9°N EPR segment. A deep thermal cracking event [*Fornari et al.*, 1998; *Sinha and Evans*, 2004; *Sohn et al.*, 1998; *Sohn et al.*, 1999] is not likely to cause the observed rapid increase in the vent temperature. The alternative diking scenario presented here explains seemingly different observations from the unified stand point of fracture mechanics. In particular, the March 1995 hypocentral pattern is consistent with both the thin, lens-like shape of the mid-oceanic ridge magma chamber and with the seismic pattern, displaced to its west margin (Figure 4.1a). It is also consistent with the variability of geochemical data and with the residence time of fluid within the crust in the order of years. The diking hypothesis yields quantitative results that are in excellent agreement (Figure 4.6) with the temperature observations at the Bio9 venting site following the March 1995 seismic event on time scales ranging from days to a year. Additionally, the mechanics of dike emplacement suggests that the March 1995 seismic swarm is indicative of the inflation (pressurization) of the 9°50' N EPR AMC between two major eruptions, in 1991 and 2006. Finally, because the orders of magnitude presented here are typical for fast and intermediate-spreading mid-ocean ridges, similar time delay is expected, should a similar perturbation occur in other places.

4.7 Acknowledgments

This work was supported in part by NSF Grants OCE-0221974 and OCE-0527208 to R.P.L and L.N.G.

4.8 References

- Advani, S. H., T. S. Lee, R. H. Dean, C. K. Pak, and J. M. Avasthi (1997), Consequences of fluid lag in three-dimensional hydraulic fractures, *Int. J. for Num. and Anal. Meth. in Geomechanics*, 21, 229-240.
- Bohnenstiehl, D. R., R. P. Dziak, M. Tolstoy, C. G. Fox, and M. Fowler (2004), Temporal and spatial history of the 1999-2000 Endeavour Segment seismic series, Juan de Fuca Ridge, *Geochem. Geophys. Geosyst.*, 5, Q09003, doi:10.1029/2004GC000735.
- Bray, A. M. (2001), The geochemistry of boron and lithium in mid-ocean ridge hydrothermal vent fluids, Ph.D. thesis, 125 pp, University of New Hampshire, Durham.
- Broberg, K. B. (1999), *Cracks and Fracture*, 752 pp., Academic Press, London.
- Crawford, W. C., S. C. Webb, and J. A. Hildebrand (1999), Constraints on melt in the lower crust and Moho at the East Pacific Rise, 9°48' N, using seafloor compliance measurements, *J. Geophys. Res.*, 104(B2), 2923-2939.
- Delaney, P. T., and D. D. Pollard (1981), Deformation of host rocks and flow of magma during growth of minette dikes and breccia-bearing intrusions near Ship Rock, New Mexico, *U.S. Geol. Surv. Prof. Paper*, 1202.
- Delaney, P. T., D. D. Pollard, J. I. Ziony, and E. H. Mckee (1986), Field relations between dikes and joints: Emplacement processes and paleostress analysis, *J. Geophys. Res.*, 91(B5), 4920-4938.
- Dyskin, A. V., and L. N. Germanovich (1993), A model of crack-growth in microcracked rock, *Int. J. Rock. Mech. & Mining Sci.*, 30, 813-820.
- Fisher, A. T. (1998), Permeability within basaltic oceanic crust, *Rev. Geophys.*, 36(2), 143-182.
- Fornari, D. J., T. Shank, K. L. Von Damm, T. K. P. Gregg, M. Lilley, G. Levai, A. Bray, R. M. Haymon, M. R. Perfit, and R. Lutz (1998), Time-series temperature measurements at high-temperature hydrothermal vents, East Pacific Rise 9°49'-51'N: evidence for monitoring a crustal cracking event, *Earth Planet. Sci. Lett.*, 160, 419-431.

Fornari, D. J., A. Soule, M. R. Perfit, K. H. Rubin, T. M. Shank, J. P. Cowen, K. L. Von Damm, and M. Tivey (2006), Variability in eruptive vents and lava morphology of the 2005-2006 EPR eruptions near 9°50' N, *Eos Trans. AGU*, 87(52), Abstract V23B-0603.

Germanovich, L. N., and R. P. Lowell (1992), Percolation Theory, Thermoelasticity, and Discrete Hydrothermal Venting in the Earth's Crust, *Science*, 255, 1564-1567.

Germanovich, L. N., and R. P. Lowell (1995), The mechanism of phreatic eruptions, *J. Geophys. Res.*, 100(B5), 8417-8434.

Germanovich, L. N., R. P. Lowell, and D. K. Astakhov (2000), Stress-dependent permeability and the formation of seafloor event plumes, *J. Geophys. Res.*, 105(B4), 8341-8354.

Germanovich, L. N., R. P. Lowell, and D. K. Astakhov (2001), Temperature-dependent permeability and bifurcations in hydrothermal flow, *J. Geophys. Res.*, 106(B1), 473-495.

Haymon, R. M., et al. (1993), Volcanic eruption of the mid-ocean ridge along the East Pacific Rise crest at 9°45-52' N: Direct submersible observations of seafloor phenomena associated with an eruption event in April, 1991, *Earth Planet. Sci. Lett.*, 119, 85-101.

Kadko, D., R. Koski, M. Tatsumoto, and R. Bouse (1985), An estimate of hydrothermal fluid residence times and vent chimney growth-rates based on Pb²¹⁰/Pb ratios and mineralogic studies of sulfides dredged from the Juan de Fuca Ridge, *Earth Planet. Sci. Lett.*, 76, 35-44.

Kent, G. M., A. J. Harding, and J. A. Orcutt (1993), Distribution of magma beneath the East Pacific Rise between the Clipperton transform and the 9°17'N deval from forward modeling of common depth point data, *J. Geophys. Res.*, 98(B8), 13,945-13,969.

Lewis, K. C., and R. P. Lowell (2004), Mathematical modeling of phase separation of seawater near an igneous dike, *Geofluids*, 4, 197-209.

Lilley, M. D., J. E. Lupton, and E. A. Olson (2002), Using CO₂ and He in vent fluids to constrain along axis magma dimension at 9°N, EPR, *Eos Trans. AGU*, 83(47), Abstract F1386.

Lister, C. R. B. (1974), On the Penetration of Water into Hot Rock, *Geophys. J. R. Astron. Soc.*, 39, 465-509.

Lister, C. R. B. (1983), The Basic Physics of Water Penetration Into Hot Rock, in *Hydrothermal Processes at Seafloor Spreading Centers*, edited by P. A. Rona, et al., pp. 141-168, Plenum Press, New York and London.

Lowell, R. P., and L. N. Germanovich (2004), Hydrothermal Processes at Mid-Ocean Ridges: Results From Scale Analysis and Single-Pass Models, in *Mid-Ocean Ridges: Hydrothermal Interactions Between the Lithosphere and Oceans*, *Geophys. Monogr. Ser.*, vol. 148, edited by C. R. German, et al., pp. 219-244, AGU, Washington, DC.

Lowell, R. P., S. R. Gosnell, and Y. Yang (2007), Numerical simulations of single-pass hydrothermal convection at mid-ocean ridges: Effects of the extrusive layer and temperature dependent permeability, *Geochem. Geophys. Geosystems*, in press.

Lowell, R. P., P. Van Cappellen, and L. N. Germanovich (1993), Silica Precipitation in Fractures and the Evolution of Permeability in Hydrothermal Upflow Zones, *Science*, 260, 192-194.

Lowell, R. P., Y. Yao, and L. N. Germanovich (2003), Anhydrite precipitation and the relationship between focused and diffuse flow in seafloor hydrothermal systems, *J. Geophys. Res.*, 108(B9), 2424, doi:10.1029/2002JB002371.

Papanastasiou, P. (1999), The effective fracture toughness in hydraulic fracturing, *Int. J. of Fract.*, 96, 127-147.

Pascoe, A. R., and J. R. Cann (1995), Modeling diffuse hydrothermal flow in black smoker vent fields, in *Hydrothermal Vents and Processes*, *Geological Society Special Publication*, vol. 87, edited by L. M. Parson, et al., pp. 159-173, The Geological Society, London, UK.

Pollard, D. D. (1987), Elementary fracture mechanics applied to the structural interpretation of dikes, in *Mafic Dyke Swarms*, edited by H. C. Halls and W. F. Fahrig, pp. 5-24.

Ramondenc, P., L. N. Germanovich, and R. P. Lowell (2006a), Effect of magma degassing on diking processes at mid-ocean ridges, *Eos Trans. AGU*, 87(52), Abstract B31B-1103.

Ramondenc, P., L. N. Germanovich, and R. P. Lowell (2008), Modeling hydrothermal response to earthquakes at oceanic spreading centers, in *Modeling Hydrothermal*

Processes at Oceanic Spreading Centers: Magma to Microbe, *Geophys. Monogr. Ser.*, edited by R. P. Lowell, et al., in review.

Ramondenc, P., L. N. Germanovich, K. L. Von Damm, and R. P. Lowell (2006b), The first measurements of hydrothermal heat output at 9°50'N, East Pacific Rise, *Earth Planet. Sci. Lett.*, *245*, 487-497, doi:10.1016/j.epsl.2006.03.023.

Rice, J. R. (1968), Mathematical Analysis in the Mechanics of Fracture, in *Fracture: An Advanced Treatise, Mathematical Fundamentals*, vol. 2, edited by H. Liebowitz, pp. 191-311, Academic Press, N.Y.

Rubin, A. M. (1993), Tensile fracture of rock at high confining pressure: Implications for dike propagation, *J. Geophys. Res.*, *98*(B9), 15,919-15,935.

Rubin, A. M. (1995), Propagation of magma-filled cracks, *Annu. Rev. Earth Planet. Sci.*, *23*, 287-336.

Rubin, A. M., and D. Gillard (1998), Dike-induced earthquakes: Theoretical considerations, *J. Geophys. Res.*, *103*(B5), 10,017-10,030.

Shlyapobersky, J. (1985), Energy Analysis of hydraulic fracturing, In: *Proceedings of the 26th US Symposium on Rock Mechanics*, Balkema, Rotterdam, pp. 539-546.

Sim, Y. (2004), Mechanics of Complex Hydraulic Fractures in the Earth's Crust, Ph.D. thesis, 324 pp, Georgia Institute of Technology, Atlanta.

Sim, Y., L. N. Germanovich, R. P. Lowell, and P. Ramondenc (2004), Diking, magma lenses, and location of hydrothermal sites at mid-ocean ridges, *Eos Trans. AGU*, *85*(47), Abstract B13A-0206.

Sinha, M. C., and R. L. Evans (2004), Geophysical Constraints Upon the Thermal Regime of the Ocean Crust, in *Mid-Ocean Ridges: Hydrothermal Interactions Between the Lithosphere and Oceans*, *Geophys. Monogr. Ser.*, vol. 148, edited by C. R. German, et al., pp. 19-62, AGU, Washington, DC.

Sohn, R. A., D. J. Fornari, K. L. Von Damm, J. A. Hildebrand, and S. C. Webb (1998), Seismic and hydrothermal evidence for a cracking event on the East Pacific Rise crest at 9°50' N, *Nature*, *396*, 159-161.

Sohn, R. A., J. A. Hildebrand, and S. C. Webb (1999), A microearthquake survey of the high-temperature vent fields on the volcanically active East Pacific Rise (9°50'N), *J. Geophys. Res.*, *104*(B11), 25,367-25,377.

Soule, S., et al. (2006), Extent and dynamics of the 2005-06 volcanic eruptions of the East Pacific Rise, 9°46'-56' N, *Eos Trans. AGU*, *87*(52), Abstract V23B-0601.

Takahashi, T., K. Tanifuji, C. Stafford, and T. Hashida (2003), Permeability enhancement by microfracturing in granite under supercritical water conditions, *JSME Int. J. Ser. A*, *46*, 24-29.

Tolstoy, M., F. Waldhauser, D. R. Bohnenstiehl, R. T. Weekly, and W.-Y Kim (2008), Seismic identification of along-axis hydrothermal flow on the East Pacific Rise, *Nature*, doi:10.1038, in press.

Tolstoy, M., et al. (2006), A Sea-Floor Spreading Event Captured by Seismometers, *Science*, *314*, 1920-1922, doi:10.1126/science.1133950.

Van Ark, E. M., R. S. Detrick, J. P. Canales, S. M. Carbotte, A. J. Harding, G. M. Kent, M. R. Nedimovic, W. S. D. Wilcock, J. B. Diebold, and J. M. Babcock (2007), Seismic structure of the Endeavour Segment, Juan de Fuca Ridge: Correlations with seismicity and hydrothermal activity, *J. Geophys. Res.*, *112*, B02401, doi:10.1029/2005JB004210.

Vera, E. E., J. C. Mutter, P. Buhl, J. A. Orcutt, A. J. Harding, M. E. Kappus, R. S. Detrick, and T. M. Brocher (1990), The Structure of 0- to 0.2-m.y.-Old Oceanic Crust at 9°N on the East Pacific Rise From Expanded Spread Profiles, *J. Geophys. Res.*, *95*(B10), 15,529-15,556.

Von Damm, K. L. (2004), Evolution of the Hydrothermal System at East Pacific Rise 9°50'N: Geochemical Evidence for Changes in the Upper Oceanic Crust, in *Mid-Ocean Ridges: Hydrothermal Interactions Between the Lithosphere and Oceans*, *Geophys. Monogr. Ser.*, vol. 148, edited by C. R. German, et al., pp. 285-304, AGU, Washington, DC.

Von Damm, K. L., and M. D. Lilley (2004), Diffuse Flow Hydrothermal Fluids from 9°50' N East Pacific Rise: Origin, Evolution and Biogeochemical Controls, in *The Subseafloor Biosphere at Mid-Ocean Ridges*, *Geophys. Monogr. Ser.*, vol. 144, edited by W. S. D. Wilcock, et al., pp. 245-268, AGU, Washington, DC.

Warpinski, N. R., S. L. Wolhart, and C. A. Wright (2004), Analysis and prediction of microseismicity induced by hydraulic fracturing, *SPE J.*, 9, 24-33.

Wilcock, W. S. D. (2004), Physical response of mid-ocean ridge hydrothermal systems to local earthquakes, *Geochem. Geophys. Geosyst.*, 5, Q11009, doi:10.1029/2004GC000701.

Wilcock, W. S. D., and A. T. Fisher (2004), Geophysical Constraints on the Subseafloor Environment Near Mid-Ocean Ridges, in *The Subseafloor Biosphere at Mid-Ocean Ridges*, *Geophys. Monogr. Ser.*, vol. 144, edited by W. S. D. Wilcock, et al., pp. 51-74, AGU, Washington, DC.

CHAPTER 5

CONCLUSIONS AND RECOMMENDATIONS

5.1 Conclusions

This dissertation addresses two important topics in the study of mid-ocean ridges: (1) the heat output at mid-ocean ridge hydrothermal sites, and (2) the hydrothermal response to earthquakes at mid-ocean ridges.

Our main results can be summarized as follows:

1. We designed and built a simple device to make direct seafloor measurements of advective fluid flow and heat output. Such measurements are important because they provide important constraints on the physics of seafloor hydrothermal processes. Though simple, it proved particularly robust and relatively easy to operate by deep submergence vehicles for both discrete and diffuse venting regimes.
2. We deployed the flow measuring device during the March 2004 expedition (AT11-09) to 9°50' N, East Pacific Rise (EPR). The measurements we made were the first ones on this portion of the ridge system, despite 20 years of intensive study of the area. They indicated that the average flow velocity at a low-temperature diffuse venting zone was an order of magnitude smaller than that obtained at the high-temperature vents (10^{-2} m/s versus 10^{-1} m/s). Our data also yielded a total hydrothermal heat output of $\sim 325 \text{ MW} \pm 160 \text{ MW}$

with $\sim 42 \text{ MW} \pm 21 \text{ MW}$ coming from high-temperature vents along this 2 km segment of ridge. Our measurements finally indicated that the heat output of the low-temperature diffuse venting at $9^{\circ}50' \text{ N}$, EPR, is approximately 10 times that of the high-temperature vents, but may also be one or two orders of magnitude greater.

3. From the experience gathered during this expedition, we re-designed our flow measuring device to make it easier to deploy at the seafloor. Two versions were actually built in an effort to improve the versatility of the measurements. They were deployed by the remotely operated vehicle *Jason II*, during the September 2006 expedition (MGLN07MV) to the Lau Basin, and later by the deep submergence vehicle *Alvin*, during the November 2006 expedition (AT15-13) to $9^{\circ}50' \text{ N}$, EPR.
4. We employed a mathematical model to investigate the response of hydrothermal systems to earthquakes at oceanic spreading centers. The correct interpretation of such events is of critical importance for understanding the links among magmatic, tectonic, and hydrothermal processes at mid-ocean ridges. It could provide a means of using seafloor observations to assess processes occurring at crustal depths.
5. In our approach, deep circulation gives rise to high temperature fluids that are assumed to arrive at the seafloor as focused, black smoker-like vents, whereas shallow circulation within the extrusives results in low-temperature diffuse flow. In this model, ascending fluids in both the high- and low-temperature branches are nearly isothermal except within thin boundary layers at the

seafloor and at the base of extrusives where fluid mixing occurs. Also, the residence time of fluid within the crust is of the order of years. In spite of some simplifications, our model is robust and based on fundamental physics underlying hydrothermal processes at mid-ocean ridges.

6. An important result of this work is that a thermal perturbation occurring at depth does not need to be advected along the whole discharge zone; it only needs to affect the thermal boundary layers situated close to the seafloor and at the junction with the shallow recharge in order to generate the observed temperature variations. We also showed that events which affect the rate of heat transfer at the base of the system do not give rise to rapid temperature changes; however, modest changes in permeability within the deep discharge zone are sufficient to give observable thermal perturbations. We tested our model with the well-documented temperature variations following the March 1995 seismic event at EPR and obtained results that are in excellent agreement with observations.
7. Previously, the seismic activity of the March 1995 event at EPR had been interpreted as a thermal cracking episode that enabled hydrothermal fluid to mine heat deeper in the reaction zone overlying the magma lens located beneath the ridge. We showed that the hypocentral pattern and mechanics of dike propagation from the magma lens, together with the temperature variations observed at the seafloor, suggested that the seismic swarm was more likely the result of a dike emplacement initiated at the west margin of the axial magma chamber (AMC). Our results are consistent with the

dynamics of the axial magma chamber at 9°50' N, EPR, between the two major eruptions of 1991 and 2006.

5.2 Recommendations for future work

Our recommendations for future work on the heat output at mid-ocean ridge hydrothermal sites include:

- Sending out the devices to different expeditions and keeping improving the design based on the received feedback. The paucity of heat measurements along the mid-ocean ridge system calls for heavy promotion of our devices, which are easy to use and do not necessitate our presence on-board research vessels.
- Allocating more time for each sampling at the seafloor, or repeating measurements at each investigated site. A larger amount of data is needed to improve the accuracy of our velocity and heat estimates. Cross-correlations with other measuring techniques could also greatly improve both our method and design.
- Repeating measurements at the same site over the years. Our method only gives a snapshot of the heat output picture.
- Finding new ways to estimate the size of areas of diffuse venting. The current means relies on the observation of biota and biological communities. Other areas, which have not yet been colonized may exist and thus be difficult to identify.

- Developing the design of a flow concentrator, similar to an inverted funnel, to make more robust measurements of diffuse flow. An advantage of this new device is the possibility to attach alternate means of measuring the flow rate and fluid temperature, such as a simple mechanical flow anemometer, or thermocouples within the interior of the device and along the walls of the tube. The latter would allow measuring temperature directly. Moreover, it could be an alternative way of measuring flow rate using the rate of heat loss through the tube and applying boundary layer theory. By having multiple means of determining flow rate, we could have redundancy and cross-checks on the data accuracy.

Our recommendations for future work on the hydrothermal response to earthquakes at mid-ocean ridges include:

- Taking into account the chemical aspect of the hydrothermal circulation. In particular, precipitation and dissolution are likely to be implicated in the long-term evolution of permeability.
- Incorporating the biological aspect in our model. Some biological communities are likely to develop in the shallow crust, as the occurrence of snowblower vents may testify.
- Extending the modeling of the single-path model to the deep and shallow recharge limbs in order to obtain a fully integrated model.
- Testing the model against other seismic events for which we have both the seismicity and temperature logs (e.g., the June 1999 microearthquake event on the Endeavour Segment, Juan de Fuca Ridge). In particular, events for which

both high-temperature and low-temperature records are available could allow determining more precisely the depth at which focusing starts occurring.

APPENDIX A

DESIGN OF HEAT FLOW MEASUREMENT DEVICES

The heat flow measurement device used for the March 2004 cruise (AT11-09) in the 9°50' N area of the East Pacific Rise has been described in Chapter 2 (see also Figure 2.2 and Figure 2.3). Details of this device are presented in Figure A.1 and Figure A.2.

This first version of the measurement device proved to be robust and versatile. Although its design was relatively simple, its dimensions and weight were still rather high for deployment at the seafloor. Since our long-term goal is to make the device widely available to any investigator going at sea, we improved some of the characteristics of our design. As before, we tried to avoid any complexities having in mind that the device will be deployed at the depth of 2 to 4 km beneath sea level.

The second version of the device was designed circular in shape in order to make it easier to transport and deploy, whether by a deep submergence vehicle (DSV) such as *Alvin* or a remotely operated vehicle (ROV) such as *Jason II*. Using titanium is a good way to reduce both the weight of the device and the likeliness it will corrode when in contact with hydrothermal fluids. Yet, this material being costly to manufacture, we preferred using exclusively stainless steel for all the parts and decrease the number of screws and bolts to the minimum. The walls, reduced in size (2 inches against 4 inches for the first version), were thus welded to the horizontal plate. The use of stainless steel remains a very good option when deploying the device over low-temperature diffuse vents, since these fluids are generally less corrosive. When deployed over black smokers,

however, the device requires slightly more maintenance (cleaning after each use) in order to limit the appearance of rust.

Using these specifications, two devices were built; the first device has just one central hole (similar to the first version) and walls on both sides of the horizontal plate (Figure A.3a, Figure A.4, and Figure A.5). It can be deployed both at sites of high-temperature (focused) venting and low-temperature (diffuse) flow. The second device features a total of 8 holes and just one wall situated on the upper side of the horizontal plate (Figure A.3b, Figure A.6 and Figure A.7). This device is specifically designed to be used at sites of low-temperature diffuse venting.

The circular instruments were deployed by the ROV *Jason II* at the Lau Basin during the September 2006 cruise (MGLN07MV) to make the first heat output measurement at that Integrated Study Site. They were also later deployed by the DSV *Alvin* during the November 2006 cruise (AT15-13) in the 9°50' N area of the East Pacific Rise. Figure A.8 and Figure A.9 show their use at both sites. The analysis of the data recovered during these two expeditions is though beyond the scope of this dissertation.

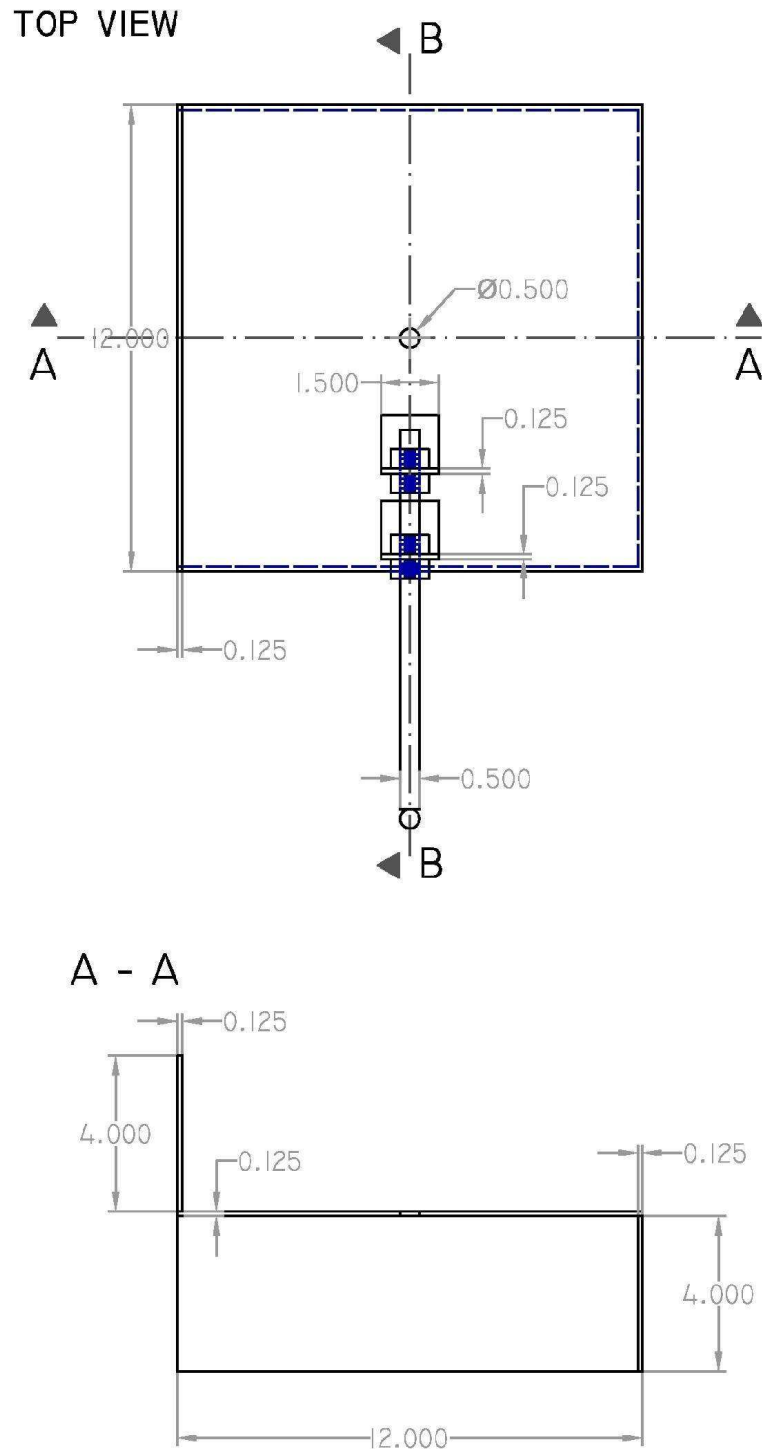


Figure A.1. Blueprints of the first version of the heat flow measurement device. This device can be used at both sites of high-temperature focused and low-temperature diffuse venting. Dimensions are in inches.

B - B

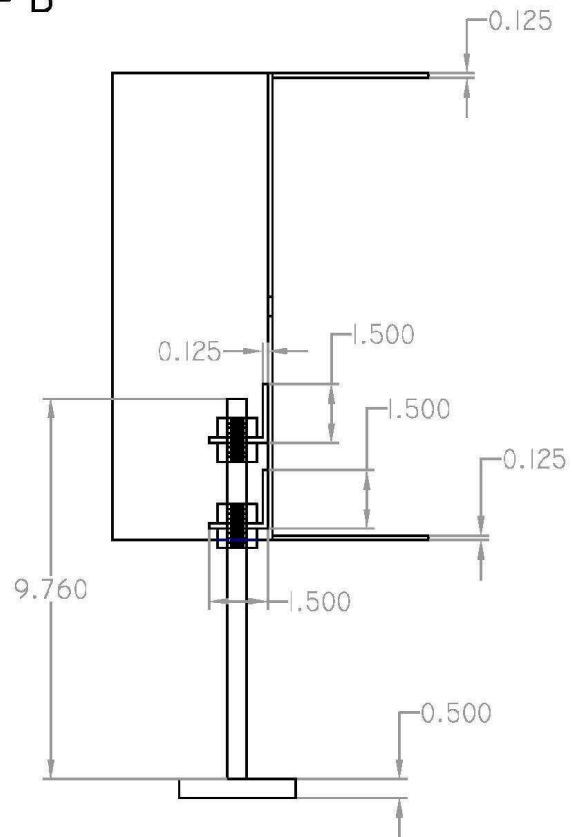
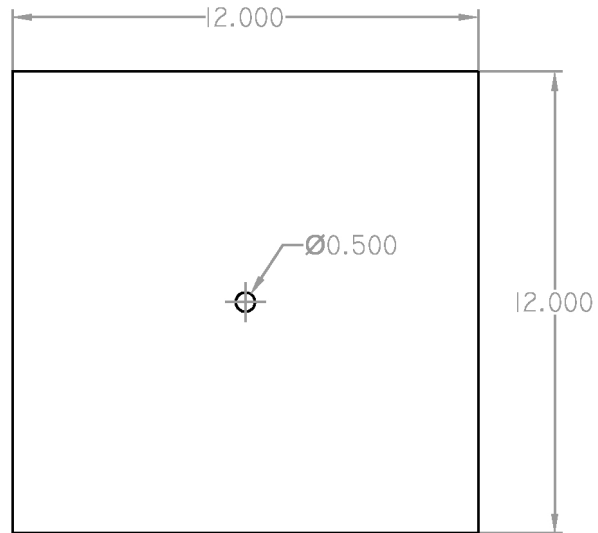
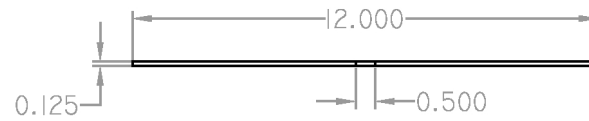


Figure A.1. (continued) Blueprints of the first version of the heat flow measurement device. This device can be used at both sites of high-temperature focused and low-temperature diffuse venting. Dimensions are in inches.

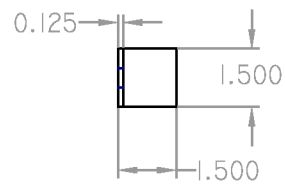
(a) TOP VIEW



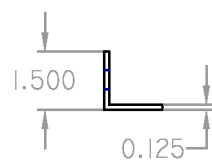
SIDE VIEW



(b) TOP VIEW



SIDE VIEW



FACE VIEW

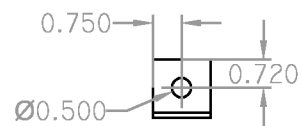
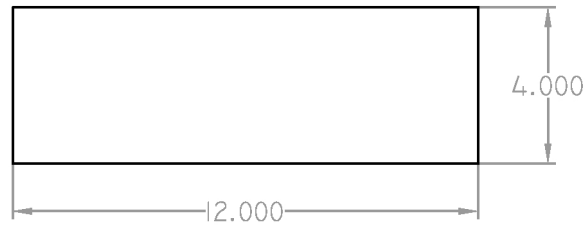


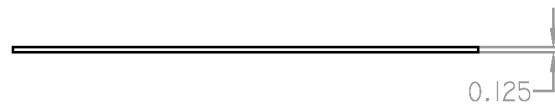
Figure A.2. Blueprints of the parts used to build the first version of the heat flow measurement device: (a) horizontal plate, (b) L-support for handle attachment on top of the plate.

(c)

TOP VIEW

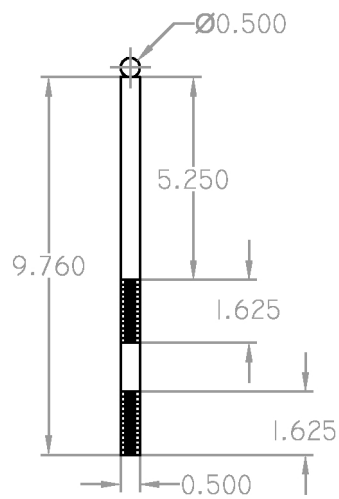


SIDE VIEW



(d)

SIDE VIEW



SIDE VIEW BIS

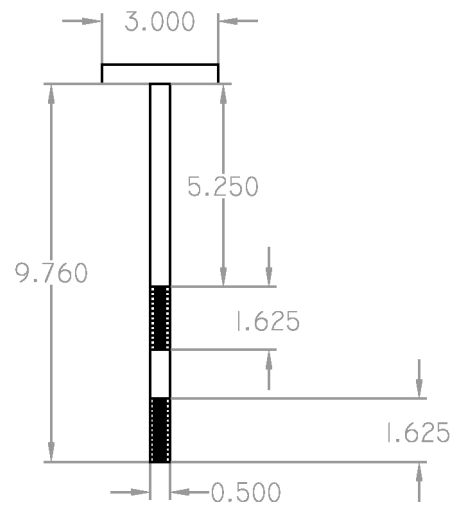


Figure A.2. (continued) Blueprints of the parts used to build the first version of the heat flow measurement device: (c) upper and lower walls, (d) handle. Dimensions are in inches.

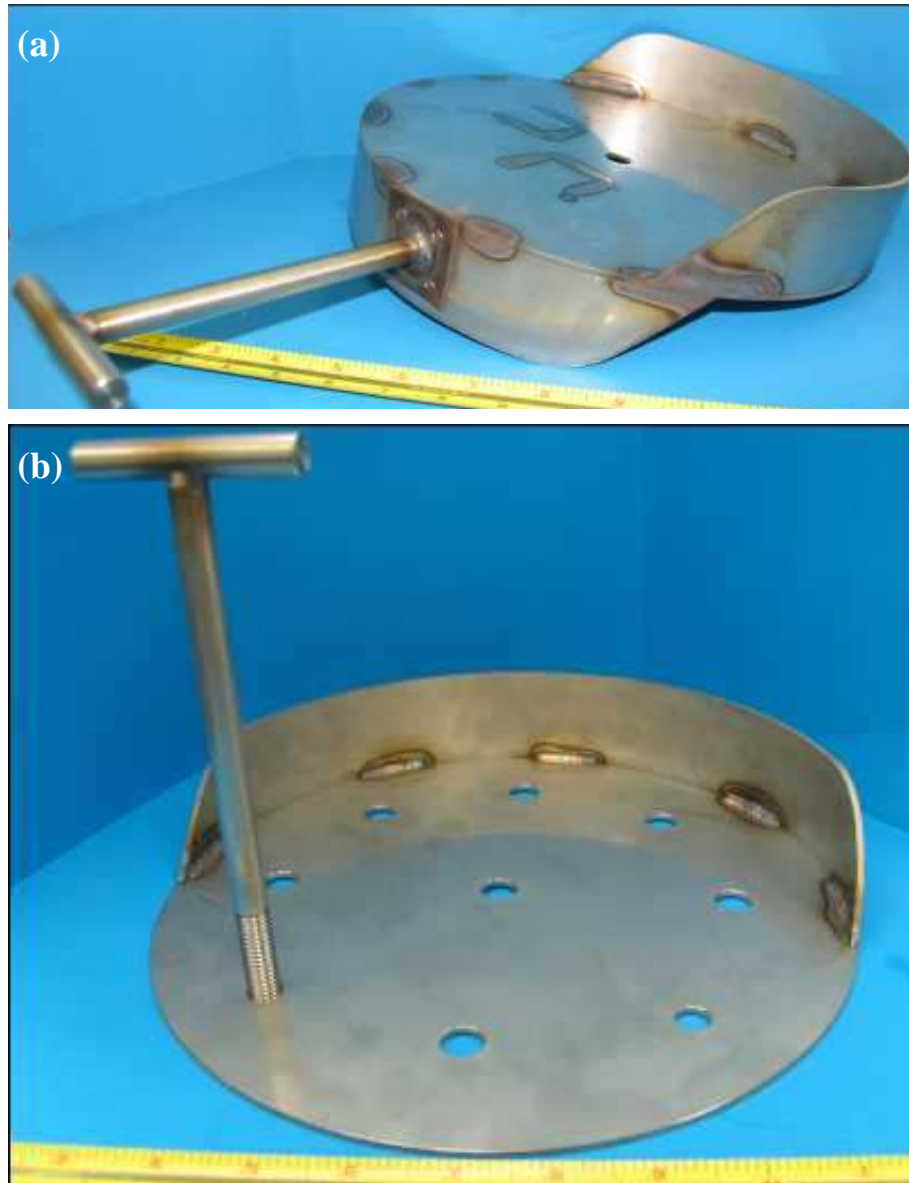
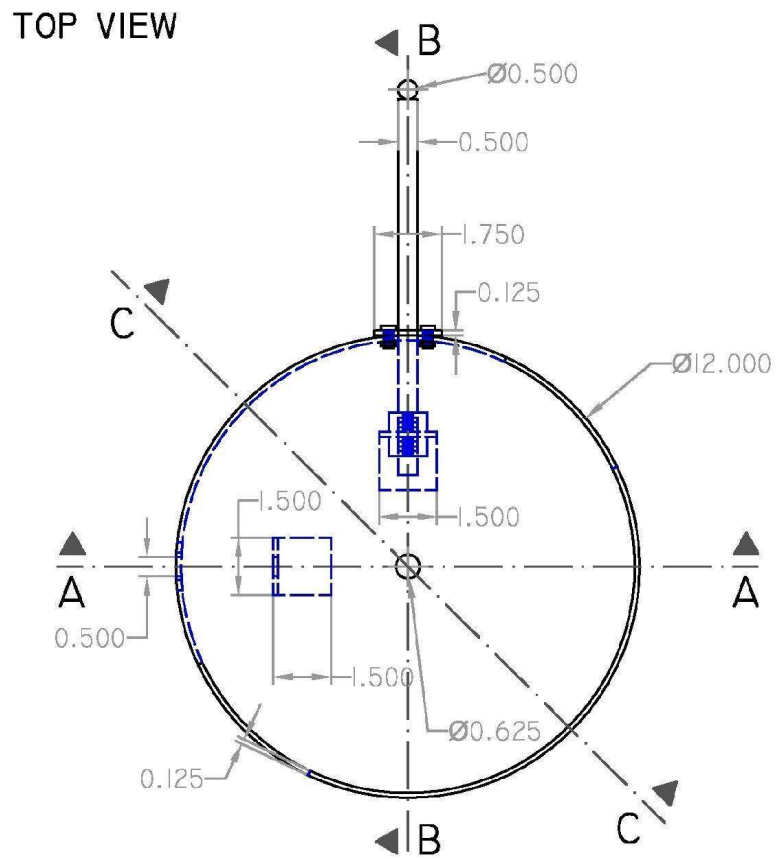


Figure A.3. Second generation of the heat flow measurement device. (a) First version with a single central hole (similar to the first generation of the device). This device can be deployed at both high-temperature focused and low-temperature diffuse venting sites. (b) Second version with multiple (8) holes. This device mainly targets sites of low-temperature diffuse flow.



A - A

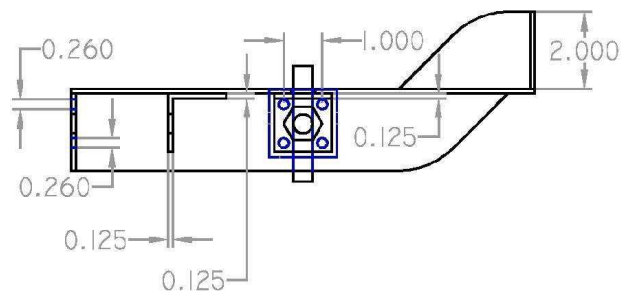
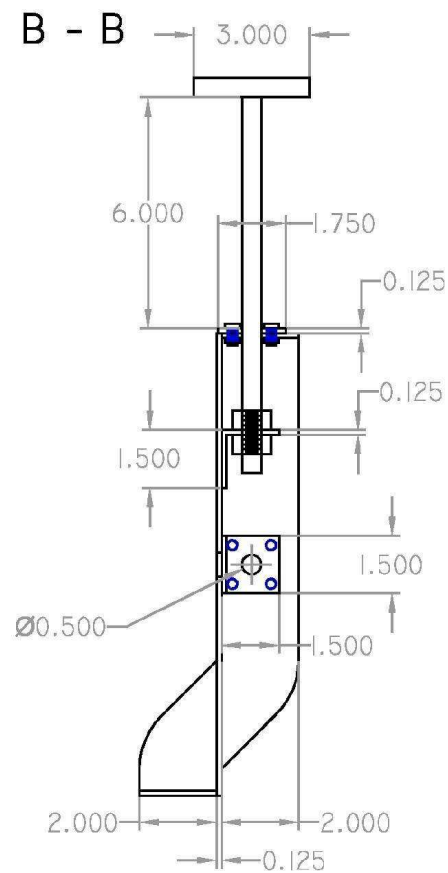


Figure A.4. Blueprints of the second version of the heat flow measurement device with a single central hole. This device can be used at both sites of high-temperature focused and low-temperature diffuse venting. Dimensions are in inches.



DETAIL C - C W/O HANDLE ATTACHED

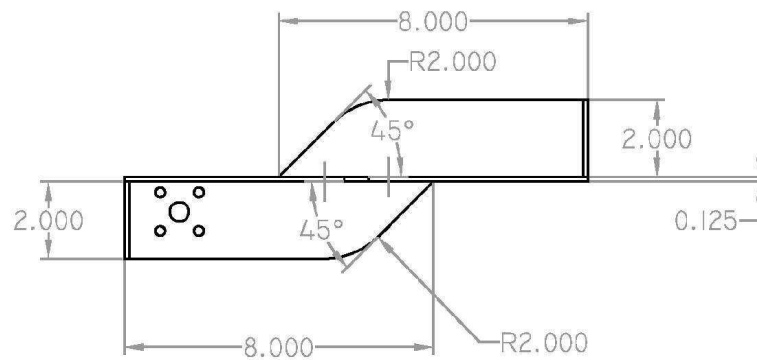
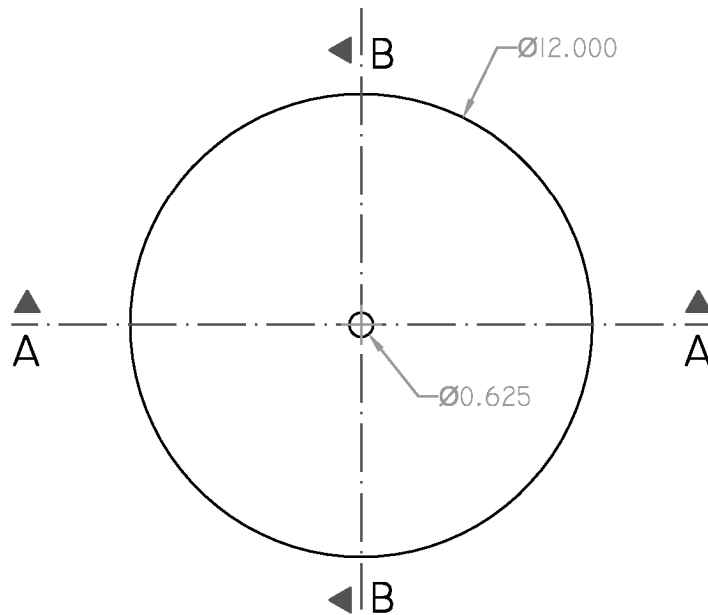
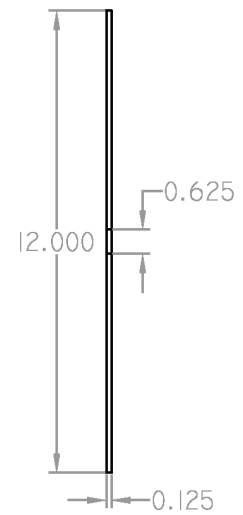


Figure A.4. (continued) Blueprints of the second version of the heat flow measurement device with a single central hole. This device can be used at both sites of high-temperature focused and low-temperature diffuse venting. Dimensions are in inches.

(a)
TOP VIEW



B - B



A - A

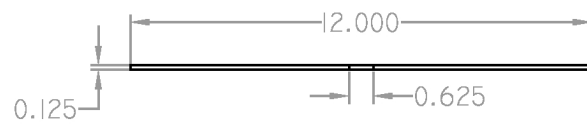
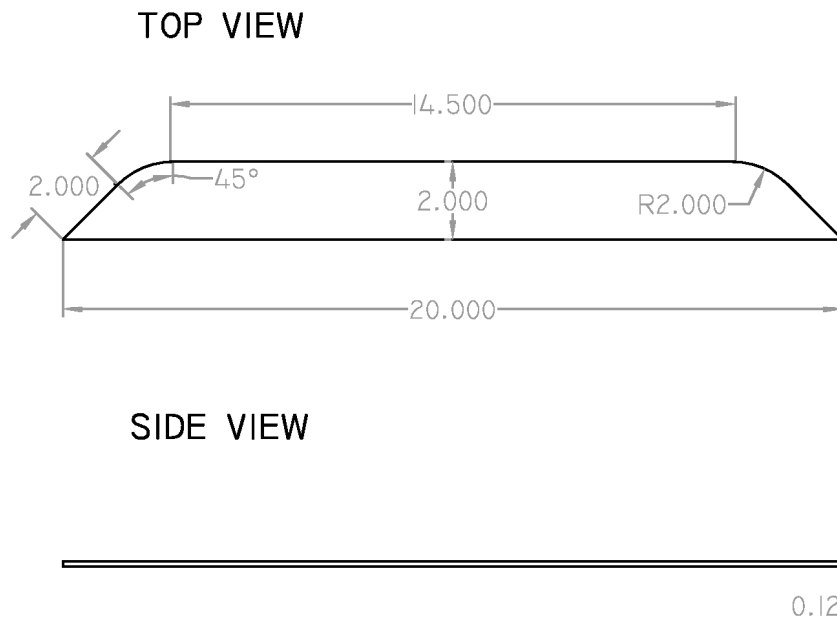


Figure A.5. Blueprints of the parts used to build the second version of the heat flow measurement device with a single central hole: (a) horizontal plate. Dimensions are in inches.

(b)



(c)

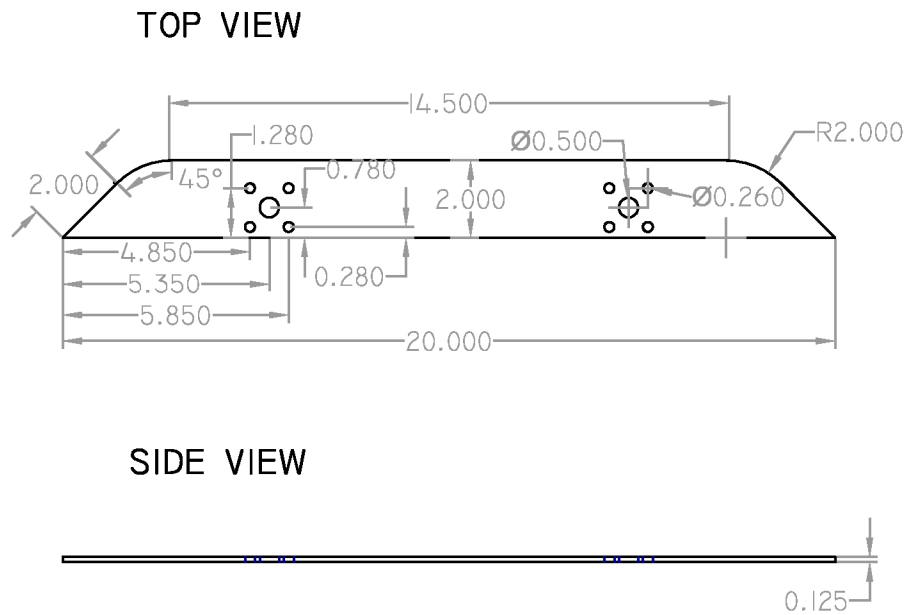
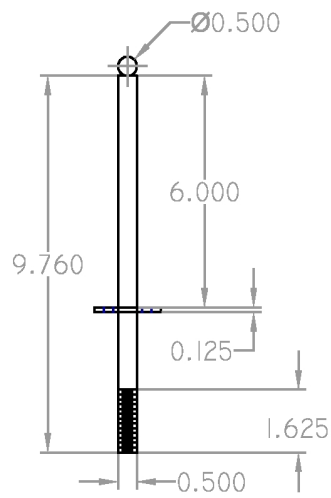
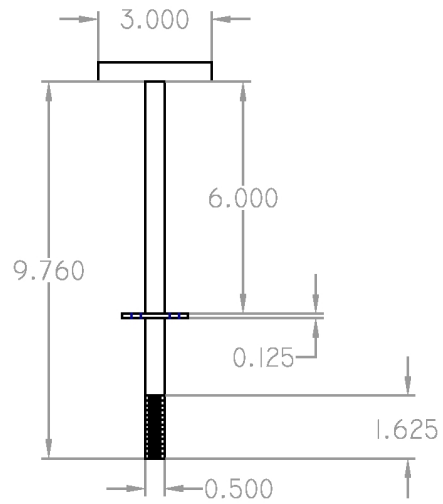


Figure A.5. (continued). Blueprints of the parts used to build the second version of the heat flow measurement device with a single central hole: (b) upper wall, (c) lower wall. Dimensions are in inches.

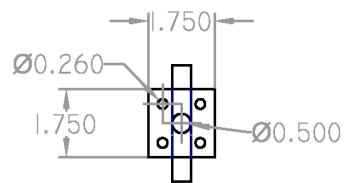
(d) SIDE VIEW



SIDE VIEW BIS



END VIEW



DETAIL PLATE

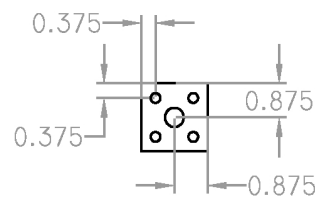


Figure A.5. (continued). Blueprints of the parts used to build the second version of the heat flow measurement device with a single central hole: (d) handle. Dimensions are in inches.

(e)

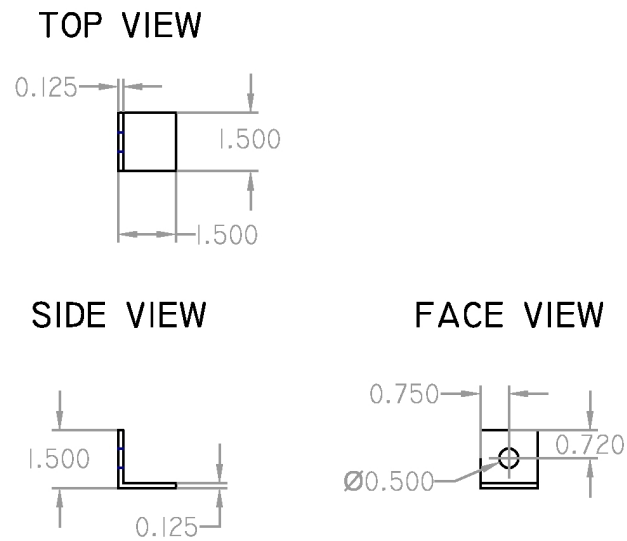


Figure A.5. (continued). Blueprints of the parts used to build the second version of the heat flow measurement device with a single central hole: (e) L-support for handle attachment underneath the plate. Dimensions are in inches.

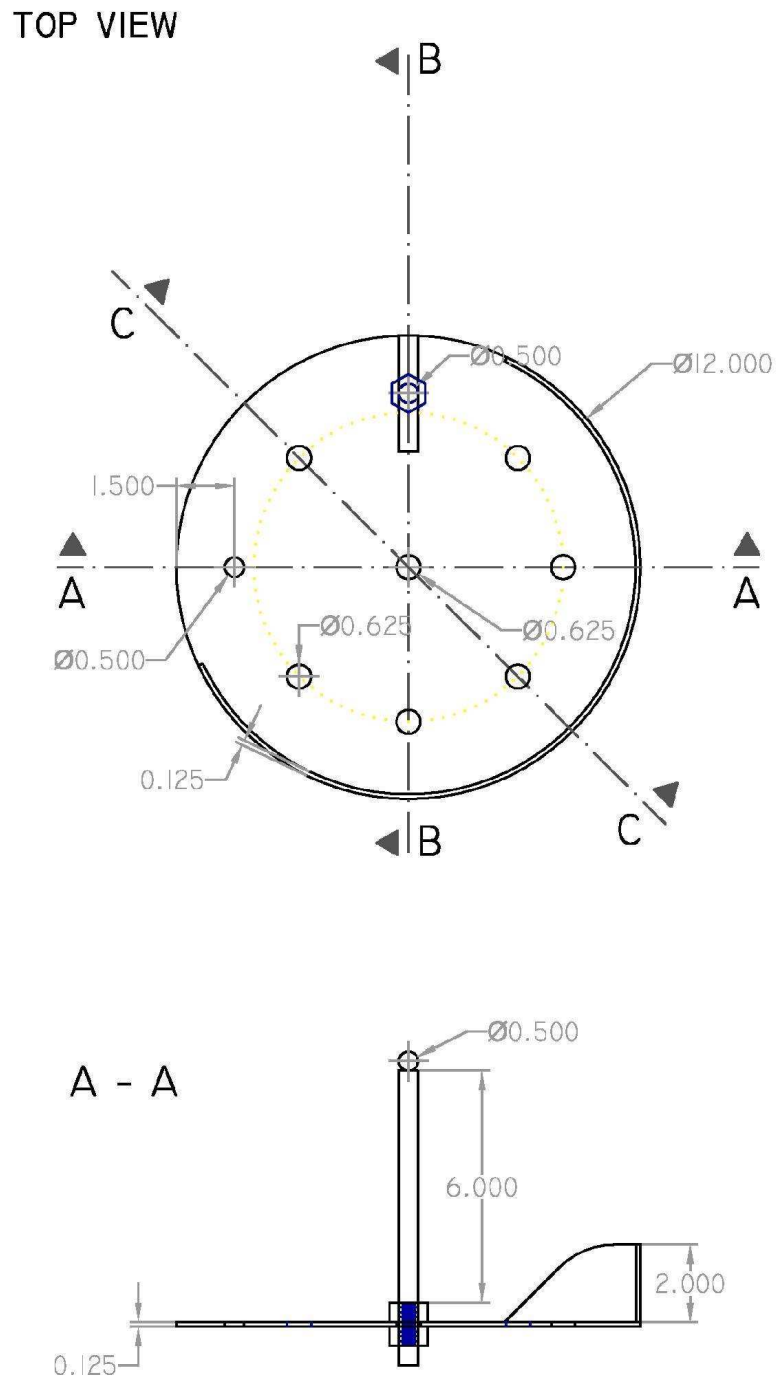
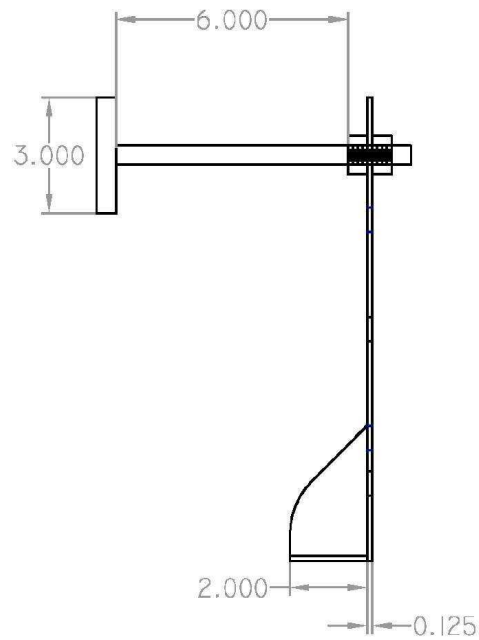


Figure A.6. Blueprints of the second version of the heat flow measurement device with multiple holes. This device was specifically designed for sites of low-temperature diffuse venting. Dimensions are in inches.

B - B



DETAIL C - C W/O HANDLE ATTACHED

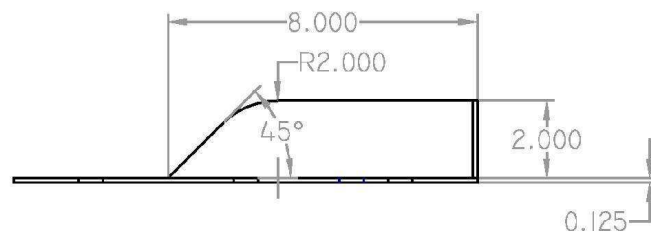
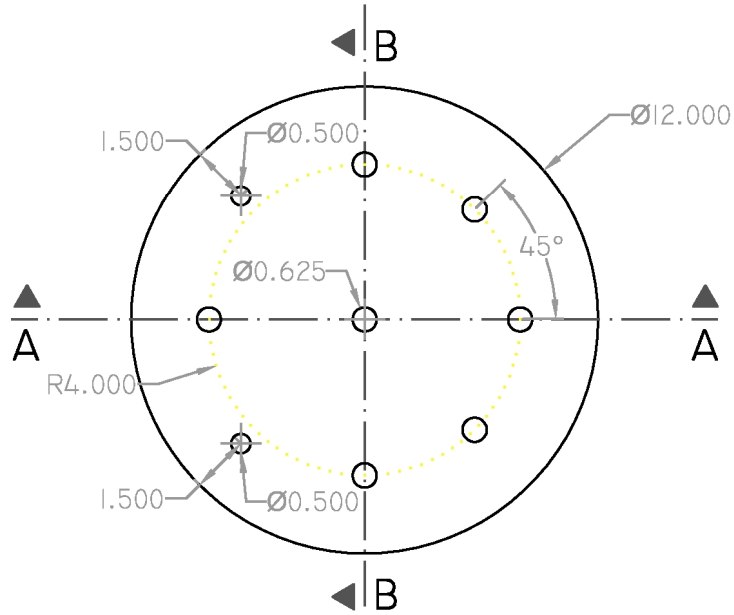


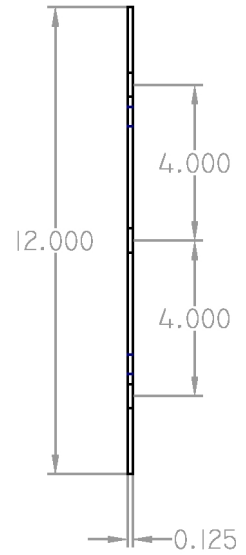
Figure A.6. (continued) Blueprints of the second version of the heat flow measurement device with multiple holes. This device was specifically designed for sites of low-temperature diffuse venting. Dimensions are in inches.

(a)

TOP VIEW



B - B



A - A

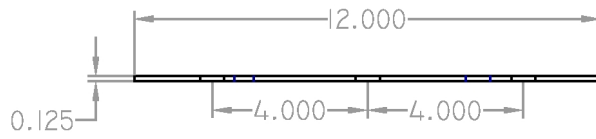
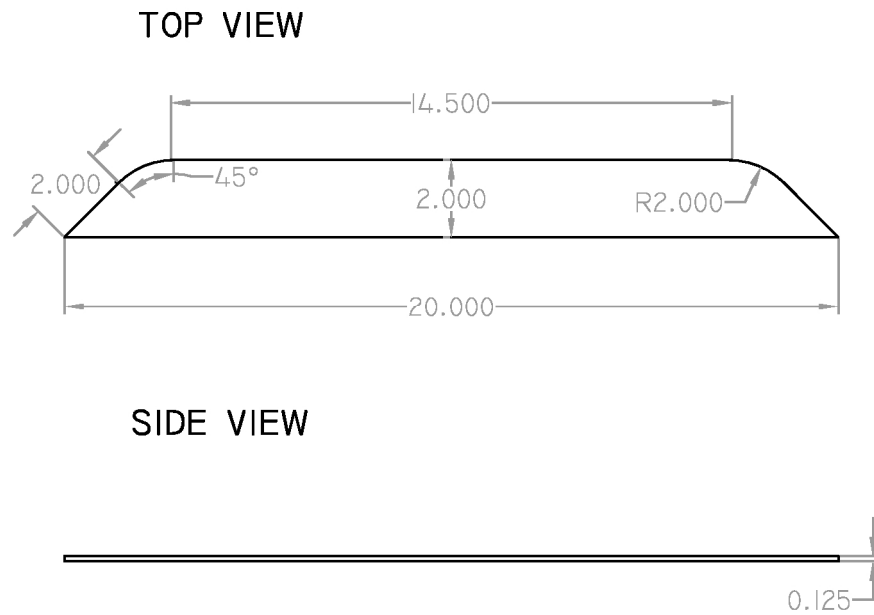


Figure A.7. Blueprints of the parts used to build the second version of the heat flow measurement device with multiple holes: (a) horizontal plate. Dimensions are in inches.

(b)



(c)

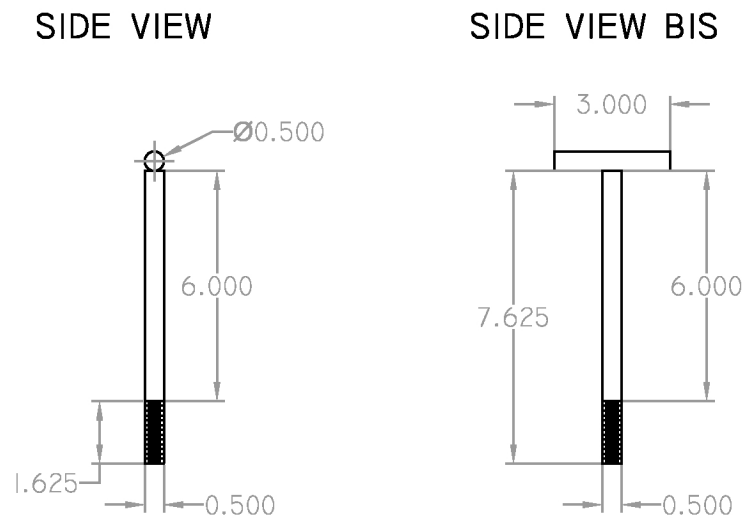


Figure A.7. (continued) Blueprints of the parts used to build the second version of the heat flow measurement device with multiple holes: (b) upper wall, (c) handle. Dimensions are in inches.

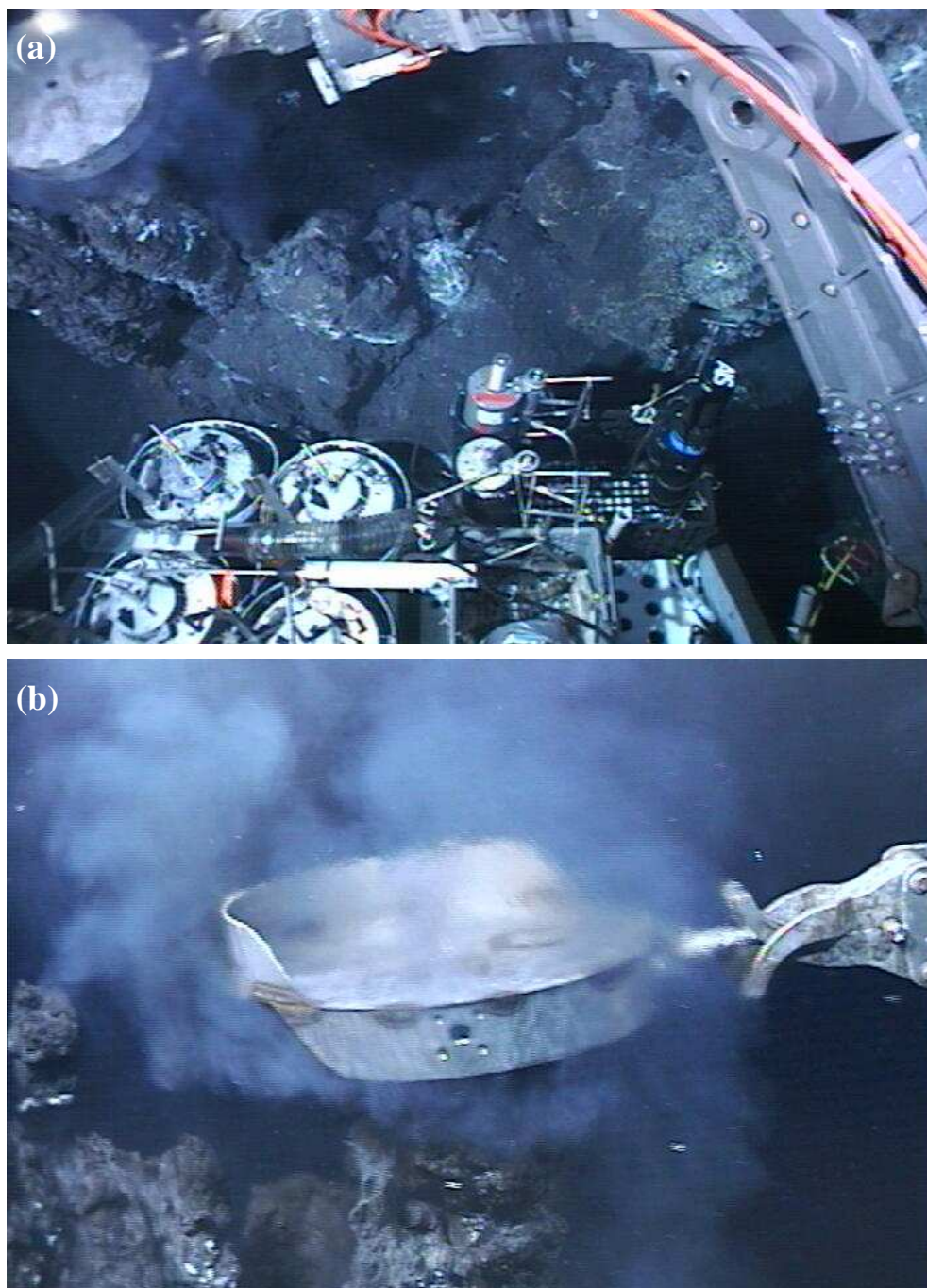


Figure A.8. Deployment of the device for flux measurements at Lau Basin during the September 2006 cruise.

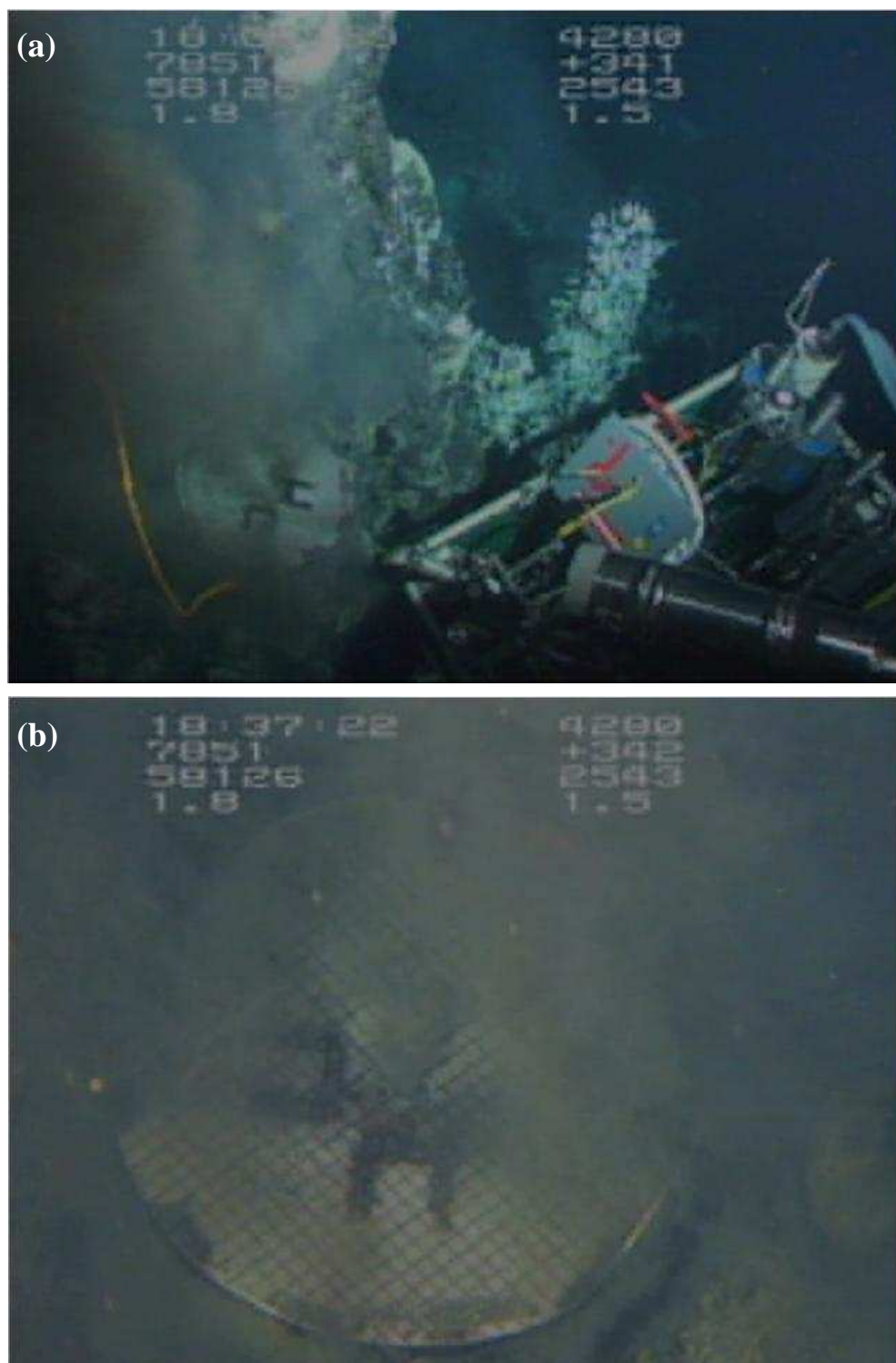


Figure A.9. Deployment of the device for flux measurements in the 9°50' N area of the East Pacific Rise during the November 2006 cruise.

APPENDIX B

DISCUSSION OF *WILCOCK'S* [2004] TEMPERATURE PERTURBATION MODEL

To describe the temperature distribution in the crack situated between two half-spaces (Figure B.1), *Wilcock* [2004] uses the following expression:

$$T(x, z, t) = T_b + \Delta T \exp\left(-x\sqrt{\frac{\omega}{2\kappa}}\right) \exp\left(-\frac{z}{H}\right) \cos\left(\omega t - x\sqrt{\frac{\omega}{2\kappa}} - \frac{z}{H}\right) \quad (\text{B.1})$$

which corresponds to the periodic temperature perturbation at the base $x = 0, z = 0$ of the crack conduit:

$$T(0, 0, t) = T_b + \Delta T \cos(\omega t) \quad (\text{B.2})$$

In (B.1), H is a characteristic length defined as

$$H = \sqrt{\frac{\kappa}{2\omega}} \frac{\rho_f c_f v w_c}{\lambda} \quad (\text{B.3})$$

In (B.1), (B.2), and (B.3), $\kappa = 5.5 \times 10^{-7} \text{ m}^2 \cdot \text{s}^{-1}$ is the thermal diffusivity, ΔT and ω the amplitude and the angular frequency of the temperature perturbation introduced at the base of the conduit, respectively. Also, T_b is the constant temperature distribution along the upflow zone before the perturbation.

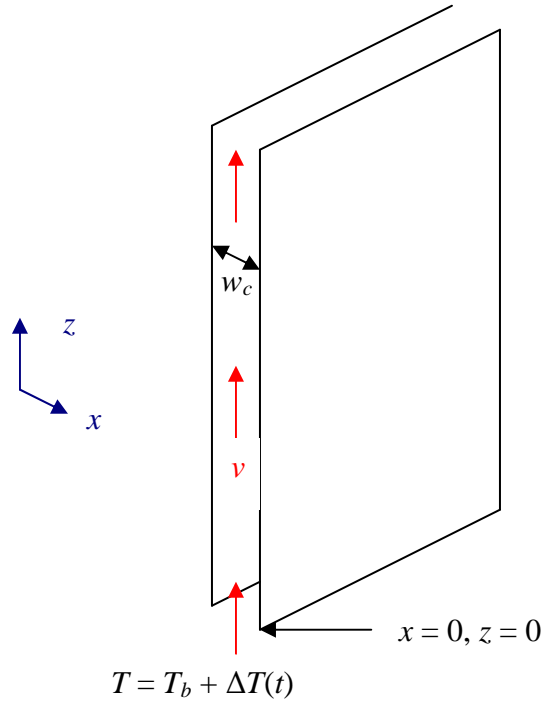


Figure B.1. Hydrothermal upflow of mean velocity v in a crack of width w_c situated between two half-spaces [modified from *Wilcock*, 2004].

To simulate the March 1995 event at 9°50' N, East Pacific Rise, *Wilcock* [2004] then uses this analytical solution to construct the response to an instantaneous basal temperature increase with subsequent linear decrease employing the Fourier method. With respect to that, we would like to comment that the Fourier integral describing the desired temperature distribution (perturbation) in dimensionless form is given by

$$\delta T(x, z, t) = \frac{2}{\pi} \int_0^\infty \left[\frac{1}{\omega} - \frac{\sin(\omega t_0)}{\omega^2 t_0} \right] \exp\left(-x \sqrt{\frac{\omega}{2\kappa}}\right) \sin\left(\omega t - x \sqrt{\frac{\omega}{2\kappa}} - \frac{z}{H}\right) d\omega \quad (\text{B.4})$$

where t_0 is the end of the linear decay time. The corresponding dependences are plotted in Figure B.2 for the bottom and the top of the upflow zone, and reproduce *Wilcock's* [2004] assumption and results, respectively.

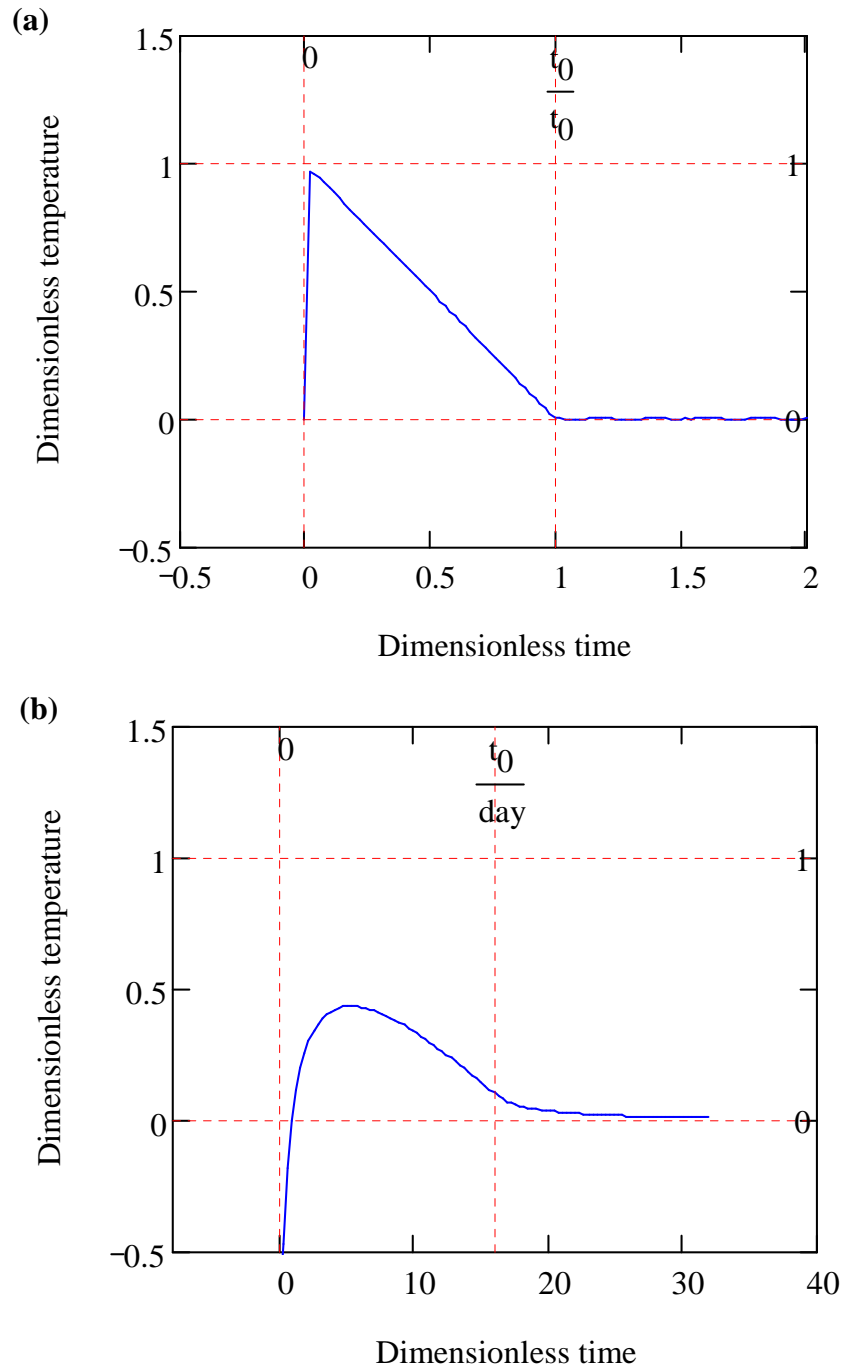


Figure B.2. Solution of equation (B.4) plotted dimensionless at (a) the bottom and (b) the top of the upflow zone.

Figure B.3 shows the temperature distribution along the upflow zone at $t = 0^+$, i.e., right after the temperature increase at the bottom. As one can see, Wilcock's [2004] solution (B.4) does not satisfy the initial condition $\delta T(x, z, t) = 0$ at $t = 0$ for any x and z . Furthermore, the deviation from zero is negative and comparable to the temperature jump ΔT at $x = 0, z = 0$ (Figure B.3).

The reason for such a behavior of solution (B.4) is due to the fact that the Fourier method assumes that the temperature perturbation at the base can be represented as a sum of harmonic functions (B.2). In this case, all the coefficients ΔT in (B.2) would be fully determined which leaves no flexibility to satisfy the boundary conditions at infinity and the initial conditions everywhere by using (B.1).

The correct solution that satisfies zero boundary conditions is well known [Lowell, 1975, 1976]. In particular, the temperature distribution in the conduit is given by (3.1).

B.1 References

Lowell, R. P. (1975), Circulation in Fractures, Hot Springs, and Convective Heat Transport on Mid-Ocean Ridge Crests, *Geophys. J. R. Astron. Soc.*, *40*, 351-365.

Lowell, R. P. (1976), Comments on 'Theory of Heat Extraction From Fractured Hot Dry Rock' by A. C. Gringarten, P.A. Witherspoon, and Yuzo Ohnishi, *J. Geophys. Res.*, *81*(2), 359.

Wilcock, W. S. D. (2004), Physical response of mid-ocean ridge hydrothermal systems to local earthquakes, *Geochem. Geophys. Geosyst.*, *5*, Q11009, doi:10.1029/2004GC000701.

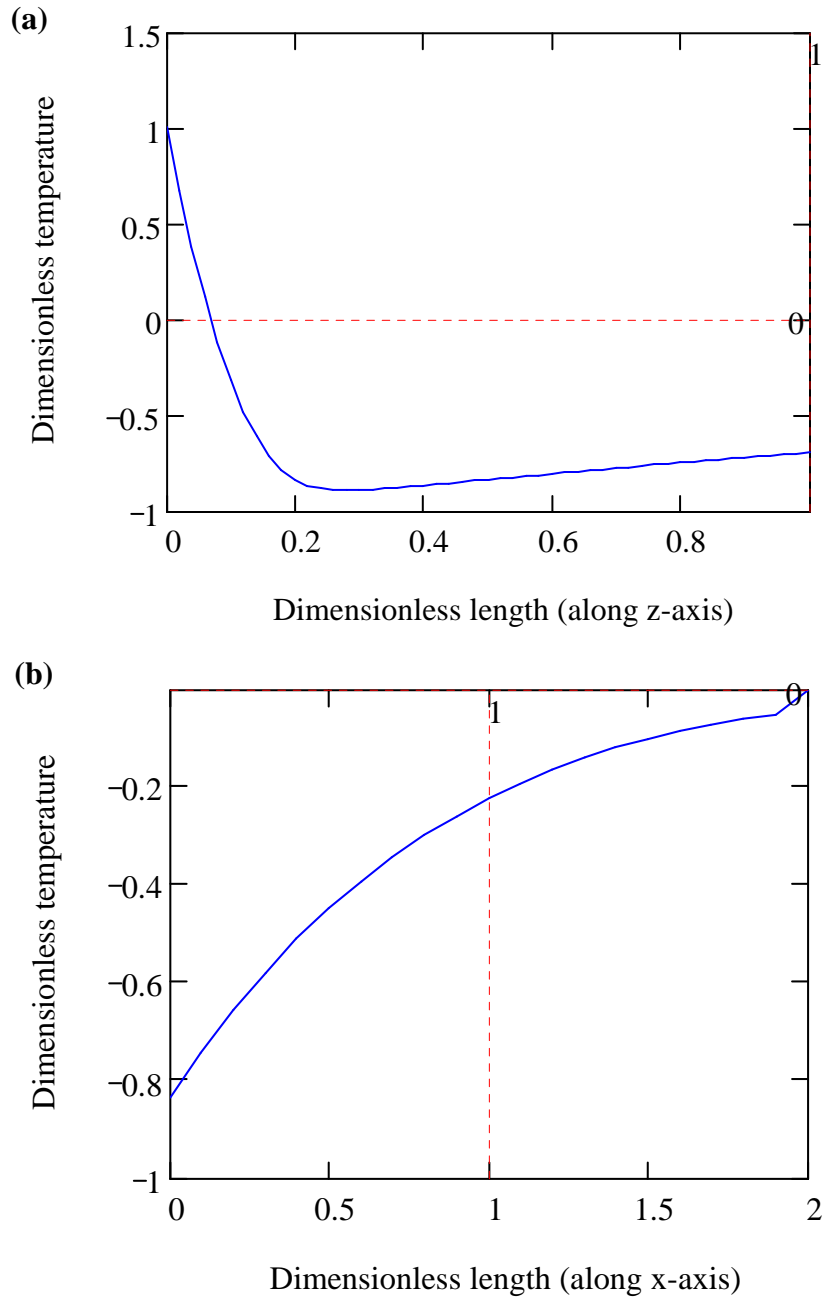


Figure B.3. Solution of equation (B.4) plotted dimensionless (a) along the upflow zone for $x = 0$, and (b) in the horizontal direction (x -axis) half way to the seafloor.

APPENDIX C

DIMENSIONLESS PARAMETERS

C.1 Summary of equations

For convenience, we summarize here the complete set of equations used in Chapter 3. All the notations used in this appendix are defined in Table 3.1 of Chapter 3.

Coordinates:

$$\begin{cases} s = z & \text{if } s \leq H \\ s = z + x & \text{if } H < s \leq H + L \end{cases} \quad (\text{C.1})$$

Velocity:

$$v = -\frac{k(T)}{\eta(T)} \left[\frac{\partial P}{\partial s} - \rho(T) g \right] \quad (\text{C.2})$$

where, for the horizontal limbs ($i = 3, 4$), the same expression is used without the gravity term $\rho(T)g$.

Fluid density:

$$\rho_f = \rho_0 [1 - \alpha_f (T - T_0)] \quad (\text{C.3})$$

Dynamic viscosity:

$$\eta(T) = \frac{C_1}{T + C_2} \quad (\text{C.4})$$

Kinematic viscosity:

$$\nu(T) = \frac{\eta(T)}{\rho(T)} \quad (\text{C.5})$$

Permeability:

$$k(T) = k_0 [1 - \gamma(T - T_{in})]^3 H[1 - \gamma(T - T_{in})] + k_{res} \quad (C.6)$$

Hydrodynamic resistance:

$$r = \int \frac{\nu(T)}{k(T)} \frac{ds}{A(s)} \quad (C.7)$$

Conservation of mass:

$$\begin{cases} Q_1 = Q_2 + Q_4 \\ Q_1 = -Q_4 \frac{r_4}{r_1} + \frac{g}{r_1} \int_0^h [\rho(T_{sh}) - \rho(T)] ds \\ Q_2 = Q_3 \\ Q_4 = \frac{g}{(r_2 + r_3)(r_1 + r_4) + r_1 r_4} \left\{ (r_1 + r_2 + r_3) \int_0^h [\rho(T_{sh}) - \rho(T)] ds - r_1 \int_0^H [\rho(T_{rech}) - \rho(T)] ds \right\} \end{cases} \quad (C.8)$$

Conservation of energy:

$$c_r \rho_r A \frac{\partial T}{\partial t} - c_f Q \frac{\partial T}{\partial s} = \lambda_r A \frac{\partial^2 T}{\partial s^2} - 2b(q_w + q_d) + 2c_f (T_h - T) AI + b q_m \quad (C.9)$$

Mass flux delivered by shallow recharge to junction region (Figure 3.5):

$$I(z) = \begin{cases} \frac{Q_4}{A_4 w_u} & \text{if } h - f/2 \leq s \leq h + f/2 \\ 0 & \text{otherwise} \end{cases} \quad (C.10)$$

Lateral heat transfer from the upflow zone:

$$q_w = -\frac{2}{\sqrt{\pi}} \frac{\lambda_r (T - T_{in})}{\sqrt{a_r t}} \quad (C.11)$$

Heat from dike:

$$q_d(z, t) = \begin{cases} -\frac{\lambda_r}{\sqrt{\pi} \operatorname{erf}(\lambda)} \frac{T_m - T}{\sqrt{a_r t}} & \text{if } 0 < t < t_c \\ -\frac{\lambda_r (T_m - T)}{\sqrt{\pi} \operatorname{erf}(\lambda) \sqrt{a_r t_c}} \exp\left(-\frac{\pi^2 a_r (t - t_c)}{w_d^2}\right) & \text{if } t \geq t_c \end{cases} \quad (\text{C.12})$$

Heat from magma chamber to deep horizontal limb:

$$q_m = \frac{\lambda_r (T_m - T)}{d} \quad (\text{C.13})$$

Distribution of Q at the junction zone:

$$Q(z, t) = Q_2(t) - AI \cdot \left(z - h - \frac{f}{2} \right) \quad (\text{C.14})$$

Boundary conditions:

$$T = T_{diffuse} \quad \text{if } s = 0, \quad t \geq 0 \quad (\text{C.15})$$

and

$$T = T_H \quad \text{if } s = H + L, \quad t \geq 0 \quad (\text{C.16})$$

where $T_{diffuse}$ and T_H are the temperatures at sites of diffuse venting and at the bottom of the recharge zone, respectively.

Initial conditions are given by the solution to the steady-state equation of energy conservation

$$-c_f Q \frac{dT}{ds} = \lambda_r A \frac{d^2 T}{ds^2} + 2c_f (T_h - T) AI + b q_m \quad (\text{C.17})$$

with the same boundary conditions (C.15) and (C.16). Mass balance conditions (C.8), mixing magnitude (C.10), and heat transfer from the magma lens (C.13) also remain the same in the steady state problem.

C.2 Scaling of problem without mixing

Studying hydrothermal circulation without mixing enables one to obtain characteristic values for the velocity, mass flux, and time scale, which can be used to non-dimensionalize the set of equations presented in the previous section. In addition, mixing in the extrusives may be not present as a result of extensive anhydrite precipitation. In that case, $Q_1 = Q_2 = Q_3$ (Figure 3.5) and, from (C.8), we have

$$Q_0 (r_u + r_h) = g \int_0^H [\rho(T_{rech}) - \rho(T)] dz \quad (C.18)$$

where $Q_0 = Q_1 = Q_2 = Q_3$, and

$$r_u = r_1 + r_2 = \int_0^H \frac{\nu(T)}{k(T)} \frac{dz}{A_1}, \quad r_h = r_3 = \int_0^L \frac{\nu(T)}{k(T)} \frac{dx}{A_3} \quad (C.19)$$

The kinematic viscosity is $\nu = \eta/\rho$ and $A_1 = A_3$. Expressions (C.3) and (C.4) give the dependence of ρ and η on temperature, respectively. In (C.19), r_u represents the hydrodynamic resistance in the upflow zone, and r_h the one in the deep horizontal limb 3.

For scaling purposes, we assume a constant permeability everywhere along the flow path (that is, $k_u = k_3 = k_0 = 10^{-13} \text{ m}^2$). As a first approximation, we ignore the conduction term, $\partial^2 T / \partial s^2$, and lateral heat loss, q_w , through the walls of the system in the conservation of energy (C.9). The temperature in the upflow zone, T_u , is thus constant and equal to the temperature at the exit of the deep horizontal limb 3 (i.e., at $x = 0$). Additionally, the far-field temperature in the recharge zone is assumed to vary linearly distributed with depth:

$$T_{rech}(z) = \beta_{rech} z \quad (C.20)$$

where β_{rech} is the thermal gradient in the recharge zone. Accordingly, we define $T_H = T_{rech}(H)$, and we can write

$$\int_0^H \rho(T_{rech}) dz = \rho_0 H \left(1 - \frac{1}{2} \alpha_f T_H \right) \quad (C.21)$$

$$\int_0^H \rho(T) dz = \rho_0 H (1 - \alpha_f T_u) \quad (C.22)$$

The distribution of temperature in limb 3 can be obtained when considering the condition of energy conservation (C.9), in which the conduction term has been ignored:

$$\frac{dT}{dx} - \frac{\lambda_r b}{c_f Q_3 d} T = - \frac{\lambda_r T_m b}{c_f Q_3 d} \quad (C.23)$$

The solution to this equation

$$T(x) = T_m + C \exp\left(\frac{\lambda_r b}{c_f Q_3 d} x\right) \quad (C.24)$$

with condition $T = T_H$ at $x = L$ (i.e., at the bottom of the recharge zone, considering that $x = 0$ corresponds to the bottom of the upflow zone) is

$$T(x) = T_m - (T_m - T_H) \exp\left(-\frac{L-x}{L_0}\right) \quad (C.25)$$

where

$$L_0 = \frac{c_f Q_3 d}{\lambda_r b} \quad (C.26)$$

is a characteristic length. When substituting expression (C.25) into (C.19) and incorporating the result into (C.18), one obtains a transcendental equation (with respect to

Q_0 , since $Q_0 = Q_1 = Q_2 = Q_3$). The solution to this equation in turn allows determining the temperature in the upflow zone $T_u = T(0)$.

To estimate the different parameters scaled in this appendix, we use $g \sim 10 \text{ m/s}^2$, $\lambda_r = 2.5 \text{ W/(m}^\circ\text{C)}$, $c_f = 4 \times 10^3 \text{ J/(kg}^\circ\text{C)}$, $k_0 \sim 10^{-13} \text{ m}^2$, $\rho_0 = 10^3 \text{ kg/m}^3$, $\alpha_f \sim 10^{-3} /^\circ\text{C}$, $T_H = 100^\circ\text{C}$, $b \sim 10^2 \text{ m}$, $d \sim 10 \text{ m}$, $H = 1500 \text{ m}$, $L = 1000 \text{ m}$, $w_u \sim 10^2 \text{ m}^2$, $A_1 \sim 10^4 \text{ m}^2$, and $A_3 \sim 10^4 \text{ m}^2$. From our computations and the observation of seafloor hydrothermal circulation, we expect temperatures up to $\sim 400^\circ\text{C}$ for the part of the upflow corresponding to black smokers (hence, in the lower part of the upflow zone; Figure 4.3). Therefore, we choose $T_u \approx 400^\circ\text{C}$, and check that our subsequent results are consistent. In turn, this fact constrains the choice of the parameters in our modeling.

Expressions (C.3) and (C.4) show that between $T_H = 100^\circ\text{C}$ and $T_u \approx 400^\circ\text{C}$, the kinematic viscosity varies between $\nu(T_H) = 3 \times 10^{-7} \text{ m}^2/\text{s}$ and $\nu(T_u) = 1.3 \times 10^{-7} \text{ m}^2/\text{s}$ (Figure C.1). For scaling purposes, we can thus consider that the kinematic viscosity is constant in the deep horizontal limb with a value $\nu_3 = \nu_0 = 10^{-7} \text{ m}^2/\text{s}$. This implies in turn that, from the order of magnitude standpoint, $\nu_u = \nu_0 = 10^{-7} \text{ m}^2/\text{s}$ in the upflow zone, since T_u is constant and equal to the temperature at the exit of the deep horizontal limb. Thereby, expressions (C.19) for r_u and r_h become

$$r_u = \frac{H\nu_0}{k_0 A_1} \quad , \quad r_h = \frac{L\nu_0}{k_0 A_3} \quad (\text{C.27})$$

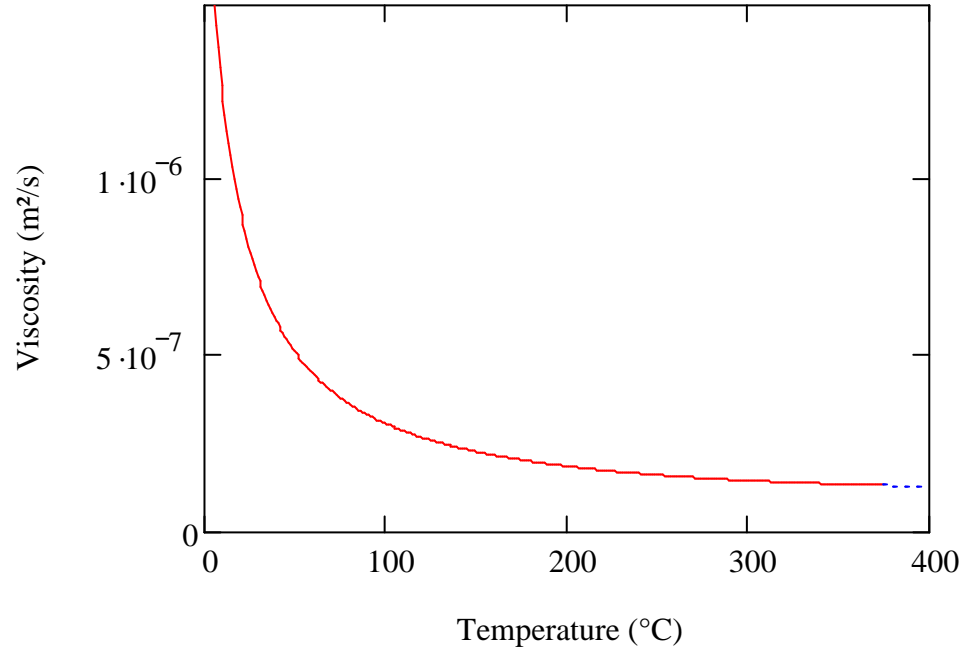


Figure C.1. Variation of viscosity of water with temperature. The dashed line indicates the region where the seawater exhibit two-phase behavior.

Substituting (C.21), (C.22), and (C.27) into (C.18) and rearranging the terms yields

$$Q_0 = \frac{g k_0 A_1 \rho_0 \alpha_f \Delta T}{\nu_0} \frac{H}{H+L} \quad (\text{C.28})$$

where $\Delta T = T_u - T_H/2$ is the difference between average temperatures in the upflow and downflow zones, and $\nu_0 = \nu_u = \nu_3$ is the typical fluid viscosity in the deep recharge and upflow zones ($\nu_0 = 10^{-7} \text{ m}^2/\text{s}$). Expression (C.28) therefore gives $Q_0 \sim 20 \text{ kg/s}$.

The velocity that corresponds to (C.28) is given by

$$\nu_0 = \frac{Q_0}{\rho_0 A_1} = \frac{g k_0 \alpha_f \Delta T}{\nu_0} \frac{H}{H+L} \quad (\text{C.29})$$

which yields $v_0 \sim 10^{-6}$ m/s ~ 10 m/year.

Recalling that heat conduction is important in the boundary layer near the seafloor (at $z = 0$), we have the scale of the thickness of the boundary layer at the top of the upflow zone:

$$\delta \sim \frac{a}{v_0} \quad (\text{C.30})$$

where $a = \lambda_r/(c_f \rho_f) \sim \lambda_r/(c_f \rho_0)$. Then,

$$\delta = \frac{a}{v_0} = \frac{\nu_0 \lambda_r}{g k_0 \rho_0 c_f \alpha_f \Delta T} \frac{L+H}{H} \quad (\text{C.31})$$

which gives $\delta \sim 1$ m.

The time scale associated with fluid flow through this boundary layer is:

$$\tau = \frac{\delta}{v_0} = \frac{\nu_0^2 \lambda_r}{(g k_0 \alpha_f \Delta T)^2 c_f \rho_0} \left(\frac{L+H}{H} \right)^2 \quad (\text{C.32})$$

which yields $\tau \sim 10^6$ s ~ 10 days.

Finally, since $Q_3 = Q_0$, substituting expression (C.28) for Q_0 in (C.25), we have the dimensionless ratio

$$\frac{L}{L_0} = \frac{\lambda_r L b}{c_f Q_0 d} = \frac{\lambda_r \nu_0}{g k_0 \rho_0 c_f \alpha_f \Delta T w_u} \frac{L}{d} \frac{H+L}{H} \quad (\text{C.33})$$

which is, as expected, independent of b . Ratio (C.33) therefore scales as

$$\frac{L}{L_0} \sim 10^{-1} \quad (\text{C.34})$$

If $L/L_0 \ll 1$, as follows from (C.25), temperature T_u in the upflow zone scales as

$$T_u = T_H + (T_m - T_H) \frac{L}{L_0} \quad (L/L_0 \ll 1) \quad (\text{C.35})$$

C.3 Dimensionless equations

To estimate the different parameters scaled thereafter, we use $g \sim 10 \text{ m/s}^2$, $\lambda_r = 2.5 \text{ W/(m}^\circ\text{C)}$, $c_f = 4 \times 10^3 \text{ J/(kg}^\circ\text{C)}$, $c_r = 10^3 \text{ J/(kg}^\circ\text{C)}$, $k_0 \sim 10^{-13} \text{ m}^2$, $\rho_0 = 10^3 \text{ kg/m}^3$, $\rho_r = 3 \times 10^3 \text{ kg/m}^3$, $\alpha_f \sim 10^{-3} /^\circ\text{C}$, $\nu_0 \sim 10^{-7} \text{ m}^2/\text{s}$, $T_H = 100^\circ\text{C}$, $b \sim 10^2 \text{ m}$, $d \sim 10 \text{ m}$, $h = 100 \text{ m}$, $H = 1500 \text{ m}$, $L = 1000 \text{ m}$, $w_u \sim 10^2 \text{ m}^2$, $A_1 \sim 10^4 \text{ m}^2$, and $A_3 \sim 10^4 \text{ m}^2$.

Coordinates. Based on (C.1), the dimensionless coordinate is defined here as

$$s' = \frac{s}{H} = \begin{cases} z' & \text{if } s' \leq 1 \\ z' + x' & \text{if } 1 < s' \leq 1 + L' \end{cases} \quad (\text{C.36})$$

where $z' = z/H$ is the dimensionless depth, $x' = x/H$ is the dimensionless coordinate in horizontal limbs 3 (Figure 3.5), and $L' = L/H$ is the dimensionless size of the horizontal limb 3 in the deep recharge (Figure 3.5).

In general, in this work, we use primes to denote the dimensionless coordinates. This does not create confusion since we do not employ this notation to represent differentiation.

Time. In the scaling of the steady-state flow without mixing (Section C.2), expression (C.32) for the time scale, τ , associated with fluid flow through the boundary layer, δ , near the top of the upflow zone can be rewritten as

$$\tau = \frac{\lambda_r}{c_f \rho_0 \nu_0^2} = \frac{\nu_0^2 \lambda_r (1 + L')^2}{(g k_0 \alpha_f \Delta T)^2 c_f \rho_0} \quad (\text{C.37})$$

where $\Delta T = T_u - T_H/2$ is the difference between average temperatures in the upflow and downflow zones, and ν_0 and k_0 are the typical fluid viscosity and permeability, respectively, in the deep recharge and upflow zones. We then use τ to introduce the dimensionless time

$$t' = \frac{t}{\tau} \quad (\text{C.38})$$

where, from (C.37), we have $\tau \sim 10^6 \text{ s} \sim 10 \text{ days}$.

Velocity. We define the dimensionless Darcian velocity as

$$v' = \frac{v}{v_0} \quad (\text{C.39})$$

where the steady-state characteristic velocity v_0 was defined in (C.29) as

$$v_0 = \frac{gk_0\alpha_f\Delta T}{\nu_0} \frac{H}{H+L} \quad (\text{C.40})$$

and scales as $v_0 \sim 10^{-6} \text{ m/s} \sim 10 \text{ m/year}$.

Temperature. It is convenient to use the typical temperature, T_u , in the upflow zone (C.35) for introducing the dimensionless temperature in the hydrothermal system:

$$T' = \frac{T}{T_u} = \frac{T}{T_H + (T_m - T_H) \frac{L}{L_0}} \quad (\text{C.41})$$

where $T_H = T_{rech}(H)$, T_m is the magma temperature, and $L_0 = c_f Q_0 d / (\lambda_r b)$ is the characteristic length defined by (C.26), where

$$Q_0 = \frac{gk_0 b w_u \rho_0 \alpha_f \Delta T}{\nu_0} \frac{H}{H+L} \quad (\text{C.42})$$

and, as described in Section C.2, $T_u \approx 400^\circ\text{C}$.

Fluid density. Based on expression (C.4), the dimensionless fluid density is defined by

$$\rho'_f(T') = \frac{\rho_f}{\rho_0} = 1 - \alpha_f T_u (T' - T'_0) \quad (\text{C.43})$$

where T' is given by (C.41) and

$$T'_0 = \frac{T_0}{T_u} \quad (\text{C.44})$$

is the dimensionless temperature at undisturbed ocean floor conditions. In (C.44), as in (C.4), fluid density, ρ_0 , corresponds to the ambient temperature, T_0 , at the seafloor.

Permeability. Following expression (C.6), we define the dimensionless permeability of the upflow zone as

$$\kappa(T') = \frac{k}{k_0} = [1 - \gamma T_H (T' - T'_{in})]^3 H[1 - \gamma T_H (T' - T'_{in})] + k'_{res} \quad (\text{C.45})$$

where

$$T'_{in} = \frac{T_{in}}{T_u} \quad (\text{C.46})$$

is the dimensionless initial (steady-state) temperature. In expression (C.45), k_0 is the typical permeability of the upflow zone at the initial steady-state temperature, T'_{in} , and $k'_{res} = k_{res}/k_0$ is the dimensionless residual permeability. While T'_{in} varies with s' , we assume for simplicity that before the system is perturbed at $t = 0$, the permeability k_0 is constant along the flow pass.

Viscosity. We introduce the dimensionless kinematic viscosity

$$\nu' = \frac{\eta}{\rho_f \nu_0} \quad (\text{C.47})$$

where ρ_f is defined by (C.3), η by (C.4), and $\nu_0 = 10^{-7} \text{ m}^2/\text{s}$ as shown in Section C.2. For diffuse flow fluid, $T \sim 1 - 10 \text{ }^\circ\text{C}$, and, the range of dimensionless kinematic viscosities is $\nu' = 0.61 - 0.94$. For black smoker fluid, the typical range of temperatures is $T \approx 300 - 400 \text{ }^\circ\text{C}$, and the corresponding range of dimensionless viscosities is $\nu' = 0.04 - 0.05$.

Hydrodynamic resistance. The hydrodynamic resistance can be normalized by $r_0 = (\nu_0 H)/(k_0 b w_u)$, which, according to (C.7), corresponds to the resistance to the flow of a fluid of viscosity, ν_0 , through the upflow zone of cross-sectional area $A_1 = A_2 = b w_u$ and permeability k_0 (Figure 3.5). The dimensionless hydrodynamic resistances thus become

$$r'_i = \frac{r_i}{r_0} \quad (\text{C.48})$$

where index i represents the i^{th} limb ($i = 1, 2, 3, 4$; Figure 3.5). With our parameters, this yields $r_0 \approx 1.5 \times 10^5 \text{ m}^{-1} \cdot \text{s}^{-1}$.

Mass fluxes. The dimensionless mass flux in the i^{th} limb is defined as

$$Q'_i = -\frac{\rho_f A_i \nu_i}{Q_0} \quad (\text{C.49})$$

where $i = 1, 2, 3, 4$ and

$$Q_0 = \frac{g k_0 b w_u \rho_0 \alpha_f \Delta T}{\nu_0} \frac{H}{H+L} \quad (\text{C.50})$$

as defined in Section C.2 ($Q_0 \sim 20$ kg/s). Following the definitions of the dimensionless Darcian velocity (C.40) and the dimensionless fluid density (C.43), the dimensionless mass fluxes Q_i' can also be defined as

$$Q_i'(s', t') = \rho_f'(s', t') v_i'(t') A_i' \quad (\text{C.51})$$

where $A_i' = A_i/(bw_u)$ is the dimensionless cross-sectional area of the i^{th} limb.

Mass flux delivered by shallow recharge to junction region (Figure 3.5). This mass flux is given by parameter I that appears in equations (C.9), (C.10), (C.14), and (C.17). With respect to the dimensionless coordinates, it is defined as

$$I(s') = \begin{cases} \frac{Q_4}{A_4 w_u} & \text{if } h' - f'/2 \leq s' \leq h' + f'/2 \\ 0 & \text{otherwise} \end{cases} \quad (\text{C.52})$$

where $h' = h/H$ is the dimensionless thickness of the extrusive layer and $f' = f/H$ is the dimensionless height of the junction zone (Figure 3.5). In (C.52), $A_4 = bf$ is the cross-sectional area of the shallow recharge limb 4 (Figure 3.5). Let us introduce

$$I_0 = \frac{Q_0}{A_4 w_u} \quad (\text{C.53})$$

so that the dimensionless mass flux per unit volume delivered by the shallow recharge to the junction region can be defined as

$$I'(s') = \frac{I}{I_0} = \begin{cases} \frac{Q_4'}{I_0} & \text{if } h' - f'/2 \leq s' \leq h' + f'/2 \\ 0 & \text{otherwise} \end{cases} \quad (\text{C.54})$$

Lateral heat transfer from the upflow zone. Based on expression (C.11), the amount of conductive heat loss, q_{w0} , that would occur at the seafloor from a fluid at temperature T_u during time τ scales as

$$q_{w0} = \frac{2}{\sqrt{\pi}} \frac{\lambda_r T_u}{\sqrt{a_r \tau}} \quad (\text{C.55})$$

Let us thus define the dimensionless lateral heat transfer from the upflow zone as

$$q'_w = \frac{q_w}{q_{w0}} \quad (\text{C.56})$$

so that according to (C.11)

$$q'_w(s', t') = - \frac{T'(s', t') - T'_{in}(s')}{\sqrt{t'}} \quad (\text{C.57})$$

Heat from dike. According to (C.12), the amount of heat, q_{d0} , that would be transferred by a dike to the upflow zone (fluid) at temperature T_u over a time τ (that is, before the dike is crystallized), scales as

$$q_{d0} = \frac{\lambda_r}{\sqrt{\pi} \text{erf}(\lambda)} \frac{T_m - T_u}{\sqrt{a_r \tau}} \quad (\text{C.58})$$

Further, we introduce the dimensionless heat generated by the dike as

$$q'_d = \frac{q_d}{q_{d0}} \quad (\text{C.59})$$

so that per (C.12)

$$q'_d(s', t') = \begin{cases} - \frac{[T'_m - T'(s', t')]}{(T'_m - 1)\sqrt{t'}} & \text{if } 0 < t' < t'_c \\ - \frac{[T'_m - T'(s', t')]}{(T'_m - 1)\sqrt{t'_c}} \exp\left[-\frac{\pi^2 a_r \tau (t' - t'_c)}{w_d^2}\right] & \text{if } t' \geq t'_c \end{cases} \quad (\text{C.60})$$

where $T'_m = T_m/T_u$ is the dimensionless magma temperature, and $t'_c = t_c/\tau$ is the dimensionless crystallization time. In this work, we have $\tau \sim 10^6$ s and $t_c \sim 10^7$ s, which yields $t'_c \sim 10$.

Heat from magma chamber. The amount of heat, q_{m0} , transferred from the magma source through the boundary layer d (Figure 3.15) to a fluid of temperature T_u is

$$q_{m0} = \frac{\lambda_r (T_m - T_u)}{d} \quad (\text{C.61})$$

Based on (C.61), we define the dimensionless heat from the magma chamber as

$$q'_m = \frac{q_m}{q_{m0}} \quad (\text{C.62})$$

so that per (C.13)

$$q'_m(s', t') = \frac{T'_m - T'(s', t')}{T'_m - 1} \quad (\text{C.63})$$

Main equations. Based on the new dimensionless parameters defined above, the condition of mass conservation (C.8) can be expressed as

$$\left\{ \begin{array}{l} Q'_1 = Q'_2 + Q'_4 \\ Q'_1 = -Q'_4 \frac{r'_4}{r'_1} + \frac{g'}{r'_1} \int_0^{h'} [\rho'(T'_{sh}) - \rho'(T')] ds' \\ Q'_2 = Q'_3 \\ Q'_4 = \frac{g'}{(r'_2 + r'_3)(r'_1 + r'_4) + r'_1 r'_4} \left\{ \begin{array}{l} (r'_1 + r'_2 + r'_3) \int_0^{h'} [\rho'(T'_{sh}) - \rho'(T')] ds' \\ - r'_1 \int_0^1 [\rho'(T'_{rech}) - \rho'(T')] ds' \end{array} \right\} \end{array} \right. \quad (\text{C.64})$$

where $h' = h/H$ and the dimensionless parameter

$$g' = \frac{g \rho_0 H}{r_0 Q_0} = \frac{g \rho_0 H}{[v_0 H / (k_0 b w_u)] \rho_0 b w_u v_0} = \frac{g k_0}{v_0 v_0} = \frac{1}{\alpha_f \Delta T} \left(1 + \frac{L}{H} \right) \quad (\text{C.65})$$

For our parameters, $g' \approx 7$.

In dimensionless form, the condition of energy conservation (C.9) along the flow path 1-2-3 (Figure 3.5) becomes

$$\begin{aligned} \frac{c_r \rho_r}{\tau} \frac{\partial T'}{\partial t'} - \frac{c_f Q_0}{b w_u H} \rho'_f v' \frac{\partial T'}{\partial s'} = \frac{\lambda_r}{H^2} \frac{\partial^2 T'}{\partial s'^2} + \frac{2c_f Q_0}{f b w_u} (T'_h - T') I' + \\ + \frac{1}{T_u w_u} \frac{2(q_{w0} q'_w + q_{d0} q'_q) + q_{m0} q'_m}{A'} \end{aligned} \quad (C.66)$$

where $T'_h = T_h/T_u$. From the definitions (C.37) and (C.50) of τ and Q_0 , expression (C.66) can further be rearranged as

$$\begin{aligned} \frac{v_0^2 H^2}{a_r a} \frac{\partial T'}{\partial t'} - \frac{v_0 H}{a} \rho'_f v' \frac{\partial T'}{\partial s'} = \frac{\partial^2 T'}{\partial s'^2} + \frac{2H^2 v_0}{f a} (T'_h - T') I' + \\ + \frac{q_{m0} H^2}{\lambda_r T_u w_u w'_i} \left[\frac{2q_{w0}}{q_{m0}} q'_w + \frac{2q_{d0}}{q_{m0}} q'_q + q'_m \right] \end{aligned} \quad (C.67)$$

where $a_r = \lambda_r/(c_r \rho_r)$, $a = \lambda_r/(c_f \rho_0)$, and $w'_i = w_i/w_u$. After introducing

$$\varepsilon = \frac{a_r}{H v_0} \quad (C.68)$$

equation (C.67) can be written as

$$\begin{aligned} \frac{a_r}{a} \frac{\partial T'}{\partial t'} - \varepsilon \frac{a_r}{a} \rho'_f v' \frac{\partial T'}{\partial s'} = \varepsilon^2 \frac{\partial^2 T'}{\partial s'^2} + \varepsilon \frac{2H}{f} \frac{a_r}{a} (T'_h - T') I' + \\ + \frac{a_r q_{m0}}{c_r \rho_r v_0^2 T_u w_u w'_i} \left[\frac{2q_{w0}}{q_{m0}} q'_w + \frac{2q_{d0}}{q_{m0}} q'_q + q'_m \right] \end{aligned} \quad (C.69)$$

Note that ε is the inverse of the Peclet number in (C.68). In equation (C.69), we have the following coefficients

$$\varepsilon = \frac{\lambda_r}{c_r \rho_r v_0 H} \sim 10^{-3} \quad (C.70)$$

$$\frac{a_r}{a} = \frac{c_0 \rho_f}{c_r \rho_r} \sim 1 \quad (\text{C.71})$$

$$\frac{2H}{f} \sim 10^3 \quad (\text{C.72})$$

$$\frac{a_r q_{m0}}{c_r \rho_r v_0^2 T_u w_u} \sim 10^{-3} \quad (\text{C.73})$$

Recalling the definition of q_{w0} , q_{d0} and q_{m0} from (C.55), (C.58) and (C.61), we can write

$$\frac{q_{w0}}{q_{m0}} = \frac{\frac{2}{\sqrt{\pi}} \frac{\lambda_r T_u}{\sqrt{a_r \tau}}}{\frac{\lambda_r (T_m - T_u)}{d}} = \frac{2\sqrt{c_r c_f \rho_0 \rho_r} v_0 d}{\lambda_r \sqrt{\pi}} \frac{1}{T'_m - 1} \quad (\text{C.74})$$

$$\frac{q_{d0}}{q_{m0}} = \frac{\frac{\lambda_r}{\sqrt{\pi} \text{erf}(\lambda)} \frac{T_m - T_u}{\sqrt{a_r \tau}}}{\frac{\lambda_r (T_m - T_u)}{d}} = \frac{1}{\sqrt{\pi} \text{erf}(\lambda)} \frac{\sqrt{c_r c_f \rho_0 \rho_r} v_0 d}{\lambda_r} \quad (\text{C.75})$$

For a typical value of $T'_m \approx 3$, we obtain

$$\frac{q_{w0}}{q_{m0}} \sim 10 \quad (\text{C.76})$$

$$\frac{q_{d0}}{q_{m0}} \sim 10^2 \quad (\text{C.77})$$

Distribution of Q' at the junction zone. Per expression (C.14) for the mass flux within the junction zone, within $h' - f/2 \leq s' \leq h' + f/2$, $\partial Q' / \partial s' = -H A I_0 I' / Q_0$, where $A = A_1 = A_2$, and the mass flux

$$Q'(s') = Q'_2 - \frac{H A' Q'_4}{f} \left(s' - \frac{h - \frac{f}{2}}{H} \right) \quad (\text{C.78})$$

is linearly distributed along this interval.

Boundary conditions. The dimensionless boundary conditions are defined based on (C.15) and (C.16) as

$$T'(s', t') = \frac{T_{diffuse}}{T_u} \quad \text{if } s' = 0, \quad t' > 0 \quad (\text{C.79})$$

and

$$T'(s', t') = \frac{T_{rech}(H)}{T_u} \quad \text{if } s = H + L, \quad t > 0 \quad (\text{C.80})$$

Initial conditions. As in Chapter 3, we define the initial conditions as the steady-state of the system prior to any perturbation. In dimensionless form, equation (C.17) becomes

$$-\frac{a_r}{a} \varepsilon \rho_f' v' \frac{\partial T'}{\partial s'} = \varepsilon^2 \frac{\partial^2 T'}{\partial s'^2} + \frac{2H}{f} \frac{a_r}{a} \varepsilon (T_h' - T') I' + \frac{a_r q_{m0}}{c_r \rho_r v_0^2 T_u w_u w_i'} \frac{T_m' - T'}{T_m' - 1} \quad (\text{C.81})$$

where in the right-hand side, the second term is only present in the junction zone (i.e., $h' - f'/2 \leq s' \leq h' + f'/2$) while the third term is present only in the deep horizontal limb 3. The initial condition is given by the solution of (C.81) with the boundary conditions (C.79) and (C.80). Given (C.63), equation (C.81) can be written as

$$a_*' \frac{d^2 (T' - T_*)}{ds^2} - v' \frac{d(T' - T_*)}{ds} - b_*' (T' - T_*) = 0 \quad (\text{C.82})$$

where $a_*' = (a\varepsilon) / (-a_r \rho_f') \sim 10^{-3}$; $T_* = T_m$ in the deep horizontal limb 3, $T_* = T_h'$ in the junction of the upflow zone with the shallow recharge, and $T_* = 0$ everywhere else; and b_*' is defined as either $b_*' = -a / (\varepsilon a_r \rho_f' v_0^2 w_u w_i' d) \sim 10^{-4}$ in limb 3, $b_*' = -(2HI') / (f \rho_f')$

$\sim 10^3$ in the junction, and $b_*' = 0$ elsewhere. The general solution of the linear, homogeneous ODE (C.82) is

$$T' = T_*' + C_1 \exp\left(\frac{v' + \sqrt{v'^2 + 4a_*'b_*'}}{2a_*'} s'\right) + C_2 \exp\left(\frac{v' - \sqrt{v'^2 + 4a_*'b_*'}}{2a_*'} s'\right) \quad (\text{C.83})$$

where dimensionless constants C_1 and C_2 are different for limbs 1, 2, 3, and the junction zone. They are determined from the boundary conditions (C.79), (C.80), and the continuity of temperatures and heat flows between the intervals. One obtains these constants as functions of the corresponding mass fluxes. Then, (C.83) is substituted into (C.64) and the resulting algebraic equations are solved to obtain the mass fluxes Q_i' in the steady-state configuration.

C.4 Concluding remarks

The presence of a small parameter in front of the highest derivative in (C.69) suggests that we have a boundary value problem of singular perturbation [e.g., *Chang and Howes*, 1984]. In regular perturbation problems, solutions vary gradually as the small parameter tends to zero. In singular perturbation problems, their solutions change rapidly as the small parameter becomes zero. If the small parameter multiplies the highest derivative, ignoring the product results in the reduction of the order of the differential equation, which typically makes the solution easier. However, this cannot be done in thin regions where the large value of the highest derivative cancels the effect of the multiplying small parameter [e.g., *Hinch*, 1991]. These regions of rapid change are known as boundary layers. In our case, the heat transport by the mechanism of heat

conduction becomes comparable to the advective heat transfer by fluid flow in the boundary layers near the surface, at $z = 0$, and near the mixing zone, at $z = h$.

In most cases, ignoring the highest derivative results in the impossibility to satisfy all boundary conditions, and corresponds to ignoring the existence of the boundary layers [e.g., *van Dyke*, 1978]. Depending upon the problem under consideration, this may or may not be acceptable [*Bender and Orszag*, 1999]. For example, for the overall consideration of flow in the hydrothermal system in Section C.2, we ignore heat conduction and, therefore, the second-order (highest) derivative, for the sake of simplifying scaling analysis. However, for the comparison of our results with field observations (Chapter 3), we need to know the detailed flow characteristics in the boundary layers, which, therefore, should be explicitly accounted for.

Although the boundary-layer problems are widely known, often equations inside or outside the boundary layer cannot be solved in closed form, and conventional techniques (e.g., matched asymptotic expansions) are difficult to implement. In particular, boundary layer problems involving non-linear differential equations frequently present this difficulty. Accordingly, these equations have to be solved numerically. There exist a number of methods that have been suggested for numerical solutions of boundary layer problems [e.g., *Bender*, 1980; *Schlichting and Gersten*, 2003; *Hegarty et al.*, 2005]. Because our problem (equations (C.2) – (C.16)) is one-dimensional, we have been able to solve it numerically by employing a finite-difference method and high-density grid, which is adequate for describing the boundary layers.

Scaling presented in Section C.2 suggests that the characteristic thickness of the boundary layers is expected to be of the order of 1 m. Therefore, we have chosen the grid spacing 1 cm or smaller, which allows treating the boundary layers with sufficient details. In our computations, we employed uniform mesh, but always made sure that the boundary layers are treated using at least $\sim 10^2$ grid points. It is well known, however, that uniform meshes are unsuitable for the numerical solution of some singularly perturbed partial differential equations because near boundary layers, the error in the numerical approximation may increase as the mesh is refined [e.g., *Hegarty et al.*, 2005]. This is why we have conducted multiple checks by refining the mesh as much as practical (up to $\sim 10^4$ grid points located within the boundary layer). In our case, the system of equations although non-linear, appeared to be stable with respect to refining the mesh.

C.5 References

Bender, C. M., and S. A. Orszag (1999), *Advanced Mathematical Methods for Scientists and Engineers*, 593 pp., Springer-Verlag, New York.

Bender, C. M., F. Cooper, G. S. Guralnik, E. Mjolsness, H. A. Rose, and D. H. Sharp (1980), A Novel Approach to the Solution of Boundary-Layer Problems, *Advances in App. Math.*, 1, 22-36.

Chang, K. W., and F. A. Howes (1984), *Nonlinear singular perturbation phenomena: theory and application*, 180 pp., Springer, New York.

Hegarty, A. F., J. J. H. Miller, E. O'riordan, and G. I. Shishkin (1995), On a novel mesh for the regular boundary layers arising in advection-dominated transport in two dimensions, *Comms in Numer. Methods. in Engineering*, 11, 435 – 441.

Schlichting, H., and K. Gersten (2003), *Boundary-Layer Theory*, 8th ed., 801 pp., Springer-Verlag, New York.

Van Dyke, M.(1975), Perturbation methods in fluid mechanics, 271 pp., Parabolic Press

APPENDIX D

FORTRAN 90 SOURCE CODE

```

!-----
! Program for Modeling the Discharge Zone of Hydrothermal Systems
!   Version 11.1 - Complete 2-loop model - Evolution version
!   Heat from Magma Lens
!-----

      PARAMETER (nz=250000)
      PARAMETER (pi=3.14159265)
      INTEGER i, iv, iz, n, nb, nd, nh, nt, nv, n1, n2
!   INTEGER iv1, iv2, iv3
      DOUBLE PRECISION, ALLOCATABLE :: T(:,,:), k(:,,:), eta(:,,:)
      DOUBLE PRECISION, ALLOCATABLE :: ro(:,,:), nu(:,,:)
      DOUBLE PRECISION bu, d, fu, hj, w, H, Hd, L, Au, As, delta
      DOUBLE PRECISION T0, TrH, Tm, Th, Q1ini, Q2ini, Q3ini
      DOUBLE PRECISION I0, sr, erf, val
      DOUBLE PRECISION alphf, alphr, cf, cr, lambr, ro0, ror, phi0
      DOUBLE PRECISION ar, g, r1, r2, r3, r4
      DOUBLE PRECISION time, dt, dz, tc, tt, tv
      DOUBLE PRECISION c1, c2, c3, c4
      DOUBLE PRECISION, ALLOCATABLE :: Q1(:,), Q2(:,), Q3(:,), rob(:,)
      DOUBLE PRECISION, ALLOCATABLE :: T1(:,), T2(:,), T3(:,), T4(:,), Qb(:,)
      DOUBLE PRECISION Tr(0:nz), xk(0:nz), a2(0:nz), Q(0:nz)
      DOUBLE PRECISION A(0:nz), B(0:nz), C(0:nz), F(0:nz)
      DOUBLE PRECISION alpha(1:nz), beta(1:nz)
      DOUBLE PRECISION a1, a3, a4, a5, a6, a7
      DOUBLE PRECISION mu1, mu2
      DOUBLE PRECISION ig1, ig2, ig4, verif1, verif2
      CHARACTER ch*10
!   CHARACTER fil*3
      ch = '0123456789'

! General Parameters
!-----
      g = 9.8                ! acceleration due to gravity
      bu = 100               ! lateral dimension of the upflow zone
      d = 100                ! width of the upflow zone
      fu = 5.0               ! dimension of the junction
      w = 5.0                ! dike thickness
      Hd = 600.0             ! height of the dike

```

cf = 4.0E3	! specific heat of water
cr = 1.0E3	! specific heat of rock
ro0 = 1.0E3	! initial density of water at the ocean floor
ror = 3.0E3	! rock density
alphf = 1.0E-3	! coefficient of thermal expansion of water
alphr = 2.0E-5	! coefficient of thermal expansion of rock
lambr = 2.5	! coefficient of thermal conductivity of rock
ar = lambr/orr/cr	! thermal diffusivity of rock
phi0 = 1.0E-2	! initial porosity of upflow zone
T0 = 20.0	! seafloor temperature
Tm = 1200	! magma temperature
delta = 7.50	! conduction layer thickness
L = 1.0E3	! length of bottom limb

! Specific Parameters From MathCAD Analysis

!-----

```

OPEN (UNIT=1, FILE="Steady.txt")
READ (1,*) c1, c2, c3, c4
TrH = c1                ! temperature of the recharge zone at the bottom
Q1ini = c2              ! initial upflow flux Q1
Q2ini = c3              ! initial upflow flux Q2
Q3ini = c4              ! initial shallow flux Q3
CLOSE (1)

```

```

OPEN (UNIT=2, FILE="Areas.txt")
READ (2,*) c1, c2, c3, c4
Au = c1                ! cross-sectional area of the discharge zone
As = c2                ! cross-sectional area of the shallow zone
H = c3                 ! height of the upflow zone
hj = c4                ! depth of the junction
CLOSE (2)
WRITE (*,*) Au, H, hj
WRITE (*,*) Q1ini, Q2ini, Q3ini

```

! Other Specific Parameters

!-----

```

time = 4.32E7
dt = 4.32E4
tv = 8.64E4
val = 0
iv = 0

```

```

PRINT*, 'Processing...'

```

! Initialization

!-----

```

tc = w*w/16.0/ar/1.0
sr = sqrt(pi*ar)
erf = 0.8427008
dz = (H+L)/nz
nt = INT(time/dt)
nv = INT(time/tv)
n1 = INT((hj-fu/2)/dz)
n2 = INT((hj+fu/2)/dz)
nh = INT(hj/dz)
nb = INT(H/dz)
nd = INT((H-Hd)/dz)

!   ALLOCATE (BCu1(1:nt))
!   ALLOCATE (BCu2(1:nt))
!   ALLOCATE (BCl1(1:nt))
!   ALLOCATE (BCl2(1:nt))
!   ALLOCATE (Dif1(1:nt))
!   ALLOCATE (Dif2(1:nt))

ALLOCATE (T(0:nz,0:2))
ALLOCATE (k(0:nz,0:2))
ALLOCATE (eta(0:nz,0:2))
ALLOCATE (ro(0:nz,0:2))
ALLOCATE (nu(0:nz,0:2))
ALLOCATE (rob(0:nb))
ALLOCATE (Q1(0:nt))
ALLOCATE (Q2(0:nt))
ALLOCATE (Q3(0:nt))
ALLOCATE (T1(0:nv))
ALLOCATE (T2(0:nv))
ALLOCATE (T3(0:nv))
ALLOCATE (T4(0:nv))
ALLOCATE (Qb(0:nv))
Q1(0) = Q1ini
Q2(0) = Q2ini
Q3(0) = Q3ini
Tr(0) = 0

OPEN (UNIT=1, FILE="Temps.txt")
DO i=0,nz
    READ (1,*) T(i,0)
    T(i,1) = T(i,0)
END DO
CLOSE (1)

OPEN (UNIT=2, FILE="Perms.txt")

```

```

DO i=0,nz
    READ (2,*) k(i,0)
    k(i,1) = k(i,0)
END DO
CLOSE (2)

OPEN (UNIT=3, FILE="Viscs.txt")
DO i=0,nz
    READ (3,*) eta(i,0)
    eta(i,1) = eta(i,0)
END DO
CLOSE (3)

OPEN (UNIT=4, FILE="Dens.txt")
DO i=0,nz
    READ (4,*) ro(i,0)
    ro(i,1) = ro(i,0)
END DO
CLOSE (4)

OPEN (UNIT=5, FILE="Denb0.txt")
DO i=0,nb
    READ (5,*) rob(i)
END DO
CLOSE (5)

DO i=0,nz
    nu(i,0)=eta(i,0)/ro(i,0)
    nu(i,1)=nu(i,0)
END DO

DO i=0,n1
    Q(i) = Q2(0)
END DO

DO i=n1+1,n2-1
    Q(i) = Q1(0)-(Q3(0)/fu/bu/d)*Au*(i*dz-hj-fu/2.0)
END DO

DO i=n2,nz
    Q(i) = Q1(0)
END DO

DO i=1,nz
    Tr(i) = Tr(i-1)+TrH*dz/H
END DO

```

```

        T1(0) = T(10240,0)
        T2(0) = T(10241,0)
!       T3(0) = T(10067,0)
!       T4(0) = T(10068,0)
!       Qb(0) = Q(10111)

!-----
!-----
! Main Block
!-----
!-----
        DO n=0,nt-1
            tt = (n+1)*dt
            I0 = Q3(n)/fu/bu/d
            Th = Tr(nh)
            a1 = ror*cr
            a3 = -lambr
            a4 = 4.0*lambr/d/sr/sqrt(tt)
            a6 = 2.0*cf*I0
            a7 = lambr/d/delta

! Term due to the dike emplacement
!-----
            IF (tt < tc) THEN
                a5 = 2.0*lambr/sr/d/erf/sqrt(tt)
            END IF

            IF (tt >= tc) THEN
                ex = exp(-1.0*pi*pi*ar*(tt-tc)/w/w)
                a5 = 2.0*lambr*ex/sr/d/erf/sqrt(tc)
            END IF

! Coefficients From the Linearization
!-----
            DO i=0,nz
                a2(i) = -cf*Q(i)/Au
                A(i) = a3/dz/dz-a2(i)/2.0/dz
                B(i) = a3/dz/dz+a2(i)/2.0/dz

                IF (i <= n1) THEN
                    C(i) = 2.0*a3/dz/dz-a1/dt-a4
                    F(i) = -T(i,1)*a1/dt-T(i,0)*a4
                END IF

                IF (i > n1) THEN

```

```

        IF (i < n2) THEN
            C(i) = 2.0*a3/dz/dz-a1/dt-a4-a6
            F(i) = -T(i,1)*a1/dt-T(i,0)*a4-a6*Th
        END IF

        IF (i >= n2) THEN
            C(i) = 2.0*a3/dz/dz-a1/dt-a4
            F(i) = -T(i,1)*a1/dt-T(i,0)*a4
        END IF

        IF (i >= nd) THEN
            C(i) = 2.0*a3/dz/dz-a1/dt-a4-a5
            F(i) = -T(i,1)*a1/dt-T(i,0)*a4-Tm*a5
        END IF

        IF (i >= nb) THEN
            C(i) = 2.0*a3/dz/dz-a1/dt-a4-a7
            F(i) = -T(i,1)*a1/dt-T(i,0)*a4-a7*Tm
        END IF

    END IF

END DO

verif1 = C(0)

IF (verif1 == 0) THEN
    STOP 0100
END IF

! Elimination Method
!-----
alpha(1) = B(0)/C(0)
beta(1) = F(0)/C(0)+T0*A(0)/C(0)

DO i=1,nz-1
    verif2 = C(i)-alpha(i)*A(i)

    IF (verif2 == 0) THEN
        OPEN (UNIT=3, File="Final.txt")
        DO iz=0,nz
            WRITE (3,100) -iz*dz, T(iz,0), T(iz,1)
        END DO
        CLOSE (3)
    END IF
END DO

```

```

!                                OPEN (UNIT=4, File="Velocity.txt")
!                                DO it=0,n
!                                    WRITE (4,*) it*dt, v(it)
!                                END DO
!                                CLOSE (4)
!                                STOP 0200
                                END IF

                                alpha(i+1) = B(i)/(C(i)-alpha(i)*A(i))
                                beta(i+1) = (A(i)*beta(i)+F(i))/(C(i)-alpha(i)*A(i))
                                END DO

                                mu1 = A(nz)/C(nz)
                                mu2 = F(nz)/C(nz)+TrH*B(nz)/C(nz)

                                T(nz,2) = (mu2+mu1*beta(nz))/(1-alpha(nz)*mu1)

                                DO i=nz-1,0,-1
                                    T(i,2) = alpha(i+1)*T(i+1,2)+beta(i+1)
                                END DO

! Computation of New Density
!-----
                                DO i=0,nz
                                    ro(i,2) = ro0*(1-alphf*(T(i,2)))
                                END DO

! Computation of New Viscosities
!-----
                                DO i=0,nz
                                    eta(i,2) = 0.032/(T(i,2)+15.4)
                                    nu(i,2) = eta(i,2)/ro(i,2)
                                END DO

! Computation of New Permeability
!-----
                                DO i=0,nz
                                    xk(i) = 1-(alphr/phi0)*(T(i,2)-T(i,0))

                                    IF (xk(i) <= 0) THEN
                                        k(i,2) = 0.01*k(i,0)
                                    END IF

                                    IF (xk(i) > 0) THEN

                                        IF (i < nd) THEN

```

```

                                k(i,2) = 0.01*k(i,0)+k(i,0)*(xk(i))**3
                                END IF

                                IF (i >= nd) THEN
                                    k(i,2) = 0.01*k(i,0)+1.5*k(i,0)*(xk(i))**3
                                END IF

                                IF (i >= nb) THEN
                                    k(i,2) = 0.01*k(i,0)+k(i,0)*(xk(i))**3
                                END IF

                                END IF

                                END DO

! Computation of Flow Resistances
!-----
                                ig1 = 0

                                DO i=nh,nb-1
                                    ig1 = ig1+(nu(i,2)/k(i,2)+nu(i+1,2)/k(i+1,2))/2.0/Au*dz
                                END DO

                                r1 = ig1

                                ig2 = 0

                                DO i=0,nh-1
                                    ig2 = ig2+(nu(i,2)/k(i,2)+nu(i+1,2)/k(i+1,2))/2.0/Au*dz
                                END DO

                                r2 = ig2

                                ig4 = 0

                                DO i=nb,nz-1
                                    ig4 = ig4+(nu(i,2)/k(i,2)+nu(i+1,2)/k(i+1,2))/2.0/10/Au*dz
                                END DO

                                r4 = ig4

                                r3 = 1.8E2

! Computation of New Mass Fluxes
!-----
                                ig1 = 0

```



```

ig2 = 0

DO i=0,nh-1
    ig1 = ig1+(rob(i)-ro(i,2)+rob(i+1)-ro(i+1,2))/2.0*dz
END DO

DO i=0,nb-1
    ig2 = ig2+(rob(i)-ro(i,2)+rob(i+1)-ro(i+1,2))/2.0*dz
END DO

Q3(n+1) = g*((r1+r2+r4)*ig1-r2*ig2)/((r1+r4)*(r2+r3)+r2*r3)
Q2(n+1) = g*ig1/r2-Q3(n+1)*r3/r2
Q1(n+1) = Q2(n+1)-Q3(n+1)

DO i=0,n1
    Q(i) = Q2(n+1)
END DO

DO i=n1+1,n2-1
    I0 = Q3(n+1)/fu/bu/d
    Q(i) = Q1(n+1)-Au*I0*(i*dz-hj-fu/2.0)
END DO

DO i=n2,nz
    Q(i) = Q1(n+1)
END DO

! Re-initialization
!-----
DO i=0,nz
    T(i,1) = T(i,2)
    k(i,1) = k(i,2)
    eta(i,1) = eta(i,2)
    ro(i,1) = ro(i,2)
    nu(i,1) = nu(i,2)
END DO

IF ((tt-val) == tv) THEN
    iv = iv+1
    ! iv1 = iv/100
    ! iv2 = (iv-iv1*100)/10
    ! iv3 = iv-iv1*100-iv2*10
    ! fil = ch(iv1+1:iv1+1)//ch(iv2+1:iv2+1)//ch(iv3+1:iv3+1)
    !
    ! OPEN (UNIT=1, File='Num'//fil//'.txt')
    ! DO iz=0,nz

```

```

!                               WRITE (1,*) T(iz,2)
!                               END DO
!                               CLOSE (1)

!                               T1(iv) = T(10240,2)
!                               T2(iv) = T(10241,2)
!                               T3(iv) = T(10067,2)
!                               T4(iv) = T(10068,2)
!                               Qb(iv) = Q(10061)
!                               val = tt
!                               END IF

!                               END DO

!-----
!-----

! Save Results in Files
!-----
OPEN (UNIT=1, File="Final.txt")
DO iz=0,nz
    WRITE (1,*) -iz*dz, T(iz,0), T(iz,2)
END DO
CLOSE (1)

OPEN (UNIT=2, File="Curve1.txt")
DO it=0,nv
    WRITE (2,*) T1(it), T2(it)
END DO
CLOSE (2)

!
! OPEN (UNIT=3, File="Curve2.txt")
! DO it=0,nv
!     WRITE (3,*) T3(it), T4(it)
! END DO
! CLOSE (3)
!
! OPEN (UNIT=2, File="Tb.txt")
! DO it=0,nv
!     WRITE (2,*) T1(it)
! END DO
! CLOSE (2)
!
! OPEN (UNIT=3, File="Qb.txt")
! DO it=0,nv
!     WRITE (3,*) Qb(it)

```

```

!      END DO
!      CLOSE (3)
!
!      OPEN (UNIT=5, File="Perm.txt")
!      DO iz=0,nz
!          WRITE (5,*) k(iz,2)
!      END DO
!      CLOSE (5)
!
!      OPEN (UNIT=6, File="Visc.txt")
!      DO iz=0,nz
!          WRITE (6,*) eta(iz,2)
!      END DO
!      CLOSE (6)
!
!      OPEN (UNIT=7, File="Parameters.txt")
!      WRITE (7,*) H, hj, time
!      CLOSE (7)
!
!      OPEN (UNIT=8, File="Qs.txt")
!      DO it=0,nt
!          WRITE (8,*) Q1(it), Q2(it), Q3(it)
!      END DO
!      CLOSE (8)
!
!      OPEN (UNIT=9, File="Dens.txt")
!      DO iz=0,nz
!          WRITE (9,*) ro(iz,2)
!      END DO
!      CLOSE (9)
!
! Format
!-----
100  FORMAT (3E12.4)
105  FORMAT (2E12.4)
!
      END

```

APPENDIX E

DIRECTION OF DIKE PROPAGATION

FROM THE MAGMA LENS

Although the dike trajectory is sub-vertical, it slightly curves inwards, so that the dike tip is located above the magma lens (e.g., slightly to the right in Figure 4.1b). It may appear that because the least principal stress is horizontal in mid-ocean ridge environment, the dike should be practically vertical rather than curved, even slightly, as in Figure 4.1b. However, the computed dike shape can be understood by considering first a vertical dike emanating from the magma lens (Figure E.1a). Kinematically, because the dike and the lens are connected, the lens opening results in shear displacements of the dike sides, so that $K_{II} \neq 0$ at the dike tip of a vertical dike. Therefore, had the dike been vertical, it would have started propagating outwards (as shown by the dashed line in Figure E.1a). Dike propagation in this direction would be reducing K_{II} , and the dike curvature would be compensating K_{II} resulting from the magma lens opening (as described above).

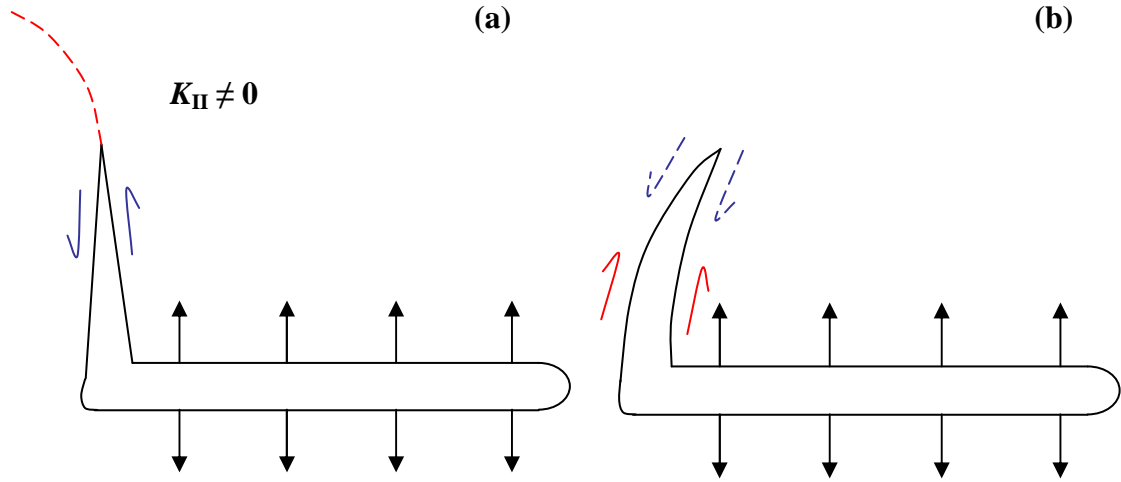


Figure E.1. Dike trajectories.

Because in our calculations we used the conventional criterion of crack growth direction, that is, $K_{II} = 0$ [Rice, 1968], the dike curves inwards instead of being vertical. This curvature compensates K_{II} (or shear displacements) due to the lens opening, which is illustrated by arrows in Figure E.1b. Displacements shown by solid arrows in Figure E.1b are due to the lens opening, while dashed arrows indicate displacements of the dike sides mainly caused by the gravity forces. These two displacement modes cancel each other at the dike tip, resulting in condition $K_{II} = 0$ satisfied during the entire period of dike propagation.

E.1 References

Rice, J. R. (1968), Mathematical Analysis in the Mechanics of Fracture, in *Fracture: An Advanced Treatise, Mathematical Fundamentals*, vol. 2, edited by H. Liebowitz, pp. 191-311, Academic Press, N.Y.

APPENDIX F

FLOW REGIME IN THE UPFLOW ZONE

We can estimate the flow regime (i.e., laminar or turbulent) by considering the case of similarly oriented fractures of width ζ . In that case, the permeability k_0 is approximatively given by

$$k_0 \sim \frac{\phi_0 \zeta^2}{12} \quad (\text{F.1})$$

where ϕ_0 is the porosity. It is typically taken within a range of 0.1-1% at mid-ocean ridges. For a value of 0.1%, and $k_0 \sim 10^{-13} \text{ m}^2$, (F.1) yields $\zeta \sim 10^{-4} \text{ m}$. Therefore, assuming that the flow occurs through such fractures of width ζ , Reynolds number Re is given by

$$\text{Re} = \frac{v_2 \zeta}{\phi_0 V_0} \sim 1 \quad (\text{F.2})$$

which places the fluid flow in the laminar domain in the discharge zone (turbulent flow is observed for $\text{Re} \sim 1000$ in laboratory experiments). Had we taken $\phi_0 = 1\%$, Reynolds number would have been $\text{Re} \sim 10^{-2}$. We can thus conclude that mixing within the junction zone occurs at laminar regime in our simulations.